Mixed Quantum/Classical Theory (MQCT) for Rotationally and Vibrationally Inelastic Scattering and Its Application to the Molecules of Astrochemical Importance

Alexander Semenov
Marquette University

MIXED QUANTUM/CLASSICAL THEORY (MQCT) FOR ROTATIONALLY AND VIBRATIONALLY INELASTIC SCATTERING AND ITS APPLICATION TO THE MOLECULES OF ASTROCHEMICAL IMPORTANCE

by

Alexander Semenov

A Dissertation Submitted to the Faculty of the Graduate School,
Marquette University,
in Partial Fulfillment of the Requirements for
the Degree of Doctor of Philosophy

Milwaukee, Wisconsin

August 2017

ABSTARCT

MIXED QUANTUM/CLASSICAL THEORY (MQCT) FOR ROTATIONALLY AND VIBRATIONALLY INELASTIC SCATTERING AND ITS APPLICATION TO THE MOLECULES OF ASTROCHEMICAL IMPORTANCE

Alexander Semenov

Marquette University, 2017

This thesis presents developments and applications of the mixed quantum/classical theory (MQCT) for inelastic scattering. In this approach, translational motion of collision partners is treated classically, while the internal degrees of freedom – rotational and/or vibrational motion – are treated quantum mechanically. Within this framework calculations of rotationally inelastic cross sections are carried out in a broad range of collision energies and results are compared against the exact full quantum data for several real systems. For CO +He, N_2 + Na and H_2 + He the agreement is excellent through six orders of magnitude range of cross sections values and for energies $1 < E < 10000$ cm^{-1}. Elastic and differential cross section for N_2 + Na are described very accurately. For ro-vibrational transitions in CO + He and H_2 +He MQCT reproduces full quantum results even for highly excited rotational states. For H_2O + He it is found that at lower energies the typical errors for cross sections are on the order of 10%, which is acceptable. It is showed that computational cost of the fully-coupled MQCT scales as n^{2-3}, where n is the number of channels which is far more favorable in comparison with full quantum scaling n^{5-6}. This enables calculations on larger molecules and at higher collision energies, than was possible using the standard approach. The largest system ever considered for rotational scattering, $HCOOCH_3$ + He, is also treated by MQCT. At energies where quantum results are available (≤ 30 cm^{-1}) the agreement is found very good. Then MQCT calculations for this system are extended up to $E = 1000$ cm^{-1}. Finally, theoretical framework for treatment of molecule + molecule scattering is developed and applied to H_2+H_2 and N_2+H_2 systems where excellent agreement with exact quantum results is found. We also apply MQCT method to H_2O + H_2O rotationally inelastic scattering and obtain the first and only data for this process in a broad range of collisional energies. Success of MQCT makes this theory a practical tool for obtaining the state-to-state transition rates for astrochemical modeling and other applications.

ACKNOWLEDGMENT

Alexander Semenov

I would like to thank my family. I as a recipient of the Jobling Assistantship and the Raynor Fellowship acknowledge the support form Marquette University and Graduate School. I also acknowledge the support from the National Science Foundation and the National Aeronautics and Space Administration.

TABLE OF CONTENTS

LIST OF TABLES

LIST OF FIGURES

INTRODUCTION

CHAPTER 1

INTRODUCTION

1.1 The Field of Astrochemistry

Collisional energy transfer plays a significant role in molecular phenomena as a leading process which determines energy distribution between reaction partners. It encompasses a broad range of processes such as recombination reactions and inelastic scattering. The substantial impact of inelastic scattering in energy balance can be seen in various processes in the astrochemical environment and in many combustion reactions.

An interdisciplinary field which involves astronomy, chemistry and physics is called astrochemisrty. The abundance and reactions of molecular species in space, their chemical composition and interaction with electromagnetic fields are the main subject of the discipline. The study includes several major research areas [1].

The first one is finding and identification molecular species in the space which is based on cosmic radiative spectra. Analysis of such spectra also allows determine to the quantitative parameters which characterize conditions in the interstellar medium (the ISM) i.e. temperature, pressure and density.

Figure 1. Orion Nebula. NASA's Hubble Space [2].

Another closely related aspect – laboratory measurements on molecules of astronomical interest such as determination of reaction rates.

The large part of astrochemistry is modeling. Quantitate analysis of accumulated data is possible due theoretical developments which includes a broad variety of different methods such as models of radiative energy transfer and reactive scattering calculations. A recent extensive development of computational facilities allows computational modeling to become a powerful and very useful tool which is widely used for needs of astrochemists [3].

Another important area of astrochemisty is searching planets which chemical composition and physical conditions are like the environment on Earth. Finding such planets using molecular signature can provide an understanding the chemical origin of life. In other words, astrochemistry is the study of the interstellar medium (ISM).

The Galaxy continuously evolves due to the processes which occur in the ISM[3]. During the life cycle of star, the nuclear reactions in the stellar interiors produce elements from light nuclei of hydrogen and helium which make up 98% of stellar mass. These products of stellar nucleosynthesis can be injected in a supernova explosion at the end of stellar evolution slowly increasing the abundances of heavy elements in the ISM. Thus the ISM serves as a repository of previous descents of stars and a birthplace of future generation of the Galaxy objects.

1.2 Major Observational Facilities

Extensive spectroscopic observations of astrochemical species in space have been carried out for decades and numerous amount of data such as rotational and vibrational spectra have been accumulated [5]. All of that is possible due to high-resolution radiospectroscopically facilities. Different equipment has been used to register and measure radiative spectra of certain wavelength regions. FUSE (Far Ultraviolet Spectroscopic Explorer), the STIS (Space Telescope Imaging Spectrograph) and COS (Cosmic Origins Spectrograph) instruments on board the Hubble Space Telescope are used to measure far-ultraviolet spectra. The Spitzer space telescope, SOFIA (Stratospheric Observatory for Infrared Astronomy), and Herschel Space Observatory (HSO) work at infrared and submillimeter wavelengths and provide the detailed probing of dark clouds including both low- and high-mass star-formation domains and showed the chemical diversity of these environments [7]. Many new species have been detected, such as water, which rotational transitions due to collision is specifically discussed in the present work, and several molecular ionic hydrides, among other new molecular species, which demonstrated unexpected aspects of chemical complexity. Finally, ground based telescopes such as APEX (Atacama Pathfinder Experiment), CSO (Caltech Submillimeter Observatory), the

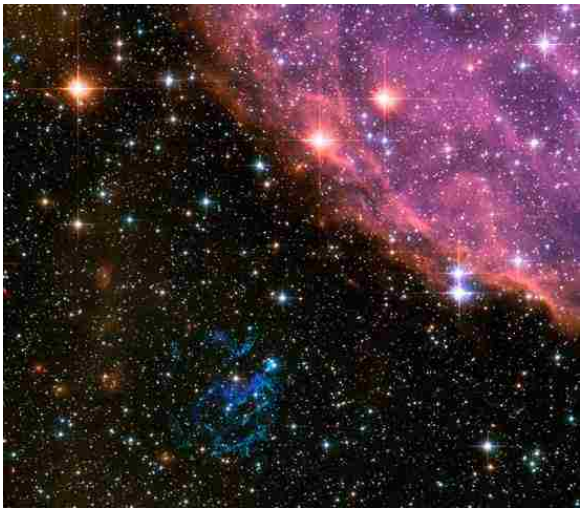

Figure 2. The supernova remnant E0102. It is the greenish-blue shell of debris below the center of the Hubble image. [4].

30-m telescope and the Plateau de Bure interferometer of IRAM (Institut de Radioastronomie Millimétrique) and The Nançay decimetric radio telescope (Le radiotélescope décimétrique de Nançay (NRT) with tilting primary mirror consists of ten panels, each 20 m long and 40 m high) have extended their spectral resolution bandwidth and sensitivity capabilities, and the ALMA (Atacama Large Millimeter Array), astronomical interferometer of radio telescopes, is in intensive development now, with both high spatial and spectral resolution [5,7].

1.3 Chemical Diversity in the ISM

Basically, the ISM is filled with rarefied hydrogen and helium gases and much smaller amount (less than 2%) of heavier elements which are found in neutral, ionized or in molecular form. These elements can be observed in the gaseous or solid state. Since the discovery of the first molecule in the interstellar medium about fifty years ago, the number of detected molecules has gradually increased with time to more than 200 molecules [5,7,10]. H_2, CO, and H_2O molecules are the first, second, and third most abundant molecules, respectively, and can be found in different regions under various conditions in the ISM. They have been the subjects of in-depth research and play a fundamental role in astrochemistry, thereby it makes them an object of comprehensive theoretical and experimental studies. Along with these keystone molecules other molecular species are frequently observed: The cyano radical (CN) [5,12] is relatively

Figure 3. The Caltech Submillimeter Observatory [6].

ubiquitous; it was the second identified interstellar molecule in diffuse gas, due to its visible absorption features; Sulfur-bearing compounds (CS,SiS,SO,SO_2) [13-15]; these species are widely distributed in various domains of the ISM and are valuable diagnostics of dark clouds, star-forming domains, and photo dissociation regions, as well as markers of shocked regions (along with the SiO molecule); ammonia (NH_3) [16,17], which was the first polyatomic molecule detected toward the galactic center because of its centimeter inversion transitions; since the inverse transitions between the energy levels can occur only through collisions the molecule was immediately considered as a potential thermometer. In addition, the energy levels involved in these transitions are quite distinguishable and take place in a relatively narrow wavelength range which is approximately 1.3 cm^{-1}, thus one can use just a single telescope to detect them. Molecules with short carbon chains(C_2,C_2H,C_3,C_4,HC_3N) present a notable pool of carbon [18] and have been found in a variety of regions of the ISM and circumstellar envelopes(CSE) ; Small organic molecules (SOMs: H_2CO,$HCOOCH_3$,CH_3OH) [19] play a significant role in the ISM study, because they have been found in many interstellar regions including hot cores [20] and low-mass protostellar environments; Molecular ions (CH^+,SiH^+,HCO^+,N_2H^+,$HOCO^+$), which present a low fractional abundance compared to H_2, are, nonetheless, a very important component of the ISM, because their presence in

Figure 4. The antennas of the Atacama Large Millimeter/submillimeter Array (ALMA) [8]. Credit: ALMA.

interstellar clouds couples the clouds with the ambient magnetic field therefore making a significant contribution to the overall cloud stability[21].

One should also mention molecules in comets, meteorites and KBOs (Kuiper Belt Objects). It is believed that Earth's water have come from icy comets that bombareded our planet during and after its formation (4 billion years ago) [7]. Thus, investigation of comet structure presents a significant interest. Several molecular species have been detected in comets since decades and in KBOs since the last decade. Here is the list of molecules which species have been detected [5,7,22]:

(i) H_2O, CO, CO_2, CH_4, C_2H_2, C_2H_6, CH_3OH, H_2CO, NH_3, HCN, HNC, CH_3CN and H_2S have been detected in more than 10 comets;

(ii) HCOOH, HNCO, HC_3N, OCS and S_2 have been detected in more than one comet;

(iii) $HOCH_2CH_2OH$, $HCOOCH_3$, CH_3CHO, NH_2CHO, SO_2, H_2CS have been observed in one comet, Hale–Bopp.

Figure 5. Hubble Space Telescope [9].

Not all species listed above are primary species, namely species present in the sublimated ices. Some, like HNC and HCN, are product species, which means that they are the products formed in chemical reactions involving the primary species once ejected in the gas from the ice. Other molecules, like H_2CO and CO, have contributions from both primary and product species [1,5].

1.4 Processes in the ISM

Local thermodynamic equilibrium(LTE) corresponds to a concept of the certainty of intensive parameters of a system (i.e. temperature) which can vary in space and time but such variation is so slow that one can assume thermodynamic equilibrium at any point which can be characterized by a single temperature that describes the energy distribution among different degrees of freedom, ionization, and molecular formation [1,22]. Whenever a gas is not in local thermodynamic equilibrium, the level populations, degree of ionization, chemical composition, and of course the temperature are defined by balancing the rates of the processes involved. The interstellar medium is quite far from being in LTE due to its low density. Collisional energy transfer cannot maintain thermal distribution because of rapid radiative decay rates of atomic and molecular levels. That is why the energy distribution, population of excited and ionized molecules and molecular composition are often very different from thermodynamic equilibrium values at a given temperature while the momentum distribution of the gas can generally be adequately described by Maxwellian distribution for this temperature. However, a large amount of mechanical energy put in the gas can vastly influence on velocities of atoms and molecules on large -scale perspective. Also, the presence of highly energetic (100 MeV) cosmic-ray particles keeps ionization and chemical composition from their equilibrium values. This is clearly due to a non-Maxwellian nature of the radiation that disperses photon field of stars which is significantly stronger than a 100-200 K medium usually has. Thus, most of the study of the ISM is devoted to identification the various processes that control the ionization and energy balance, setting up the detailed statistical

equilibrium equations and solving them for the conditions corresponding to the specific region of the medium [2,5].

1.5 State-to-State Rate Coefficients

Radiative spectra of space are the primarily source of information about the components of the ISM and they are extensively used to determine physical conditions of different regions [1,5,7,22]. This exploits the fact that molecular lines are formed under specific temperatures and pressures that, in turn, depend on the precise molecular structure and its energy level arrangement. Consequently, observations in a broad frequency range can be used to reconstruct the physical composition of the studied object. However, in practice this is only possible if the collisional rate coefficients are known. Indeed, LTE is rarely fulfilled in the ISM and one of the processes which significantly contribute in the energy balance is ro-vibrational transitions due to molecular collisions. Collisional excitation and quenching are one of the basic processes, and their efficiency depend on the medium structure. The medium composition defines density of quenchers and the temperature, which establishes the degree of excitation and, consequently, makes up the intensities of the radiated emission.

As it was mentioned above it is required to know the collisional rate coefficients involving molecular species and electrons. Using them one can solve the differential kinetics equations describing the evolution of the different excited states of each molecule. These equations are the coupled differential equations and they are essentially nonlinear which, in turn, leads to the fact that the radiation sources terms themselves depend on the populations of the individual levels involved in the emitted transitions [5,22]. Solving these kinetics equations and converting an observed signal into a species

column density allows one to determine density and temperature of the emitting or absorbing gas.

Since collisional rate coefficients are indispensable for the quantitative interpretation of radiative spectra, the experimental and theoretical studies of collision-induced ro-vibrational energy transfer have received a lot of attention during the past 50 years. That was possible thanks to the development of laser spectroscopy and combined molecular beam experiments, along with the extensive growth of computer performance which allows to carry out fully quantum time-independent mechanical treatments of collision dynamics based on accurate potential energy surfaces (PESs). However, until the beginning of XXI century, only a few molecular systems of astrochemical interest have been studied and investigated in details. [24].

1.6 Experimental Studies of Ro-Vibrational Energy Transfer

Manifold experimental studies of inelastic scattering and ro-vibrational energy transfer have been done in recent years [25]. However, measurements of inelastic rate coefficients of astrochemical species are challengeable. The determination of these rate coefficients at physical conditions which the interstellar medium would usually have is hardly affordable in terms of both collisional partners and temperature. The use of

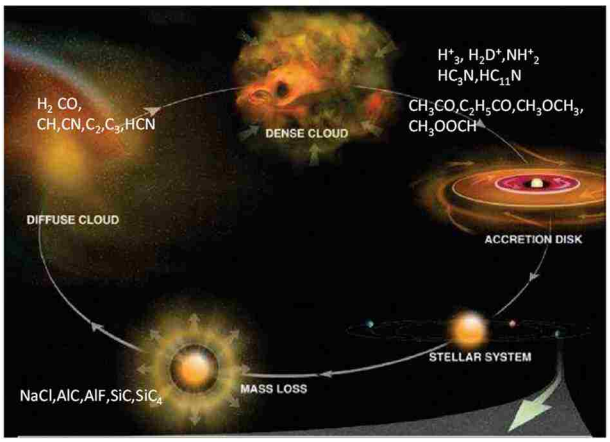

Figure 6. Diversity of chemical compounds in the ISM and life cycle of star. Credit: Phys.org [11]

astrochemically important colliders such as H_2 and He may complicate experimental procedures because these molecules are light. Thus, most of the experiments have been performed at room temperature and with heavy collisional partners such as Ar, Ne, N_2, etc. that are not relevant for astrochemical applications.

To carry out a state-resolved scattering experiment one needs to prepare the initial state and detect the final states population during the collision process which could be achieved in double-resonance (DR) methods. The main concept of DR is the usage of two sources of radiation. In such experiments, one source of radiation, the pump, induces radiative dipole transitions and perturbs the rotational thermal distribution of the sample molecules in the gas phase. After the molecules have been exposed to the radiation and become excited, the probe, a second source of radiation, is used to track the following time evolution of molecular levels towards equilibrium as the collisional energy transfer redistributes molecules among the rotational levels. Performing DR experimental studies, one can obtain not only total inelastic rate coefficients for collisionally induced transitions from the initial rotational level j to all other rotational levels within the same vibrational state, but state-to-state rate coefficients for the rotational energy transfer of molecules from the initial state j to the final state j'. Using this method Oka and co-workers [26] performed experimental studies for rotational transitions in ammonia due to collisions with helium and molecular hydrogen. They used microwave-microwave DR method and were able to obtain some propensity rules for the Δj-induced collisions of NH_3 at room temperature (300K) for both quenchers. Later, this technique was extended to ground-breaking infrared experiments (IR DR) by Bréchignac *et al*[27] and applied for $CO-H_2$ collisional system at room temperature and 77 K.

Figure 7. Hale-Bopp Comet [23].

One more way to study rotational energy transfer is using spectroscopic line-broadening measurements [28] under very low-temperature conditions. Rotational scattering and pressure broadening cross sections can be expressed through terms of S-matrix and even *the same* terms [29] in so-called impact approximation. However, those expressions involve different combinations of matrix elements: the pressure broadening cross section can be obtained through the total removal cross section and a pure elastic term related with the optical theorem [30]. Therefore, to extract cross sections and rate coefficients for rotational energy transfer from pressure-broadening data, theoretical scattering calculations should be carried out [5]. A good example of the technique was demonstrated by Willey and co-workers[31] who measured pressure broadening of the (J,K)=(1,1), (2,2), and (3,3) inversion transitions of ammonia NH_3 in collisions with H_2 as the broadening agent at temperatures of 15 to 40 K. They also obtained H_2 pressure broadening cross sections and compared them to low-temperature He pressure broadening of the same transitions.

Another experimental method for studying collision-induced rotational energy transfer involves molecular beams. In such experiments, only relative values of cross section can be measured which represent a significant technique limitation. Generally,

scaling is performed with a theoretical result involving a cross section of relatively large magnitude to minimize possible uncertainties. The crossed-molecular-beam experiments reported by ter Meulen *et al* [32] serve as examples. In these studies sample of molecules were prepared in a single initial state by electrostatic state selection. This jet of molecules (NH_3, OH, or D_2CO) was crossed with a second beam of He or H_2. Relative state-to-state cross sections were determined by measuring the distribution of molecules over final states using either laser-induced fluorescence or resonance enhanced multiphoton ionization. Another recent example of such experiments is provided by the work of Yang *et al* [33] on the inelastic rotationally scattering of H_2O in collisions with He atoms and H_2 molecules. They extracted differential cross sections and compared them with the results from full-quantum coupled-channel (CC) calculations, and excellent agreement was found. Finally, very recently [34], crossed-beam measurements of inelastic ro-vibrational transitions of CO by collision with H_2 were performed up to kinetic energies as low as ~4 cm^{-1}. This valuable work opens the way to verification the quality of PESs and a detailed validation of theoretical calculations at low temperature.

1.7 Theoretical Studies of Inelastic Scattering Dynamics

1.7.1 Potential Energy Surface

As far as we see the experimental studies are essential but can be done with reasonable accuracy at very limited range of temperatures (typically, room temperature) and for astrophysically irrelevant scattering atoms/systems. Thus, experimental data usually serve as a reference. In practice, state-to-state collisional rate coefficients are computed. The computation of collisional inelastic rate coefficients usually takes place

within the Born−Oppenheimer approximation where electronic and nuclear motions are separated. Scattering cross sections are thus obtained by solving the motion of the nuclei on an electronic potential energy surface (PES) that is independent of the masses and spins of the nuclei [22,5]. The potential energy surfaces must be computed accurately for a number reasons. The main reason is that typical interstellar collisional energies can be very low – orders of wavenumber – which means that dynamical calculations are very sensitive to the PES quality in the range of moderate intermolecular distances which practically correspond to the potential well scattering region.

The most accurate description of PES can be achieved using modern methods of ab initio quantum chemistry. For example, the process of rotational excitation of a molecule colliding with He or H_2 usually corresponds to systems in their electronic ground state as temperatures are generally medium ($T < 300$ K) in the ISM which relates to the described above collisional region of the PES. Thus, He + H_2 collisional system can be considered as a closed-shell system for the purposes stated above. A single electronic configuration usually adequately represents the treatment of closed-shell systems. It allows using of monoconfigurational methods such as coupled-cluster or perturbative methods which are relatively cheap in terms of computational cost. The coupled-cluster approach, usually (partially spin-restricted) coupled cluster with single, double, and perturbative triple excitations [(R)CCSD(T)], are recommended to use for the determination of nonreactive PESs owing to its high accuracy (on the order of one cm^{-1}). For open-shell radicals that generally cannot be correctly described by a single electronic configuration, PES calculations should be done using of configuration interaction methods. To the present day multireference configuration interaction (MRCI) [35]is

currently the most accurate method. It is used to describe all geometries that could be accessible by the nuclei during the collisional process. Such approach is also can be useful for molecule-atomic hydrogen interactions because the open-shell character of H usually implies the use of the method.

In all the methods described above, the quality of the result is also determined by the correct choice of atomic orbitals which describe the molecular orbitals and the electronic configuration. The chosen atomic-orbital basis set, from which the molecular orbitals are built, must be large enough to correctly represent the correlation energy but not so extended that the computation time becomes unacceptable. In practice one can uses the augmented correlation-consistent valence triple-ζ (aug-cc-pVTZ), quadruple-ζ (aug-cc-pVQZ), or quintuple-ζ (aug-cc-pV5Z) basis sets of Dunning *et al* [36] because they are quite well adapted and have been widely used to construct PES for scattering calculations. The quality of the results can be improved by the addition of bond functions in the middle of a van der Waals bond [37]. The majority of calculations describing van der Waals interactions involve these bond functions. However, it was noticed that bond functions have a tendency to increase basis set superposition error and to change the electrostatic energy significantly. Therefore they should be included in basis set with caution. The described standard quantum chemistry approaches are employed in several widely used numerical codes such as MOLPRO [38], Gaussian [39], and SAPT2008 [40].

1.7.2 Coupled Channel Formalism

Having a determined PES, one can compute the collisional cross sections and corresponding rate coefficients from numerical solution of the nuclear Schrödinger equations within the given PES. The computation of rotationally inelastic cross sections

is usually based on so-called close-coupling (CC) approach. In this method, the independent Schrodinger equation has to be solved. The solution is expanded in terms of the finite set of spherical harmonics multiplied by unknown radial functions i.e. so-called wave expansion. Substituting the solution in the following form into the Schrodinger equation, the problem is re-formulated to solving of coupled second-order differential equation systems. This quantum formalism was developed by Arthurs and Dalgarno 50 years ago [41] for collisions between a rigid rotor and a spherical atom. Later [42] Green developed an extension of the approach for inelastic scattering problem between asymmetric top rotor and atom and two rigid rotors. This method, exploited in several numerical codes (MOLSCAT [43], MOLCOL [44], and Hibridon [45]), is now the most accurate approach as far as all considered channels and all coupling terms between them are taken into account. The computing time typically varies as N^3, where N is size of the scattering matrix which includes all possible transition between initial states and finale states. Each state corresponds to a certain channel (quantum state of molecule), orbital moment of relative motion, total angular momentum of the system and its projection. Then, when N becomes very large which is a typical situation when calculations need to be done at high-energy collisions with many degrees of freedom or for scattering systems with low spectroscopic rotational constants, approximations can be applied. The coupled-states (CS) approximation, which excludes Coriolis coupling in the collision process, can be implemented for heavy systems [46], and usually maintains a reasonable accuracy at high energies of collision. In case when the number of rotational states to consider is too large, the infinite-order sudden (IOS) approximation can help. This method neglects the internal structure of the molecule. It generally predicts the correct order of magnitude of

the rate coefficients in reasonable CPU time. The CC method, as well as the CS and IOS approximations, have been implemented to treatment of rigid symmetric and asymmetric tops in collisions with an atom and/or a rigid rotor [47]. Alexander made further extension of the method to open-shell molecules such as $^2\Sigma$ and $^2\Pi$, rotationally excited and involed in collisions with a spherical atom[48]. The discussed scattering systems can be treated by the basis routines exploited in the Hibridon public code.

1.7.3 Classical Trajectories

As another option or possibility, calculations of the inelastic rate coefficients can be carried out using so-called the quasi-classical trajectory (QCT) method [49,50]. The QCT method combines the use of classical mechanics, to treat the scattering process, with simple quantization of the energy and angular momentum of reactants. Quantization is simulated by means of so called binning procedure, which involves allocating the final states to discrete values of the corresponding quantum numbers -- bins. However, the QCT method is valid only to the extent of the classical mechanics that supports it. When the collision energy decreases, the cross sections cannot satisfy detailed balance, which is a sign of the breakdown of the method. Another deficiency is that the QCT cannot take into account zero point energy which presents a significant drawback especially for vibrational transition in molecules. Another crucial issue is the binning procedure which is also questionable and usually the technique is adjusted to existing quantum theoretical or experimental data. For example, comparison between the exact quantum mechanics and classical trajectories studies of inelastic ro-vibrational inelastic scattering for He + H_2 system shows the discrepancy to be one order of magnitude for all transitions considered in the work at collisional energies below 1000 cm^{-1}. Even for energies above 4000cm^{-1}

the difference between CC and QCT cross sections is still about 20%[50]. Then, this method cannot be adapted to the calculations of collisional data for cold ISM.

1.8 Inelastic Scattering in Combustion

There are fields of study along with astrochemistry where state-to-state rate coefficients are necessary. Flames and other chemically reactive environments, such as internal combustion engines, present an example of complicated interaction between chemical kinetics and collisional energy transfer [51]. The energy released in the chemical reactions is the driven source of ro-vibrational excitation.

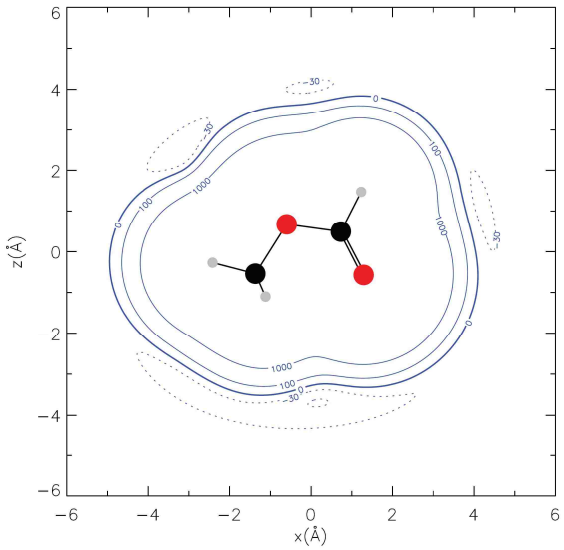

Figure 8. Contour plot of the potential in the (x, z) plane of methyl formate CH_3OOCH. The minimum in this plane is for β = 183◦ at -48.0 cm^{-1}. The molecule is shown as projected on the (x, z) plane[54]. Reproduced with permission from A. Faure, K. Szalewicz and L. Wiesenfeld, J. Chem. Phys. 135, 024301 Copyright 2011 AIP Publishing LLC

A chemical reaction never produces products with Boltzman internal state energy distributions for rotational, vibrational, and electronic degrees of freedom or momentum distribution because the reactions usually take place on complex potential energy surfaces. The collisional energy transfer rearranges the energy distribution of the accessible degrees of freedom toward thermal equilibrium. In order to determine the rates of energy transfer this process has to be studied in bulk for many systems. The process involves such collisional energy transfer mechanism as electronic quenching, vibrational relaxation, and rotational energy transfer. The energetics and mechanisms of these bulk processes are described by simplified dependencies as energy gap law and are

parameterized by probability of so-called energy transfer functions, $P(E,E')$ [52]. These transfer function can be incorporated into combustion models. To obtain energy transfer function, one may require collisional rate coefficients.

One of the good and interesting examples which is important for combustion is rotationally inelastic scattering of methyl radicals (CD_3 and CH_3). The methyl radical plays an important role in the combustion of hydrocarbons, chemical vapor deposition (CVD) of diamond films, and in the chemistry of the atmospheres of the outer planets in the solar system. In addition, CH_3 has been detected in the interstellar medium via its infra-red emission bands. Very recently Alexander *et al* [53] have carried out scattering calculations for this system on the PES of CH_3 + He [55]. This system has been chosen as a good benchmark which provides very useful information about the collisional energy transfer of methyl radicals. The computed results were compared with cross-beam experiment data showing excellent agreement between theory and experiment.

Another relevant case is rotationally inelastic state-to-state transitions in hydroxyl radical, OH. The hydroxyl radical is one of the most fascinating molecules in molecular dynamics. In particular, inelastic collisions of free radicals such as OH are profoundly important in environments ranging from combustion to astrochemistry. OH is also a primary product of the photolysis of many prevalent molecules, including, of course, water, as well as inorganic oxo-acids and various classes of hydroxyl-containing organic compounds such as alcohols, carboxylic acids and so on. Consequently, the detection of OH has long been the keystone of fundamental studies of the excited-state photophysics of these important organic molecules. McKendrick *et. al.* [56] have carried out series of so called velocity-map imaging (VMI) experiments in order to measure inelastic

rotational cross sections in OH + Ar/He collisions and compared them with the results of exact quantum scattering dynamics. The comparison shows generally very good agreement between experimental and theoretical studies with some exceptions which can be explained if uncertainties of the beam energy are taken into account. And again, the experiment being essential to justify theoretical calculations is less favorable in terms of accuracy and range of data which it can provide.

1.9 Mixed Quantum/Classical Theory(MQCT)

As far as we see calculations of inelastic scattering cross section and corresponding temperature rates are essential for various fields of study. Therefore the exact quantum formalism serves as a powerful instrument for collisional studies where the experimental data is used for justification of PES and since high level *ab initio* methods have been developed we can rely on the quality of PES in most cases for obtaining a reasonable description of dynamics.

But the exact quantum mechanics faces another problem -- computational affordability. Indeed, the numerical cost grows significantly with energy of collision: numbers of accessible channels included in calculations should be increased and the number of partial waves should be expanded in order to maintain converged cross sections as well which leads to dramatic growth of the size of transition matrix and drastically increases the computational cost. Is there any way to overcome the issue?

The QCT method discussed above is computationally affordable, but the discrepancy between exact quantum results and classical trajectories simulations may reach several orders of magnitude, which is unacceptable for practical use. Moreover

obtaining small cross sections is a quite challengeable task for QCT, due to the binning procedure. In these conditions an alternative approach is needed.

One appealing idea is to treat some degrees of freedom quantum mechanically (internal degrees of freedom) and the rest quantum mechanically (typically, the translational motion). This idea is not new. Some first works on this topic were done in the 60-70s of the last century by, for example, Delos, Thorson, and Knudson [57]. They derived classical and semi-classical approaches for electronic transitions in atomic collisions. They also tried to formulate practical criteria to determine when their approach works and when it does not. In 80s Gert Billing [58] laid the groundwork for ro-vibrationally inelastic scattering within semi-classical framework. His work basically focused on quantum treatment of vibrational transitions while other degrees of freedom (scattering and rotation) were treated classically. For rotational transitions very little was done: in terms of applications he considered a case where a very approximate version of this theory was applied to $He+H_2$ for two energies and just for a few transitions.

This approach has been successfully applied for treatment of recombination reaction of ozone which occurs in atmosphere [59-63]: $O + O_2 \leftrightarrow O_3$. These studies were focused on computing the absolute value of the recombination rate coefficient, its pressure and temperature dependencies. The authors showed excellent agreement between experimental data and their calculated results. It is worth to note that such calculations within full quantum framework are computationally unfordable.

The present work is devoted to extension of MQCT onto the cases of rotationally and ro-vibrationally inelastic transitions due to collisions, and its applications to several systems important both methodologically and practically. This work is organized as

follows: In Chapter 1 we demonstrate that MQCT proposed earlier in [59] is equivalent to a general and rigorous Ehrenfest theorem approach to the time-dependent Schrodinger equation. This is done for the case of a diatomic + atom scattering, when vibrational motion is treated quantum mechanically and scattering coordinates along with rotational motion is treated classically. This new formulation of MQCT is then applied to treat ro-vibrational transitions of CO + He. The comparison between the exact quantum data and our results shows a good agreement. In Chapter 2 we formulate MQCT in the body-fixed (BF) and space-fixed (SF) reference frames for ro-vibrational transitions in diatomic + atom, where rotational motion is treated quantum mechanically. This serves as a theory basis for the chapters that follow. In Chapter 3 we apply the BF formulation of MQCT for treatment of Na + N_2 and He + H_2 rotationally inelastic scattering, and compare against the full quantum results. For both cases a detailed agreement with the exact quantum data is obtained. In Chapter 4 we formulate MQCT for treatment of symmetric-top and asymmetric-top rotors collided with an atom, and present the results of calculations for H_2O + He system. The study shows excellent agreement with the full quantum data. Preliminarily results for $HCOOCH_3$ + He are also discussed. For rotational excitation of methylfomate ($HCOOCH_3$) in collisions with helium we obtained excellent agreement in the energy range (up to 30 cm^{-1}) where the quantum data is available. We also significantly extended the collisional energy range and calculated rotational cross sections up to collisional energy 300 cm^{-1}. To the present day it is the largest molecule which has been ever computed. In Chapter 5 the theoretical framework for molecular – molecular collisional is formulated and applied to rotational inelastic scattering of H_2+N_2 and H_2+H_2. In Chapter 6, we carry out inelastic scattering calculations for

astrochemically important $H_2O + H_2O$ system and present the first and only data for this process. In Conclusion, we discuss the impact of MQCT in the field of inelastic scattering calculations.

BIBLIOGRAPHY for Introduction

1. A.G. Tielens. The Physics and Chemistry of the Interstellar Medium, CUP (2006).
2. The image can be found here https://apod.nasa.gov/apod/ap120715.html
3. L. Spitzer, Physical Processes in the Interstellar Medium, Wiley Classic Library Edition (1998).
4. The image can be found here https://apod.nasa.gov/apod/ap060829.html
5. E. Roueff and F.Lique, *Chem. Rev.* **113**, 8906 (2013).
6. The image can be found here http://cso.caltech.edu/
7. P. Caselli and C. Ceccarelli, *Astron, Astrophys Rev*. **20:56** (2012).
8. The picture can be found here https://www.nsf.gov/mobile/news/news_images.jsp?cntn_id=127233&org=MPS
9. The image can be found https://www.nasa.gov/mission_pages/hubble/multimedia/index.html
10. M.-L. Dubernet, M. H. Alexander, Y. A. Ba, N. Balakrishnan *et al. Astron. Astrophys* **553**, A50 (2012).
11. The scheme can be found here https://phys.org/news/2016-04-earthsthe-chemistry-star-planet-formation.html
12. P. Hily-Blant, M. Walmsley, G. Pineau Des Forêts. D. Flower. *Astron. Astrophys.* **480**, L5 (2008).
13. F. Dayou, C. Balança, *Astron. Astrophys*. **459**, 297 (2006).
14. L.Vincent, A. Spielfiedel, F. Lique. *Astron. Astrophys*. **472**,1037 (2007).
15. F. Lique, A. Spielfiedel, J. Cernicharo. *Astron. Astrophys*. **451**, 1125 (2006).
16. C. M. Persson, J. H. Black, J. Cernicharo *et al*. *Astron. Astrophys*. **521**, L45 (2010).
17. P. Hily-Blant, S. Maret, A. Bacmann*, et al*. *Astron. Astrophys*. **521**, ***L52*** (2010).
18. M Guelin, J. Cernicharo, M. Travers, M. McCarthy, *Astron. Astrophys*. **317**, L1 (1997).
19. N. Sakai, C. Ceccarelli, S. Bottinelli, T. Sakai, S. Yamamoto, *Astrophys. J.* **754**, 70 (2012)

20. E. Caux, C. Kahane, A. Castets, A. Coutens, *et al*. *Astron.& Astrophys*. **532**, A23 (2011).

21. K. Hammami, L. Owono Owono, P. Stäuber, *Astron.Astrophys.* **507**, 1083 (2009).

22. D. Flower, Molecular Collisions in the Interstellar Medium, Cambridge Astrophysics (2012)

23. The image can be found here http://stardustnext.jpl.nasa.gov/multimedia/comets.html

24. G. Paterson, M.L. Costen, K. McKendrick, *Int. Rev. Phys Chem.* **31**, 69 (2012).

25. I.W. Smith, *Annu. Rev. Astron. Astrophys*. **49**, 29 (2011).

26. P. Daly, T. Oka*, Chem. Phys.* **53**, 3272 (1970).

27. P. Bréchignac, A. Picard-Bersellini, N. Charneau, J. Launay, *Chem. Phys.* **53**, 165 (1980).

28. D. Willey, D. Bittner, F. De Lucia, *Mol. Phys.* **67**, 455 (1989).

29. M. Beaky, T. Goyette, F. de Lucia, *Chem. Phys.* **105**, 3994 (1996).

30. D. Willey, D. Bittner, F. de Lucia, *Mol. Phys.* **67**, 455 (1989).

31. D. Willey, R. Timlin, M. Deramo, P. Pondillo, D. Wesolek, R. Wig, *J. Chem. Phys.* **113**, 611 (2000).

32. J.J. ter Meulen, E.F. van Dishoeck, *In Molecules in Astrophysics: Probes and Processes;* Ed.; IAU Symposium; Kluwer Academic Publishers: Dordrecht, The Netherlands, **178**, 241 (1997).

33. C. Yang, G. Sarma, J. ter Meulen, *et al*. *J. Chem. Phys* **133**, 131103 (2010).

34. C. Yang, G. Sarma, D. Parker, J. ter Meulen, L. Wiesenfeld, *J.Chem. Phys.* **134**, 204308 (2011).

35. H. Werner, P. Knowles, *Chem. Phys.* **89**, 5803 (1988).

36. R. Kendall, T. Dunning, R. Harrison, *Chem. Phys.* **96**, 6796 (1992).

37. D. Woon, T. Dunning, *J. Chem. Phys.* **98**, 1358 (1993).

38. H. Werner, P. Knowles, R. Lindh *et al* Molpro, A Package of AbInitio Programs; University College Cardiff Consultants Limited: Cardiff, U.K. (2012).

39. M. Frisch, G. Trucks, H. Schlegel, *et al* Gaussian 09, revision A.1; Gaussian Inc.: Wallingford, CT (2009).

40. R. Bukowski, W. Cencek, P. Jankowski, *et al* SAPT2008: An Ab Initio Program for Many-Body Symmetry-Adapted Perturbation Theory Calculations of Intermolecular Interaction Energies; University of Delaware and University of Warsaw (2008).

41. A. Arthurs, A. Dalgarno, *Proc. R. Soc. A* **256**, 540 (1960).

42. S. Green, *J. Chem. Phys.* **64**, 3463 (1976);

43. J. Hutson, S. Green, MOLSCAT Computer Code, version 14; Distributed by Collaborative Computational Project No. 6 of the Engineering and Physical Sciences Research Council, Swindon, U.K. (1994)

44. D. Flower, G. Bourhis, J. Launay, *Comput. Phys. Commun.* **131**, 187 (2000).

45. M. Alexander, D. Manolopoulos, H. Werner, *et al*, Hibridon; University of Maryland: College Park, MD, (2011). http://www2.chem.umd.edu/groups/alexander/hibridon/hib43/

46. R. Toboła, J. Kłos, F. Lique, G. Chałasiński, M. Alexander, *Astron. Astrophys.* **468**, 1123 (2007).

47. M. Alexander, *J. Chem. Phys.* **76**, 5974 (1982).

48. M. Alexander, *J. Chem. Phys.* **76**, 3637 (1982).

49. L. Bonnet, J. Rayez, *Chem. Phys. Lett.* **397**, 106 (2004).

50. N. Balakrishnan, M. Vieira, J. F. Babb, *et al. The Astrophysical Journal*, **524**:1122-1130 (1999).

51. M. Mandy, *Chem. Phys.* **365**, 1 (2009).

52. "Theoretical methods for combustion kinetics: Collisional energy transfer and spin-forbidden chemistry," Departmental Colloquium, University of Missouri http://www.sandia.gov/~ajasper/

53. O. Tkáč, A. Sage, S. J. Greaves, *et al*. *Chem. Sci.* **4**, 4199-4211(2013).

54. A. Faure, K. Szalewicz and L. Wiesenfeld, *J. Chem. Phys.* **135**, 024301 (2011).

55. P. J. Dagdigian and M. H. Alexander, *J. Chem. Phys.* **135**, 064306 (2011)

56. G. Sarma, S. Marinakis, J. J. ter Meulen, D. H. Parker and K. G. McKendrick. *Nature Chemistry* **4**, 985–989 (2012).

57. J.B. Delos, W. R. Thorson, and S. K. Knudson. *Phys. Rev. A* **6**, 720 (1972).

58. G. D. Billing, The Quantum Classical Theory, Oxford University Press: New York, (2003).

59. M. V. Ivanov and D. Babikov, *J. Chem. Phys.* **134**, 144107 (2011).

60. M. V. Ivanov and D. Babikov, *J. Chem. Phys*. **134**, 174308 (2011).

61. M. V. Ivanov and D. Babikov, *J. Chem. Phys*. **136**, 184304 (2012).

62. M. V. Ivanov and D. Babikov, *PNAS* **110**, 44,17708–17713 (2013).

63. A. Teplukhin and D. Babikov, *Phys. Chem. Chem. Phys*.**18**, 19194 (2016).

CHAPTER 1. EHRENFEST THEOREM AND ITS APPLICATION TO RO-VIBRATIONAL ENERGY TRANSFER IN CO+HE INELASTIC SCATTERING

1.1 Theoretical Studies of Collisional Energy Transfer

Collisional energy transfer [1] encompasses a relatively broad spectrum of molecular phenomena where the energized molecule (typically small polyatomic molecule or a diatomic molecule) exchanges translational, rotational and vibrational energy with a quencher (an atom, molecule or even a surface). The result of such collision is usually a non-reactive inelastic scattering process, but dissociation of the molecule and/or the quencher may also occur. In some applications the focus is on quenching of the low-lying internal states of the molecule (e.g., few quanta of ro-vibrational excitation [2-8]) while in other processes, such as recombination reactions [9-13], the molecule is initially at energy above the dissociation threshold (scattering resonance). Several processes that are reverse to quenching, such as collisional excitation and the collision-induced dissociation, also fall into category of the collisional energy transfer.

The relevant range of temperatures is broad. In recent years the interest in collisional energy transfer at ultra-cold conditions has been high [14-16] and in those cases the inelastic scattering calculations must be done using the full-fledged quantum mechanics [17,18]. On the other hand, for the processes relevant to combustion [19,20], photochemistry [21,22] or hyper-thermal phenomena [23,24], when high energies are involved, the classical-trajectory picture is quite appropriate [25-29]. In between of those limits the quantum mechanical calculations of collisional energy transfer become

unaffordable computationally even for the smallest molecular systems (due to large number of coupled channels and partial waves) while the classical trajectory calculations are not entirely justified and contain serious drawbacks (such as vibrational zero-point energy leakage [30,31]). Indeed, the vibrational frequencies are typically on order of one-to-few thousand wave numbers, so, the classical approximation for vibrational motion becomes truly valid only at very high temperatures. In polyatomic molecules the vibrational spacing may be smaller but still, for the temperature range $30 < T < 3000$ K (depending on system) there is no practical method of computing the collisional energy transfer. And this is exactly the temperature interval where the majority of chemical processes occur.

The general idea to use a mixture of quantum and classical mechanics for description of collisional energy transfer is not new [32-34]. However it has never been developed to the level of predictive computational tool. The literature on this topic is surprisingly sparse. Some authors neglect rotational motion of the molecule [35-37], which is physically incorrect because the rotational energy transfer is usually a major pathway of the process. There are very few papers where rotational excitation of the molecule by the quencher was actually treated [33,34], but even there the molecule was assumed to have zero angular momentum prior to collision. Such approach is able to give some insight into rotational excitation, but no information about rotational quenching. It is also obvious that collision of a rotationless molecule with quencher would lead to overestimated rotational excitation (even statistically) since all the available rotational states are unpopulated before collision. It is desirable to specify adequate thermal initial conditions for rotation.

Clearly, there are ample opportunities for development of new theories of collisional energy transfer. Recently, the mixed quantum/classical theory (MQCT) for collisional energy transfer (CET) and ro-vibrational energy flow (RVEF) was proposed [11-12] and applied to treat a very complicated problem – the recombination reaction that forms ozone [13,38]. In this approach the time-dependent quantum mechanics (wave packet method) is used to treat vibrational motion of the energized molecule, while its rotational motion and scattering of the quencher are treated with classical trajectories. The rotation-vibration interaction is included in an adiabatic manner, within the fluid-rotor model. Energy is exchanged between translational, rotational and vibrational degrees of freedom, while the total energy of the system is conserved. This method allows one to capture major quantum effects associated with vibrational motion of the molecule (i.e., zero-point energy, quantization of states, tunneling, scattering resonances) while advantage is taken of the quasi-classical regime usually valid for rotational and translational degrees of freedom. This mixed quantum/classical approach is expected to be accurate in the intermediate temperature range $30 < T < 3000$ K and computationally affordable for small polyatomic molecules.

In present section we review this approach and demonstrate that it is, in fact, equivalent to the Ehrenfest theorem treatment of the process. Detailed theory is presented for the simplest energy-transfer process – collision of a diatomic molecule with a quencher. The section is organized as follows. In Sec. 1.2 we outline major components of MQCT for CET and RVEF. In Sec. 1.3 we review the Ehrenfest theorem treatment of the diatom + atom collision and show analytically that it is equivalent to the fluid-rotor

model. Some illustrative numerical results are presented in Sec. 1.4. Conclusions and possible applications of this theory are given in Sec. 1.5.

1.2 Theoretical Framework

A set of internal coordinates of the molecule is denoted $\mathbf{R}_{\mathrm{Q}}$, where subscript "Q" is used to stress that these degrees of freedom are treated quantum mechanically. The vibrational wave function $\Psi(\mathbf{R}_{\mathrm{Q}})$ is expressed in these coordinates and is represented by a suitable grid of points. For example, in the case of a diatomic molecule $\mathbf{R}_{\mathrm{Q}}$ represents only one degree of freedom -- the bond length R . In the case of a triatomic molecule $\mathbf{R}_{\mathrm{Q}} = \{R_1, R_2, \theta\}$ defines two bond lengths and bending angle, so, the grid is three-dimensional. The time-dependent Schrödinger equation for vibrational motion (neglecting rotation)

$$i\frac{\partial}{\partial t}\Psi(\mathbf{R}_{\mathrm{Q}},t) = \hat{H}(t)\Psi(\mathbf{R}_{\mathrm{Q}},t) \ , \tag{1}$$

$$\hat{H}(t) = \hat{T} + V(\mathbf{R}_{\mathrm{Q}};\mathbf{R}_{\mathrm{C}}(t)) , \tag{2}$$

is propagated using the wave packet method [39]. Note that Hamiltonian $\hat{H}(t)$ is time dependent and this dependence comes from the potential energy term. If the quencher is at infinity this term represents potential energy surface of the molecule $V(\mathbf{R}_{\mathrm{Q}})$. As the collsion partner approaches and scatters off the molecule, the potential energy surface is continuously modified due to the quencher interaction, which is formally written as $V(\mathbf{R}_{\mathrm{Q}};\mathbf{R}_{\mathrm{C}}(t))$ dependence. Here, $\mathbf{R}_{\mathrm{C}}$ denotes the external (scattering) degrees of freedom, treated classically. If rotational motion is neglected, those are just the center-of-

mass positions for molecule and collision partner -- six Cartesian coordinates in the laboratory-fixed reference frame, $\mathbf{R}_C = \{\mathbf{q}_{mol}, \mathbf{q}_{que}\}$. So, the time-dependence of $\mathbf{R}_C(t)$ is governed by classical trajectory of motion, which introduces time-dependence into the Hamiltonian $\hat{H}(t)$. In this way, scattering of the quencher affects vibrational motion of the molecule and classical part of the system affects its quantum part.

For the translational (scattering) degrees of freedom the classical equations of motion are simply

$$\dot{\mathbf{q}} = \mathbf{p} / m, \tag{3}$$

$$\dot{\mathbf{p}} = -\nabla \widetilde{V}, \tag{4}$$

where subscripts were omitted for transparency. The moiety $\widetilde{V}$ is the mean-field potential, which represents average of the potential energy of the system over the vibrational wave function of the molecule (quantum expectation value)

$$\widetilde{V}(\mathbf{R}_C) = \left\langle \Psi(\mathbf{R}_Q) \middle| V(\mathbf{R}_Q, \mathbf{R}_C) \middle| \Psi(\mathbf{R}_Q) \right\rangle, \tag{5}$$

where integration is over $\mathbf{R}_Q$. Thus, gradients of the mean-field potential with respect to classical variables $\mathbf{R}_C = \{\mathbf{q}_{mol}, \mathbf{q}_{que}\}$ drive the scattering process. Note also that $\widetilde{V}$ reflects the internal vibrational state of the molecule, through average over the vibrational wave function $\Psi(\mathbf{R}_Q)$. In this way the vibrational degrees of freedom affect the dynamics of scattering, and the quantum part of the system affects motion of its classical part.

1.2.1 The Fluid-Rotor Model

If the rotational motion of molecule is included and is treated classically, the set of classical degrees of freedom should be expanded to include Euler angles [40] used to define orientation of molecule in space: $\mathbf{R}_{\mathrm{C}} = \{\mathbf{q}_{\mathrm{mol}}, \mathbf{q}_{\mathrm{que}}, \alpha, \beta, \gamma\}$. The effect of rotational motion on vibration is taken into account adiabatically [41-46], by introducing the centrifugal potential term V_{rot} into the Hamiltonian operator

$$\hat{H}(t) = \hat{T}_{J=0} + V(\mathbf{R}_{\mathrm{Q}}; \mathbf{R}_{\mathrm{C}}(t)) + V_{\mathrm{rot}}(\mathbf{R}_{\mathrm{Q}}; \mathbf{R}_{\mathrm{C}}(t)). \tag{6}$$

This term represents rotational energy of the molecule and is a continuous smooth function of its shape (*i.e.*, of the internal coordinates $\mathbf{R}_{\mathrm{Q}}$). Also, V_{rot} is a function of time, since rotational energy changes along the trajectory $\mathbf{R}_{\mathrm{C}}(t)$. At every moment of time and for every point $\mathbf{R}_{\mathrm{Q}}$ of the grid we compute this potential numerically as

$$V_{\mathrm{rot}}(\mathbf{R}_{\mathrm{Q}}) = \tfrac{1}{2}(\mathbf{J}, \mathbf{I}^{-1}(\mathbf{R}_{\mathrm{Q}})\mathbf{J}) \ , \tag{7}$$

where $\mathbf{I}(\mathbf{R}_{\mathrm{Q}})$ is tensor of inertia on the grid and $\mathbf{J}(t)$ is instantaneous vector of angular momentum of the molecule, both expressed in the laboratory reference frame. Note that this adiabatic rotation approximation is expected to work better than any other method of angular momentum decoupling, simply because tensor of inertia of the molecule is not fixed at a single chosen molecular configuration (e.g., equilibrium position), but changes smoothly as molecular shape is distorted by vibration. This feature is important for treatment of the large-amplitude vibrational motion (e.g., highly-excited vibrations or even dissociation).

Equation (7) is also used to define the average tensor of inertia of the classical rotor, $\widetilde{\mathbf{I}}$, that corresponds to vibrational wave function $\Psi(\mathbf{R}_{\mathrm{Q}})$. For this, we require that quantum expectation value of rotational energy,

$$\widetilde{E}_{\mathrm{rot}}^{\mathrm{Q}} = \left\langle \Psi(\mathbf{R}_{\mathrm{Q}}) \middle| V_{\mathrm{rot}}(\mathbf{R}_{\mathrm{Q}}) \middle| \Psi(\mathbf{R}_{\mathrm{Q}}) \right\rangle, \tag{8}$$

coincides with energy of the average classical rotor,

$$E_{\mathrm{rot}}^{\mathrm{C}} = \tfrac{1}{2}(\mathbf{J}, \widetilde{\mathbf{I}}^{-1}\mathbf{J}), \tag{9}$$

at every moment of time. From $\widetilde{E}_{\mathrm{rot}}^{\mathrm{Q}} = E_{\mathrm{rot}}^{\mathrm{C}}$ one obtains [11]

$$\widetilde{\mathbf{I}} = \left\langle \Psi(\mathbf{R}_{\mathrm{Q}}) \middle| \mathbf{I}^{-1}(\mathbf{R}_{\mathrm{Q}}) \middle| \Psi(\mathbf{R}_{\mathrm{Q}}) \right\rangle^{-1}, \tag{10}$$

which guarantees conservation of total ro-vibrational energy and describes how evolution of vibrational wave function (treated with quantum mechanics) affects the tensor of inertia of the classical rotor.

Thus, vibrational and rotational degrees of freedom are treated explicitly and self-consistently. The rigid-rotor assumption of any sort is avoided and we deal with *fluid rotor*, whose tensor inertia $\widetilde{\mathbf{I}}(t)$ is affected by vibration and is time-dependent. Equations for rotation of such fluid rotor are obtained as follows. Start with $\mathbf{J} = \widetilde{\mathbf{I}}\boldsymbol{\omega}$ and, assuming that each of these quantities is time dependent, differentiate this expression (by parts) with respect to time: $d\mathbf{J}/dt = \dot{\widetilde{\mathbf{I}}}\boldsymbol{\omega} + \widetilde{\mathbf{I}}\dot{\boldsymbol{\omega}}$. Introduce average torque as

$$\widetilde{\boldsymbol{\tau}} = d\mathbf{J}/dt\ . \tag{11}$$

Express angular velocities $\boldsymbol{\omega}(t)$ and accelerations $\dot{\boldsymbol{\omega}}(t)$ through Euler angles:

$$\boldsymbol{\omega} = \mathbf{G}\begin{pmatrix} \dot{\alpha} \\ \dot{\beta} \\ \dot{\gamma} \end{pmatrix}, \tag{12}$$

where, for convenience, we defined

$$\mathbf{G} = \begin{pmatrix} 0 & \cos\alpha & \sin\beta\sin\alpha \\ 0 & \sin\alpha & -\sin\beta\cos\alpha \\ 1 & 0 & \cos\beta \end{pmatrix}. \tag{13}$$

Further manipulations [11] lead to the following final system of second-order differential equations for rotation of the fluid rotor

$$\begin{pmatrix} \ddot{\alpha} \\ \ddot{\beta} \\ \ddot{\gamma} \end{pmatrix} = \mathbf{G}^{-1}\left[\tilde{\mathbf{I}}^{-1}\left[\tilde{\boldsymbol{\tau}} - \dot{\tilde{\mathbf{I}}}\mathbf{G}\begin{pmatrix} \dot{\alpha} \\ \dot{\beta} \\ \dot{\gamma} \end{pmatrix} \right] - \dot{\mathbf{G}}\begin{pmatrix} \dot{\alpha} \\ \dot{\beta} \\ \dot{\gamma} \end{pmatrix} \right]. \tag{14}$$

Time-derivative of the mean tensor, $\dot{\tilde{\mathbf{I}}}$ in Eq. (14), can be computed by differentiating over time the definition of $\tilde{\mathbf{I}}$, Eq. (10)

$$\dot{\tilde{\mathbf{I}}} = \tilde{\mathbf{I}}\mathbf{A}\tilde{\mathbf{I}}, \tag{15}$$

where

$$\mathbf{A} = \left\langle \Psi \middle| \mathbf{I}^{-1}\left(\frac{d\mathbf{I}}{dt}\right)\mathbf{I}^{-1} \middle| \Psi \right\rangle - 2\,\mathrm{Re}\left\langle \Psi \middle| \mathbf{I}^{-1} \middle| \frac{d}{dt}\Psi \right\rangle. \tag{16}$$

Note that in the rigid-rotor case, when vibrational wave function of the molecule does not evolve, $d\Psi/dt = 0$ and the second term in Eq. (17) vanishes.

The mean torque $\tilde{\boldsymbol{\tau}}$ in Eq. (14) is computed as average over the vibrational wave function:

$$\tilde{\boldsymbol{\tau}} = -\left\langle \Psi(\mathbf{R}_{\mathrm{Q}}) \middle| \sum_i \mathbf{r}_i \times \nabla V \middle| \Psi(\mathbf{R}_{\mathrm{Q}}) \right\rangle, \tag{17}$$

where $\mathbf{r}_i \times \nabla V$ represents torque of the quencher on each atom in the molecule, $\mathbf{r}_i = \{x_i, y_i, z_i\}$ is radius vector of i^{th} atom relative to molecular center or mass, the gradient ∇V is computed with respect to Cartesian position of each atom. Summation in Eq. (17) is over all atoms in the molecule (*e.g.*, three for a triatomic molecule).

In the way formulated above this theory can be applied to small polyatomic molecules. The fluid rotor treatment of rotation is computationally inexpensive. The most demanding part is propagation of the time-dependent Schrodinger equation for vibration, Eq. (1) with Hamiltonian (6). As size of the molecule increases ($3N-6$ vibrational degrees of freedom for *N*-atomic molecule), integrating the quantum expectation values in Eqs. (5), (10), (15) and (17) also becomes costly. The case of triatomic molecule was discussed in detail in Ref. [11]. Diatomic molecule is a special case, discussed in Sec. 1.2.2 below.

1.2.2 Application to Diatomic Molecule

Relative to molecular center of mass, the coordinates of two atoms (i = 1, 2) are given by:

$$x_i = R\frac{m_i}{m_1+m_2}\cos\alpha\sin\gamma, \tag{18a}$$

$$y_i = R\frac{m_i}{m_1+m_2}\sin\alpha\sin\gamma, \tag{18b}$$

$$z_i = R\frac{m_i}{m_1+m_2}\cos\gamma. \tag{18c}$$

Substitution of Eqs. (18) into standard expression for the tensor of inertia,

$$\mathbf{I} = \begin{pmatrix} \sum m_i (y_i^2 + z_i^2) & -\sum m_i x_i y_i & -\sum m_i z_i x_i \\ -\sum m_i x_i y_i & \sum m_i (x_i^2 + z_i^2) & -\sum m_i z_i y_i \\ -\sum m_i z_i x_i & -\sum m_i z_i y_i & \sum m_i (x_i^2 + y_i^2) \end{pmatrix}, \tag{19}$$

leads to:

$$\mathbf{I} = I\,\mathbf{M}\,, \tag{20}$$

where matrix $\mathbf{M}$ is defined as

$$\mathbf{M} = \begin{pmatrix} \sin^2\gamma \sin^2\alpha + \cos^2\gamma & -\sin^2\gamma \sin\alpha\cos\alpha & -\sin\gamma\cos\gamma\cos\alpha \\ -\sin^2\gamma \sin\alpha\cos\alpha & \sin^2\gamma\cos^2\alpha + \cos^2\gamma & -\sin\gamma\cos\gamma\sin\alpha \\ -\sin\gamma\cos\gamma\cos\alpha & -\sin\gamma\cos\gamma\sin\alpha & \sin^2\gamma \end{pmatrix}, \tag{21}$$

and a scalar $I = \mu R^2$ gives the moment of inertia of the diatomic, expressed through its reduced mass $\mu = m_1 m_2 / (m_1 + m_2)$. The matrix $\mathbf{M}$ is singular. Thus, the tensor of inertia $\mathbf{I}$ can't be inverted, and all equations above that contain $\mathbf{I}^{-1}$ should be rewritten in the way suitable for the case of diatomic molecule. Those are Eqs. (7), (9), (10) and (14).

For rotational potential and rotational energy of the diatomic fluid rotor, instead of Eqs. (7) and (9), we can write

$$V_{\text{rot}}(\mathbf{R}_{\text{Q}}) = \frac{\mathbf{J}^2}{2\mu R^2} = \frac{\mathbf{J}^2}{2I(R)}\,, \tag{7′}$$

$$E_{\text{rot}}^{\text{C}} = \frac{\mathbf{J}^2}{2\widetilde{I}}\,. \tag{9′}$$

Substituting Eq. (7′) into Eq. (8) and equating the result to Eq. (9′), leads to the following expression for the mean moment of inertia of the diatomic fluid rotor:

$$\widetilde{I} = \left\langle \Psi(R) \middle| \frac{1}{\mu R^2} \middle| \Psi(R) \right\rangle^{-1}. \tag{10′}$$

Here the vibrational wave function $\Psi(R)$ is one-dimensional. This scalar expression replaces the vector expression of Eq. (10). From Eq. (20) it also follows that $\widetilde{\mathbf{I}} = \widetilde{I}\ \mathbf{M}$.

Positioning the diatomic molecule in space requires only two Euler angles, α and γ, that correspond to spherical polar coordinates. The value of β is constant, arbitrary and can be set to $\beta = \pi/2$, for convenience. Thus, equations (12-13) transform into

$$\boldsymbol{\omega} = \mathbf{G} \begin{pmatrix} \dot{\alpha} \\ 0 \\ \dot{\gamma} \end{pmatrix} \tag{12′}$$

and

$$\mathbf{G} = \begin{pmatrix} 0 & \cos\alpha & \sin\alpha \\ 0 & \sin\alpha & -\cos\alpha \\ 1 & 0 & 0 \end{pmatrix} \quad . \tag{13′}$$

Equation (14) can be formally rewritten as

$$\widetilde{\mathbf{I}}\mathbf{G} \begin{pmatrix} \ddot{\alpha} \\ 0 \\ \ddot{\gamma} \end{pmatrix} = \widetilde{\boldsymbol{\tau}} - [\dot{\widetilde{\mathbf{I}}}\mathbf{G} + \widetilde{\mathbf{I}}\dot{\mathbf{G}}] \begin{pmatrix} \dot{\alpha} \\ 0 \\ \dot{\gamma} \end{pmatrix}. \tag{14′}$$

Note that although many elements of these 3×3 matrixes are zero, it is impossible to express Eq. (14′) through 2×2 matrixes, simply because the torque $\tilde{\boldsymbol{\tau}}$, occurring during the molecule-partner collision, is represented by a 3×3 matrix and, in general, none of its elements are zero. This property is also related to evolution of the angular momentum vector, due to torque supplied by the quencher, according to Eq. (11). Of course, in the absence of external torque, rotation of a diatomic is essentially two-dimensional and could be described by 2×2 matrixes in the appropriate reference frame.

1.3. The Ehrenfest Theorem

The theorem of Ehrenfest provides a link between the expectation values of quantum operators $\langle\hat{\mathbf{q}}\rangle$ and $\langle\hat{\mathbf{p}}\rangle$, and their classical counterparts -- generalized positions and momenta, $\mathbf{q}$ and $\mathbf{p}$. This theorem is employed in order to obtain classical equations of motion for the system which contains quantum and classical degrees of freedom. The main idea is to start with "mixed" Hamiltonian of the system, which already includes classical variables and quantum operators, and derive classical Hamiltonian by averaging quantum part over the wave function. From such classical Hamiltonian, one can derive equations of motion for classical variables. The Ehrenfest approach involves assumption that each classical trajectory is independent from other individual trajectories [47]. Generally, the Ehrenfest approach is valid if state-to-state transitions in the quantum part of the system do not modify drastically the dynamics of its classical part [48]. This is the case if transition probabilities are relatively small, or if wave functions of different quantum states lead to similar expectation values.

1.3.1 Application to Diatomic + Atom

Using notations of the previous Section, the total Hamiltonian operator for the system of diatomic molecule + atom can be written as

$$\hat{H} = -\frac{\hbar^2}{2\mu R^2}\frac{\partial}{\partial R}R^2\frac{\partial}{\partial R} + \hat{T}_{\text{rot}} + \frac{\hat{\mathbf{p}}_{\text{mol}}^2}{2m_{\text{mol}}} + \frac{\hat{\mathbf{p}}_{\text{que}}^2}{2m_{\text{que}}} + V(R,\alpha,\gamma,\mathbf{q}_{\text{mol}},\mathbf{q}_{\text{que}}). \tag{22}$$

Replacing the radial wave function $\Phi(R)$ by new wave function $\Psi(R) = \Phi(R)/R$ permits to simplify the kinetic energy operator and calculate the volume element as $|\Psi(R)|^2\, dR = |\Phi(R)|^2\, R^2 dR$. Expressing the rotational kinetic energy operator in spherical polar coordinates in the Laplace-Beltrami form [49], using $\hat{p}_\alpha = -i\hbar\partial/\partial\alpha$ and $\hat{p}_\gamma = -i\hbar\partial/\partial\gamma$, leads to the following expression for the Hamiltonian operator:

$$\hat{H} = -\frac{\hbar^2}{2\mu}\frac{\partial^2}{\partial R^2} + \frac{\hat{p}_\gamma \sin\gamma\, \hat{p}_\gamma}{2\mu R^2 \sin\gamma} + \frac{\hat{p}_\alpha^2}{2\mu R^2 \sin^2\gamma} + \frac{\hat{\mathbf{p}}_{\text{mol}}^2}{2m_{\text{mol}}} + \frac{\hat{\mathbf{p}}_{\text{que}}^2}{2m_{\text{que}}} + V(R,\alpha,\gamma,\mathbf{q}_{\text{mol}},\mathbf{q}_{\text{que}}). \tag{23}$$

Next step is to separate all degrees of freedom in the system onto quantum (vibration) and classical (rotation and translation). Thus, $\mathbf{R}_{\text{Q}} = \{R\}$ and $\mathbf{R}_{\text{C}} = \{\mathbf{q}_{\text{mol}}, \mathbf{q}_{\text{que}}, \alpha, \gamma\}$. For classical degrees of freedom we replace quantum operators $\hat{p}_\alpha$, $\hat{p}_\gamma$, $\hat{\mathbf{p}}_{\text{mol}}$ and $\hat{\mathbf{p}}_{\text{que}}$ by their classical analogues, and split Hamiltonian onto two parts. The quantum Hamiltonian is:

$$\hat{H}_{\text{Q}} = -\frac{\hbar^2}{2\mu}\frac{\partial^2}{\partial R^2} + \frac{p_\gamma^2}{2\mu R^2} + \frac{p_\alpha^2}{2\mu R^2 \sin^2\gamma} + V(\mathbf{R}_{\text{Q}}; \mathbf{R}_{\text{C}}(t)). \tag{24}$$

The classical Hamiltonian is obtained as expectation value:

$$\begin{aligned} H_{\mathrm{C}} &= \langle \Psi(R) | \hat{H} | \Psi(R) \rangle \\ &= \frac{\mathbf{p}_{\mathrm{mol}}^2}{2m_{\mathrm{mol}}} + \frac{\mathbf{p}_{\mathrm{que}}^2}{2m_{\mathrm{que}}} + \langle \Psi(R) | \hat{H}_{\mathrm{Q}} | \Psi(R) \rangle \\ &= \frac{\mathbf{p}_{\mathrm{mol}}^2}{2m_{\mathrm{mol}}} + \frac{\mathbf{p}_{\mathrm{que}}^2}{2m_{\mathrm{que}}} + \left(\frac{p_\gamma^2}{2\mu} + \frac{p_\alpha^2}{2\mu \sin^2 \gamma} \right) \langle \Psi(R) | \frac{1}{R^2} | \Psi(R) \rangle + \widetilde{T}_{\mathrm{Q}} + \widetilde{V}(\mathbf{R}_{\mathrm{C}}). \end{aligned} \tag{25}$$

Note that this expression can be conveniently rewritten by introducing $\widetilde{I}$ defined in Eq. (10′). Indeed

$$H_{\mathrm{C}} = \frac{\mathbf{p}_{\mathrm{mol}}^2}{2m_{\mathrm{mol}}} + \frac{\mathbf{p}_{\mathrm{que}}^2}{2m_{\mathrm{que}}} + \frac{p_\gamma^2}{2\widetilde{I}} + \frac{p_\alpha^2}{2\widetilde{I} \sin^2 \gamma} + \widetilde{T}_{\mathrm{Q}} + \widetilde{V}(\mathbf{R}_{\mathrm{C}}) . \tag{26}$$

Here $\tilde{V}(\mathbf{R}_{\mathrm{C}})$ is the mean field potential, just as one in Eq. (5). Expectation value of quantum kinetic energy in Eq. (26),

$$\tilde{T}_{\mathrm{Q}} = -\frac{\hbar^2}{2\mu} \langle \Psi(R) | \frac{\partial^2}{\partial R^2} | \Psi(R) \rangle , \tag{27}$$

is not a function of any classical coordinates. It is only a function of time.

From classical Hamiltonian of Eq. (26) the equations of motions can be obtained in a standard way: $\dot{\mathbf{q}} = \partial H_{\mathrm{C}} / \partial \mathbf{p}$ and $\dot{\mathbf{p}} = -\partial H_{\mathrm{C}} / \partial \mathbf{q}$. For translational degrees of freedom $\mathbf{q}_{\mathrm{mol}}$ and $\mathbf{q}_{\mathrm{que}}$ one obtains equations exactly equivalent to Eqs. (3-5). For rotational degrees of freedom α and γ this gives

$$\dot{\alpha} = \frac{p_\alpha}{\widetilde{I} \sin^2 \gamma} , \tag{28a}$$

$$\dot{\gamma} = \frac{p_\gamma}{\widetilde{I}}, \tag{28b}$$

$$\dot{p}_\alpha = -\frac{\partial \tilde{V}}{\partial \alpha}, \tag{28c}$$

$$\dot{p}_\gamma = -\frac{\partial \tilde{V}}{\partial \gamma} + \frac{p_\alpha^2 \cos\gamma}{2\tilde{I}\sin^3\gamma}. \tag{28d}$$

Similar equations for rigid rotor are well known [49], but here the emphasis is on definition of the average moment of inertia $\widetilde{I}$ given by Eq. (10′).

One could erroneously think that $\widetilde{I}$ should be computed using the average value of vibrational coordinate $\tilde{R} = \langle \Psi(R) | R | \Psi(R) \rangle$, but the theory presented above shows that $\tilde{I} \neq \mu \tilde{R}^2$. Another possibility that may seem quite appropriate (but is also incorrect) is to compute $\widetilde{I}$ as the average value of $I(R)$. However, one should realize that $\widetilde{I} \neq \langle \Psi(R) | I(R) | \Psi(R) \rangle$. Instead, $\widetilde{I}$ must be computed as inverse of average of the inverse: $\widetilde{I} = \langle \Psi(R) | I^{-1}(R) | \Psi(R) \rangle^{-1}$. This expression is not trivial and, to our best knowledge, is not well known, even for a diatomic molecule. It originates from averaging the rotational energy, rather than vibrational coordinate or the moment of inertia.

What are the consequences of using an incorrect expression to compute $\widetilde{I}$? For a *compact* wave packet $\Psi(R)$, like the ground vibrational state wave function, the differences between $\langle \Psi(R) | R | \Psi(R) \rangle^2$, $\langle \Psi(R) | R^2 | \Psi(R) \rangle$ and $\langle \Psi(R) | R^{-2} | \Psi(R) \rangle^{-1}$ can be small. However, for the large-amplitude vibrational motion characterized by a *broad* wave function the effect can be sizable. Examples include such processes as collision-induced dissociation, dynamics of the van-der-Waals states, or large-amplitude bending

motion of a floppy molecule. Also, from the fundamental theory perspective, the total energy of the mixed quantum/classical system is conserved only if the correct expression $\widetilde{I} = \langle \Psi(R) | I^{-1}(R) | \Psi(R) \rangle^{-1}$ is used for the classical rotor (see Sec. 1.4).

1.3.2 Equivalence of the Two Methods

It is interesting that the expression $\widetilde{I} = \langle \Psi(R) | I^{-1}(R) | \Psi(R) \rangle^{-1}$ appears in both the fluid-rotor equations and in the Ehrenfest theorem treatment. In the first case it emerges from the requirement that expectation value of quantum rotational energy $\widetilde{E}^{\mathrm{Q}}_{\mathrm{rot}}$ equals to classical energy of the fluid rotor $E^{\mathrm{C}}_{\mathrm{rot}}$, at every moment of time, which guaranteed conservation of total energy. In the second case it comes from averaging the quantum Hamiltonian, with the purpose of obtaining its classical counterpart. These sources seem to be related.

There are, however, two pronounced differences between the two methods. First, the rigid rotor equations (14) include $\dot{\widetilde{\mathbf{I}}}$ and require the knowledge of $d\Psi/dt$ in Eq. (16), while there is no time-derivative of wave function involved in Eqs. (28). Second, expression (17) for the mean torque includes summation over all atoms in a molecule, while there in nothing like that in Eqs. (28). So, the question can be raised: *Are those two methods entirely equivalent, or the expression for* $\widetilde{I}$ *is the only thing they have in common?*

On one side, the Hamiltonian equations (28) can be combined into the second-order equations, by differentiating over time both sides of Eqs. (28a) and (28b), and substituting Eqs. (28c) and (28d) as appropriate:

$$(\widetilde{I}\ddot{\alpha}+\dot{\widetilde{I}}\dot{\alpha})\sin^2\gamma=-2\widetilde{I}\dot{\alpha}\dot{\gamma}\cos\gamma\sin\gamma-\frac{\partial\widetilde{V}}{\partial\alpha}\ , \tag{29}$$

$$\widetilde{I}\ddot{\gamma}+\dot{\widetilde{I}}\dot{\gamma}=2\widetilde{I}\dot{\alpha}^2\cos\gamma\sin\gamma-\frac{\partial\widetilde{V}}{\partial\gamma}\,. \tag{30}$$

On the other side, we can work with the fluid rotor equations and substite (13′) and (20-21) into (14′). This leads to the matrix equation given in Appendix 1A. Let's look at its *z*-component first, Eq. (1A3):

$$\widetilde{I}\ddot{\alpha}\sin^2\gamma=\widetilde{\tau}_z-\dot{\widetilde{I}}\dot{\alpha}\sin^2\gamma-2\widetilde{I}\dot{\gamma}\dot{\alpha}\sin\gamma\cos\gamma. \tag{31}$$

Interestingly, this equation becomes equivalent to Eq. (29), if we can show that:

$$\widetilde{\tau}_z=-\frac{\partial\widetilde{V}}{\partial\alpha}\,. \tag{32}$$

This is done in Eqs. (1B1) and (1B2) of Appendix B, which proves that *z*-component of Eq. (14′) is equivalent to Eqs. (28a,c).

In a similar manner, we can combine *x*- and *y*-components of Eq. (14′), given as expressions (1A1) and (1A2) in Appendix, into the expression similar to Eq. (30). Namely, multiplying (1A1) by $\sin\alpha$ and subtracting (1A2) multiplied by $\cos\alpha$, we obtain:

$$\begin{aligned}&\widetilde{I}(\ddot{\gamma}\sin\alpha-\ddot{\alpha}\sin\gamma\cos\gamma\cos\alpha)\sin\alpha-\widetilde{I}(-\ddot{\gamma}\cos\alpha-\ddot{\alpha}\sin\gamma\cos\gamma\sin\alpha)\cos\alpha=\\&[\widetilde{\tau}_x-\dot{\widetilde{I}}(\dot{\gamma}\sin\alpha-\dot{\alpha}\sin\gamma\cos\gamma\cos\alpha)-\widetilde{I}\dot{\alpha}^2\sin\gamma\cos\gamma\sin\alpha]\sin\alpha\\&-[\widetilde{\tau}_y-\dot{\widetilde{I}}(-\dot{\gamma}\cos\alpha-\dot{\alpha}\sin\gamma\cos\gamma\sin\alpha)+\widetilde{I}\dot{\alpha}^2\sin\gamma\cos\gamma\cos\alpha]\cos\alpha\end{aligned} \tag{33}$$

In this expression several terms cancel and it becomes, indeed, equivalent to Eq. (30), if we can prove that:

$$\tilde{\tau}_x \sin\alpha - \tilde{\tau}_y \cos\alpha = -\frac{\partial \tilde{V}}{\partial \gamma}. \qquad (34)$$

This finalizes our proof that Eqs. (28) are equivalent to Eq. (14′). Here we showed that not only the definition of $\tilde{I}$ is the same in both methods, but also that the heuristic "fluid-rotor" approach (introduced *ad hoc* in Ref. [11] and used to treat the collisional energy transfer in recombination reaction [13,38]) is, in fact, entirely equivalent to the Ehrenfest theorem treatment of this process.

1.4 Numerical Tests

In order to gain further insight into the mixed quantum/classical approach to collisional energy transfer we carried out numerical simulations of CO ($v=1$) quenching by He impact, using Eqs. (28) and (10′). Potential energy surface from Ref. [7] was employed. Calculations of converged cross sections for this process in a broad range of temperatures, $30 < T < 3000$ K, will be reported elsewhere [50]. Here we focus on fundamentally important issues of ro-vibrational energy transfer, total energy conservation and time evolution of $\tilde{I}(t)$. We used the Runge-Kutta method of 4th order [51] for classical degrees of freedom and the Lanczos propagator [39] for quantum degrees of freedom.

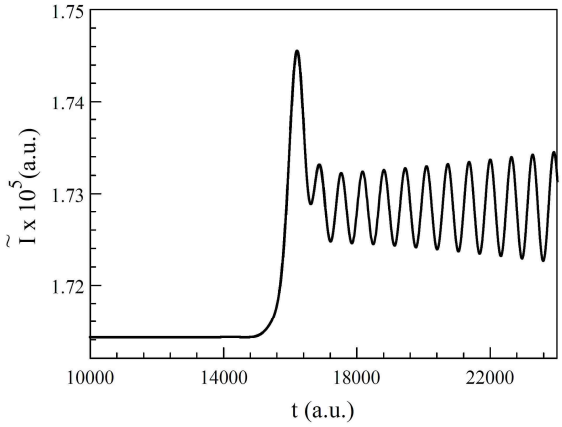

Figure 1. Time evolution of the average moment of inertia of CO molecule along the example trajectory discussed in the text. The post-collisional dynamics is clearly seen.

We will analyze one representative trajectory that starts with CO ($v=1$) in a highly excited rotational state $J=45$. The He atom collides the molecule with relatively small impact parameter $b=2.58\,a_0$ and the center-of-mass translational energy $E_{\rm col}=4000\,{\rm cm}^{-1}$. The collision geometry is rather arbitrary, neither planar nor perpendicular.

Figure 1 shows evolution of $\tilde{I}(t)$. Before collision the vibrational wave packet corresponds to an eigenstate $v=1$ and we see that the value of $\tilde{I}$ remains constant. During the collision it starts changing, and oscillates quite dramatically at the post-collisional state. Clearly, oscillations of $\tilde{I}(t)$ correspond to the motion of vibrational wave packet which, in this case, includes appreciable populations of eigenstates up to $v=3$. This is illustrated by Fig. 2, where we plotted populations of vibrational states along the trajectory, determined by projecting the vibrational wave packet onto the instantaneous vibrational basis, *i.e.*, the vibrational eigenstates computed at each moment of time using the instantaneous value of $J(t)=\sqrt{p_\gamma^2+p_\alpha^2/\sin^2\gamma}$. Vibrational state-to-state transitions are clearly seen for $v=0$, 1, 2 and 3. Note that for this trajectory the angular momentum transfer is quite significant, $\Delta J\approx -19$, so that the initial and the final vibrational spectra are very

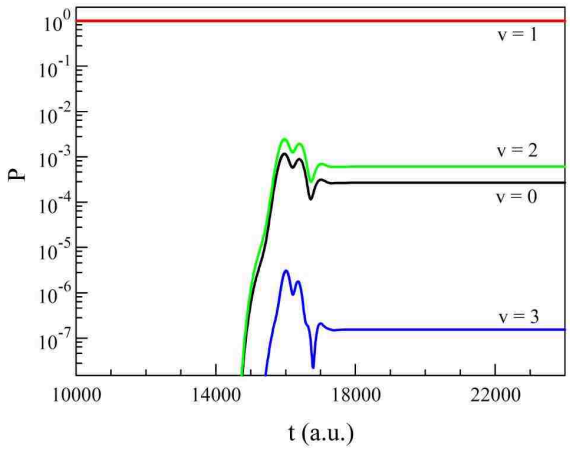

Figure 2. Evolution of vibrational state populations in CO during its collision with He atom, as they follow the example trajectory discussed in the text. Vibrational state-to-state transitions occur during the relatively short time of collision.

different. However, despite of dramatic vibrational motion and oscillations of $\tilde{I}(t)$ during the post-collisional dynamics, the value of J remains constant (within accuracy of the numerical method, very high here, $\delta J \approx 10^{-6}$). This demonstrates conservation of the angular momentum.

Figure 3 shows expectation value of quantum vibrational energy $\tilde{E}_{\text{vib}} = \left\langle \Psi(R) \middle| \hat{T} + V(R) \middle| \Psi(R) \right\rangle$ computed along the trajectory and Fig. 4 shows evolution of classical rotational energy $\tilde{E}_{\text{rot}} = J^2 / 2\tilde{I}$. Clearly, the post-collisional stage of the process exhibits very pronounced and ongoing ro-vibrational energy exchange, with amplitude close to 10 cm^{-1}. Indeed, comparing Figs. (3) and (4) one can see that oscillations of $\tilde{E}_{\text{vib}}$ and $\tilde{E}_{\text{rot}}$ are out of phase (shifted by π). The total energy is conserved with very high precision, $\delta E \approx 10^{-2}\,\text{cm}^{-1}$, defined only by accuracy of the numerical integration method.

Overall, in this collision the molecule lost about $\Delta E_{\text{tot}} = 2580\ \text{cm}^{-1}$. On average, $\Delta\tilde{E}_{\text{rot}} \approx 2560\,\text{cm}^{-1}$ and $\Delta\tilde{E}_{\text{vib}} \approx 20\,\text{cm}^{-1}$.

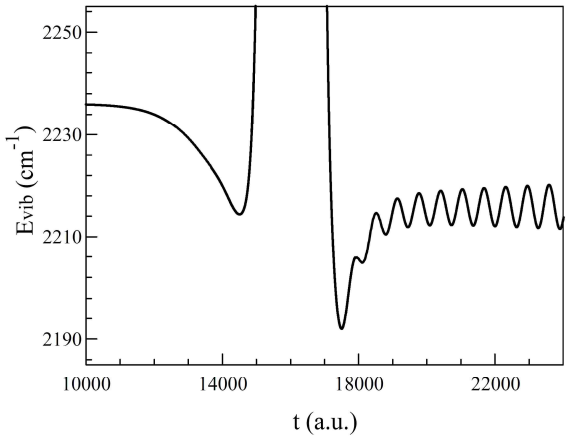

Figure 3. Evolution of average vibrational energy of CO (quantum expectation value) during its collision with He atom, as they follow the example trajectory discussed in the text. The post-collisional dynamics is seen.

Careful analysis of the long time behavior during the post-collisional stage shows two characteristic frequencies of oscillations in $\tilde{I}(t)$, $\tilde{E}_{\text{vib}}$ and $\tilde{E}_{\text{rot}}$. One (higher) frequency is

very obvious from Figs. (1), (3) and (4), corresponding to vibrational motion of the molecule. The second (lower) frequency corresponds to vibrational inharmonicity. It manifests as slight modulation of the vibrational oscillation amplitude in $\widetilde{I}(t)$, $\widetilde{E}_{\text{vib}}$ and $\widetilde{E}_{\text{rot}}$. Although not very clear, still this effect can be seen in Fig. 1, which captures one quarter-period of this low frequency dynamics.

Figure 5 shows evolution of three components of the mean torque $\widetilde{\boldsymbol{\tau}}$ during the moment of collision. All of them contribute to rotational de-excitation of the molecule and vanish when the collision is over. This is expected, since the geometry of collision is pseudo-arbitrary and the process is treated in the three-dimensional space, even though the instantaneous rotation of the diatomic molecule at each moment of time is essentially two-dimensional.

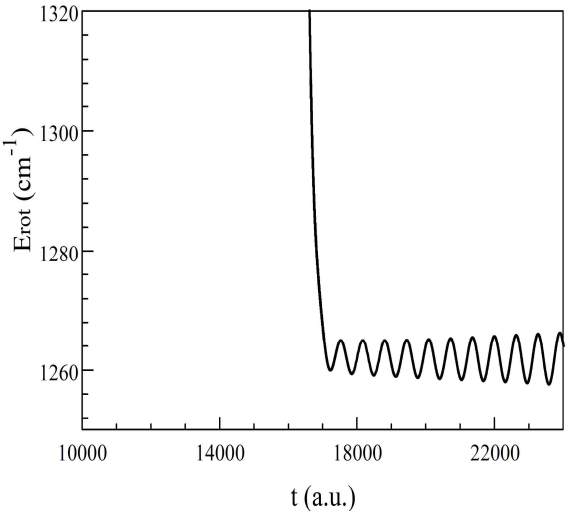

Figure 4. Evolution of classical rotational energy of CO during its collision with He atom, as colliding partners follow the example trajectory discussed in the text. The post-collisional dynamics is seen.

Coming back to the question of energy conservation, we repeated calculations for the same trajectory two more times: one using $\mu\langle\Psi(R)|R|\Psi(R)\rangle^2$ and second using $\mu\langle\Psi(R)|R^2|\Psi(R)\rangle$ for $\widetilde{I}$, instead of the correct $\widetilde{I} = \mu\langle\Psi(R)|R^{-2}|\Psi(R)\rangle^{-1}$ of Eq. (10′). In each test-case we computed the change of total energy in the system, δE. Results are presented in Fig. 6 and we see that the total energy is conserved only in the original

correct case (green line). In two test-cases some energy was lost: $\delta E \approx 6.0\ \mathrm{cm}^{-1}$ and $8.7\ \mathrm{cm}^{-1}$, respectively. Figure 6 shows that energy is lost during the short time interval of the molecule-quencher collision, when response of the molecule to torque of the quencher is essential. We also checked probabilities of state-to-state transitions in the two test-cases and found that they changed by ~5% and ~10%, respectively. This demonstrates that in dynamics calculations one should use only the correct expression for $\widetilde{I}$, that of Eq. (10′).

We just reviewed theory of two mixed quantum/classical approaches to collisional energy transfer and ro-vibrational energy flow: the heuristic fluid-rotor method (introduced earlier to treat recombination reactions [11]) and the more rigorous method based on the Ehrenfest theorem [47]. For the case of diatomic molecule + quencher we showed analytically that these two methods are entirely equivalent. Notably, they both make use of the average moment of inertia expressed as $\widetilde{I} = \langle \Psi(R) | I^{-1}(R) | \Psi(R) \rangle^{-1}$. Although diatomic molecule is the simplest case, this work serves as a proof-of-principle and gives us transparent tools for similar treatments of triatomic and small polyatomic molecules.

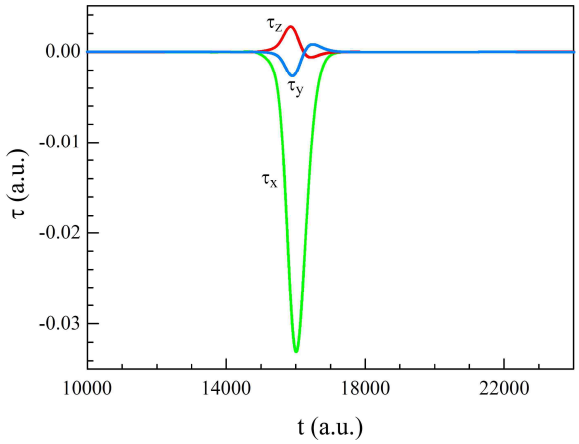

Figure 5. Evolution of three Cartesian components of torque $\tilde{\boldsymbol{\tau}}$, as CO collides with He atom, following the example trajectory discussed in the text.

Despite the equivalence discussed above, each of the two formulations has its own advantages, and is interesting on its own. For example, the Hamiltonian equations (28) for the diatomic molecule are easier to propagate numerically compared to the fluid-rotor equations (14′). But the fluid-rotor approach gives some additional insight, not immediately present in the Hamiltonian equations of motion (28). One example is the equivalence of the expectation value of quantum rotational potential, Eq. (8), and the classical rotational energy, Eq. (9), which is built into the fluid-rotor approach and leads to the central equation (10). Second example is the role played by the angular momentum and the torque in Eq. (11). These intuitive features provide better understanding of the mixed quantum/classical methodology. Another important aspect is the generality of the fluid-rotor approach. Namely, equations (10), (14) and (17) are expressed in Cartesian coordinates and can be directly applied to basically any molecule (triatomic, small polyatomic), irrespectively to the choice of the internal vibrational coordinates.

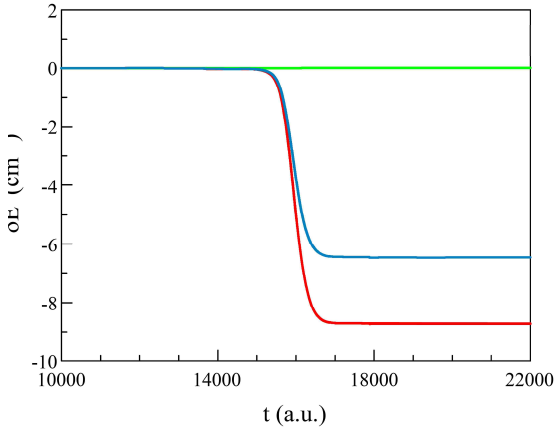

Figure 6. Total energy conservation in the mixed quantum/classical calculations. Correct method (green) uses Eq. (10′) for the mean tensor of inertia. Alternative methods discussed in the text (blue and red) give wrong results, $\delta E \neq 0$.

Numerical results presented here illustrate energy and momentum conservation in the mixed quantum/classical approach and open opportunities for computationally affordable treatment of collisional energy transfer. Calculations of converged cross

sections for CO ($v=1$) quenching by He impact in a broad range of temperatures, 30 < T < 3000 K, are presented below in the next section. [50].

1.5. Ro-Vibrational Quenching of CO (v = 1) by He Impact

Collisional energy transfer in carbon monoxide plays a significant role in atmospheric chemistry [52, 52], astrophysics [54-55] and condensed matter physics at ultra-cold temperatures [57, 58]. It has been studied in the past both theoretically [59-70] and experimentally [54, 69] in a broad range of temperatures. For example, rotational-vibrational transitions of CO is a valuable diagnostic probe of diverse astrophysical environments, such as interstellar and circumstellar media [71-75], where the temperatures of interest are very high, up to $T \sim 2500\ K$. Ro-vibrational transitions in the intermediate temperature range, $300\ K < T < 1000\ K$, are important to the post-combustion kinetics of CO [74-76]. Finally, these processes play critical role in developing the methods for cooling (and trapping) molecules to (at) sub-Kelvin temperatures, because efficiency of experimental techniques depends on the ratio between elastic and inelastic scattering cross sections. Thus, experimental studies of inelastic transitions in CO + He is an important benchmark, which has many potential applications including the high resolution molecular spectroscopy and controlled chemical reactions [77, 78]. Also, the study of vibrational relaxation of CO by collisions with He atoms provides a convenient general model which could be used for analysis of relaxation processes involving other diatomic molecules and other low-mass collision partners [64].

In the past, significant efforts have been devoted to testing and refining the potential energy surface (PES) for interaction between CO and He. Despite the fact that this system is relatively simple from the chemical point of view, a satisfactory agreement between calculated and experimental rate coefficients could not be achieved for a long period of time [60-73, 79]. The improvement of detection techniques [80, 81] and development of the PES [82-84] went through several refinement cycles. Finally, an acceptable agreement between theory and experiment has been reached in different parts of the desired broad range of temperatures. Two latest very similar PESs for this system have been reported [85, 86] and used for calculations of inelastic scattering. The PES from Ref. [85] was used in this work in order to enable direct comparison of our results with those of Refs [66] and [68].

Due to this past interest, the $\mathrm{CO}(v=1)+\mathrm{He}$ seems to represent an ideal benchmark system for developing and testing new theoretical methods for description of ro-vibrational quenching. The exact inelastic quantum scattering approach (coupled-channel) is expected to be accurate, but appears to be computationally affordable for $T < 500\ K$ only [60, 66,67,69]. At higher temperatures the approximate quantum calculations (coupled states) are usually accurate in predicting the transition probabilities and cross sections, but inclusion of the highly excited rotational states is still very expensive [67-68, 87]. In the contrast, the classical trajectory calculations, although highly affordable, are not able to provide good agreement with experimental data [88]. The main drawback of classical approach is leakage of zero-point energy, which becomes severe in the molecules with large vibrational quanta.

One reasonable way to tackle the inelastic ro-vibrational quenching is a mixed quantum/classical theory (MQCT) where the vibrational motion of the molecule is treated quantum mechanically while translational and rotational degrees of freedom are treated classically [89]. This approach eliminates the problem of zero-point energy leakage, and also allows capturing other quantum mechanical phenomena, such as scattering resonances (including calculations of their lifetimes [92,93]), quantization of vibrational states, their normal *vs.* local mode character and, finally, quantum symmetry [94].

The MQCT method [90-93] is expected to work well when the rotational quantum is small compared to thermal energy. This condition may not be fulfilled entirely for the lightest rotors only, such as methane or water (both contain H atoms), but it is satisfied well for majority of molecules, including heavy diatomics such as CO, O_2, N_2, *etc*. The second requirement is a semi-classical regime of scattering. In this respect the $\mathrm{CO}(v=1)+\mathrm{He}$ system studied here is not an easy one. The helium atom is light and one expects to see deviations from classical scattering at lower temperatures.

So, the purpose of this work was to carry out calculations of ro-vibrational quenching using the MQCT method and compare results with experiment in a broad range of temperatures, in order to see whether the classical approximation breaks down or not and, if it does, at what temperature does this happen and how inaccurate the MQCT results become, or they still remain acceptable? The findings from these calculations came out very encouraging.

Several sets of results in the range $5\ K < T < 2500\ K$ are presented, analyzed and compared in this chapter. Some of our results are from "direct" calculations of *quenching*, where the initial vibrational state of CO is $v=1$, and cross sections for

transitions to the final ground state $v=0$ are computed directly and used to derive the quenching rates. Another set of data is from the "reverse" approach, where cross sections for *excitations* from $v=0$ to $v=1$ are computed first, and then converted into the quenching rates using the principle of microscopic reversibility [70, 95]. One more set of data is from the average-velocity (symmetrized) approach of Billing [96], where the principle of macroscopic reversibility is built in by construction, and the results of direct and reverse calculations are very similar to each other.

This part of the chapter is organized as follows. In Sec. 1.6 we outline major components of the MQCT for the simplest energy-transfer process – collision of a diatomic molecule with an atomic quencher. Numerical results for $CO(v=1)+He$ are presented and discussed in Sec. 1.7. The last Sec. 1.8 is devoted to the symmetrized approach. Conclusions and possible applications of this theory are given in Sec. 1.9.

1.6 Equations for the Mixed Quantum/Classical Treatment

Detailed derivations of equations for the mixed quantum/classical treatment of inelastic diatomic quencher + molecule scattering have been reviewed recently [97]. Here we briefly recap only the major points of this theory.

1.6.1 Mixed Quantum/Classical Dynamics

Vibrational motion of the molecule is treated quantum mechanically by introducing the vibrational wave function $\Psi(R,t)$ and propagating numerically the time-dependent Schrodinger equation,

$$i\frac{\partial}{\partial t}\Psi(R,t)=\hat{H}(t)\Psi(R,t), \tag{35}$$

on a grid of points using the wave packet technique [47]. The Hamiltonian operator

$$\hat{H}(t)=-\frac{\hbar^2}{2\mu}\frac{\partial^2}{\partial R^2}+V_{\text{rot}}(R;t)+V_{\text{pot}}(R;t) \tag{36}$$

is time-dependent (implicitly) because the centrifugal term

$$V_{\text{rot}}(R;t)=\frac{p_\gamma^2}{2\mu R^2}+\frac{p_\alpha^2}{2\mu R^2\sin^2\gamma} \tag{37}$$

and the potential energy surface $V_{\text{pot}}(R;t)=V_{\text{pot}}(R,\alpha,\gamma,\mathbf{q})$ both depend on the classical variables: $\alpha(t)$, $\gamma(t)$ and $\mathbf{q}(t)$. Azimuthal angle α and polar angle γ describe orientation of the molecule in space. Its rotational motion is treated classically by introducing their conjugate momenta $p_\alpha(t)$ and $p_\gamma(t)$, and propagating the Hamiltonian equations

$$\dot{\alpha}=\frac{p_\alpha}{\tilde{I}\sin^2\gamma}, \tag{38a}$$

$$\dot{\gamma}=\frac{p_\gamma}{\tilde{I}}, \tag{38b}$$

$$\dot{p}_\alpha=-\frac{\partial\tilde{V}}{\partial\alpha}, \tag{38c}$$

$$\dot{p}_\gamma=-\frac{\partial\tilde{V}}{\partial\gamma}+\frac{p_\alpha^2\cos\gamma}{2\tilde{I}\sin^3\gamma}, \tag{38d}$$

The instantaneous mean moment of inertia $\widetilde{I}(t)$ of such "fluid" rotor is determined by vibrational wave function [90,97]

$$\widetilde{I}(t) = \left\langle \Psi(R,t) \middle| \frac{1}{\mu R^2} \middle| \Psi(R,t) \right\rangle^{-1}. \tag{39}$$

The mean-field potential

$$\widetilde{V}(\alpha,\gamma,\mathbf{q},t) = \left\langle \Psi(R,t) \middle| V_{\text{pot}}(R,\alpha,\gamma,\mathbf{q}) \middle| \Psi(R,t) \right\rangle, \tag{40}$$

drives the classical trajectory of motion for rotation and the process of quencher + molecule scattering, described by Cartesian coordinates $\mathbf{q}(t)$ and their conjugate momenta $\mathbf{p}(t)$:

$$\dot{\mathbf{q}} = \mathbf{p} / m, \tag{41a}$$

$$\dot{\mathbf{p}} = -\nabla \widetilde{V}. \tag{41b}$$

In this way the vibrational motion, treated with quantum mechanics, affects the classical degrees of freedom (rotation and scattering) through the mean values of $\widetilde{I}$ and $\widetilde{V}$ in Eqs. (38) and (41). In turn, the classical trajectory for rotation and scattering affects evolution of quantum vibrational wave function, through time-dependence of V_{rot} and V_{pot} in the Hamiltonian operator of Eq. (36). Energy is exchanged between vibrational, rotational and scattering degrees of freedom, while the total energy is conserved. Spectral analysis of the final vibrational wave packet gives information about probabilities of state-to-state transitions $P_{v'}^{jj'}(E)$, which is easy to convert into cross sections $\sigma_{v'}^{jj'}(E)$, as shown below.

1.6.2 Quenching Rate Coefficient from Direct Calculations

In this section, we will discuss ro-vibrational transitions and will label final states by primed indexes. For example, cross section for a transition from the initial ro-vibrational state (v, j) into the final state (v', j') at collision energy E is denoted by $\sigma_{w'}^{jj'}(E)$. Quantum mechanical expression for the rate coefficient of vibrational quenching from $v = 1$ into $v' = 0$ is [66-68,70]:

$$\kappa_{10}^{\mathrm{dir}}(T) = \sqrt{\frac{8kT}{\mu\pi}} \frac{1}{(kT)^2} \frac{\sum_{j'} \sum_{j} (2j+1) \exp\left(-\frac{\varepsilon_1^j}{kT}\right) \int_0^\infty \sigma_{10}^{jj'}(E)\, E \exp\left(-\frac{E}{kT}\right) dE}{\sum_{j} (2j+1) \exp\left(-\frac{\varepsilon_1^j}{kT}\right)}. \qquad (42)$$

Note that in this expression cross sections for the vibrational transition of interest (from $v = 1$ to $v' = 0$) are summed over the final rotational states (j') and are averaged over the initial rotational states (j), assuming thermal distribution and taking into account the rotational degeneracy. Ro-vibrational energies of the initial states are denoted by ε_1^j. Subscript "dir" means that these are "direct" calculations of quenching, as opposed to "reverse" calculations discussed in the next section.

Now recall that in our approach the rotational motion is treated classically. Distributions of the initial and final rotational states are continuous and smooth (not quantized). In this situation Eq. (8) should be rewritten in the following way:

$$\kappa_{10}^{\mathrm{dir}}(T) = \sqrt{\frac{8kT}{\mu\pi}} \frac{1}{(kT)^2} \int_0^\infty \widetilde{\sigma}_{10}(E)\, E \exp\left(-\frac{E}{kT}\right) dE\,, \qquad (43)$$

where we introduced

$$\widetilde{\sigma}_{10}(E) = \frac{\sum_{j'}\sum_{j}(2j+1)\exp\left(-\frac{\varepsilon_1^j}{kT}\right)\sigma_{10}^{jj'}(E)}{\sum_{j}(2j+1)\exp\left(-\frac{\varepsilon_1^j}{kT}\right)}. \qquad (44)$$

This emphasizes that only the vibrational motion is quantized, while the rotational motion is treated classically. Strictly speaking, our mixed quantum/classical calculations can't produce well-defined values of the individual $\sigma_{10}^{jj'}$. They can only give the average value of $\widetilde{\sigma}_{10}$.

From practical perspective, this also means that sampling of the initial rotational states can be optimized (at a given T) for calculations of $\widetilde{\sigma}_{10}(E)$ as a whole. There is no need to converge the value of each individual $\sigma_{10}^{jj'}(E)$; only the accuracy of average $\widetilde{\sigma}_{10}(E)$ matters. In this respect, some values of j are more important than others and it is convenient to introduce *weights* of the initial ro-vibrational states as

$$w_v^j(T) = \frac{(2j+1)\exp\left(-\frac{\varepsilon_v^j}{kT}\right)}{\sum_{j}(2j+1)\exp\left(-\frac{\varepsilon_v^j}{kT}\right)}. \qquad (45)$$

Using this definition we can convert Eq. (10) into

$$\widetilde{\sigma}_{10}(E) = \sum_{j} w_1^j \sum_{j'} \sigma_{10}^{jj'}(E). \qquad (46)$$

This transparent expression emphasizes summation over the final j' and averaging (weighted sum) over the initial j.

1.6.3 Quenching Rate Coefficient from Microscopic Reversibility

Microscopic reversibility plays fundamental role in the reaction dynamics [95]. In practice it is sometimes advantageous to carry out calculations in the "reverse" direction (*e.g.*, excitation instead of quenching) and then convert these raw data into the final data for "direct" process, using the principle of microscopic reversibility [72,95,100]. This approach works well for the full-quantum dynamics [99]. In the mixed quantum/classical dynamics the microscopic reversibility is not automatically built in [96], and we felt it is important to do calculations in the reverse direction as well, namely, for collisional excitation from $v' = 0$ into $v = 1$.

Calculations carried out for vibrational excitation at collision energy E' give us cross sections $\sigma_{01}^{j'j}(E')$. In notations of this section we switch the order of indexes, because the process is reversed, but we still keep association of unprimed and primed indexes with excited and ground vibrational states, respectively. The principle of microscopic reversibility states that [90]:

$$(2j+1)\sigma_{10}^{jj'}(E)E = (2j'+1)\sigma_{01}^{j'j}(E')E' . \qquad (47)$$

This assumes that the total energy (collisional + internal) of the direct processes is equal to that of the reverse process:

$$E + \varepsilon_1^j = E' + \varepsilon_0^{j'} . \qquad (48)$$

Rotational energy is included into the ro-vibrational eigenvalues ε_1^j and $\varepsilon_0^{j'}$, but it gives minor contribution compared to the quantum of vibration: $\Delta\varepsilon = \varepsilon_1^0 - \varepsilon_0^0 \approx 2143\ \mathrm{cm}^{-1}$

(using the PES of CO from Ref. [66]). Thus, for CO, calculations of direct and reverse processes should be carried out at very different collision energies. For example, if for the direct process $E = kT \approx 200\ \text{cm}^{-1}$ at room temperature, then for the reverse process $E' \approx E + \Delta\varepsilon = 2342\ \text{cm}^{-1} \approx 12kT$.

Substitution of Eqs. (47-48) into Eq. (42) allows obtaining the following formula (see Appendix):

$$\kappa_{10}^{\text{rev}}(T) \approx \sqrt{\frac{8kT}{\mu\pi}} \frac{1}{(kT)^2} \int_0^\infty \widetilde{\sigma}_{01}(E+\Delta\varepsilon)(E+\Delta\varepsilon)\exp\left(-\frac{E}{kT}\right) dE\ , \tag{49}$$

where rate coefficient of the direct process κ_{10} is expressed through average cross section for the reverse process $\widetilde{\sigma}_{01}(E+\Delta\varepsilon)$. We see that, indeed, the scattering calculations of the reverse process should be carried out at energy raised by $\Delta\varepsilon$, compared to calculations of the direct process.

Note that Eq. (49) is approximate. In order to make this formula look similar to Eq. (43) we used two approximations described in Appendix, but they hold well for the CO + He quenching. Furthermore, those approximations are related to how the rotational energy is treated. In the absence of rotation the Eq. (49) is exact. The general expression is also discussed in Appendix.

1.6.4 Numerical Approach

The initial conditions for CO + He collisions were generated in the following way. At $t = 0$ the center of mass of CO is at the origin of the laboratory reference frame, while He is at a distance of ~ 35 Bohr. The incident direction of He atom is sampled

randomly and uniformly as explained in Ref. [97]. The impact parameter b is sampled randomly and uniformly (independently from sampling the incident direction) in the range $0 \le b \le b_{\max}$, where $b_{\max} = 8$ Bohr. Initial momenta $p(t=0) = \sqrt{2\mu E}$ of the incident He atoms are determined by the center-of-mass collision energy E, constant for a batch of trajectories.

The initial rotational states of CO are chosen randomly, but taking into account their weights in Eq. (11). For example, for the direct calculations (quenching) at a given temperature T, first, the weights $w_1^j(T)$ are computed and truncated at some large value of j, giving n_j numbers. Then, the range $[0,1]$ is split onto n_j intervals with lengths proportional to $w_1^j(T)$. Finally, a random number is generated in the range $[0,1]$ and the initial rotational state j is chosen based on which of n_j sectors this number falls in.

When the initial rotation state j is chosen, the vibrational eigenstate $v = 1$ is computed for the Hamiltonian (2) with $V_{\text{rot}}(R;t) = j^2 / (2\mu R^2)$ and is used to set up the initial wave packet $\Psi(R, t=0)$. The non-uniform grid of 64 points is optimized as explained in Ref. [39]. The initial values of classical variables for rotation are $\alpha = 0$, $\gamma = \pi/2$, $p_\gamma = 0$ and $p_\alpha = j$. Classical equations of motion are propagated using 4$^{\text{th}}$-order Runge-Kutta method with adaptive step-size control [101]. Vibrational wave packet is propagated using Lanczos method [102]. Kinetic energy operator is applied using FFT [101].

At the final moment of time the spectrum of vibrational eigenstates of the final rotational state $j' = \sqrt{p_\gamma^2 + p_\alpha^2 / \sin^2 \gamma}$ is computed, and, the vibrational wave packet $\Psi(R,t)$ is projected onto $v' = 0$ to obtain the corresponding transition probability $P_{10}^{jj'}(E)$. If needed, these could be converted into individual cross sections $\sigma_{10}^{jj'}(E)$ by binning the values of final j' (the values of initial j are already integer by set up). Instead, we focused on computing the rotationally averaged cross sections for vibrational quenching $\tilde{\sigma}_{10}(E)$ using:

$$\tilde{\sigma}_{10}(E) = 2\pi b_{\max} \sum_{n=1}^{N} b\, P_{10}^{jj'}(E) / N \,. \qquad (50)$$

In this expression the sum over N trajectories in a batch replaces two sums in Eq. (46) -- the simple sum over final j' and the weighted sum over initial j.

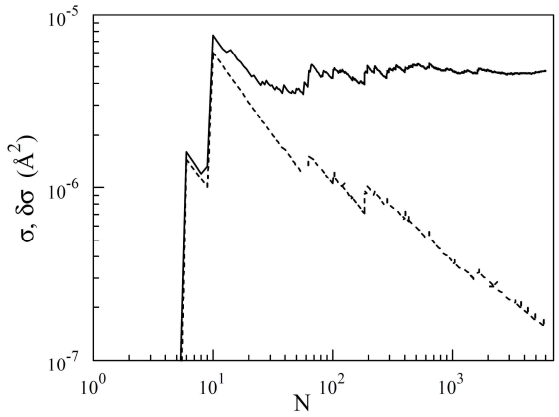

Figure 7. Convergence of average excitation cross section $\tilde{\sigma}_{01}$ (solid line) and its statistical error $\delta\tilde{\sigma}_{01}$ (dotted line) as a function of the number of trajectories N in a sample.

For calculations in the reverse direction (excitation) the procedure is similar, but the weights $w_0^{j'}(T)$ are used and the initial wave function is that of $v' = 0$ eigenstate. The incident momentum $p'(t=0) = \sqrt{2\mu E'}$ is determined by $E' = E + \Delta\varepsilon$, and the final projection is onto $v = 1$ eigenstate. The result of such calculation is $\tilde{\sigma}_{01}(E + \Delta\varepsilon)$.

Figure 7 gives example of convergence study for $\tilde{\sigma}_{01}(E)$ at $E = 800$ cm^{-1} and $T = 200$ K. The value of statistical error $\delta\tilde{\sigma}$ is also shown. We see that after $N \sim 6000$ trajectories the error drops to the level of ~2%, which we consider a converged result. It is worth noting, and is rather surprising, that after only as few as 20 trajectories one gets a reasonable estimate of averaged cross section $\tilde{\sigma}$. Of course, after 20 trajectories the statistical error is still high, $\delta\tilde{\sigma} = 60\%$. Anyway, this is a very useful property: it appears that one can generate a good estimate of rotationally averaged $\tilde{\sigma}$ at very little computational cost. This must be due to efficiency of the multi-dimensional Monte-Carlo integration in Eq. (50), which utilizes the importance sampling according to the weights w_v^j given by Eq (45). In Table 1 we listed how many values of j were included in Eq. (44) and how many trajectories were propagated in Eq. (50), in order to obtain converged results at different temperatures.

T (K)	j_{max}	N	δσ/σ×100%
5*	2	120	31
20*	5	120	33
50*	9	240	25
100	18	3800	2
500	35	4700	2
1000	52	5900	2
1500	64	7800	2
2000	70	8600	2
2300	75	9500	2

Table 1: Requirements and convergence in terms of the rotational excitation and the number of trajectories in the MQCT calculations at different temperatures.

1.7 Results and Discussion

Figure 2a shows examples of computed cross sections for quenching, $\tilde{\sigma}_{10}(E)$, in a broad range of relevant energies for five chosen values of temperature: from $T = 100$ K to $T = 900$ K with 200 K steps. Figure 2b shows the same for excitation, $\tilde{\sigma}_{01}(E + \Delta\varepsilon)$. Note that Figs. 8a and 8b have different horizontal axes: E and $E+\Delta\varepsilon$, respectively. The

overall trends of $\tilde{\sigma}_{10}(E)$ and $\tilde{\sigma}_{01}(E+\Delta\varepsilon)$ are similar (except at low energies, see below). Their monotonic behavior is easy to fit by the well-known analytic expression for energy dependence of state-to-state transition cross section [103]:

$$\sigma(E) = aE\ \exp(-b/\sqrt{E}) \quad .(17)$$

The fitting coefficients a and b carry physical meaning: a corresponds to the average magnitude (well depth) while b corresponds to the average distance (well size) of the molecule + quencher interaction potential. We found that this dependence describes well both excitation and quenching processes -- $\tilde{\sigma}_{10}(E)$ and $\tilde{\sigma}_{01}(E+\Delta\varepsilon)$, with E in Eq. (51) replaced by $E+\Delta\varepsilon$ for the latter case, and slightly different fitting coefficients. The coefficients are collected in Table 2. The dependencies of $a(T)$ and $b(T)$ on temperature are smooth and monotonic.

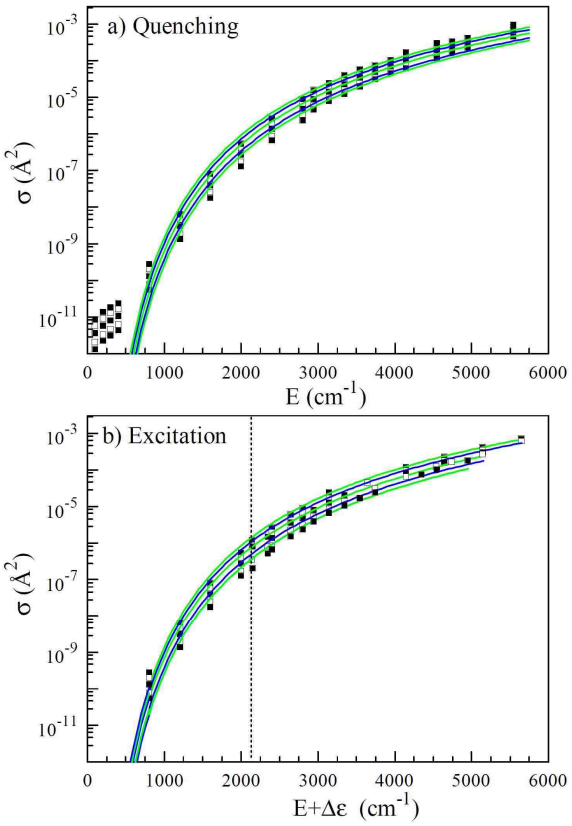

Figure 8. Computed cross sections (symbols) and their analytic fits (lines) for: **a)** quenching $\tilde{\sigma}_{10}(E)$; and **b)** excitation $\tilde{\sigma}_{01}(E+\Delta\varepsilon)$. Each frame shows data obtained at five values of temperature: from T=100 K to T = 900 K with 200 K steps. Vertical dotted line in frame (b) corresponds to $E=0$, or $E'=\Delta\varepsilon$.

The quenching cross section $\tilde{\sigma}_{10}(E)$ tends to vanish as $E \to 0$. Four points computed in the range $E < 500$ cm^{-1} exhibit cross sections on order of $\tilde{\sigma}_{10} \approx 10^{-11}$ Å^2, and this is probably an overestimation. These numbers may not be particularly accurate because they are so small. The fit using Eq. (51), with these points excluded, suggests even smaller values for quenching cross section at $E < 500$ cm^{-1}.

In contrast, the excitation cross section $\tilde{\sigma}_{01}(E + \Delta\varepsilon)$ is finite (non-zero) at $E = 0$ and exhibits values on order of $\tilde{\sigma}_{01} \approx 10^{-6}$ Å^2. Note that the values of excitation cross sections $\tilde{\sigma}_{01}(E + \Delta\varepsilon)$ are finite even at $E \le 0$ (in Fig. 8b this part of energy range is to the left of the vertical dashed line $E' = \Delta\varepsilon$). This is so because, as explained in the previous section, the reverse calculations are done at collision energy $E' = E + \Delta\varepsilon$. At $E = 0$ we still have some residual collision energy $E' = \Delta\varepsilon \approx 2143$ cm^{-1}, just sufficient to reach the channel threshold. Below this energy the quantum mechanical cross section for excitation would be zero, but the MQCT approach yields a (small but) non-zero cross section at $E < 0$. This is an artifact, apparently, due to the mean-field treatment of collision. According to Eq. (49) the energy range $E < 0$ is not included in the integral of the rate coefficient κ_{10}^{rev}.

	$a\times10^3$ (Å^2/cm^{-1})		$b\times10^{-2}$ (cm$^{-1/2}$)	
T (K)	excitation	quenching	excitation	quenching
100	1.66	1.61	7.51	7.47
200	1.65	1.60	7.43	7.39
300	1.65	1.60	7.35	7.32
400	1.64	1.60	7.28	7.24
500	1.62	1.59	7.22	7.15
600	1.62	1.58	7.12	7.06
700	1.61	1.55	7.05	6.98
800	1.58	1.51	7.00	6.91
900	1.52	1.47	6.93	6.83

Table 2: Temperature dependence of fitting coefficients in the analytic expression for excitation and quenching cross sections

To further clarify this point we plotted in Figs. 9a and 9b the values of integrand in Eq. (43) for direct calculations $f^{\mathrm{dir}}(E) = \widetilde{\sigma}_{10}(E)\, E \exp\{-E/kT\}$ and in Eq. (49) for reverse calculations $f^{\mathrm{rev}}(E') = \widetilde{\sigma}_{01}(E')\, E' \exp\{-(E'-\Delta\varepsilon)/kT\}$, respectively. One sees that in Fig. 3a the integrand vanishes at $E = 0$ as it should, while in Fig. 3b the integrand is finite at $E = 0$. At higher temperatures this does not affect the value of κ_{10} significantly, since the integrand shows maximum at $E > 0$, and its behavior near $E = 0$ is less important. However, at $T \le 400$ K the maximum of the integrand is at $E \le 0$ (to the left of the vertical dashed line $E' = \Delta\varepsilon$) so that the energy region near $E = 0$ plays the dominant role. Thus, the artificially large values of $\widetilde{\sigma}_{01}(E + \Delta\varepsilon)$ at low energies E lead to artificially large values of integrand in Eq. (49) which, at the end, may result in overestimated values of $\kappa_{10}(T)$ at low temperatures.

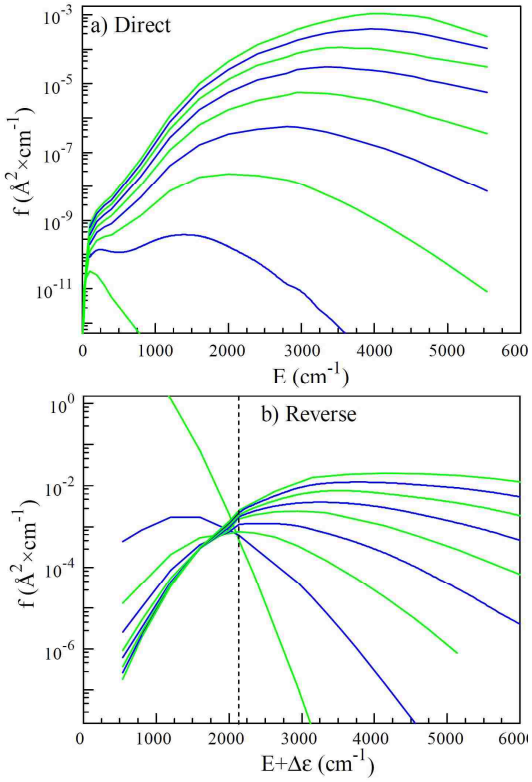

Figure 9. Energy dependence of the integrand in the expression for quenching rate coefficient: **a)** $f^{\mathrm{dir}}(E)$ in Eq. (9) for direct calculations; and **b)** $f^{\mathrm{rev}}(E + \Delta\varepsilon)$ in Eq. (15) for reverse calculations. Each frame shows data obtained at nine values of temperature: from $T = 100$ K to $T = 900$ K with 100 K steps. Vertical dotted line in frame (b) corresponds to $E = 0$, or $E' = \Delta\varepsilon$.

The results for $\kappa_{10}(T)$ from direct and from reverse calculations, and the available experimental data [55, 71, 104], are shown all together in Fig. 10 (solid lines for calculations, symbols for experiments). The $\kappa_{10}(T)$ dependence from direct calculations shows correct trend in the entire range of temperatures, but the absolute values are underestimated compared to experiment, particularly at low temperatures (three orders of magnitude difference at $T = 100$ K). Interestingly, the $\kappa_{10}(T)$ dependence from reverse calculations follows experiment very closely at all temperatures higher than $T \approx 400$ K. However, at $T \leq 400$ K the reverse calculations deviate from the experiment up, giving overestimated values of $\kappa_{10}(T)$, which could be expected from the discussion above.

Given the success of reverse approach at $T > 400$ K, it would be desirable to find a practical fix for the problem at low temperatures. An *ad hoc* solution is simply to force $\tilde{\sigma}_{01}(E + \Delta\varepsilon)$ to go to zero at $E = 0$, analytically. We tried this, and multiplied the computed cross section $\tilde{\sigma}_{01}(E + \Delta\varepsilon)$ by a smooth masking function (related to arctangent) that starts from zero at $E = 0$ and goes to one at $E \approx 700$ cm^{-1}. The same function was used for all temperatures. The result is in excellent agreement with experiment in the entire range of

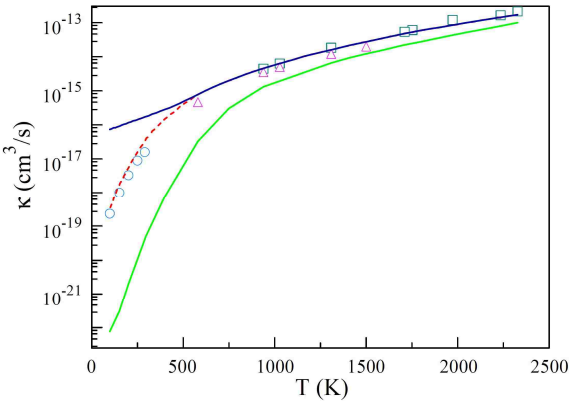

Figure 10. Rate coefficients for quenching of $CO(v = 1)$ by He impact from direct calculations (solid green line) and from reverse calculations (solid blue line), in comparison to experimental results (symbols) taken from Refs. [4, 18, 51]. Dashed red line shows results of empirical correction to the reverse approach at low collision energies. See text for details.

temperatures (see Fig. 10, dashed line). Although this approach is entirely empirical, its simplicity and success makes it quite useful.

It is worth noting that at high temperatures we see a much better agreement between direct and reverse calculations. For example, at $T = 2300$ K two values of κ_{10} are less than one order of magnitude different (75% different, to be more precise) and the trend is such that at even higher temperatures the difference is expected to decrease even further. Recall that direct and reverse calculations are done with two different collision energies, E and $E + \Delta\varepsilon$, respectively. When E is small the effect of extra-energy (equal to the vibrational quantum $\Delta\varepsilon$) is very significant, but when energy E is high by itself the effect of $\Delta\varepsilon$ is much less important. So, one can deduce that the difference between direct and reverse calculations is manifestation of quantization of vibrational states in the MQCT method. In the case of CO the vibrational quantum is particularly large, $\Delta\varepsilon = 2143$ cm^{-1}, and it is not surprising that high temperature is needed in order to see the direct and reverse results

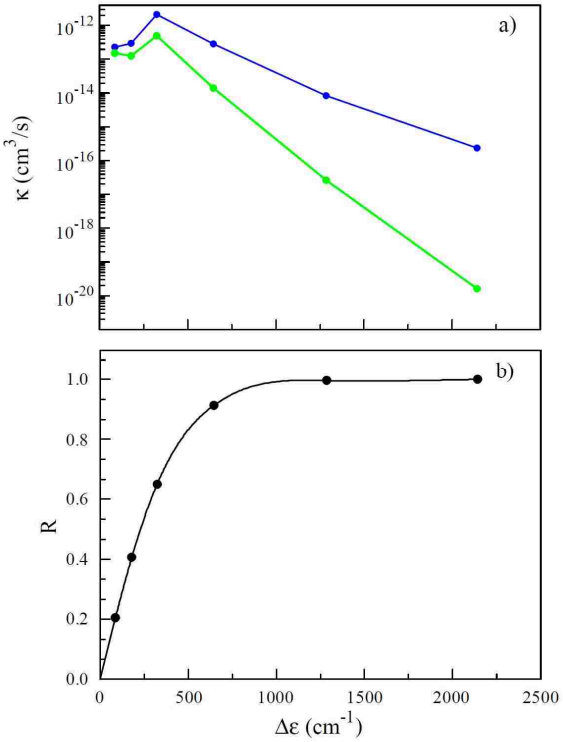

Figure 11. The dependence of: a) κ_{10}^{rev} and κ_{10}^{dir}, and b) the ratio $R = (\kappa_{10}^{\text{rev}} - \kappa_{10}^{\text{dir}})/(\kappa_{10}^{\text{rev}} + \kappa_{10}^{\text{dir}})$, on the value of vibrational quantum $\Delta\varepsilon$ in a series of computational experiments with theoretically modified CO potential.

merging to the same value of κ_{10}. Indeed, the quenching of fundamental transition in $\mathrm{CO}(v=1)$ is one of the worst cases scenario. Near the dissociation limit, where the density of states is much higher, the mixed quantum classical method would work much better.

Moreover, the problem of non-vanishing $\tilde{\sigma}_{01}(E+\Delta\varepsilon)$ at $E=0$ (discussed above) is also related to the large value of quantum $\Delta\varepsilon$ in CO. If $\Delta\varepsilon$ would be smaller, the value of $\kappa_{10}(T)$ from reverse calculations would agree with experiment even at lower temperatures. In order to test this hypothesis we carried out a set of additional calculations for one chosen value of $T=300$ K, but for several different CO molecules. Impossible in experiment, but straightforward in theory is to flatten the PES of CO, producing new molecule with smaller vibrational quantum! In such computational experiments we studied the values of vibrational quantum down to $\Delta\varepsilon=100$ cm^{-1}. Figure 11a gives the values of $\kappa_{10}^{\mathrm{rev}}$ and $\kappa_{10}^{\mathrm{dir}}$ vs. $\Delta\varepsilon$, while Figure 11b gives the ratio $R=(\kappa_{10}^{\mathrm{rev}}-\kappa_{10}^{\mathrm{dir}})/(\kappa_{10}^{\mathrm{rev}}+\kappa_{10}^{\mathrm{dir}})$. The last points in Fig. 5 (a,b) corresponds to true CO, where at $T=300$ K the value of κ_{10} obtained from the reverse calculations is several orders of magnitude larger than that obtained from the direct calculations. In this case the ratio R is very close to one. As we reduced $\Delta\varepsilon$ we first saw a plateau for the ratio R, expanding down to $\Delta\varepsilon\sim1000$ cm^{-1}, but then, in the range of $\Delta\varepsilon<400$ cm^{-1}, we observed a fast (close to linear) decrease of the ratio R down to zero (see Fig. 11b). At $\Delta\varepsilon=100$ cm^{-1} the values of κ_{10} from direct and reverse calculations were only 20% different.

We believe this numerical experiment proves that direct and reverse calculations are expected to be equivalent (and, in fact, both accurate) in the semi-classical regime, when the vibrational quantum $\Delta\varepsilon$ is on the order of thermal energy, or smaller. However, our results for CO with large vibrational quantum show that at low temperatures they produce different results, which means that microscopic reversibility is not built automatically in the MQCT method.

1.8 The Average Velocity (Symmetrized) Approach

During the process of finalizing this chapter we found a book of Billing [96], which we did not know about. It appears that Gert Due Billing found an ingenious solution that allows merging the results of direct and reverse calculations, even in the case of low temperature and large vibrational quantum $\Delta\varepsilon$. We are not going to repeat his arguments here, but will present our own viewpoint on his method.

We believe that the problem of unsatisfied reversibility is due to the Ehrenfest (mean-field) treatment of the scattering process in the MQCT method. Indeed, in the full-quantum approach the incoming wave in the entrance channel and the outgoing wave in the exit channel of the process correspond to two different energies (very different in the case of large vibrational quantum $\Delta\varepsilon$). The approximate method of trajectory surface hopping [105] takes this information into account, by adjusting momentum in the exit channel to reflect the change of internal energy (by $\Delta\varepsilon$). But the Ehrenfest approach is, in a sense, an antithesis of the trajectory surface hopping. If the transition probability is very small (which is the case here at low *T*) the trajectory in the inelastic exit channel is almost equivalent to the elastic trajectory, because the mean field potentials, given by Eq.

(6), are very similar and momenta are very close to $p = \sqrt{2\mu E}$. In order to fix the Ehrenfest approach we must use, somehow, the information from reverse trajectories that have momentum $p' = \sqrt{2\mu E'}$, which corresponds to energy of the exit channel $E' = E + \Delta\varepsilon$. Our results for CO presented above show that experiment is between the direct and reverse results, which is encouraging.

1.8.1 Transition Cross-Section

One technical thing we have to do first is to replace the classical-like expression for cross section, Eq. (16), with a quantum-like formula

$$\sigma_{10}^{jj'} = \frac{\pi}{k^2} \sum_{J=0}^{J_{\max}} \frac{1}{N_J} \frac{(2J+1)}{(2j+1)} \sum_{l=|J-j|}^{l=J+j} P_{10}^{jj'} . \qquad (52)$$

Here J is total angular momentum of the molecule + quencher system, l is orbital momentum of the quencher. As in Eq. (50) the probability is summed over the final rotational states but Eq. (52) is for one given value of j; it should be thermally averaged over the initial j, similar to Eq. (44). This expression originates from the standard full-quantum expression [106].

Practical implementation of this formula uses sampling procedure different from the one described in Sec. 1.6.4. Here, for each given j one should sample J randomly and uniformly between 0 and $J_{\max}$ (determined by $b_{\max}$) and then sample l randomly and uniformly between $|J - j|$ and $J + j$. However, we checked and found that both sampling methods produce practically equivalent distributions. We also checked and found that expressions of Eq. (50) and Eq. (52) give very similar results for cross

sections. Indeed, one can show that in the limit of small j and high collision energy, when $J \approx l$ (here we take $j = 0$ for simplicity) and $l \approx bk$, which follows from $l(l+1) = (bk)^2$, expression of Eq. (52) gives:

$$\begin{aligned} \sigma &\approx \frac{\pi}{k^2} \sum_l \frac{(2l+1)}{N_l} P = \frac{\pi}{k^2} \frac{l_{\max}}{N} \sum_l (2l+1)\, P \\ &\approx \frac{\pi}{k^2} \frac{l_{\max}}{N} \sum 2bk\ P = \frac{2\pi\, b_{\max}}{N} \sum b\, P\,, \end{aligned} \tag{53}$$

equivalent to Eq. (50). Our numerical results showed that Eq. (50) slightly underestimates cross section compared to Eq. (52), but (even in the worst case of low collision energy, $E = \Delta\varepsilon / 4 \sim 536\ \ \mathrm{cm}^{-1}$) by no more than 20%.

1.8.2 Microscopic Reversibility

An important property of Eq. (52), in the context of reversibility, is the explicit dependence of cross section on collision energy ($k^2 = 2\mu E/\hbar^2$ in the case of direct and $k'^2 = 2\mu E'/\hbar^2$ in the case of reverse calculations) and on rotational degeneracy ($2j+1$ and $2j'+1$, respectively). Substitution of Eq. (52) into the principle of microscopic reversibility, Eq. (47), leads to numerous cancellations and gives:

$$P_{10}^{jj'}(E) = P_{01}^{j'j}(E')\,. \tag{54}$$

This expression tells us that microscopic reversibility is satisfied only if the transition probabilities for direct and reverse processes are equal. (Note that this is third version of the principle, now in terms of individual trajectories, in addition to that in terms of cross sections in Eq. (47), and rate coefficients in Eq. (1C8)).

Now recall that probability of vibrationally inelastic (and in general any non-adiabatic) transition depends on collision velocity. We can't possibly satisfy Eq. (54) at low energy E if $p=\sqrt{2\mu E}$ but $p'=\sqrt{2\mu(E+\Delta\varepsilon)}$ (*i.e.*, much larger). One straightforward solution to the problem would be to launch direct and reverse trajectories with *equal* velocities. The average between direct and reverse velocities seems to be a reasonable chose, which leads to: $(\sqrt{E}+\sqrt{E+\Delta\varepsilon})/2=\sqrt{U}$, where we introduced the *actual* collision energy U that permits to satisfy microscopic reversibility. This equation can be easily solved for E (taking square of left and right parts, twice) which gives

$$E=U-\frac{\Delta\varepsilon}{2}+\frac{\Delta\varepsilon^2}{16U}. \tag{55}$$

In a similar way, starting with $(\sqrt{E'-\Delta\varepsilon}+\sqrt{E'})/2=\sqrt{U}$, one obtains

$$E'=U+\frac{\Delta\varepsilon}{2}+\frac{\Delta\varepsilon^2}{16U}. \tag{56}$$

Note that these expressions satisfy $E'=E+\Delta\varepsilon$ and $E<U<E'$.

Thus, in the symmetrized approach we will satisfy microscopic reversibility through $P_{10}^{jj'}(U)=P_{01}^{j'j}(U)$, but then we will express E and E' through U according to Eqs. (55,56), and will integrate the resultant probabilities in Eq. (43) for direct and in Eq. (1C10) for reversed processes, using cross section in the form of Eq. (52). An important thing to note is that k^2 in the denominator of Eq. (52) should correspond to the integration variable, namely, $k^2=2\mu E/\hbar^2$ in the case of direct and $k'^2=2\mu E'/\hbar^2$ in the case of reverse calculations.

Furthermore, one can express U through E

$$U = \frac{E + \sqrt{E(E+\Delta\varepsilon)}}{2} + \frac{\Delta\varepsilon}{4}, \tag{57}$$

or U through E'

$$U = \frac{E' + \sqrt{E'(E'-\Delta\varepsilon)}}{2} - \frac{\Delta\varepsilon}{4}. \tag{58}$$

These expressions show that at the lower integration limit in Eq. (43), when $E = 0$, we have $U = \Delta\varepsilon/4$. Similar, at the lower integration limit in Eq. (1C10), when $E' = \Delta\varepsilon$, we have $U = \Delta\varepsilon/4$. So, the actual collision energy U of our trajectories is never less than one quarter of the vibrational quantum. In the case of CO quenching this is about $E = 536$ cm^{-1}.

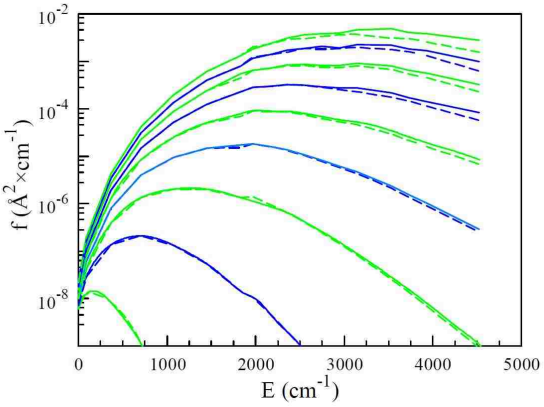

Figure 12. Energy dependence of the integrands $f^{\mathrm{dir}}(E)$ of Eq. (25) and $f^{\mathrm{rev}}(E)$ of Eq. (27) for the symmetrized average-velocity approach. The data obtained at nine values of temperature are presented: from $T = 100$ K to $T = 900$ K with 100 K steps. Note that results from both direct (solid line) and reverse (dashed line) calculations are shown in one frame.

1.8.3 Numerical Results

It has to be stressed that in order to implement the symmetrized average-velocity approach we did not have to redo the scattering calculations. All we had to do was to reintegrate the cross sections we already had from the direct and reverse calculations discussed in Sec. III, but treating E and E' in their old meaning as U in its new meaning. Namely, for the direct process we integrated over E from 0 to $+\infty$, according to Eq. (43), the following integrand:

$$f^{\mathrm{dir}}(E) = \widetilde{\sigma}_{10}(U)\, E \exp\{-E/kT\}, \tag{59}$$

where the $U = U(E)$ dependence is that of Eq. (57) and where for the reverse process we integrated over E' from $\Delta\varepsilon$ to $+\infty$, according to Eq. (1C10), the following integrand:

$$f^{\mathrm{rev}}(E') = \widetilde{\sigma}_{01}(U)\, E' \exp\{-(E' - \Delta\varepsilon)/kT\}, \tag{26}$$

where the $U = U(E')$ dependence is that of Eq. (24). Alternatively, for the reverse process one can re-express $f^{\mathrm{rev}}(E')$ through E

$$f^{\mathrm{rev}}(E) = \widetilde{\sigma}_{01}(U) E \exp\{-E/kT\}, \tag{27}$$

and integrate it from 0 to $+\infty$, according to Eq. (A11).

In Fig. 12 we plotted $f^{\mathrm{dir}}(E)$ and $f^{\mathrm{rev}}(E)$ together, using solid and dashed lines, respectively, for nine chosen values of temperature from $T = 100$ K to $T = 900$ K with 100 K steps. This picture demonstrates very clearly that $f^{\mathrm{dir}}(E) \cong f^{\mathrm{rev}}(E)$, particularly at low energies. It is almost unbelievable that Fig. 6 contains all exactly the same data as Figs. 3a and 3b, only their arrangement is different (now in terms of $U = U(E)$).

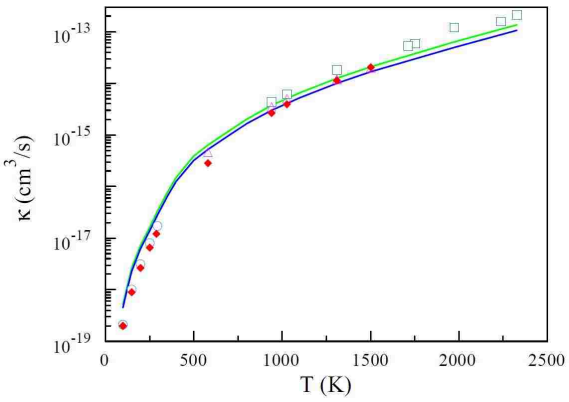

Figure 13. Rate coefficients for quenching of $\mathrm{CO}(v = 1)$ by He impact obtained according to the symmetrized average-velocity approach from direct (green line) and reverse (blue line), calculations. Experimental results from Refs. [4, 18, 53] are shown by empty symbols. Full quantum results from Ref. [35] are shown by filled red diamonds.

The results for $\kappa_{10}(T)$ from the symmetrized calculations, both direct and reverse (lines), are shown in Fig. 13 and compared to available experimental data (empty symbols). The results from direct and reverse calculations are very close to each other, particularly at low temperatures, when transition probabilities are small and the perturbative picture discussed in Sec. IV-B is applicable. The experimental dependence of $\kappa_{10}(T)$ is reproduced really well by these calculations, through the six orders of magnitude range of values and in a broad range of temperatures, without any empirical adjustments. The MQCT results also compare well with full quantum results of K. Peterson and G. McBane from Ref. [35] shown in Fig. 13 by filled red diamonds (obtained using a different PES).

Finally, we looked at the very low temperature range, where the full quantum calculations of N. Balakrishnan [66] showed the switch of the monotonic $\kappa_{10}(T)$ behavior near the $T = 20$ K from decreasing to growing. Interestingly, our MQCT calculations show similar behavior. Figure 8 demonstrates that at very low temperature the rate coefficient $\kappa_{10}(T)$ starts growing, in contrast to the monotonic decrease, expected from *T*-dependence in Fig. 7. In fact, one can show this analytically: As $E \to 0$ we have $U \to \Delta\varepsilon/4$ and, at zero-order, we can replace the dependence of $\tilde{\sigma}_{10}(U) \cdot E$ by a constant number proportional to $P_{10}(\Delta\varepsilon/4)$

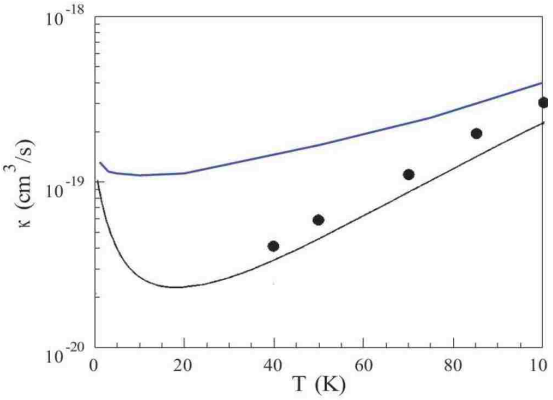

Figure14. Rate coefficients for quenching of $CO(v=1)$ by He impact in the low temperature range obtained here (blue line) in comparison with full quantum calculations of Ref. [15] (black line) and experimatal values from Ref. [53] (symbols).

which corresponds to rotation-less transition at $T = 0$. Then, from Eq. (43) we can obtain the lower boundary estimate:

$$\kappa_{10}^{\mathrm{dir}}(T) \geq \sqrt{\frac{8kT}{\mu\pi}} \frac{\pi\hbar^2}{2\mu(kT)^2} P_{10}(\Delta\varepsilon/4) \int_0^\infty \exp\left(-\frac{E}{kT}\right) dE = \sqrt{\frac{2\pi\hbar^4}{\mu^3 kT}} P_{10}(\Delta\varepsilon/4) \ . \qquad (28)$$

So, we see that in the $T \to 0$ limit one should expect to observe $\kappa_{10}(T) \to \infty$, and our calculations near $T = 5\ \mathrm{K}$ really show this. Note that this is a classical behavior, different from the quantum mechanical Wigner law that becomes valid at sub-Kelvin temperatures [107].

As for the absolute value of rate coefficient, the largest discrepancy between the MQCT rate and the full-quantum rate of N. Balakrishnan is observed near $T = 20\ \mathrm{K}$. There, our result is about a factor of ×4 higher, which can probably be judged as semi-quantitative agreement. Note that at $T < 100\ \mathrm{K}$ we did not try to reach convergence and run only few hundred trajectories to obtain an estimate of cross section (20-30% statistical error). Also, like N. Balakrishnan, we included only the values of j up to $j = 3$, in order to make comparison straightforward.

Finally, we computed the values of converged quenching cross sections for a broad range of collision energies. Note that such cross sections are not really needed anywhere in the mixed quantum/classical treatment of kinetics.

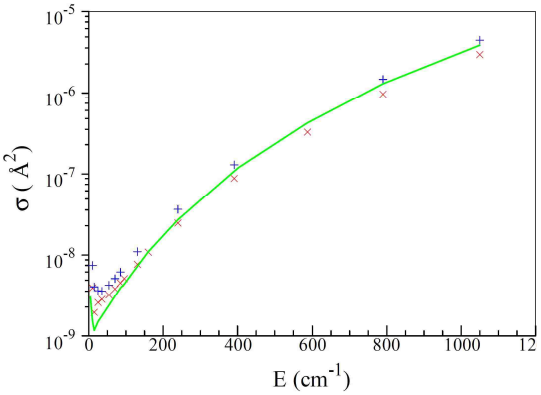

Figure 15. Cross sections for quenching of $\mathrm{CO}(v = 1)$ by He impact obtained by MQCT method (green line) in comparison with full quantum CC results from Ref. [15] and CS results from Ref. [17] (blue and red symbols, respectively).

We did these calculations only in order to conduct a detailed comparison of the MQCT results against results of the full quantum methods. Figure 15 shows our data (green line) in comparison with CC calculations of N. Balakrishnan [66] (blue symbols), and CS calculations of R. Krems [68] (red symbols) on the same PES. The overall trend of energy dependence is reproduced really well. At collision energies above 100 cm^{-1} the MQCT results lie between CC and CS results. At lower energies the MQCT cross sections are somewhat underestimated (*e.g.*, by a factor of ×4 compared to CC results of N. Balakrishnan at $E = 10\,\mathrm{cm}^{-1}$) and are closer to CS results of R. Krems. Note, however, that in this energy range there is a discrepancy by about a factor ×2 even between results of two quantum methods. Overall, the agreement of MQCT with full quantum methods can be judged as good.

1.9 Conclusions for Chapter 1

The mixed quantum/classical approach was applied to the problem of ro-vibrational energy transfer in the inelastic collisions of $\mathrm{CO}(v = 1)$ with He atom, in order to predict the quenching rate coefficient in a broad range of temperatures $5K < T < 2500\ K$. Scattering calculations were done in two different ways: (i) direct calculations of quenching cross sections or, alternatively (ii) calculations of excitation cross sections plus microscopic reversibility. At temperatures $T > 500\ K$ the second approach gives quenching rate coefficients in excellent agreement with experiment.

At $T < 500\ K$ the second approach overestimates rate coefficients, but this problem can be easily fixed by forcing the excitation cross section to vanish in the physically irrelevant energy range (below the reaction threshold) and grow smoothly just

above the threshold. In contrast, the first approach (direct quenching) underestimates the reaction rate coefficient for $CO(v = 1) + He$, but we showed that this problem must be less severe in the molecules and/or processes with smaller vibrational quanta involved (*e.g.*, near the dissociation limit).

Furthermore, the problem at low energies can be easily avoided by using (iii) a symmetrized average-velocity approach of Billing. It gives good agreement with experiment at $T < 500\ K$ using either cross sections for direct quenching, or those for excitation + reversibility. Note that no extra scattering calculations are needed for this third approach: the data used in either (i) or (ii), or both simultaneously, can be utilized. Even at very low temperatures $5 < T < 50\ K$ the agreement of predicted quenching rates with experimental data and with full quantum calculations was within half order of magnitude.

In one statement we can formulate our overall recommendation as follows: The MQCT calculations of the relaxation rate coefficients should be carried out in the reverse direction (excitation) using the principle of microscopic reversibility; at low collision energies the symmetrized (average velocity) approach of Billing is essential, but at high collision energies it is not really needed.

It should be emphasized that the $CO(v = 1) + He$ system studied here represents a stringent test of the MQCT method. First, the vibrational quantum in CO is rather large and, second, the He quencher is very light. For heavier quenchers and closer to dissociation limit of the molecule, the MQCT method is expected to work even better.

Appendix 1A: Components of Torque Through Derivatives of Angles

Substitution of Eq. (13′) and Eqs. (20-21) into Eq. (14′) gives:

$$\widetilde{I}\begin{pmatrix}\sin^2\gamma\sin^2\alpha+\cos^2\gamma & -\sin^2\gamma\sin\alpha\cos\alpha & -\sin\gamma\cos\gamma\cos\alpha\\ -\sin^2\gamma\sin\alpha\cos\alpha & \sin^2\gamma\cos^2\alpha+\cos^2\gamma & -\sin\gamma\cos\gamma\sin\alpha\\ -\sin\gamma\cos\gamma\cos\alpha & -\sin\gamma\cos\gamma\sin\alpha & \sin^2\gamma\end{pmatrix}\begin{pmatrix}0 & \cos\alpha & \sin\alpha\\ 0 & \sin\alpha & -\cos\alpha\\ 1 & 0 & 0\end{pmatrix}\begin{pmatrix}\ddot{\alpha}\\ 0\\ \ddot{\gamma}\end{pmatrix}$$

$$=\begin{pmatrix}\tau_x\\ \tau_y\\ \tau_z\end{pmatrix}-\begin{pmatrix}\sin^2\gamma\sin^2\alpha+\cos^2\gamma & -\sin^2\gamma\sin\alpha\cos\alpha & -\sin\gamma\cos\gamma\cos\alpha\\ -\sin^2\gamma\sin\alpha\cos\alpha & \sin^2\gamma\cos^2\alpha+\cos^2\gamma & -\sin\gamma\cos\gamma\sin\alpha\\ -\sin\gamma\cos\gamma\cos\alpha & -\sin\gamma\cos\gamma\sin\alpha & \sin^2\gamma\end{pmatrix}$$

$$\times\left(\dot{\widetilde{I}}\begin{pmatrix}0 & \cos\alpha & \sin\alpha\\ 0 & \sin\alpha & -\cos\alpha\\ 1 & 0 & 0\end{pmatrix}+\widetilde{I}\dot{\alpha}\begin{pmatrix}0 & -\sin\alpha & \cos\alpha\\ 0 & \cos\alpha & \sin\alpha\\ 0 & 0 & 0\end{pmatrix}\right)\begin{pmatrix}\dot{\alpha}\\ 0\\ \dot{\gamma}\end{pmatrix}$$

$$-\widetilde{I}\dot{\gamma}\begin{pmatrix}\sin 2\gamma\sin^2\alpha-\sin 2\gamma & -\sin 2\gamma\sin\alpha\cos\alpha & -\cos 2\gamma\cos\alpha\\ -\sin 2\gamma\sin\alpha\cos\alpha & \sin 2\gamma\cos^2\alpha-\sin 2\gamma & -\cos 2\gamma\sin\alpha\\ -\cos 2\gamma\cos\alpha & -\cos 2\gamma\sin\alpha & 2\sin\gamma\cos\gamma\end{pmatrix}\begin{pmatrix}0 & \cos\alpha & \sin\alpha\\ 0 & \sin\alpha & -\cos\alpha\\ 1 & 0 & 0\end{pmatrix}\begin{pmatrix}\dot{\alpha}\\ 0\\ \dot{\gamma}\end{pmatrix}$$

$$-\widetilde{I}\dot{\alpha}\begin{pmatrix}\sin^2\gamma\sin 2\alpha & -\sin^2\gamma\cos 2\alpha & \sin\gamma\cos\gamma\sin\alpha\\ -\sin^2\gamma\cos 2\alpha & -\sin^2\gamma\sin 2\alpha & -\sin\gamma\cos\gamma\cos\alpha\\ \sin\gamma\cos\gamma\sin\alpha & -\sin\gamma\cos\gamma\cos\alpha & 0\end{pmatrix}\begin{pmatrix}0 & \cos\alpha & \sin\alpha\\ 0 & \sin\alpha & -\cos\alpha\\ 1 & 0 & 0\end{pmatrix}\begin{pmatrix}\dot{\alpha}\\ 0\\ \dot{\gamma}\end{pmatrix}$$

Three components of this matrix equation can be analyzed separately. For *x*-component we obtain:

$$\begin{aligned}&\widetilde{I}\left(\ddot{\gamma}\sin\alpha-\ddot{\alpha}\sin\gamma\cos\gamma\cos\alpha\right)=\widetilde{\tau}_x-\dot{\widetilde{I}}\left(\dot{\gamma}\sin\alpha-\dot{\alpha}\sin\gamma\cos\gamma\cos\alpha\right)\\ &-\widetilde{I}\dot{\alpha}\dot{\gamma}\cos^2\gamma\cos\alpha+\widetilde{I}\dot{\alpha}\dot{\gamma}\cos 2\gamma\cos\alpha+\widetilde{I}\dot{\alpha}\dot{\gamma}\sin^2\gamma\cos\alpha-\widetilde{I}\dot{\alpha}^2\sin\gamma\cos\gamma\sin\alpha\\ &=\widetilde{\tau}_x-\dot{\widetilde{I}}\left(\dot{\gamma}\sin\alpha-\dot{\alpha}\sin\gamma\cos\gamma\cos\alpha\right)-\widetilde{I}\dot{\alpha}^2\sin\gamma\cos\gamma\sin\alpha\end{aligned}\qquad(1A1)$$

For *y*-component we obtain:

$$\begin{aligned}&\widetilde{I}\left(-\ddot{\gamma}\cos\alpha-\ddot{\alpha}\sin\gamma\cos\gamma\sin\alpha\right)=\widetilde{\tau}_y-\dot{\widetilde{I}}\left(-\dot{\gamma}\cos\alpha-\dot{\alpha}\sin\gamma\cos\gamma\sin\alpha\right)\\ &-\widetilde{I}\dot{\alpha}\dot{\gamma}\cos^2\gamma\sin\alpha+\widetilde{I}\dot{\alpha}\dot{\gamma}\cos 2\gamma\sin\alpha+\widetilde{I}\dot{\alpha}\dot{\gamma}\sin^2\gamma\sin\alpha+\widetilde{I}\dot{\alpha}^2\sin\gamma\cos\gamma\cos\alpha\\ &=\widetilde{\tau}_y-\dot{\widetilde{I}}\left(-\dot{\gamma}\cos\alpha-\dot{\alpha}\sin\gamma\cos\gamma\sin\alpha\right)+\widetilde{I}\dot{\alpha}^2\sin\gamma\cos\gamma\cos\alpha\end{aligned}\qquad(1A2)$$

For z-component we obtain:

$$\begin{aligned}\widetilde{I}\ddot{\alpha}\sin^2\gamma &= \widetilde{\tau}_z - (\dot{\widetilde{I}}\dot{\alpha}\sin^2\gamma + \widetilde{I}\dot{\gamma}\dot{\alpha}\sin\gamma\cos\gamma + 2\widetilde{I}\dot{\gamma}\dot{\alpha}\sin\gamma\cos\gamma - \widetilde{I}\dot{\gamma}\dot{\alpha}\sin\gamma\cos\gamma) = \\ &= \widetilde{\tau}_z - \dot{\widetilde{I}}\dot{\alpha}\sin^2\gamma - 2\widetilde{I}\dot{\gamma}\dot{\alpha}\sin\gamma\cos\gamma.\end{aligned} \tag{1A3}$$

Appendix 1B: Equivalence of Components of Torque and the Potential Derivatives

Although in Sec. 1.3.1 we expressed $\widetilde{V}$ as a function of $\mathbf{R}_C = \{\mathbf{q}_{mol}, \mathbf{q}_{que}, \alpha, \gamma\}$, here we will have to switch variables to Cartesian coordinates with respect to molecular center of mass, $\mathbf{r}_1 = \{x_1, y_1, z_1\}$ and $\mathbf{r}_2 = \{x_2, y_2, z_2\}$, defined by Eqs. (18) and consistent with Eq. (17). Using the chain rule of differentiation we can write:

$$\begin{aligned}\frac{\partial\widetilde{V}}{\partial\alpha} &= \frac{\partial\widetilde{V}}{\partial x_1}\frac{\partial x_1}{\partial\alpha} + \frac{\partial\widetilde{V}}{\partial x_2}\frac{\partial x_2}{\partial\alpha} + \frac{\partial\widetilde{V}}{\partial y_1}\frac{\partial y_1}{\partial\alpha} + \frac{\partial\widetilde{V}}{\partial y_2}\frac{\partial y_2}{\partial\alpha} + \frac{\partial\widetilde{V}}{\partial z_1}\frac{\partial z_1}{\partial\alpha} + \frac{\partial\widetilde{V}}{\partial z_2}\frac{\partial z_2}{\partial\alpha} \\ &= -\frac{\partial\widetilde{V}}{\partial x_1}y_1 - \frac{\partial\widetilde{V}}{\partial x_2}y_2 + \frac{\partial\widetilde{V}}{\partial y_1}x_1 + \frac{\partial\widetilde{V}}{\partial y_2}x_2.\end{aligned} \tag{1B1}$$

Here we used the following properties: $\partial x_i/\partial\alpha = -y_i$, $\partial y_i/\partial\alpha = x_i$ and $\partial z_i/\partial\alpha = 0$, which follow from the definitions of Eqs. (18). Introducing forces expressed in Cartesian coordinates, rearranging the terms, and using the definition of torque $\boldsymbol{\tau} = \mathbf{r}\times\mathbf{F}$, we obtain:

$$\begin{aligned}\frac{\partial\widetilde{V}}{\partial\alpha} &= \widetilde{F}_{x_1}y_1 - \widetilde{F}_{y_1}x_1 + \widetilde{F}_{x_2}y_2 - \widetilde{F}_{y_2}x_2 \\ &= -\widetilde{\tau}_{z_1} - \widetilde{\tau}_{z_2} = -\sum_i \widetilde{\tau}_{z_i} = -\widetilde{\tau}_z.\end{aligned} \tag{1B2}$$

Here summation is over two atoms in the diatomic, just as in Eq. (17).

Similarly, using Eqs. (18) we can write:

$$\begin{aligned}\frac{\partial \widetilde{V}}{\partial \gamma} &= \frac{\partial \widetilde{V}}{\partial x_1}\frac{\partial x_1}{\partial \gamma} + \frac{\partial \widetilde{V}}{\partial x_2}\frac{\partial x_2}{\partial \gamma} + \frac{\partial \widetilde{V}}{\partial y_1}\frac{\partial y_1}{\partial \gamma} + \frac{\partial \widetilde{V}}{\partial y_2}\frac{\partial y_2}{\partial \gamma} + \frac{\partial \widetilde{V}}{\partial z_1}\frac{\partial z_1}{\partial \gamma} + \frac{\partial \widetilde{V}}{\partial z_2}\frac{\partial z_2}{\partial \gamma} \\ &= \frac{\partial \widetilde{V}}{\partial x_1} z_1 \cos\alpha + \frac{\partial \widetilde{V}}{\partial x_2} z_2 \cos\alpha + \frac{\partial \widetilde{V}}{\partial y_1} z_1 \sin\alpha + \frac{\partial \widetilde{V}}{\partial y_2} z_2 \sin\alpha - \\ &- \frac{\partial \widetilde{V}}{\partial z_1}\left(x_1 \cos\alpha + y_1 \sin\alpha\right) - \frac{\partial \widetilde{V}}{\partial z_2}\left(x_2 \cos\alpha + y_2 \sin\alpha\right).\end{aligned} \tag{1B3}$$

Introducing forces expressed in Cartesian coordinates, rearranging the terms and using the definition of torque, we obtain:

$$\begin{aligned}\frac{\partial \widetilde{V}}{\partial \gamma} &= (\widetilde{F}_{z_1} x_1 - \widetilde{F}_{x_1} z_1 + \widetilde{F}_{z_2} x_2 - \widetilde{F}_{x_2} z_2)\cos\alpha + (\widetilde{F}_{z_1} y_1 - \widetilde{F}_{y_1} z_1 + \widetilde{F}_{z_2} y_2 - \widetilde{F}_{y_2} z_2)\sin\alpha \\ &= \sum_i \widetilde{\tau}_{y_i} \cos\alpha - \sum_i \widetilde{\tau}_{x_i} \sin\alpha \\ &= \widetilde{\tau}_y \cos\alpha - \widetilde{\tau}_x \sin\alpha.\end{aligned} \tag{1B4}$$

Appendix 1C: Quenching Rate Coefficient Expressed Through Cross Section for Excitation

First consider the numerator of Eq. (42):

$$\sum_{j'}\sum_{j}(2j+1)\exp\left(-\frac{\varepsilon_1^j}{kT}\right)\int_0^\infty \sigma_{10}^{jj'}(E)\,E\exp\left(-\frac{E}{kT}\right)dE\,, \tag{1C1}$$

and move the integral sign outside of the double-sum. Then rearrange the order of factors as follows:

$$\int_0^\infty \sum_{j'}\sum_{j}(2j+1)\sigma_{10}^{jj'}(E)\,E\exp\left(-\frac{E+\varepsilon_1^j}{kT}\right)dE\,. \tag{1C2}$$

This version allows using Eq. (47) and Eq. (48) straight in order to replace the pre-exponential factor and the numerator of the exponent, respectively. These substitutions give:

$$\int_{\Delta\varepsilon}^{\infty} \sum_{j'} \sum_{j} (2j'+1)\,\sigma_{01}^{j'j}(E')\,E' \exp\left(-\frac{E'+\varepsilon_0^{j'}}{kT}\right) dE' . \qquad (1C3)$$

Note also that we have changed the variable of integration and the limits of integration. Indeed, based on Eq. (48), for integration over the collision energy of each individual state-to-state transition we have $dE = dE'$ and we also see that $E' = \varepsilon_1^j - \varepsilon_0^{j'} \approx \Delta\varepsilon$ when $E = 0$. The latter approximation is based on the fact that rotational quantum of energy is much smaller than vibrational quantum. One can easily avoid this approximation, but then each term of the double-sum in Eq. (1C3) will have its own specific lower limit of integration. This is inconvenient, and for simplicity we use $\Delta\varepsilon \approx \varepsilon_1^j - \varepsilon_0^{j'}$.

Now consider denominator of Eq. (42). It represents the rotational partition function of the excited vibrational state $v = 1$:

$$Q_1 = \sum_j (2j+1) \exp\left(-\frac{\varepsilon_1^j}{kT}\right). \qquad (1C4)$$

Introducing similar partition function for the ground vibrational state, Q_0, and formally replacing Q_1 in the denominator of Eq. (42) by $Q_0 \times (Q_1 / Q_0)$, we obtain the following expression:

$$\kappa_{10}^{\text{rev}}(T) = \frac{Q_0}{Q_1} \sqrt{\frac{8kT}{\mu\pi}} \frac{1}{(kT)^2} \int_{\Delta\varepsilon}^{\infty} \tilde{\sigma}_{01}(E')\,E' \exp\left(-\frac{E'}{kT}\right) dE' . \qquad (1C5)$$

Here, by analogy with Eq. (44) we introduced the rotationally averaged cross section for the reverse vibrational transition (excitation):

$$\widetilde{\sigma}_{01}(E') = \frac{\sum_{j}\sum_{j'}(2j'+1)\exp\left(-\frac{\varepsilon_0^{j'}}{kT}\right)\sigma_{01}^{j'j}(E')}{\sum_{j'}(2j'+1)\exp\left(-\frac{\varepsilon_0^{j'}}{kT}\right)}. \tag{1C6}$$

Also, by analogy with Eq. (43), we can define rate coefficient for the reverse transition (excitation) as

$$\kappa_{01}(T) = \sqrt{\frac{8kT}{\mu\pi}}\frac{1}{(kT)^2}\int_{\Delta\varepsilon}^{\infty}\widetilde{\sigma}_{01}(E')\,E'\exp\left(-\frac{E'}{kT}\right)dE'. \tag{1C7}$$

Note, however, that integration in Eq. (1C7) starts at $E' = \Delta\varepsilon$, different from Eq. (9), where integration starts at $E = 0$. This makes physical sense because if we start from $v' = 0$ the channel $v = 1$ is open only when the collision energy E' exceeds the excitation energy $(E' \geq \Delta\varepsilon)$, while if we start from $v = 1$ the channel $v' = 0$ is open at any collision energy $(E \geq 0)$. Formally, one could expand the limits of integration in Eq. (1C7) down to $E' = 0$, but only if the excitation cross section $\widetilde{\sigma}_{01}(E')$ exhibits the correct property: $\widetilde{\sigma}_{01} = 0$ when $E' < \Delta\varepsilon$. In any case, using Eq. (1C7) in Eq. (1C5) we obtain:

$$\kappa_{10}Q_1 = \kappa_{01}Q_0, \tag{1C8}$$

which is a thermally averaged (canonical) analogue of the micro-canonical expression of Eq. (47).

Now take a look at the ratio Q_0/Q_1 in Eq. (1C5). Each of Q_0 and Q_1 can be written as a product of rotational partition function and vibrational factor. For the low lying vibrational states the rotational partition functions are approximately equal and they

approximately cancel in the Q_0/Q_1 ratio. Only the ratio of vibrational factors survives and gives

$$\frac{Q_0}{Q_1} = \frac{\sum_{j'} (2j'+1) \exp\left(-\frac{\varepsilon_0^{j'}}{kT}\right)}{\sum_{j} (2j+1) \exp\left(-\frac{\varepsilon_1^{j}}{kT}\right)} \approx \exp\left(\frac{\Delta\varepsilon}{kT}\right). \tag{1C9}$$

This term can be brought inside the integral in Eq. (1C5), which gives

$$\kappa_{10}^{\text{rev}}(T) \approx \sqrt{\frac{8kT}{\mu\pi}} \frac{1}{(kT)^2} \int_{\Delta\varepsilon}^{\infty} \widetilde{\sigma}_{01}(E') E' \exp\left(-\frac{E'-\Delta\varepsilon}{kT}\right) dE'. \tag{1C10}$$

Expression (1C10) suggests to change the integration variable back to $E = E' - \Delta\varepsilon$, which finally leads to:

$$\kappa_{10}^{\text{rev}}(T) \approx \sqrt{\frac{8kT}{\mu\pi}} \frac{1}{(kT)^2} \int_{0}^{\infty} \widetilde{\sigma}_{01}(E+\Delta\varepsilon)(E+\Delta\varepsilon) \exp\left(-\frac{E}{kT}\right) dE\ . \tag{1C11}$$

So, this expression is approximate. In order to make it look similar to Eq. (43) we, first, introduced a single lower integration limit $\Delta\varepsilon \approx \varepsilon_1^j - \varepsilon_0^{j'}$ in Eq. (1C3) and, second, neglected the ratio of rotational partition functions in Eq. (1C9). The exact (much bulkier) version of Eq. (1C11) can be easily recovered, if needed.

BIBLIOGRAPHY for Chapter 1

1. V. Bernshtein and I. Oref, *Israel Journal of Chemistry* **47**, 205 (2008).

2. M.-L. Dubernet, F. Daniel, A. Grosjean, and C. Y. Lin, *Astronomy & Astrophysics* **497**, 911 (2009).

3. F. Daniel, M.-L. Dubernet, F. Pacaud and A. Grosjean, *Astronomy & Astrophysics* **517**, A13 (2010).

4. F. Daniel, M.-L. Dubernet, and A. Grosjean, *Astronomy & Astrophysics* **536**, A76 (2011).

5. L. Wiesenfeld, Y. Scribano, and A. Faure, *Phys. Chem. Chem. Phys.* **13**, 8230 (2011).

6. C. H. Yang, G. Sarma, D. H. Parker, J. J. ter Meulen, and L. Wiesenfeld, *J. Chem. Phys*. **134**, 204308 (2011).

7. N. Balakrishnan, A. Dalgarno, and R. C. Forrey, *J. Chem. Phys.* **113**, 621 (2000).

8. C. Cecchi-Pestellini, E. Bodo, N. Balakrishnan and A. Dalgarno, *The Astrophysical Journal* **571**, 1015 (2002) .

9. B. Kendrick and R. Pack, *Chem. Phys. Let.* **235**, 291 (1995).

10. R. T Pack, R. B. Walker, and B. K. Kendrick, *J. Chem. Phys.* **109**, 6701 (1998).

11. M. Ivanov and D. Babikov, *J. Chem. Phys.* **134**, 144107 (2011).

12. M. Ivanov and D. Babikov, *J. Chem. Phys.* **134**, 174308 (2011).

13. M. Ivanov and D. Babikov, *J. Chem. Phys.* **136**, 184304 (2012).

14. M. Tacconi and F. A. Gianturco, *J. Chem. Phys.* **131**, 094301 (2009).

15. N. Balakrishnan, G. Quéméner, R. C. Forrey, R. J. Hinde, and P. C. Stancil, *J. Chem. Phys.* **134**, 014301 (2011).

16. L. M. C. Janssen, P. S. Zuchowsky, A. van der Avoird, J. M. Hudson and G. C. Groenenboom, *J. Chem. Phys.* **134**, 124309 (2011).

17. G. Quéméner, N. Balakrishnan, and B. K. Kendrick, *J. Chem. Phys.* **129**, 224309 (2008).

18. G. A. Parker, R. B. Walker, B. K. Kendrick, and R. T Pack, *J. Chem. Phys.* **117**, 6083 (2002).

19. D. K. Havey, Q. Liu, Z. Li, M. Elioff and A. S. Mullin, *J. Phys. Chem. A* **111**, 13321 (2007).

20. D. K. Havey, J. Du and A. S. Mullin, *J. Phys. Chem. A* **114**, 1569 (2010).

21. T. D. Sechler, L. P. Dempsey and M. I. Lester, *J. Phys. Chem. A* **113**, 8845 (2009).

22. L. P. Dempsey, T. D. Sechler, C. Murray and M. I. Lester, *J. Phys. Chem. A* **113**, 6851 (2009).

23. A. L. Brunsvold, D. J. Garton, T. K. Minton, D. Troya, and G. C. Schatz, *J. Chem. Phys.* **121**, 11702 (2004).

24. C.-L. Liu, H. C. Hsu, J.-J. Lyu and C.-K. Ni, *J. Chem. Phys.* **123**, 131102 (2005).

25. R. X. Fernandes, K. Luther, J. Troe and V. G. Ushakov, Phys. Chem. Chem. Phys. **10**, 4313 (2008).

26. V. Bernshtein and I. Oref, *J. Chem. Phys*. **125**, 133105 (2006).

27. A. W. Jasper and J. A. Miller, *J. Phys. Chem. A* **113**, 5612 (2009).

28. J. R. Barker*, Journal of Chemical Kinetics* **41**, 748 (2009).

29. D. M. Golden and J. R. Barker*, Combustion and Flame* **158**, 602 (2011).

30. A. L. Kaledin, X. Huang, J. M Bowman, *Chem. Phys. Lett.* **384**, 80 (2004).

31. G. Czakó, A. L. Kaledin, and J. M. Bowman, *J. Chem. Phys.* **132**, 164103 (2010).

32. G. D. Billing, *Comp. Phys. Rep.* **1**, 237 (1984).

33. G. S. Whittier and J. C. Light, *J. Chem. Phys.* **110**, 4280 (1999)

34. D. Babikov, F. Aguillon, M. Sizun, and V. Sidis, *Phys. Rev. A* **59**, 330 (1999).

35. M. Sizun, F. Aguillon, V. Sidis, V. Zenevich, G. D. Billing and N. Markovi, *Chem. Phys.* **209**, 327 (1996).

36. F. Aguillon, V. Sidis, and J. P. Gauyacq, *J. Chem. Phys.* **95**, 1020 (1991).

37. M Sizun and F Aguillon, *Chem. Phys.* **226**, 47 (1998).

38. A. Teplukhin and D. Babikov, *Phys. Chem. Chem. Phys*. **18**, 19194 (2016).

39. T. J. Park and J. C. Light, *J. Chem. Phys*. **85**, 5870 (1986).

40. H. Goldstein, Classical Mechanics, Addison-Wesley, Reading, Mass., (1965).

41. J. M. Bowman, *Chem. Phys. Lett*. **217**, 36 (1994).

42. J. Qi and J. M. Bowman, *J. Chem. Phys.* **105**, 9884 (1996).

43. J. Qi and J. M. Bowman, *J. Chem. Phys.* **107**, 9960 (1997).

44. S. Carter and J. M. Bowman, *J. Chem. Phys.* **108**, 4397 (1998).

45. S. Skokov and J. Bowman, *J. Chem. Phys.* **110**, 9789 (1999).

46. S. Zou, S. Skokov, and J. M. Bowman, *J. Phys. Chem. A* **105**, 2423 (2001)

47. D. J. Tannor, Introduction to quantum mechanics. A Time-Dependent Perspective University Science Books, (2007).

48. J.C.Tully*, J. Chem. Phys.* **93**, 1061 (1990).

49. B. Podolsky, *Phys. Rev.* **32**, 812 (1928).

50. A. Semenov, M. Ivanov and D. Babikov, *J. Chem. Phys.* **139**, 074306 (2013).

51. W. H. Press, B. P. Flannery, S. A. Teukolsky, and W. T. Vetterling, Numerical Recipes,Cambridge University Press, (1989).

52. J. C. Stephenson and E. R. Mosburg, Jr., *J. Chem. Phys*. **60**, 3562 (1974).

53. G. Quéméner and N. Balakrishnan, *Phys. Rev. A* **77**, 030704 (R) (2008).

54. W. H. Green and J. K. Hancock, *J. Chem. Phys*. **59**, 4326 (1973).

55. R. C. Millikan, *J. Chem. Phys*. **40**, 2594 (1964).

56. D. J. Miller and R. C. Millikan, *J. Chem. Phys*. **53**, 3384 (1970).

57. Y. B. Band and P. S. Julienne, *Phys. Rev. A* **51**, R4317 (1995).

58. A. Fioretti, D. Comparat, A. Crubellier, O. Dulieu, F. Masnou-Seeuws, and P. Pillet, *Phys. Rev. Lett*. **80**, 4402 (1998).

59. F. A. Gianturco, F. Paesani, M.F. Laranjeira, V. Vassilenko, M. A. Cunha, A. G. Shashkov, and A. F. Zolotukhina, *Mol. Phys.* **94**, 605 (1998).

60. E. Bodo, F. A. Gianturco, and F. Paesani, *Z. Phys. Chem.* (Leipzig) **214**, 1013

(2000).

61. F. A. Gianturco, N. Sanna, and S. Serna, *J. Chem. Phys.* **98**, 3833 (1993).

62. R. Kobayashi, R. D. Amos, J. P. Reid, H. M. Quiney, and C. J. S. M. Simpson, *Mol. Phys.* **98**, 1995 (2000).

63. S. Antonova, A. Lin, A. P. Tsakotellis, and G. C. McBane, *J. Chem. Phys.* **110**, 2384 (1999).

64. J. P. Reid, C. J. S. M. Simpson, H. M. Quiney, and J. M. Hutson, *J. Chem. Phys.* **103**, 2528 (1995).

65. J. P. Reid, C. J. S. M. Simpson, and H. M. Quiney, *J. Chem. Phys*. **107**, 9929 (1997).

66. N. Balakrishnan, A. Dalgarno, and R. C. Forrey, *J. Chem. Phys.* **113**, 621 (2000).

67. R. V. Krems, *J. Chem. Phys*. **116**, 4517 (2002).

68. R. V. Krems*, J. Chem. Phys*. **116**, 4525 (2002).

69. C. T. Wickham-Jones, H. T. Williams, and C. J. S. M. Simpson, *J. Chem.Phys.* **87**, 5294 (1987).

70. C. Cecchi-Pestellini , E. Bodo , N. Balakrishnan , and A.Dalgarno, *The Astrophysical Journal*, **571**,1015 (2002).

71. H. Uitenbroek, *The Astrophysical Journal*, **536**, 481 (2000).

72. A.Evans, ,T. R. Geballe, , J. M. C. Rawlings and A. D Scott, *Monthly Notices of the Royal Astronomical Society*, **282**, 1049(1996).

73. W. Liu, and A. Dalgarno, *The Astrophysical Journal*, **454**, 472 (1995).

74. P. Saxena, F. A. Williams, *Combust. Flame* **145**, 316 (2006).

75. J. B. Howard, G. C. Williams, D. H. Fine, *Symposium (International) on Combustion* **14**, 975 (1973) .

76. N. Balakrishnan and G. D. Billing, *J. Chem. Phys.* **104**, 9482 (1996).

77. H. L. Bethlem, G. Berden, and G. Meijer, *Phys. Rev. Lett*. **83**, 1558 (1999).

78. J. A. Maddi, T. P. Dinneen, and H. Gould, *Phys. Rev. A* **60**, 3882 (1999).

79. M. Thachuk, C. E. Chuaqui, and R. J. Le Roy, *J. Chem. Phys.* **105**, 4005 (1996).

80. F. A. Gianturco, F. Paesani, M. F. Laranjeira, V. Vassilenko, M. A. Cunha, A. G. Shashkov, and A. F. Zolotoukhina, *Mol. Phys.* **92**, 957 (1997).

81. M.-C. Chan and A. R. W. McKellar, *J. Chem. Phys.* **105**, 7910 (1996).

82. R. Moszynski, T. Korona, P. E. S. Wormer, and A. van der Avoird, *J. Chem. Phys*. **103**, 321 (1995).

83. F.-M. Tao, S. Drucker, R. C. Cohen, and W. Klemperer, *J. Chem. Phys*. **101**, 8680 (1994).

84. B. Kukawska-Tarnawska, G. Chalasinski, and K. Olszewski, *J. Chem. Phys.* **101**, 4964 (1994).

85. T. G. A. Heijmen, R. Moszynski, P. E. S. Wormer, and A. van der Avoird, *J. Chem. Phys.* **107**, 9921 (1997).

86. K. A. Peterson and G. C. McBane, *J. Chem. Phys*. **123**, 084314 (2005).

87. N. BalakrishnanV. Kharchenko and A. Dalgarno, *J. Geophys. Res*. **103**, 23393 (1998).

88. W. H. Miller,W. L. Hase, and C. L. Darling, *J. Chem. Phys*. **91**, 2863 (1989).

89. G.D.Billing, *Comput. Phys. Rep.* **1**, 239 (1984).

90. M. Ivanov and D. Babikov, *J. Chem. Phys*. **134**, 144107 (2011).

91. M. Ivanov and D. Babikov, *J. Chem. Phys*. **134**, 174308 (2011).

92. M. Ivanov and D. Babikov, *J. Chem. Phys*. **136**, 184304 (2012).

93. M. Ivanov and D. Babikov, *PNAS.* **110**,17708–17713(2013).

94. D. Babikov, R. B. Walker, and R. T Pack, *J. Chem. Phys.* **117**, 8613 (2002).

95. R. T Pack, R. B. Walker, and B. K. Kendrick*, J. Chem. Phys*. **109**, 6714 (1998).

96. G. D. Billing, The Quantum-Classical Theory, Oxford University Press (2003).

97. A. Semenov and D. Babikov, *J. Chem. Phys.* **138**, 164110 (2013).

98. C. Leforestier, R. H. Bisseling, C. Cerjan, M. D. Feit, R. Friesner, A. Guldberg, A. Hammerich, G. Jolicard, W. Karrein, H.-D. Meyer, N. Lipkin, O. Roncero, and R. Kosloff, *J. Comput. Phys.* **94**, 59 (1991).

99. G. Billing, *J. Chem. Phys*. **99**, 5849 (1993).

100. R. K. Preston and R. T Pack, J. Chem. Phys. **66**, 2480 (1977).

101. W. H. Press, B. P. Flannery, S. A. Teukolsky, and W. T. Vetterling, Numerical Recipes, Cambridge University Press (1989).

102. T. J. Park and J. C. Light, *J. Chem. Phys.* **85**, 5870 (1986).

103. G. S. Whittier and J.C. Light, *J. Chem. Phys.* **110**, 4280 (1999).

104. G. J. Wilson, M. L. Turnidge, A. S. Solodukhin, and C. J. S. M. Simpson, *Chem. Phys. Lett.* **207**, 521 (1993).

105. J. C. Tully, *J. Chem. Phys.* **93**, 1061 (1990).

106. R. D. Levine, Quantum Mechanics of Molecular Rate Processes Clarendon, Oxford (1969).

107. E. P. Wigner, *Phys. Rev.* **73**, 1002 (1948).

CHAPTER 2. MIXED QUANTUM/CLASSICAL THEORY OF ROTATIONALLY AND VIBRATIONALLY INELASTIC SCATTERING IN SPACE-FIXED AND BODY-FIXED REFERENCE FRAMES

2.1 Ro–Vibrationally Inelastic Scattering: Importance for Astrochemistry

Theoretical predictions of inelastic scattering cross sections for ro-vibrationally excited molecules become increasingly important for quantitative interpretation of molecular spectra observed in a wide variety of astrophysical objects, such as pre-stellar cores and proto-stellar environments, interstellar media and surcumstellar envelopes [1-11]. The range of relevant temperatures is very broad, from 5 K up to 2500 K, and the role of scattering partner (quencher) is played by the interstellar background gasses, mostly He and H_2, but also by H_2O in cometary comas. Usually, calculations of inelastic cross sections [12] are carried out using quantum scattering codes such as MOLSCAT [13]. These calculations are not trivial [14-20], but recently a significant progress has been achieved in the rotational quenching of H_2O by H_2 [21-25]. Another outstanding example of such calculations is rotational quenching of methyl formate, $HCOOCH_3$ (astrophysically relevant small organic molecule, SOM) by He with collision energy $E <$ 30 cm^{-1} [26].

One should admit, however, that quantum mechanics, indispensable (and affordable) at low temperatures and for the low-mass collision partners, becomes prohibitively demanding at higher temperatures and/or for larger molecules and quenchers. Computational time increases with kinetic energy of collision (more partial waves should be included) and with the number of internal quantum levels (e.g., $j \geq 50$

becomes prohibitive). Today it is possible to do 6D diatom-diatom inelastic scattering calculations using exact quantum mechanics, in a broad range of collision energies and without resorting to any decoupling approximation. Beyond that the calculations become prohibitive. For example, quantum inelastic scattering calculations of $H_2O + H_2O$ and their deuterated forms are not yet computationally affordable, same as quenching calculations for several important SOMs (*e.g.*, methanol, acetaldehyde, dimethyl ether) in the temperature range of interest.

It is also a question whether the exact full-quantum framework is really needed in those cases. *Can we switch from full-quantum mechanics to a simpler and more affordable theory in the temperature range where this theory becomes accurate? And what theory is suitable for this purpose?* If the answer to the first question is positive and the answer to the second question is found, many of the astrophysically relevant inelastic scattering calculations could become possible.

It is probably true to say that at $T > 10$ K the translational motion (scattering) can be described classically for most collision partners except the lightest, such as $H + H_2$. An attractive method for dynamics emerges if the classical trajectory treatment of scattering is interfaced with quantum treatment of internal (rotational and/or vibrational) states in a self-consistent way, which allows energy exchange between collisional and internal degrees of freedom, but keeps total energy conserved. The idea of such mixed quantum/classical approach isn't entirely new, but it has never been fully developed to the level of a predictive computational tool.

Foundations of the quantum/classical theory were laid by Gert Billing in 80's and 90's and published in several journal articles [27-29], one large paper [30] and one book

[31]. He also did calculations for a number of systems to support his theory. In recent years we tried to revive this quantum/classical approach, and took a closer look at the ranges of its validity. Sometimes it is argued that two Delos criteria must be satisfied [32]: 1) the de Broglie wavelength should be very small, $(\lambda\!\!\!^{-} / a_0)^{1/2} << 1$, and 2) the translation energy of reduced mass should be much larger than energy of transition $E_t >> |\Delta\varepsilon_{if}|$. With respect to the second criterion, a distinction should be made between vibrationally- and rotationally-inelastic transitions. The vibrational quanta are particularly large and, formally, it looks like this property limits significantly the range of applicability of the mixed quantum/classical approach, to high-energy collisions only. Recently, we carried out the mixed quantum/classical calculations of vibrational quenching of CO(v=1) by He impact in a broad range of collision energies using the method where only vibrations of CO are treated quantum mechanically, while rotation of CO and scattering of He are both treated classically [33-34]. Excellent agreement with full quantum calculations has been obtained at collision energies down to 100 cm^{-1}, despite the fact that vibrational quantum of CO is rather large, 2140 cm^{-1}. Similar mixed quantum/classical method was also very useful for description of collisional energy transfer in the recombination reaction that forms ozone, O_3 [35-38]. Finally, our recent calculations of rotationally-inelastic transitions in N_2 + Na [39] show that for excitation cross sections the mixed quantum/classical approach becomes accurate at energies roughly equal to ¼ of rotational quantum above the channel threshold, while the quenching cross sections are described accurately down to very low energies (few wavenumbers, consistent with first Delos criterion, rather than second). This is very encouraging and probably, means that the mixed quantum/classical approach for ro-

vibrational transitions remains accurate at energies much smaller than those indicated by the second Delos criterion.

In this part of the work we focus on the mixed quantum/classical treatment of purely rotational quenching, where the vibrational motion is not important, rotational motion is treated quantum mechanically, and only the scattering is treated classically. It appears that such theory is very easy to formulate in the space-fixed (SF) reference frame, but the corresponding state-to-state transition matrix may be hard-to-handle numerically. Much simpler transition matrix is obtained in the body-fixed (BF) reference frame, but the underlying derivations are notably difficult and the resultant equations of motion are rather complicated. Gert Billing published some of the final equations [31] but not all of them, and did not provide enough details about their derivation. So, one purpose of this chapter it to present a complete and detailed mixed quantum/classical theory (MQCT) of rotationally inelastic scattering in the BF reference frame. The second goal is to present an equivalent theory in the SF reference frame, which Billing didn't do, and compare numerical results of two theories for a model system in order to ensure that final equations of both theories are correct. Finally, it appears that Billing carried out his MQCT calculations only within framework of the coupled-states (CS) approximation, where transitions between different m-states, within the same rotational energy level j, are neglected [31]. In this chapter we go well beyond this assumption by formulating and numerically testing the fully-coupled version of MQCT.

2.2 Theoretical Framework

Here we present MQCT method for treatment of inelastic diatomic molecule + atom scattering:

$$AB^{*} + M \rightarrow AB + M,$$

where the rotational and vibrational (internal) motion of the molecule are treated quantum mechanically, while the translational motion of both particles (scattering) is treated classically. So, the molecule is AB and the quencher atom is M.

2.2.1 The Ehrenfest Approach in General Case

Consider a system characterized by a set of variables treated classically (some of coordinates and their conjugate momenta) and another set of variables described by quantum mechanics (the remaining coordinates). In this situation wave function of the system depends *explicitly* on classical variables. This dependence can be written as $\Psi(\mathbf{q};\mathbf{Q},\mathbf{P})$, where $\mathbf{q}$ denotes all quantum variables, while $(\mathbf{Q},\mathbf{P})$ denotes a set of classical generalized coordinates and their conjugate momenta. Our goal is to derive equations for evolution of such quantum/classical system.

Quantum part of the Hamiltonian operator $\hat{H}_{\mathrm{q}}(\mathbf{q};\mathbf{Q},\mathbf{P})$ and its classical part $H_{\mathrm{c}}(\mathbf{Q},\mathbf{P})$ are used to set up the full Hamiltonian for evolution of the classical sub-system, according to the Ehrenfest theorem [40]

$$H(\mathbf{Q},\mathbf{P}) = H_{\mathrm{c}}(\mathbf{Q},\mathbf{P}) + \left\langle \Psi(\mathbf{q};\mathbf{Q},\mathbf{P}) \middle| \hat{H}_{\mathrm{q}}(\mathbf{q};\mathbf{Q},\mathbf{P}) \middle| \Psi(\mathbf{q};\mathbf{Q},\mathbf{P}) \right\rangle . \tag{1}$$

The Hamilton's equations of motion are then obtained as

$$\dot{\mathbf{Q}} = \frac{\partial H(\mathbf{Q},\mathbf{P})}{\partial \mathbf{P}}; \quad \dot{\mathbf{P}} = -\frac{\partial H(\mathbf{Q},\mathbf{P})}{\partial \mathbf{Q}}. \tag{2}$$

Substitution of (2) into (1) and differentiation using the chain-rule give

$$\dot{\mathbf{Q}} = \frac{\partial H_{\mathrm{c}}(\mathbf{Q},\mathbf{P})}{\partial \mathbf{P}} + \left\langle \Psi(\mathbf{q};\mathbf{Q},\mathbf{P}) \middle| \frac{\partial \hat{H}_{\mathrm{q}}(\mathbf{q};\mathbf{Q},\mathbf{P})}{\partial \mathbf{P}} \middle| \Psi(\mathbf{q};\mathbf{Q},\mathbf{P}) \right\rangle + 2\,\mathrm{Re}\left\langle \Psi(\mathbf{q};\mathbf{Q},\mathbf{P}) \middle| \hat{H}_{\mathrm{q}}(\mathbf{q};\mathbf{Q},\mathbf{P}) \middle| \frac{\partial \Psi(\mathbf{q};\mathbf{Q},\mathbf{P})}{\partial \mathbf{P}} \right\rangle, \tag{3a}$$

$$\dot{\mathbf{P}} = -\frac{\partial H_{\mathrm{c}}(\mathbf{Q},\mathbf{P})}{\partial \mathbf{Q}} - \left\langle \Psi(\mathbf{q};\mathbf{Q},\mathbf{P}) \middle| \frac{\partial \hat{H}_{\mathrm{q}}(\mathbf{q};\mathbf{Q},\mathbf{P})}{\partial \mathbf{Q}} \middle| \Psi(\mathbf{q};\mathbf{Q},\mathbf{P}) \right\rangle - 2\,\mathrm{Re}\left\langle \Psi(\mathbf{q};\mathbf{Q},\mathbf{P}) \middle| \hat{H}_{\mathrm{q}}(\mathbf{q};\mathbf{Q},\mathbf{P}) \middle| \frac{\partial \Psi(\mathbf{q};\mathbf{Q},\mathbf{P})}{\partial \mathbf{Q}} \right\rangle. \tag{3b}$$

For evolution of quantum part of the system we should solve the time-dependent Schrodinger equation (TDSE)

$$\hat{H}_{\mathrm{q}}(\mathbf{q};\mathbf{Q},\mathbf{P})\Psi(\mathbf{q};\mathbf{Q},\mathbf{P}) = i\hbar \frac{\partial \Psi(\mathbf{q};\mathbf{Q},\mathbf{P})}{\partial t} \tag{4}$$

The system of equations (3-4) completely describes behavior and time evolution of any quantum-classical system.

It is important to note several points. The wave function evolves (depends on time) but we also have to differentiate it with respect to classical variables, since it depends on them too. These classical coordinates also evolve. It is just a formal mathematical rule which has very important physical consequence: without the last term in Eqs. (3a-b) we will not satisfy the energy conservation law. In what follows we will see that in the SF reference frame only the second term in Eqs. (3a-b) is important, while in the BF reference frame only the third term matters.

2.2.2 MQCT in the SF Reference Frame

Figure 1 is used to define coordinates of the system. The quantum Hamiltonian is

$$\hat{H}_{\mathrm{q}} = \hat{H}_{\mathrm{vib}} + \frac{\hat{\mathbf{j}}^2}{2\mu_{\mathrm{AB}} r^2} + V(R,\Theta,\Phi,r,\theta,\varphi)\,, \tag{5}$$

where μ_{AB} is the reduced mass of the molecule, $\mathbf{Q}=\mathbf{Q}_M-\mathbf{Q}_{AB}=(R,\Theta,\Phi)$ describes the relative position of quencher and center of mass of the diatomic molecule, angles (θ,φ) describe molecular orientation, and r is the interatomic distance in the molecule. The vibrational Hamiltonian contains potential of the diatomic only: $\hat{H}_{vib}=\hat{T}_{vib}+V_{AB}(r)$, while the potential V in Eq. (5) has everything but this term

$$V(R,\Theta,\Phi,r,\theta,\varphi)=V_{ABM}(R,\Theta,\Phi,r,\theta,\varphi)-V_{AB}(r). \quad (6)$$

The PES of the entire system V_{ABM} doesn't have to be separable.

For convenience we will switch to the radial wave function ψ defined as $\Psi=\psi(r,\theta,\varphi)/r$, with corresponding vibrational kinetic energy operator:

$$\hat{T}_{vib}=-\frac{\hbar^2}{2\mu_{AB}}\frac{\partial^2}{\partial r^2}. \quad (7)$$

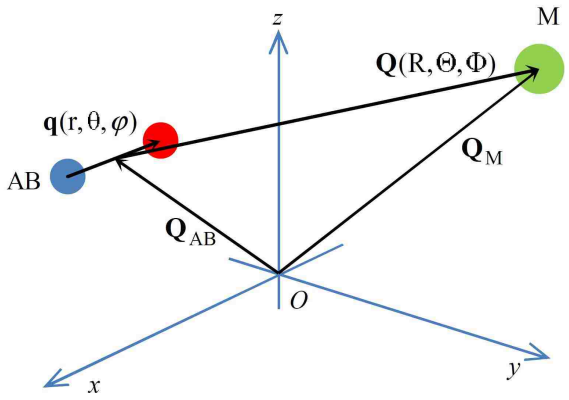

Figure 1: Space-fixed (SF) reference frame. Cartesian coordinates *x*, *y* and *z* are introduced for convenience.

For solution of TDSE we will use expansion over the basis set of ro-vibrational eigenstates with time-dependent coefficients:

$$\psi(r,\theta,\phi,t)=\sum a_{njm}(t)\,\varphi_{nj}(r)\,Y_{jm}(\theta,\phi)\exp\{-iE_{nj}t/\hbar\}. \quad (8)$$

To simplify notations we will leave out the time dependence: $a_{njm}=a_{njm}(t)$. Substituting Eqs. (5-8) into TDSE (4) and projecting out eigenstates in a standard way, we obtain the system of coupled equations

$$i\hbar\frac{\partial a_{njm}}{\partial t}=\sum_{n'j'm'}a_{n'j'm'}\exp\{i(E_{nj}-E_{n'j'})t/\hbar\}\,M_{njm}^{n'j'm'}(R,\Theta,\Phi), \quad (9)$$

where

$$M_{njm}^{n'j'm'}(R,\Theta,\Phi) = \left\langle \phi_{n'j'}(r)Y_{j'm'}(\theta,\varphi)\middle|V(R,\Theta,\Phi,r,\theta,\varphi)\middle|\phi_{nj}(r)Y_{jm}(\theta,\varphi)\right\rangle$$
$$= A_{j'm'jm}\int_0^{2\pi} e^{i(m-m')\varphi}\int_0^{\pi} P_{j'm'}(\cos\theta)P_{jm}(\cos\theta)\int_0^{\infty}\phi_{n'j'}(r)\phi_{nj}(r)V(R,\Theta,\Phi,r,\theta,\varphi)dr\sin\theta d\theta d\varphi. \tag{10}$$

Here

$$A_{j'm'jm} = \frac{1}{4\pi}\sqrt{\frac{(2j+1)(2j'+1)(j-m)!(j'-m')!}{(j+m)!(j'+m')!}}$$

is a constant factor that comes from normalization coefficients. The Jacobian with respect to r is just dr. Notice that $M_{njm}^{n'j'm'}$ is a function of variables (R,Θ,Φ). Summation in Eq. (10) goes over all quantum states, including the diagonal element njm. In general the matrix elements of $M_{njm}^{n'j'm'}$ are complex-valued and non-zero for $m\neq m'$, because wave functions depend on φ.

So, the quantum coordinates here are $\mathbf{q} = (r,\theta,\phi)$, while classical coordinates are $\mathbf{Q} = (R,\Theta,\Phi)$. The wave function $\Psi(\mathbf{q})$ depends on quantum coordinates only, which is the simplest case, no explicit $\Psi(\mathbf{q};\mathbf{Q},\mathbf{P})$ dependence. The classical equations of motion can be derived either in the reference frame associated with center-of-mass of the entire ABM system using spherical polar coordinates, or in the reference frame where AB is initially at rest using Cartesian coordinates. In the first case, according to Eq. (1)

$$H = \frac{P_R^2}{2\mu} + \frac{P_\Theta^2}{2\mu R^2} + \frac{P_\Phi^2}{2\mu R^2\sin^2\Theta} + H_{\mathbf{0}} + \widetilde{V}(R,\Theta,\Phi)\ , \tag{11}$$

where μ is the reduced mass of AB+M, and we introduced

$$H_{\mathbf{0}} = \left\langle \psi(r,\theta,\varphi)\middle|\hat{T}_q + V_{\mathrm{AB}}(r)\middle|\psi(r,\theta,\varphi)\right\rangle = \sum_{nj}\sum_{m}\left|a_{njm}\right|^2 E_{nj} \tag{12}$$

and

$$\begin{aligned}\widetilde{V}(R,\Theta,\Phi) &= \left\langle \psi(r,\theta,\varphi)\middle| V(R,\Theta,\Phi,r,\theta,\varphi)\middle|\psi(r,\theta,\varphi)\right\rangle \\ &= \sum_{n'j'm'}\sum_{njm} a^{*}_{n'j'm'}a_{njm}\exp\{i(E_{n'j'}-E_{nj})t/\hbar\}\,M^{n'j'm'}_{njm}(R,\Theta,\Phi).\end{aligned} \tag{13}$$

This average potential is a real number (for detailed prove see Appendix C), which means that all forces produced by partial derivatives with respect to classical variables (R,Θ,Φ) are also real. The equations of motion, from Eq. (3), are

$$\dot{R} = \frac{P_R}{\mu}, \tag{14a}$$

$$\dot{\Theta} = \frac{P_\Theta}{\mu R^2}, \tag{14b}$$

$$\dot{\Phi} = \frac{P_\Phi}{\mu R^2 \sin^2\Theta}, \tag{14c}$$

$$\dot{P}_R = -\frac{\partial \widetilde{V}(R,\Theta,\Phi)}{\partial R} + \frac{P_\Theta^2}{\mu R^3} + \frac{P_\Phi^2}{\mu R^3 \sin^2\Theta}, \tag{14d}$$

$$\dot{P}_\Theta = -\frac{\partial \widetilde{V}(R,\Theta,\Phi)}{\partial \Theta} + \frac{P_\Phi^2 \cos\Theta}{\mu R^2 \sin^3\Theta}, \tag{14e}$$

$$\dot{P}_\Phi = -\frac{\partial \widetilde{V}(R,\Theta,\Phi)}{\partial \Phi}. \tag{14f}$$

Alternatively, using six Cartesian coordinates, the Hamiltonian is:

$$\begin{aligned}H = &\frac{P_{X_{\mathrm{M}}}^2}{2m_{\mathrm{M}}} + \frac{P_{Y_{\mathrm{M}}}^2}{2m_{\mathrm{M}}} + \frac{P_{Z_{\mathrm{M}}}^2}{2m_{\mathrm{M}}} + \frac{P_{X_{\mathrm{AB}}}^2}{2m_{\mathrm{AB}}} + \frac{P_{Y_{\mathrm{AB}}}^2}{2m_{\mathrm{AB}}} + \frac{P_{Z_{\mathrm{AB}}}^2}{2m_{\mathrm{AB}}} \\ &+ \widetilde{V}(X_{\mathrm{M}}-X_{\mathrm{AB}}, Y_{\mathrm{M}}-Y_{\mathrm{AB}}, Z_{\mathrm{M}}-Z_{\mathrm{AB}}).\end{aligned} \tag{15}$$

The equations of motion are simply:

$$\dot{Q}_i = \frac{P_i}{m_i}; \quad \dot{P}_i = -\frac{\partial \widetilde{V}}{\partial Q_i}. \tag{16}$$

2.2.3 MQCT in the BF Reference Frame

The body-fixed frame is an inertial reference frame. Its origin is placed into the center-of-mass of the entire ABM system. The same classical variables $\mathbf{Q} = (R, \Theta, \Phi)$ are used [41], but the quantum degrees of freedom are described by Jacobi coordinates $\mathbf{q} = (r, \gamma, \varphi')$, as shown in Fig. 2. The potential does not depend on classical angles and angle φ' due to symmetry, so $V = V(R, r, \gamma)$. In these new coordinates the basis function $Y_{jm'}(\gamma, \phi')$ can be re-expressed through the SF basis functions $Y_{jm}(\theta, \varphi)$ and the Wigner rotation functions [42,43] (see Appendix A):

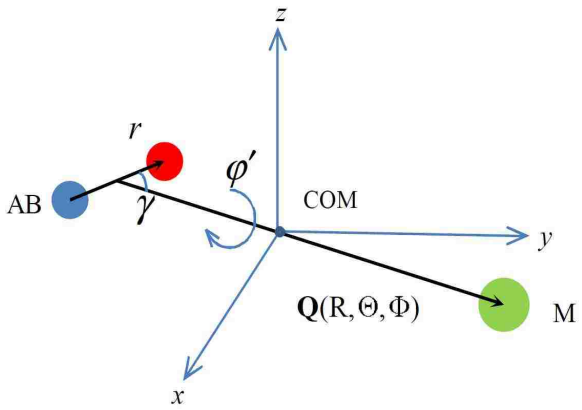

Figure 2. Body-fixed (BF) reference frame. Origin of Cartesian coordinates is in the center of mass (COM) of the entire AB+M system.

$$Y_{jm'}(\gamma, \phi') = \sum_{m} D^{j}_{mm'}(\Phi, \Theta, 0)\, Y_{jm}(\theta, \phi)\,. \tag{17}$$

Note that in this section, and in Appendix A, we use unprimed index m to label spherical harmonics of angle φ in the SF reference frame, while we use primed index m' (and later m'') to label spherical harmonics of angle φ' in the BF reference frame. (In contrast, indexes j and n are the same in both SF and BF reference frames and we will use j, j' and j'' below as needed, without association with SF or BF.)

The wave function $\psi(r, \gamma, \varphi')$ is, again, expanded in a basis set:

$$\psi(r,\gamma,\phi',t)=\sum_{n\,j\,m'}a_{njm'}(t)\varphi_{nj}(r)\,Y_{jm'}(\gamma,\phi')\exp\{-iE_{nj}t/\hbar\}\,. \tag{18}$$

It is important to note that in the BF the quantum angles (γ,φ') depend on classical variables (Θ,Φ) that change over time as collision progresses, and now the wave function depends on classical variables explicitly: $\psi=\psi(r,\gamma,\varphi';\Theta,\Phi)$. To be more specific, this dependence is through spherical harmonics $Y_{jm'}(\gamma,\varphi';\Theta,\Phi)$ that, in turn, depend on $D^{j}_{mm'}(\Phi,\Theta,0)$. The angles (Θ,Φ) depend on time, so, the time derivative in the TDSE should be computed as:

$$\begin{aligned}\frac{\partial\psi}{\partial t}=\sum_{n\,j\,m'}\exp\{-iE_{nj}t/\hbar\}\,\phi_{nj}(r)\Bigg(&\frac{\partial a_{njm'}}{\partial t}Y_{jm'}(\gamma,\varphi')-a_{njm'}\frac{iE_{nj}}{\hbar}Y_{jm'}(\gamma,\varphi')\\&+a_{njm'}\sum_{m}\frac{\partial D^{j}_{mm'}(\Phi,\Theta,0)}{\partial t}Y_{jm}(\theta,\varphi)\Bigg).\end{aligned} \tag{19}$$

Analytic expression for time derivative of the Wigner function is derived in Appendix 2B:

$$\begin{aligned}\frac{\partial D^{j}_{mm'}(\Phi,\Theta,0)}{\partial t}&=\frac{\partial D^{j}_{mm'}}{\partial\Theta}\dot{\Theta}+\frac{\partial D^{j}_{mm'}}{\partial\Phi}\dot{\Phi}\\=\frac{1}{2}\Big[\sqrt{j(j+1)-m'(m'-1)}D^{j}_{mm'-1}(\Phi,\Theta,0)&-\sqrt{j(j+1)-m'(m'+1)}D^{j}_{mm'+1}(\Phi,\Theta,0)\Big]\dot{\Theta}+\\\sin\Theta\frac{1}{2}\Big[\sqrt{j(j+1)-m'(m'-1)}D^{j}_{mm'-1}(\Phi,\Theta,0)&+\sqrt{j(j+1)-m'(m'+1)}D^{j}_{mm'+1}(\Phi,\Theta,0)\Big]\dot{\Phi}\\&-im'\cos\Theta D^{j}_{mm'}(\Phi,\Theta,0)\,\dot{\Phi}.\end{aligned} \tag{20}$$

Using (20) in (19), substituting (19) into the TDSE and projecting out eigenstates, we obtain:

$$i\hbar\frac{\partial a_{njm'}}{\partial t}=\sum_{n'j'}a_{n'j'm'}\exp\{i(E_{nj}-E_{n'j'})t/\hbar\}\,M^{n'j'}_{n\,j}(R)-i\hbar\sum_{m''}a_{njm''}W^{m''}_{m'}\,. \tag{21}$$

Here we introduced for every m' the state-to-state transition matrix:

$$M_{n\,j}^{n'j'}(R) = A_{j'm'j\,m'}\left\langle \phi_{nj}(r)P_{jm'}(\cos\,\gamma)\middle|V\,(R,r,\gamma)\middle|\phi_{n'j'}(r)P_{j'm'}(\cos\,\gamma)\right\rangle \tag{22}$$

and for every j the state-to-state matrix:

$$W_{m'}^{m''} = \frac{1}{2}\left[\sqrt{j(j+1)-m''(m''-1)}\delta_{m',m''-1} - \sqrt{j(j+1)-m''(m''+1)}\delta_{m',m''+1}\right]\dot{\Theta} +$$
$$i\left(\sin\Theta\frac{1}{2}\left[\sqrt{j(j+1)-m''(m''-1)}\delta_{m',m''-1} + \sqrt{j(j+1)-m''(m''+1)}\delta_{m',m''+1}\right] - m''\cos\Theta\,\delta_{m',m''}\right)\dot{\Phi}. \tag{23}$$

The structure of coupled equations (21) is such that the matrix $M_{n\,j}^{n'j'}(R)$ describes only transitions from $(n\,j)$ to $(n'j')$, within the same value of m'. It is computed for every m', separately, because its elements depend on m' through Legendre polynomials and the constant factor in Eq. (22). Each such matrix is symmetric, $M_{n\,j}^{n'j'}(R) = M_{n'j'}^{n\,j}(R)$, and its elements are real (see Appendix 2C). Each element is a function of *R* only. This matrix does not depend on time; it is computed once.

In contrast, the matrix $W_{m'}^{m''}$ is not a constant matrix, due to time evolution of classical entities $\Theta(t)$, $\dot{\Theta}(t)$ and $\dot{\Phi}(t)$. It describes transitions between m' and $m''=m'\pm1$, within the same energy level $(n\,j)$. This matrix is computed for every j, separately, because its elements depend on j. In Appendix C we also show that this matrix is anti-Hermitian: $(W_{m'}^{m''})^* = -W_{m''}^{m'}$. The last imaginary term in $W_{m'}^{m''}$ is diagonal. It corresponds to the non-intermultiplet transition. Simply speaking, it is responsible for the change of wave function's phase, $im\,\Phi$, during rotation by angle Φ. The coupled-states (CS) approximation is easily formulated by setting $W_{m'}^{m''} = 0$.

For future reference it is convenient to introduce two simpler real-valued matrixes:

$$U_{m'}^{m''} = \frac{1}{2}\left[\sqrt{j(j+1)-m''(m''-1)}\,\delta_{m',m''-1} - \sqrt{j(j+1)-m''(m''+1)}\,\delta_{m',m''+1}\right] \tag{24a}$$

and

$$V_{m'}^{m''} = \frac{1}{2}\left[\sqrt{j(j+1)-m''(m''-1)}\,\delta_{m',m''-1} + \sqrt{j(j+1)-m''(m''+1)}\,\delta_{m',m''+1}\right], \tag{24b}$$

so that we can express

$$W_{m'}^{m''} = U_{m'}^{m''}\,\dot{\Theta} + i\left(\sin\Theta V_{m'}^{m''} - m''\cos\Theta\,\delta_{m',m''}\right)\dot{\Phi}\,. \tag{25}$$

Matrixes $U_{m'}^{m''}$ and $V_{m'}^{m''}$ are time-independent and should be computed only once.

As for classical degrees of freedom, the equations of motion for $\dot{R}$, $\dot{\Theta}$, $\dot{\Phi}$ and $\dot{P}_R$ are exactly the same as in the SF reference frame, Eqs. (14a-d), with one difference that in the BF the average potential $\widetilde{V}$ depends on *R* only:

$$\widetilde{V}(R) = \left\langle \psi(r,\gamma,\varphi') \middle| V(R,r,\gamma) \middle| \psi(r,\gamma,\varphi') \right\rangle. \tag{26}$$

However, equations for $\dot{P}_\Theta$ and $\dot{P}_\Phi$ are more complicated in the BF reference frame, because they use the last term in Eqs. (3a-b). Namely, instead of Eqs. (16e-f) in the SF, we have in the BF:

$$\dot{P}_\Theta = -2\,\mathrm{Re}\left\langle \psi(r,\gamma,\varphi') \middle| V(R,r,\gamma) \middle| \frac{\partial\psi(r,\gamma,\varphi')}{\partial\Theta} \right\rangle + \frac{P_\Phi^2\cos\Theta}{\mu\,R^2\sin^3\Theta}, \tag{27a}$$

$$\dot{P}_\Phi = -2\,\mathrm{Re}\left\langle \psi(r,\gamma,\varphi') \middle| V(R,r,\gamma) \middle| \frac{\partial\psi(r,\gamma,\varphi')}{\partial\Phi} \right\rangle. \tag{27b}$$

Analytic expressions for these matrix elements are derived in Appendix 2B. They can be conveniently expressed through the commutator matrixes $[\mathbf{M},\mathbf{U}]$ and $[\mathbf{M},\mathbf{V}]$. The final expressions are:

$$\dot{P}_\Theta = \sum_{n''j''m''} \sum_{n'j'm'} a^*_{n''j''m''} a_{n'j'm'} \exp\{i(E_{n''j''} - E_{n'j'})t/\hbar\} [\mathbf{M},\mathbf{U}]^{n''j''m''}_{n'j'm'} + \frac{P_\Phi^2 \cos\Theta}{\mu R^2 \sin^3\Theta}, \qquad (28a)$$

and

$$\dot{P}_\Phi = -i \sum_{n''j''m''} \sum_{n'j'm'} a^*_{n''j''m''} a_{n'j'm'} \exp\{i(E_{n''j''} - E_{n'j'})/\hbar\} \sin\Theta [\mathbf{M},\mathbf{V}]^{n''j''m''}_{n'j'm'}. \qquad (28b)$$

These formula look rather complicated but, in fact, each commutator is a time-independent matrix computed once (since **M**, **U** and **V** are all time independent). In the case of CS-approximation these equations reduce to much simpler formula:

$$\dot{P}_\Theta = \frac{P_\Phi^2 \cos\Theta}{\mu R^2 \sin^3\Theta}, \qquad (29a)$$

$$\dot{P}_\Phi = 0. \qquad (29b)$$

Before finalizing this section we want to stress again the difference between SF and BF formulations. In the SF reference frame the third term of Eqs. (3a-b) is zero, and only the second term makes contribution to the equations of motion. This term involves *gradients of potential*. In contrast, in the BF reference frame the second term of Eqs. (3a-b) is zero, and only the third term makes contribution, which has no gradients of potential. Instead, it involves *derivatives of wave functions*. Indeed, in the BF reference frame the potential does not depend on (classical) angles Θ and Φ, but the basis functions do!

2.3 Numerical Results

Without the purpose of computing converged quenching cross sections for any real system, but in order to test the correctness of our theory (in particular, the equivalence of SF and BF formulations) we conducted some numerical calculations using the model PES of the rigid rotor

$$V(R,\gamma) = D((\exp\{-(R-R_e)/a\}-1)^2-1)\left(1+\frac{\cos\gamma}{2}\right). \quad (30)$$

The Morse parameters were as follows: $D = 50\ \mathrm{cm}^{-1}$, $R_e = 5\,a_0$ and $a = \sqrt{2D/\mu}/\omega$, where $\omega = D$. The values of reduced mass and equilibrium inter-nuclear distance $r_e = 2.79\,a_0$ in the molecule correspond to He + SO system [44]. Equations (14a-e) and (28a-b) are propagated using 4th-order Runge-Kutta method. Energies of rotational levels were computed analytically, $E_j = j(j+1)B$, where $B = 1/(2\mu_{SO}r_e^2)$. In order to compute analytic gradients of this potential with respect to Θ and Φ for equations of motion in the SF reference frame we used:

$$\cos\gamma = \cos\theta\cos\Theta + \cos\varphi\sin\theta\cos\Phi\sin\Theta + \sin\varphi\sin\theta\sin\Phi\sin\Theta. \quad (31)$$

This expression is obtained from the scalar product of two unit vectors: $\mathbf{n}_\mathbf{q}(\theta,\varphi)$ and $\mathbf{n}_\mathbf{Q}(\Theta,\Phi)$, with γ being the angle between them. The minimal rotational basis set of $j = 0,1$ and $m = 0,\pm 1$ was used (four states). In the following two tests we took the rotationally excited state $j = 1$ and computed probability of its stabilization into $j = 0$ in several different ways. In each case the impact parameter was $b = 3\,a_0$ and the collision energy was $E_\mathbf{Q} = 300\ \mathrm{cm}^{-1}$. The initial relative orientation (and the trajectory of

collision) was physically equivalent in each calculation, but it was intentionally made different mathematically, in order to check the equations of motion, as explained below.

2.3.1 Testing BF Equations

Namely, in the BF reference frame we launched three different trajectories. For one of them the vector of initial velocity was placed in the $\Phi = 0$ plane. This situation corresponds to $\dot{P}_\Phi = 0$ and $\dot{\Phi} = 0$. Such trajectory stays in the polar plane, $\Phi = const$. In practice, the equation of motion (28b) for $\dot{P}_\Phi$ can be ignored. All we have to do is to propagate Eq. (28a) for $\dot{P}_\Theta$ and Eq. (14b) for $\dot{\Theta}$, since the value of Θ changes along such trajectory.

For the second trajectory the vector of initial velocity was placed in the $\Theta = \pi/2$ plane. This situation corresponds to $\dot{P}_\Theta = 0$ and $\dot{\Theta} = 0$. Such trajectory stays in the equatorial plane, $\Theta = const$. Now the equation of motion (28a) for $\dot{P}_\Theta$ can be ignored. All we have to do is to propagate Eq. (28b) for $\dot{P}_\Phi$ and Eq. (14c) for $\dot{\Phi}$, since the value of Φ changes along such trajectory.

For the third (most general) trajectory the vector of initial velocity was placed arbitrarily. The trajectory is still planar, but both angles Θ and Φ evolve and we have to propagate both Eqs. (28a-b) for $\dot{P}_\Theta$ and $\dot{P}_\Phi$, and both Eqs. (14b-c) for $\dot{\Theta}$ and $\dot{\Phi}$.

In all these cases the initial state was $j = 1$, $m' = 0$ and we looked at the probability of its quenching into $j = 0, m' = 0$.

2.3.2 Testing BF *vs.* SF Equations

In the SF reference frame we launched two more trajectories. One was launched from the point on *z*-axis towards the $j=1$, m=0 state (with some arbitrary value of Φ). Such trajectory stays in the $\Phi = const$ plane. The second trajectory was launched from the point on the *x*-axis, towards the superposition state $(m^{+}-m^{-})/\sqrt{2}$ of $j=1$ (with an arbitrarily directed velocity vector). In these two cases we looked at the probability of quenching into $j=0$, $m=0$.

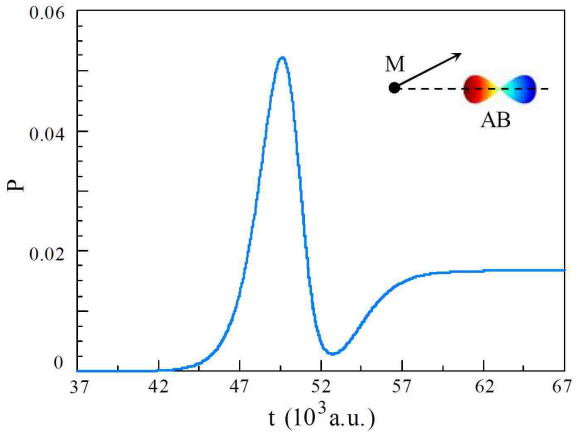

Figure 3. Time evolution of population in the ground rotational state $j=0$ during the process of quenching of the excited state $j=1$ for a typical trajectory. Initial orientation of the velocity vector of M with respect to the wave function of AB is shown schematically on the insert. See text for details.

Note that in all these (five) trajectories the relative orientation of the velocity vector and the wave function of the system at the initial moment of time were physically equivalent. We propagated all five and found that the quenching probability at the end of trajectory, as well as population of the ground state $j=0$ during the course of trajectory, were all identical (within small numerical errors). Population of the (final) ground state, as a function of time, is shown in Fig. 3. All five curves coincide, which means that all five trajectories are identical.

One practical result of these tests is that in the BF reference frame we do not really need the classical equations of motion for both Θ and Φ. The trajectory is planar (exception is discussed below), so that without the loss of generality we can restrict our

calculations to $\Phi = 0$ plane, where $\dot{\Phi} = 0$ and $\dot{P}_{\Phi} = 0$. In most situations we only have to propagate Eqs. (14b) and (28a) for $\dot{\Theta}$ and $\dot{P}_{\Theta}$.

Still, the value of Eqs. (14c) and (28b) for $\dot{\Phi}$ and $\dot{P}_{\Phi}$ in the BF reference frame is clear. First of all, they allow testing the theory and the computer code. Second, they become important if the initial state of the system is a superposition of rotational eigenstates (see below) that has no cylindrical symmetry around the vector $\mathbf{Q} = (R, \Theta, \Phi)$. In such cases the trajectory is not planar, which may be important for some applications.

2.3.3 Testing BF to SF projection

In this test we took the $j = 1$, $m = +1$ eigenstate as initial state in the SF calculations. In order to start the equivalent BF calculations from this very state, we projected this m -state onto the m' eigenstates of the BF at the initial moment of time and for the initial position of the quencher (to determine the expansion coefficients). Then, as initial state in the BF calculations, we took the corresponding superposition of

m' states (with coefficients determined by projection). Wave function of such initial state has no cylindrical symmetry around the vector $\mathbf{Q} = (R, \Theta, \Phi)$, so, in the BF calculations we had to propagate classical equations of motion for both Θ and Φ .

The impact parameter was $b = 5.4\, a_0$, the initial position of quencher M was on *x*-axis, but the initial velocity vector was directed arbitrarily. As trajectory progressed, we determined populations of the m -states along the trajectory directly from the SF calculations, and indirectly from the BF calculations, by projecting the BF wave function (superposition of m' states) onto m -states in the SF reference frame after each time step.

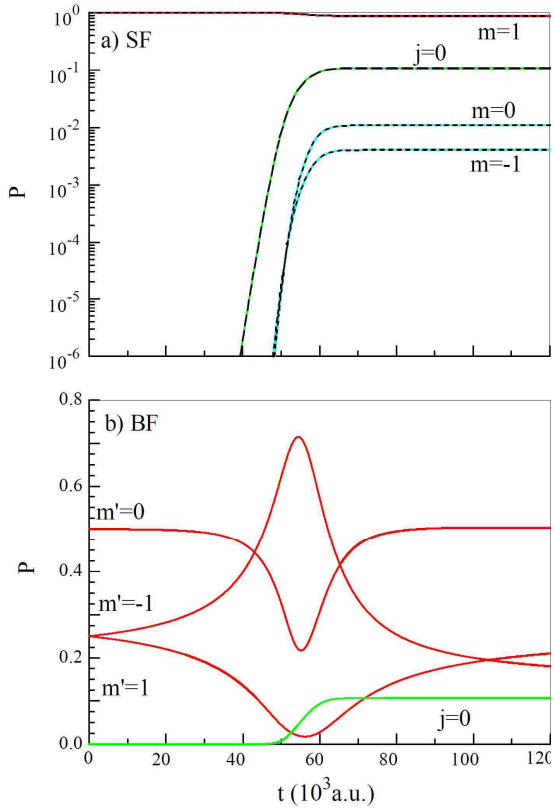

Figure 4. Time evolution of rotational state populations in SF reference frame (a) and BF reference frame (b) for a typical trajectory. The initial quantum state was $j = 1,\ m = 1$ in the SF reference frame. Red curve in (a) corresponds to this state. Green curve in (a) and (b) corresponds to the ground state $j = 0$ and describes quenching. Blue curves in (a) correspond to the inter-multiplet transitions. Red curves in (b) correspond to different states of $j = 1$ level in the BF, all populated (arbitrarily) at the initial moment of time. Black dashed lines in (a) are obtained by projection of the BF results (b) onto SF basis functions. They entirely coincide with SF results.

Results are presented in Fig. 4. For this trajectory the most notable process is a transfer of ~10% of population from the excited initial state (red) to the ground state $j = 0$ (green). This transition occurs within a short time interval of the molecule-atom encounter around $t \sim 5500$ *a.u.*, which is seen in both the SF (Fig. 4a) and BF (Fig. 4b)

calculations. However, transitions within the multiplet states of $j=1$ occur very differently in the SF and BF calculations. In the SF calculations transitions from $m=+1$ to $m=0$ and $m=-1$ states also occur only during the short time-interval of the molecule-atom encounter (blue in Fig. 4a, probabilities are 1.09% and 0.41%, respectively). In contrast, in the BF calculations at the initial moment of time the population is distributed between different m'-states, and the transitions between them occur *continuously* (Fig. 4b). When the molecule and the atom are close these transitions are more intense (due to geometric considerations) but, strictly speaking, they never end. Nor the populations of $m'=\pm 1$ states reach any asymptotic values. However, if the corresponding BF wave functions are used to obtain the populations of m states in the SF (dashed black lines in Fig. 4a), the results of direct SF calculations are accurately reproduced.

From these three tests we can conclude that all our equations for calculations in the SF and BF reference frames are correct.

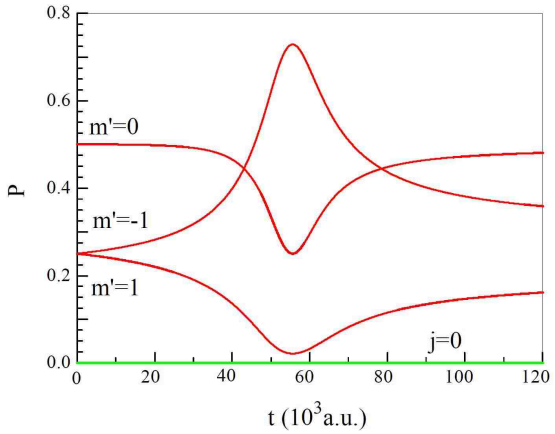

Figure 5. Same as in Fig. 4b, but with interaction potential "switched-off". No quenching to $j=0$ occur, but population of different multiplet states within $j=1$ level evolves continuously in the BF reference frame, and very similar to that in Fig. 4b.

2.3.4 Numerical Testing matrixes U and V

In this test (BF only) we artificially switched off the molecule-quencher interaction potential. This makes matrix **M** null, so that time-evolution includes only transitions between different m'-states, within the initial constant value of $j=1$, due to action of matrixes **U** and **V**. Initial

conditions were identical to those of the previous example. Results are plotted in Fig. 5. As expected, transition to $j=0$ is suppressed, but transitions between m'-states are still there. The peaks in Fig. 5 correspond to the distance of closest approach, not to the maximum of any interaction (the interaction is zero in this test). Overall, time evolution is very similar to what we saw in the previous test, Fig. 4b. This is because the scattering angle of the trajectory in the previous test was relatively small, less than 13 deg. Without interaction the trajectory is a straight line, of course.

2.3.5 Numerical Testing Impact Parameter

In this test (SF only) we scanned the impact parameter along z-axis for the initial state $m=0$ and separately for the initial state $(m^+ - m^-)/\sqrt{2}$ of $j=1$. These two initial states correspond to mainly perpendicular and mainly parallel relative orientation of the molecular axis and the collision velocity vector, respectively. While such calculations are restricted, they scan pretty well the range of possible transition probabilities. Results are presented in Fig. 6. We see that transition probability is higher for perpendicular arrangement. This property carries rather clear classical meaning. However, the transition probability oscillates (as a function of impact parameter), which reflects quantum properties of these calculations.

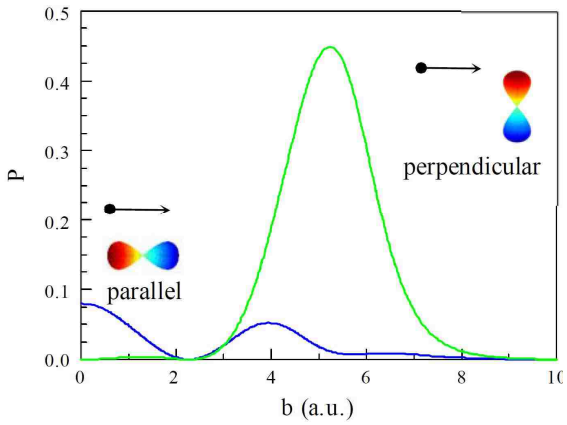

Figure 6. Probability of $j=1$ quenching as a function of impact parameter for perpendicular (green) and parallel (blue) initial orientations of the wave function of AB with respect to the velocity vector of M.

2.3.6 Numerical Testing Microscopic Reversibility

Here we carried out calculations of excitation probability (SF only), in order to compare with probability of quenching and assess how well the principle of microscopic reversibility is satisfied (or how badly it is violated). It is known that the principle of microscopic reversibility is not immediately built into the MQCT [34], but expected that it is approximately satisfied when the value of internal energy quantum is small, compared to scattering energy. Thus, we performed calculations with different scattering energies. Results are presented in Fig. 7a and 7b, that correspond two different trajectories, one with intermediate impact parameter $b = 5.4\, a_0$, and one with larger impact parameter $b = 9\, a_0$. As expected, the microscopic reversibility is violated at low collision energies. Here the value of rotational quantum is 1.6 cm^{-1}. In Fig. 7a the difference between excitation and quenching probabilities changes smoothly and reaches ~ 35% when the collision energy is reduced to 25 cm^{-1}. In Fig. 7b the difference between excitation and quenching remains small even at 25 cm^{-1}. Conclusion

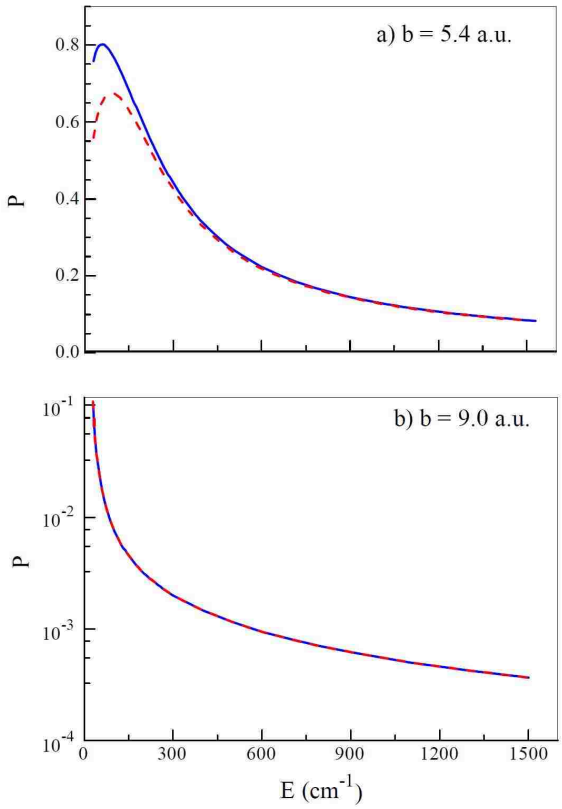

Figure 7. Probabilities of quenching (solid blue line) and excitation (dashed red line) as functions of collision energy for two typical trajectories with small (a) and large (b) values of impact parameter.

is that the microscopic reversibility is not automatically satisfied at low collision energies, particularly when the transition probability is large. In order to build it into the MQCT one has to use the idea of collision energy symmetrization [31,33].

2.4 Conclusions for Chapter 2

We formulated the mixed quantum/classical theory, MQCT, for rotationally (and vibrationally) inelastic scattering process in the diatomic molecule + atom system. Two versions of theory are presented: first in the SF and second in the BF reference frames. The SF version is easy to derive and the resultant equations of motion are transparent, but the state-to-state transition matrix is complex-valued and dense (many non-zero elements). Such calculations may be computationally demanding for heavier molecules and/or higher temperatures, when the number of accessible channels becomes large. In contrast, the BF version of theory requires some tedious derivations and the final equations of motion are rather complicated (not particularly intuitive). However, the state-to-state transitions are driven by real-valued near-diagonal matrixes of smaller size. Thus, the BF formulation is the method of choice from the computational point of view, while the SF formulation can serve as a test of the BF equations of motion, and the code. Rigorous numerical tests were carried out for a model system to ensure that all equations, matrixes and computer codes in both SF and BF reference frames are correct. These tests also helped to better understand differences and similarities of two physically equivalent but mathematically different formulations.

We want to emphasize again that MQCT is not thought to replace the full-quantum calculations. At low temperatures and/or light collision partners the full-quantum calculations are indispensable (accurate and affordable). It is at higher

temperatures and for heavier molecules/quenchers we expect that MQCT can successfully complement the existing methods. In its current form this theory can be applied to a number of important diatomic molecule + atom inelastic scattering processes, such as SO + He [44], NH + He [45], and CO + Ar [46]. Our recent MQCT calculations of rotational state-to-state transition cross sections for N_2 + Na system show excellent agreement with full quantum results for both excitation and quenching processes in a broad range of collision energies [39]. Another ongoing project is to develop MQCT further, for treatment of general asymmetric top rotor molecules (bent triatomics and small polyatomic molecules) in order to treat the quenching of H_2O and SOMs. Some (very) preliminary data for H_2O + He scattering are also encouraging.

Appendix 2A: Derivative of Wigner Rotation Function

Transformation of the basis set of rotational eigenstates is:

$$Y_{jm'}(\gamma,\phi') = \sum_{m=-j}^{j} D^{j}_{mm'}(\Phi,\Theta,0)\, Y_{jm}(\theta,\phi)\,. \tag{2A1}$$

In general:

$$D^{j}_{mm'}(\Phi,\Theta,\Lambda) = \exp(-im\Phi) d^{j}_{mm'}(\Theta) \exp(-im'\Lambda)\,, \tag{2A2}$$

where $d^{j}_{mm'}(\Theta)$ are small Wigner d-functions, or explicitly:

$$\begin{aligned} d^{j}_{mm'}(\Theta) &= \left[(j+m')!(j-m')!(j+m)!(j-m)!\right]^{1/2} \\ &\times \sum_{s} \frac{(-1)^{m-m'+s}}{(j+m'-s)!\,s!\,(m-m'+s)!\,(j-m-s)!} \left(\cos\left(\frac{\Theta}{2}\right)\right)^{2j+m'-2s-m} \left(\sin\left(\frac{\Theta}{2}\right)\right)^{m+2s-m'}. \end{aligned} \tag{2A3}$$

The index s takes only such values that the factorials are nonnegative. The *d*-matrix elements defined here are real and correspond to the $z-y-z$ convention [41,42].

For an atomic quencher the last rotation (by angle Λ around the mole-quencher axis) is meaningless. So, one can set $\Lambda=0$ without loss of generality. The purpose of this appendix is to derive expressions for $\partial D^{j}_{mm'}(\Phi,\Theta,\Lambda)/\partial\Phi$ and $\partial D^{j}_{mm'}(\Phi,\Theta,\Lambda)/\partial\Theta$. It is quite clear that

$$\partial D^{j}_{mm'}(\Phi,\Theta,\Lambda)/\partial\Lambda = -im' D^{j}_{mm'}(\Phi,\Theta,\Lambda). \tag{2A4}$$

One could also write immediately $\partial D^{j}_{mm'}(\Phi,\Theta,\Lambda)/\partial\Phi = -imD^{j}_{mm'}(\Phi,\Theta,\Lambda)$ but this expression is useless because it contains m, while the sum in Eq. (28) is also over m. In order to obtain a useful expression for $\partial/\partial\Phi$, and derive the expression for $\partial/\partial\Theta$ without differentiating Eq. (2A3) for d-function directly, we will use the raising and lowering operators as explained below.

There is a deep connection between Wigner *d*-functions and a quantum rotation of the symmetric top. *D*-function is an eigenfunction of the symmetric top Hamiltonian. In terms of Schrodinger equation: $\Im^2 D^{j}_{mm'} = j(j+1)D^{j}_{mm'}$, where the kinetic energy operator is:

$$\Im^2 = -\frac{1}{\sin\Theta}\frac{\partial}{\partial\Theta}\sin\Theta\frac{\partial}{\partial\Theta} - \frac{1}{\sin^2\Theta}\left(\frac{\partial^2}{\partial^2\Lambda} + \frac{\partial^2}{\partial^2\Phi} + 2\cos\Theta\frac{\partial^2}{\partial\Lambda\partial\Phi}\right).$$

Reference [40] emphasizes that Wigner functions have the same properties as spherical harmonics. We know that for spherical harmonics there are raising and lowering operators, *e.g.*:

$$(\hat{j}_x \pm i\,\hat{j}_y)Y_{jm} = \hat{j}_{\pm}Y_{jm} = \sqrt{j(j+1)-m(m\pm1)}\,Y_{jm\pm1}$$

Similar operators exist for Wigner functions. They are called the *space fixed angular momentum operators of rigid rotor*:

$$\Im_x = i\left(\cos\Lambda\cot\Theta\frac{\partial}{\partial\Lambda} + \sin\Lambda\frac{\partial}{\partial\Theta} - \frac{\cos\Lambda}{\sin\Theta}\frac{\partial}{\partial\Phi}\right), \tag{2A5}$$

$$\Im_y = i\left(\sin\Lambda\cot\Theta\frac{\partial}{\partial\Lambda} - \cos\Lambda\frac{\partial}{\partial\Theta} - \frac{\sin\Lambda}{\sin\Theta}\frac{\partial}{\partial\Phi}\right), \tag{2A6}$$

$$\Im_z = -i\frac{\partial}{\partial\Lambda}. \tag{2A7}$$

Then, the raising and lowering operators $\Im_+ = \Im_x - i\Im_y$ and $\Im_- = \Im_x + i\Im_y$ (note: minus sign in raising and plus sign in lowering) result in:

$$\Im_\pm D^j_{mm'} = \sqrt{j(j+1) - m'(m'\pm 1)}\,D^j_{mm'\pm 1}. \tag{2A8}$$

The kinetic energy operator can be expressed as $\Im^2 = \Im_+\Im_- + \Im_-\Im_+ + \Im_z^2$. Raising and lowering operators allow expressing the partial derivatives of *D*-function through other *D*-functions. In other words, action of a derivative operator is a mapping of one quantum state (the rotational state of symmetric top) onto other states.

In the $\Lambda = 0$ case relevant to the diatomic molecule Eqs. (2A5-7) simplify to:

$$\tilde{\Im}_x = i\left(\cot\Theta\frac{\partial}{\partial\Lambda} - \frac{1}{\sin\Theta}\frac{\partial}{\partial\Phi}\right), \tag{2A9}$$

$$\tilde{\Im}_y = -i\frac{\partial}{\partial\Theta}, \tag{2A10}$$

$$\tilde{\Im}_z = -i\frac{\partial}{\partial\Lambda}. \tag{2A11}$$

Derivative over Θ is obtained from the second of these equations, which gives $\partial/\partial\Theta = i\tilde{\Im}_y$. Using $\tilde{\Im}_y = (\tilde{\Im}_- - \tilde{\Im}_+)/2i$ one arrives to:

$$\frac{\partial}{\partial\Theta} = \frac{(\tilde{\Im}_- - \tilde{\Im}_+)}{2}. \tag{2A12}$$

One can also restrict consideration to $\Phi = 0$ and $\Lambda = 0$ using the following relation:

$$\frac{\partial D^j_{mm'}(\Phi,\Theta,\Lambda)}{\partial\Theta} = \exp(-i\Phi m - im'\Lambda)\frac{\partial D^j_{mm'}(0,\Theta,0)}{\partial\Theta}. \tag{2A13}$$

This is so because only $d^j_{mm'}(\Theta)$ depend on Θ. So:

$$\begin{aligned}\frac{\partial D^j_{mm'}(0,\Theta,0)}{\partial\Theta} &= \left(\frac{\tilde{\mathfrak{I}}_- - \tilde{\mathfrak{I}}_+}{2}\right)D^j_{mm'}(0,\Theta,0)\\ &= \frac{1}{2}\left[\sqrt{j(j+1)-m'(m'-1)}D^j_{mm'-1}(0,\Theta,0) - \sqrt{j(j+1)-m'(m'+1)}D^j_{mm'+1}(0,\Theta,0)\right].\end{aligned} \tag{2A14}$$

Finally, for derivative over Θ we obtain:

$$\begin{aligned}&\frac{\partial D^j_{mm'}(\Phi,\Theta,0)}{\partial\Theta} = \exp(-im\Phi)\ \frac{\partial D^j_{mm'}(0,\Theta,0)}{\partial\Theta}\\ &= \exp(-im\Phi)\frac{1}{2}\left[\sqrt{j(j+1)-m'(m'-1)}D^j_{mm'-1}(0,\Theta,0) - \sqrt{j(j+1)-m'(m'+1)}D^j_{mm'+1}(0,\Theta,0)\right]\\ &= \frac{1}{2}\left[\sqrt{j(j+1)-m'(m'-1)}\exp(-im\Phi)D^j_{mm'-1}(0,\Theta,0) - \sqrt{j(j+1)-m'(m'+1)}\exp(-im\Phi)D^j_{mm'+1}(0,\Theta,0)\right]\\ &= \frac{1}{2}\left[\sqrt{j(j+1)-m'(m'-1)}D^j_{mm'-1}(\Phi,\Theta,0) - \sqrt{j(j+1)-m'(m'+1)}D^j_{mm'+1}(\Phi,\Theta,0)\right].\end{aligned} \tag{2A15}$$

This is the final expression for $\partial/\partial\Theta$.

Now focus on derivative over Φ. Combining Eq. (A8) with $\mathfrak{I}_+ = \mathfrak{I}_x - i\mathfrak{I}_y$ and using Eq. (2A9-10), one obtains:

$$\begin{aligned}&\mathfrak{I}_+ D^j_{mm'}(\Phi,\Theta,0) = \sqrt{j(j+1)-m'(m'+1)}D^j_{mm'+1}(\Phi,\Theta,0) =\\ &\left\{i\left(\cot\Theta\frac{\partial}{\partial\Lambda} - \frac{1}{\sin\Theta}\frac{\partial}{\partial\Phi}\right) - \frac{\partial}{\partial\Theta}\right\}D^j_{mm'}(\Phi,\Theta,0).\end{aligned} \tag{2A16}$$

Using Eq. (2A15) for derivative over Θ and Eq. (A4) for derivative over Λ one obtains:

$$\begin{aligned}&\frac{\partial D^j_{mm'}(\Phi,\Theta,0)}{\partial\Phi} =\\ &i\frac{1}{2}\left[\sqrt{j(j+1)-m'(m'-1)}D^j_{mm'-1}(\Phi,\Theta,0) + \sqrt{j(j+1)-m'(m'+1)}D^j_{mm'+1}(\Phi,\Theta,0)\right]\sin\Theta\\ &- im'D^j_{mm}(\Phi,\Theta,0)\cos\Theta.\end{aligned} \tag{2A17}$$

This is the final expression for $\partial/\partial\Phi$. Note that this expression depends on m' (not on m) so that summation in Eq. (19) can be carried out analytically as follows:

$$\begin{aligned}
&\sum_m \frac{\partial}{\partial\Phi} D^j_{mm'}(\Phi,\Theta,0)Y_{jm}(\theta,\varphi) = \\
&= \sum_m \Bigg(i\frac{1}{2}\Big[\sqrt{j(j+1)-m'(m'-1)}D^j_{mm'-1}(\Phi,\Theta,0) + \sqrt{j(j+1)-m'(m'+1)}D^j_{mm'+1}(\Phi,\Theta,0)\Big]\sin\Theta \\
&\qquad - im' D^j_{mm'}(\Phi,\Theta,0)\cos\Theta\Bigg) Y_{jm}(\theta,\varphi) = \\
&= i\frac{1}{2}\Big[\sqrt{j(j+1)-m'(m'-1)}Y_{jm'-1}(\gamma,\varphi') + \sqrt{j(j+1)-m'(m'+1)}Y_{jm'+1}(\gamma,\varphi')\Big]\sin\Theta \\
&\qquad - im' Y_{jm'}(\gamma,\varphi')\cos\Theta.
\end{aligned} \tag{2A18}$$

Expressions (2A17) and (2A15) can be found in the handbook [43], where they are given without any prove.

Appendix 2B: Matrix Elements in the BF

Using the expansions of Eqs. (17) and (18) and the expression (2A15) for partial derivative over Θ we can write:

$$\begin{aligned}
&\frac{\partial\psi(r,\gamma,\varphi')}{\partial\Theta} = \sum_{n'j'm'} a_{n'j'm'}\phi_{n'j'}(r)\frac{\partial Y_{j'm'}(\gamma,\varphi')}{\partial\Theta}\exp\{-\frac{iE_{n'j'}t}{\hbar}\} \\
&= \sum_{n'j'm'} a_{n'j'm'}\phi_{n'j'}(r)\sum_m \frac{\partial D^{j'}_{mm'}(\Phi,\Theta,0)}{\partial\Theta}Y_{j'm}(\theta,\varphi)\exp\{-\frac{iE_{n'j'}t}{\hbar}\} \\
&= \sum_{n'j'm'} a_{n'j'm'}\phi_{n'j'}(r)\frac{1}{2}\Big[\sqrt{j'(j'+1)-m'(m'-1)}Y_{j'm'-1}(\gamma,\varphi') - \sqrt{j'(j'+1)-m'(m'+1)}Y_{j'm'+1}(\gamma,\varphi')\Big]\exp\{-\frac{iE_{n'j'}t}{\hbar}\}.
\end{aligned} \tag{2B1}$$

Now we need to substitute (2B1) into the first of term of Eq. (27a), which for convenience can be split onto two terms as follows:

$$\begin{aligned}
&-2\,\mathrm{Re}\Big\langle\psi(r,\gamma,\varphi')\,|\,V(R,r,\gamma)\,|\,\frac{\partial\psi(r,\gamma,\varphi')}{\partial\Theta}\Big\rangle = \\
&= -\Big\langle\psi(r,\gamma,\varphi')\,|\,V(R,r,\gamma)\,|\,\frac{\partial\psi(r,\gamma,\varphi')}{\partial\Theta}\Big\rangle - \Big\langle\frac{\partial\psi(r,\gamma,\varphi')}{\partial\Theta}\Big|V(R,r,\gamma)\Big|\psi(r,\gamma,\varphi')\Big\rangle.
\end{aligned} \tag{2B2}$$

The substitution gives:

$$\left\langle \psi(r,\gamma,\varphi') \middle| V(R,r,\gamma) \middle| \frac{\partial \psi(r,\gamma,\varphi')}{\partial \Theta} \right\rangle =$$

$$= \sum_{n''j''m''} \sum_{n'j'm'} a^*_{n''j''m''} a_{n'j'm'} \exp\left(i \frac{E_{n''j''} - E_{n'j'}}{\hbar} t \right) \left\langle \phi_{n''j''}(r) Y_{j''m''}(\gamma,\varphi') \middle| V(R,r,\gamma) \right|$$

$$\times \phi_{n'j'}(r) \frac{1}{2} \left[\sqrt{j'(j'+1) - m'(m'-1)} Y_{j'm'-1}(\gamma,\varphi') - \sqrt{j'(j'+1) - m'(m'+1)} Y_{j'm'+1}(\gamma,\varphi') \right] \rangle =$$

$$= \sum_{n''j''m''} \sum_{n'j'm'} a^*_{n''j''m''} a_{n'j'm'} \exp\left(i \frac{E_{n''j''} - E_{n'j'}}{\hbar} t \right)$$

$$\times \frac{1}{2} \left[\sqrt{j'(j'+1) - m'(m'-1)} \left\langle \phi_{n''j''}(r) Y_{j''m''}(\gamma,\varphi') \middle| V(R,r,\gamma) \middle| \phi_{n'j'}(r) Y_{j'm'-1}(\gamma,\varphi') \right\rangle \right.$$

$$\left. - \sqrt{j'(j'+1) - m'(m'+1)} \left\langle \phi_{n''j''}(r) Y_{j''m''}(\gamma,\varphi') \middle| V(R,r,\gamma) \middle| \phi_{n'j'}(r) Y_{j'm'+1}(\gamma,\varphi') \right\rangle \right]$$

$$= \sum_{n''j''m''} \sum_{n'j'm'} a^*_{n''j''m''} a_{n'j'm'} \exp\left(i \frac{E_{n''j''} - E_{n'j'}}{\hbar} t \right)$$

$$\times \frac{1}{2} \left[\sqrt{j'(j'+1) - m'(m'+1)} M^{n''j''m''}_{n'j'm'+1}(R) - \sqrt{j'(j'-1) - m'(m'-1)} M^{n''j''m''}_{n'j'm'-1}(R) \right]. \quad (2B3)$$

And similarly

$$\left\langle \frac{\partial \psi(r,\gamma,\varphi')}{\partial \Theta} \middle| V(R,r,\gamma) \middle| \psi(r,\gamma,\varphi') \right\rangle = \sum_{n''j''m''} \sum_{n'j'm'} a^*_{n''j''m''} a_{n'j'm'} \exp\left(i \frac{E_{n''j''} - E_{n'j'}}{\hbar} t \right)$$

$$\times \frac{1}{2} \left[\sqrt{j''(j''+1) - m''(m''+1)} M^{n''j''m''+1}_{n'j'm'}(R) - \sqrt{j''(j''-1) - m''(m''-1)} M^{n''j''m''-1}_{n'j'm'}(R) \right]. \quad (2B4)$$

Combining these two expressions we finally obtain:

$$-2\,\mathrm{Re}\left\langle \psi(r,\gamma,\varphi') \middle| V(R,r,\gamma) \middle| \frac{\partial \psi(r,\gamma,\varphi')}{\partial \Theta} \right\rangle =$$

$$= -\left\langle \frac{\partial \psi(r,\gamma,\varphi')}{\partial \Theta} \middle| V(R,r,\gamma) \middle| \psi(r,\gamma,\varphi') \right\rangle - \left\langle \psi(r,\gamma,\varphi') \middle| V(R,r,\gamma) \middle| \frac{\partial \psi(r,\gamma,\varphi')}{\partial \Theta} \right\rangle$$

$$= \sum_{n''j''m''} \sum_{n'j'm'} a^*_{n''j''m''} a_{n'j'm'} \exp\left(i \frac{E_{n''j''} - E_{n'j'}}{\hbar} t \right) \frac{1}{2} \left[M^{n''j''m''-1}_{n'j'm'} \sqrt{j''(j''+1) - m''(m''-1)} - M^{n''j''m''+1}_{n'j'm'} \sqrt{j''(j''+1) - m''(m''+1)} \right.$$

$$\left. + \sqrt{j'(j'+1) - m'(m'-1)} M^{n'j'm'-1}_{n''j''m''} - \sqrt{j'(j'+1) - m'(m'+1)} M^{n'j'm'+1}_{n''j''m''} \right]. \quad (2B5)$$

It is shown in Appendix C that this expression can be conveniently re-written through the commutator of matrixes **M** and **U**:

$$-2\,\mathrm{Re}\left\langle \psi(r,\gamma,\varphi') \middle| V(R,r,\gamma) \middle| \frac{\partial \psi(r,\gamma,\varphi')}{\partial \Theta} \right\rangle = \sum_{n''j''m''} \sum_{n'j'm'} a^*_{n''j''m''} a_{n'j'm'} \exp\left(i \frac{E_{n''j''} - E_{n'j'}}{\hbar} t \right) \left[\mathbf{M}, \mathbf{U} \right]^{n''j''m''}_{n'j'm'}. \quad (2B6)$$

which leads to Eq. (28a). Furthermore, we can split the sum in Eq. (B6) onto a pair of terms:

$$a^{*}_{n''j''m''}a_{n'j'm'}\exp\left(i\frac{E_{n''j''}-E_{n'j'}}{\hbar}t\right)\left[\mathbf{M},\mathbf{U}\right]^{n''j''m''}_{n'j'm'}$$

and

$$a_{n''j''m''}a^{*}_{n'j'm'}\exp\left(i\frac{E_{n'j'}-E_{n''j''}}{\hbar}t\right)\left[\mathbf{M},\mathbf{U}\right]^{n'j'm'}_{n''j''m''}.$$

Because $\left[\mathbf{M},\mathbf{U}\right]$ is symmetric and real (according to Eq. (2C17)) we have the sum of these two numbers is a real number. If $n'j'm'=n''j''m''$ the diagonal term (which does not have a pair) is real by itself: $|a_{n'j'm'}|^2\left[\mathbf{M},\mathbf{U}\right]^{n'j'm'}_{n'j'm'}$. Thus, the expression of Eq. (2B6) always gives real numbers. Its physical meaning corresponds to the torque.

Now consider $\partial\psi/\partial\Phi$ in Eq. (27b):

$$\frac{\partial\psi(r,\gamma,\varphi')}{\partial\Phi}=\sum_{n'j'm'}a_{n'j'm'}\phi_{n'j'}(r)\frac{\partial Y_{j'm'}(\gamma,\varphi')}{\partial\Phi}\exp\{-\frac{iE_{n'j'}t}{\hbar}\}=i\sum_{n'j'm'}a_{n'j'm'}\phi_{n'j'}(r)\exp\{-\frac{iE_{n'j'}t}{\hbar}\}$$
$$\times\left(\sin\Theta\frac{1}{2}\left[\sqrt{j'(j'+1)-m'(m'-1)}Y_{j'm'-1}(\gamma,\varphi')+\sqrt{j'(j'+1)-m'(m'+1)}Y_{j'm'+1}(\gamma,\varphi')\right]-m'\cos\Theta Y_{j'm'}(\gamma,\varphi')\right).$$

(2B7)

Then, for the matrix element in Eq. (27b) we can write:

$$\left\langle\psi(r,\gamma,\varphi')\middle|V(R,r,\gamma)\middle|\frac{\partial\psi(r,\gamma,\varphi')}{\partial\Phi}\right\rangle=i\sum_{n''j''m''}\sum_{n'j'm'}a^{*}_{n''j''m''}a_{n'j'm'}\exp\left(i\frac{E_{n''j''}-E_{n'j'}}{\hbar}t\right)$$
$$\times\left(\sin\Theta\frac{1}{2}\left[\sqrt{j'(j'+1)-m'(m'-1)}M^{n'j'm'-1}_{n''j''m''}+\sqrt{j'(j'+1)-m'(m'+1)}M^{j'm'+1}_{n''j''m''}\right]-m'\cos\Theta M^{n''j''m''}_{n'j'm'}\right).$$

(2B8)

and similarly

$$\left\langle \frac{\partial\psi(r,\gamma,\varphi')}{\partial\Phi}\middle| V\ (R,r,\gamma)\middle|\psi(r,\gamma,\varphi')\right\rangle = -i\sum_{n''j''m''}\sum_{n'j'm'} a^{*}_{n''j''m''}a_{n'j'm'}\exp\left(i\frac{E_{n''j''}-E_{n'j'}}{\hbar}t\right)$$
$$\times\left(\frac{1}{2}\sin\Theta\left[\sqrt{j''(j''+1)-m''(m''-1)}M^{n''j''m''-1}_{n'j'm'}+\sqrt{j''(j''+1)-m''(m''+1)}M^{n''j''m''+1}_{n'j'm'}\right]-m''\cos\Theta M^{n''j''m''}_{n'j'm'}\right).$$

(2B9)

Combining these two expressions:

$$2\,\mathrm{Re}\left\langle\psi(r,\gamma,\varphi')\middle|V\ (R,r,\gamma)\middle|\frac{\partial\psi(r,\gamma,\varphi')}{\partial\Phi}\right\rangle = i\sum_{n''j''m''}\sum_{n'j'm'} a^{*}_{n''j''m''}a_{n'j'm'}\exp\left(i\frac{E_{n''j''}-E_{n'j'}}{\hbar}t\right)$$
$$\times\left(\sin\Theta\frac{1}{2}\left[\sqrt{j''(j''+1)-m''(m''-1)}M^{n''j''m''-1}_{n'j'm'}+\sqrt{j''(j''+1)-m''(m''+1)}M^{n''j''m''+1}_{n'j'm'}\right]-m''\cos\Theta M^{n''j''m''}_{n'j'm'}\right.$$
$$\left.-\sin\Theta\frac{1}{2}\left[\sqrt{j'(j'+1)-m'(m'-1)}M^{n'j'm'-1}_{n''j''m''}+\sqrt{j'(j'+1)-m'(m'+1)}M^{n'j'm'+1}_{n''j''m''}\right]+m'\cos\Theta M^{n'j'm'}_{n''j''m''}\right).$$

(2B10)

According to (2C1) $m'M^{n'j'm'}_{n''j''m''} = m''M^{n''j''m''}_{n'j'm'}$ and Appendix C shows that this expression can be conveniently rewritten through the commutator of matrixes **M** and **V**:

$$-2\,\mathrm{Re}\left\langle\psi(r,\gamma,\phi')\middle|V\ (R,r,\gamma)\middle|\frac{\partial\psi(r,\gamma,\phi')}{\partial\Phi}\right\rangle = -i\sum_{n''j''m''}\sum_{n'j'm'} a^{*}_{n''j''m''}a_{n'j'm'}\sin\Theta\exp\left(i\frac{E_{n''j''}-E_{n'j'}}{\hbar}t\right)[\mathbf{M},\mathbf{V}]^{n''j''m''}_{n'j'm'}.$$

(2B11)

This leads to Eq. (28b). Furthermore, we can split the sum in Eq. (2B11) onto a pair of terms:

$$-ia^{*}_{n''j''m''}a_{n'j'm'}\exp\left(i\frac{E_{n''j''}-E_{n'j'}}{\hbar}t\right)[\mathbf{M},\mathbf{V}]^{n''j''m''}_{n'j'm'}$$

and

$$-ia^{*}_{n'j'm'}a_{n''j''m''}\exp\left(i\frac{E_{n'j'}-E_{n''j''}}{\hbar}t\right)[\mathbf{M},\mathbf{V}]^{n'j'm'}_{n''j''m''}.$$

Due to Eq. (2C8) we have

$$-ia^{*}_{n''j''m''}a_{n'j'm'}\exp\left(i\frac{E_{n''j''}-E_{n'j'}}{\hbar}t\right)[\mathbf{M},\mathbf{V}]^{n''j''m''}_{n'j'm'}-ia^{*}_{n'j'm'}a_{n''j''m''}\exp\left(i\frac{E_{n'j'}-E_{n''j''}}{\hbar}t\right)[\mathbf{M},\mathbf{V}]^{n'j'm'}_{n''j''m''}=$$
$$-i\left\{a^{*}_{n''j''m''}a_{n'j'm'}\exp\left(i\frac{E_{n''j''}-E_{n'j'}}{\hbar}t\right)-a^{*}_{n'j'm'}a_{n''j''m''}\exp\left(i\frac{E_{n'j'}-E_{n''j''}}{\hbar}t\right)\right\}[\mathbf{M},\mathbf{V}]^{n''j''m''}_{n'j'm'}. \quad (2B12)$$

Because

$$a^{*}_{n''j''m''}a_{n'j'm'}\exp\left(i\frac{E_{n''j''}-E_{n'j'}}{\hbar}t\right)-a^{*}_{n'j'm'}a_{n''j''m''}\exp\left(i\frac{E_{n'j'}-E_{n''j''}}{\hbar}t\right)=2i\,\mathrm{Im}\,a^{*}_{n''j''m''}a_{n'j'm'}\exp\left(i\frac{E_{n''j''}-E_{n'j'}}{\hbar}t\right)$$

is an imaginary number, the value of (2B12) is always real and $[\mathbf{M},\mathbf{V}]^{n''j''m''}_{n'j'm'}$ is real too. Note that the diagonal term in this matrix is null: $[\mathbf{M},\mathbf{V}]^{n'j'm'}_{n'j'm'}=0$, *i.e.*, also real. This demonstrates that the torque (2B11) in the classical equation of motion (28) is always a real number.

Appendix 2C: Properties of M, U, V and their Commutators

The expanded matrix **M** (labeled by three indexes) is obtained by combining the smaller matrixes (labelled by two indexes) for different values of m' given by Eq. (31) in the following way:

$$M^{n''j''m''}_{n'j'm'}(R)=\delta_{m'm''}M^{n''j''}_{n'j'}(R). \quad (2C1)$$

By this construction, and according to the definition of Eq. (22), the entire matrix **M** is symmetric, $M^{n''j''m''}_{n'j'm'}=M^{n'j'm'}_{n''j''m''}$, and is diagonal in m': $M^{n''j''m''}_{n'j'm'}=0$ if $m''\neq m'$.

Similarly, the expanded matrixes **U** and **V** (labeled by three indexes) are obtained by combining the smaller matrixes (labelled by one index) for different values of $(n\,j)$ given by Eqs. (24a-b). Namely:

$$U^{n''j''m''}_{n'j'm'}=\delta_{n'j',n''j''}U^{m''}_{m'}\quad\text{and}\quad V^{n''j''m''}_{n'j'm'}=\delta_{n'j',n''j''}V^{m''}_{m'}. \quad (2C2)$$

So, the matrixes **U** and **V** are diagonal in $(n\,j)$. Their elements are zero if $n'' \neq n'$ or $j'' \neq j'$. Consider $m'' = m' + 1$. In this case, due to the first term in Eq. (24a), we obtain

$$U^{n''j''m'+1}_{n'j'm'} = \delta_{n'j',n''j''} \frac{1}{2} \sqrt{j'(j'+1) - m'(m'+1)} \,. \tag{2C3}$$

Here we replaced m'' by $m' + 1$, including the expression

$$\sqrt{j'(j'+1) - m''(m''-1)} = \sqrt{j'(j'+1) - (m'+1)m'} \,. \tag{2C4}$$

Now consider $m'' = m' - 1$. In this case, due to the second term in Eq. (24a), we obtain

$$U^{n''j''m'}_{n'j'm'+1} = -\delta_{n'j',n''j''} \frac{1}{2} \sqrt{j'(j'+1) - m'(m'+1)} \,. \tag{2C5}$$

Here we deliberately used $m' + 1$ and m' as lower and upper indexes, respectively. Comparing Eqs. (C3) and (C5) we conclude that:

$$U^{n''j''m'}_{n'j'm'+1} = -U^{n''j''m'+1}_{n'j'm'} = U^{n'j'm'+1}_{n''j''m'} \tag{2C6}$$

Since $U^{n''j''m''}_{n'j'm'} = 0$ if $m'' \neq m' \pm 1$ (according to the definition of Eq. (24a) and by construction) we also obtain from Eq. (C6) that:

$$U^{n''j''m''}_{n'j'm'} = -U^{n'j'm'}_{n''j''m''} \,. \tag{2C7}$$

Thus, matrix **U** is anti-symmetric.

Similar considerations apply to the matrix **V**, but it appears to be symmetric:

$$V^{n''j''m''}_{n'j'm'} = V^{n'j'm'}_{n''j''m''} \,. \tag{2C8}$$

The commutator of **M** and **U** is by definition:

$$\left[\mathbf{M}, \mathbf{U}\right]^{n''j''m''}_{n'j'm'} = \sum_{n'''j'''m'''} M^{n'''j'''m'''}_{n'j'm'} U^{n''j''m''}_{n'''j'''m'''} - U^{n'''j'''m'''}_{n'j'm'} M^{n''j''m''}_{n'''j'''m'''} \,. \tag{2C9}$$

Consider the first term in this expression. Using Eq. (24a) we obtain:

$$\sum_{n'''j'''m'''} M^{n'''j'''m'''}_{n'j'm'} U^{n''j''m''}_{n'''j'''m'''}$$

$$= \sum_{m'''} \frac{1}{2} M^{n''j''m'''}_{n'j'm'} \left[\delta_{m''',m''-1} \sqrt{j''(j''+1) - m''(m''-1)} - \delta_{m''',m''+1} \sqrt{j''(j''+1) - m''(m''+1)} \right] =$$

$$= \frac{1}{2} \left[M^{n''j''m''-1}_{n'j'm'} \sqrt{j''(j''+1) - m''(m''-1)} - M^{n''j''m''+1}_{n'j'm'} \sqrt{j''(j''+1) - m''(m''+1)} \right].$$

(2C10)

And similar expression for the second term in Eq. (C9):

$$\sum_{n'''j'''m'''} U^{n'''j'''m'''}_{n'j'm'} M^{n''j''m''}_{n'''j'''m'''} = \sum_{m'''} U^{n'j'm'''}_{n'j'm'} M^{n''j''m''}_{n'j'm'''} =$$

$$\sum_{m'''} \frac{1}{2} \left[M^{n'j'm''}_{n''j''m'''} \delta_{m',m'''-1} \sqrt{j'(j'+1) - m'''(m'''-1)} - M^{n'j'm''}_{n''j''m'''} \delta_{m',m'''+1} \sqrt{j'(j'+1) - m'''(m'''+1)} \right] =$$

$$= \frac{1}{2} \left[M^{n'j'm'+1}_{n''j''m''} \sqrt{j'(j'+1) - m'(m'+1)} - M^{n'j'm'-1}_{n''j''m''} \sqrt{j'(j'+1) - m'(m'-1)} \right].$$

(2C11)

Or,

$$-\sum_{n'''j'''m'''} U^{n'j'm'}_{n'''j'''m'''} M^{n'''j'''m'''}_{n''j''m''} = \frac{1}{2} \left[M^{n'j'm'-1}_{n''j''m''} \sqrt{j'(j'+1) - m'(m'-1)} - M^{n'j'm'+1}_{n''j''m''} \sqrt{j'(j'+1) - m'(m'+1)} \right].$$

(2C12)

Finally, substitution of expressions (C10) and (C12) into (C8) gives:

$$\left[\mathbf{M}, \mathbf{U}\right]^{n''j''m''}_{n'j'm'} = \frac{1}{2} \left[M^{n'j'm'}_{n''j''m''+1} \sqrt{j''\left(j''+1\right) - m''\left(m''+1\right)} - M^{n'j'm'}_{n''j''m''-1} \sqrt{j''\left(j''+1\right) - m''\left(m''-1\right)} \right]$$
$$+ \frac{1}{2} \left[M^{n'j'm'+1}_{n''j''m''} \sqrt{j'(j'+1) - m'(m'+1)} - M^{n'j'm'-1}_{n''j''m''} \sqrt{j'(j'+1) - m'(m'-1)} \right].$$

(2C13)

All similar considerations apply to the commutator of **M** and **V**:

$$\sum_{n'''j'''m'''} M^{n'''j'''m'''}_{n'j'm'} V^{n''j''m''}_{n'''j'''m'''} = \frac{1}{2} \left[M^{n'j'm'}_{n''j''m''+1} \sqrt{j''\left(j''+1\right) - m''\left(m''+1\right)} + M^{n'j'm'}_{n''j''m''-1} \sqrt{j''\left(j''+1\right) - m''\left(m''-1\right)} \right]$$

, (2C14)

and

$$\sum_{n'''j'''m'''} V^{n'j'm'}_{n'''j'''m'''} M^{n'''j'''m'''}_{n''j''m''} = \sum_{m'''} V^{n'j'm'}_{n'j'm'''} M^{n'j'm'''}_{n''j''m''}$$
$$= \frac{1}{2}\left[M^{n'j'm'+1}_{n''j''m''} \sqrt{j(' j'+1) - m'(m'+1)} + M^{n'j'm'-1}_{n''j''m''} \sqrt{j'(j'+1) - m'(m'-1)} \right],$$

(2C15)

and finally

$$[\mathbf{M},\mathbf{V}]^{n''j''m''}_{n'j'm'} = \frac{1}{2}\left[M^{n'j'm'}_{n''j''m''+1} \sqrt{j''(j''+1) - m''(m''+1)} + M^{n'j'm'}_{n''j''m''-1} \sqrt{j''(j''+1) - m''(m''-1)} \right]$$
$$- \frac{1}{2}\left[M^{n'j'm'+1}_{n''j''m''} \sqrt{j(' j'+1) - m'(m'+1)} + M^{n'j'm'-1}_{n''j''m''} \sqrt{j'(j'+1) - m'(m'-1)} \right].$$

(2C16)

Several properties of the commutator matrixes are worth noting. Namely:

$$[\mathbf{M},\mathbf{U}]^{n''j''m''}_{n'j'm'} = [\mathbf{M},\mathbf{U}]^{n'j'm'}_{n''j''m''}$$

(2C17)

which means that this matrix is symmetric. This is easy to prove using the properties (2C1) and (2C7) as follows:

$$[\mathbf{M},\mathbf{U}]^{n''j''m''}_{n'j'm'} = \sum_{n'''j'''m'''} M^{n'''j'''m'''}_{n'j'm'} U^{n''j''m''}_{n'''j'''m'''} - U^{n'''j'''m'''}_{n'j'm'} M^{n''j''m''}_{n'''j'''m'''} = \sum_{n'''j'''m'''} U^{n'j'm'}_{n'''j'''m'''} M^{n'''j'''m'''}_{n''j''m''} - M^{n'j'm'}_{n'''j'''m'''} U^{n'''j'''m'''}_{n''j''m''}$$
$$= \sum_{n'''j'''m'''} M^{n'''j'''m'''}_{n''j''m''} U^{n'j'm'}_{n'''j'''m'''} - U^{n'''j'''m'''}_{n''j''m''} M^{n'j'm'}_{n'''j'''m'''} = [\mathbf{M},\mathbf{U}]^{n'j'm'}_{n''j''m''}$$

In contrast, the commutator

$$[\mathbf{M},\mathbf{V}]^{n''j''m''}_{n'j'm'} = -[\mathbf{M},\mathbf{V}]^{n'j'm'}_{n''j''m''}$$

(2C18)

is an anti-symmetric matrix. This is shown using Eq. (2C8) as follows:

$$[\mathbf{M},\mathbf{V}]^{n''j''m''}_{n'j'm'} = \sum_{n'''j'''m'''} M^{n'''j'''m'''}_{n'j'm'} V^{n''j''m''}_{n'''j'''m'''} - V^{n'''j'''m'''}_{n'j'm'} M^{n''j''m''}_{n'''j'''m'''} = \sum_{n'''j'''m'''} M^{n'j'm'}_{n'''j'''m'''} V^{n'''j'''m'''}_{n''j''m''} - V^{n'j'm'}_{n'''j'''m'''} M^{n'''j'''m'''}_{n''j''m''}$$
$$= -\left(\sum_{n'''j'''m'''} M^{n'''j'''m'''}_{n''j''m''} V^{n'j'm'}_{n'''j'''m'''} - V^{n'''j'''m'''}_{n''j''m''} M^{n'j'm'}_{n'''j'''m'''} \right) = -[\mathbf{M},\mathbf{V}]^{n'j'm'}_{n''j''m''}$$

BIBLIOGRAPHY for Chapter 2

1. C. Ceccarelli, A. Castets, E. Caux, D. Hollenbach, L. Loinard, S. Molinari, and A. G. G. M. Tielens, *Astronomy & Astrophysics* **355**, 1129 (2000).

2. C. Codella, B. Leoch, C. Ceccarelli, J. Cernicharo, E. Caux, A. Lorenzani, S. Viti, P. Hily-Blant, B. Parise, S. Maret, B. Nisini, P. Caselli, S. Cabrit, L. Pagani, M. Benedettini, A. Boogert, F. Gueth, G. Melnick, D. Neufeld, S. Pacheco, M. Salez, K. Schuster, A. Bacmann, A. Baudry, T. Bell, E. A. Bergin, G. Blake, S. Bottinelli, A. Castets, C. Comito, A. Coutens, N. Crimier, C. Dominik, K. Demyk, P. Encrenaz, E. Falgarone, A. Fuente, M. Gerin, P. Goldsmith, F. Helmich, P. Hennebelle, T. Henning, E. Herbst, T. Jacq, C. Kahane, M. Kama, A. Klotz, W. Langer, D. Lis, S. Lord, J. Pearson, T. Phillips, P. Saraceno, P. Schilke, X. Tielens, F. van der Tak, M. van der Wiel, C. Vastel, V. Wakelam, A. Walters, F. Wyrowski, H. Yorke, C. Borys, Y. Delorme, C. Kramer, B. Larsson, I. Mehdi, V. Ossenkopf, and J. Stutzki, *Astronomy & Astrophysics* **518**, L112 (2010).

3. T. G. Phillips, E. A. Bergin, D. C. Lis, D. A. Neufeld, T. A. Bell, S. Wang, N. R. Crockett, M. Emprechtinger, G.A. Blake, E. Caux, C. Ceccarelli, J. Cernicharo, C. Comito, F. Daniel, M.-L. Dubernet, P. Encrenaz, M. Gerin, T. F. Giesen, J. R. Goicoechea, P. F. Goldsmith, E. Herbst, C. Joblin, D. Johnstone, W. D. Langer, W.D. LatterS. D. Lord, S. Maret, P. G. Martin, G. J. Melnick, K. M. Menten, P. Morris, H. S. P. Müller, J. A. Murphy, V. Ossenkopf, J. C. Pearson, M. Pérault, R. Plume, S.-L. Qin, P. Schilke, S. Schlemmer, J. Stutzki, N. Trappe, F. F. S. van der Tak, C. Vastel, H. W. Yorke, S. Yu, J. Zmuidzinas, A. Boogert, R. Güsten, P. Hartogh, N. Honingh, A. Karpov, J. Kooi, J.-M. Krieg and R. Schieder, *Astronomy and Astrophysics* **518**, L109 (2010).

4. C. Vastel, C. Ceccarelli, E. Caux, A. Coutens, J. Cernicharo, S. Bottinelli, K. Demyk, A. Faure, L. Wiesenfeld, Y. Scribano, A. Bacmann, P. Hily-Blant, S. Maret, A. Walters, E. A. Bergin, G. A. Blake, A. Castets, N. Crimier, C. Dominik, P. Encrenaz, M. Gérin, P. Hennebelle, C. Kahane, A. Klotz, G. Melnick, L. Pagani, B. Parise, P. Schilke, V. Wakelam, A. Baudry, T. Bell, M. Benedettini, A. Boogert, S. Cabrit, P. Caselli, C. Codella, C. Comito, E. Falgarone, A. Fuente, P. F. Goldsmith, F. Helmich, T. Henning, E. Herbst, T. Jacq, M. Kama, W. Langer, B. Lefloch, D. Lis, S. Lord, A. Lorenzani, D. Neufeld, B. Nisini, S. Pacheco, J. Pearson, T. Phillips, M. Salez, P. Saraceno, K. Schuster, X. Tielens, F. van der Tak, M. H. D. van der Wiel, S. Viti, F. Wyrowski, H. Yorke, P. Cais, J. M. Krieg, M. Olberg and L. Ravera, *Astronomy & Astrophysics* **521**, L31 (2010).

5. S. Wang, E. A. Bergin, N. R. Crockett, P. F. Goldsmith, D. C. Lis, J. C. Pearson, P. Schilke, T. A. Bell, C. Comito, G. A. Blake, E. Caux, C. Ceccarelli, J. Cernicharo, F. Daniel, M.-L. Dubernet , M. Emprechtinger, P. Encrenaz, M. Gerin, T. F. Giesen, J. R. Goicoechea, H. Gupta, E. Herbst , C. Joblin , D. Johnstone , W. D. Langer, W. B. Latter , S. D. Lord, S. Maret, P. G. Martin, G. J. Melnick, K. M. Menten, P. Morris, H. S. P. Müller, J. A. Murphy, D. A. Neufeld, V. Ossenkopf,

M. Pérault, T. G. Phillips, R. Plume, S.-L. Qin, S. Schlemmer, J. Stutzki, N. Trappe, F. F. S. van der Tak, C. Vastel, H. W. Yorke, S. Yu and J. Zmuidzinas, *Astronomy and Astrophysics* **527**, A95+ (2011).

6. E. Caux, C. Kahane, A. Castets, A. Coutens, C. Ceccarelli, A. Bacmann, S. Bisschop, S. Bottinelli, C. Comito, F. P. Helmich, B. Leoch, B. Parise, P. Schilke, A. G. G. M. Tielens, E. van Dishoeck, C. Vastel, V. Wakelam, and A. Walters, *Astronomy & Astrophysics* **532**, A23 (2011).

7. E. F. van Dishoeck, L. E. Kristensen, A. O. Benz, E. A. Bergin, P. Caselli, J. Cernicharo, F. Herpin, M. R. Hogerheijde, D. Johnstone, R. Liseau, B. Nisini, R. Shipman, M. Tafalla, F. van der Tak, F. Wyrowski, Y. Aikawa, R. Bachiller, A. Baudry, M. Benedettini, P. Bjerkeli, G. A. Blake, S. Bontemps, J. Braine, C. Brinch, S. Bruderer, L. Chavarria, C. Codella, F. Daniel, T. de Graauw, E. Deul, A. M. di Giorgio, C. Dominik, S. D. Doty, M. L. Dubernet, P. Encrenaz, H. Feuchtgruber, M. Fich, W. Frieswijk, A. Fuente, T. Giannini, J. R. Goicoechea, F. P. Helmich, G. J. Herczeg, T. Jacq, J. K. Jorgensen, A. Karska, M. J. Kaufman, E. Keto, B. Larsson, B. Leoch, D. Lis, M. Marseille, C. McCoey, G. Melnick, D. Neufeld, M. Olberg, L. Pagani, O. Pani_c, B. Parise, J. C. Pearson, R. Plume, C. Risacher, D. Salter, J. Santiago-Garcffa, P. Saraceno, P. Stöauber, T. A. van Kempen, R. Visser, S. Viti, M.Walmsley, S. F.Wamper, and U. A. Yildiz, *Pub. Astron. Soc. Pacific* **123**, 138 (2011).

8. P. Hartogh, D. C. Lis, D. Bockelée-Morvan, M. de Val-Borro, N. Biver, M. Küppers, M. Emprechtinger, E. A. Bergin, J. Crovisier, M. Rengel, R. Moreno, S. Szutowicz and G. A. Blake, *Nature* **478**, 218 (2011).

9. D. Bockelée-Morvan, N. Biver, B. Swinyard, M. de Val-Borro, J. Crovisier, P. Hartogh, D. C. Lis, R. Moreno, S. Szutowicz, E. Lellouch, M. Emprechtinger, G. A. Blake, R. Courtin, C. Jarchow, M. Kidger, M. Küppers, M. Rengel, G. R. Davis, T. Fulton, D. Naylor, S. Sidher, H. Walker, *Astronomy and Astrophysics* **544**, L15 (2012).

10. V. Dislaire, P. Hily-Blant, A. Faure, S. Maret, A. Bacmann, and G. Pineau Des Forrets, *Astronomy and Astrophysics* **537**, A20 (2012).

11. A. Coutens, C. Vastel, E. Caux, C. Ceccarelli S. Bottinelli, L. Wiesenfeld, A. Faure, Y. Scribano and C .Kahane, *Astronomy & Astrophysics* **539,** A312 (2012).

12. A. M. Arthurs and A. Dalgarno, *Proc. R. Soc. Lond. A* **256,** 540 (1960).

13. J. M. Hutson and S. Green, MOLSCAT computer code, version 14 (1994), distributed by Collaborative Computational Project No. 6 of the Engineering and Physical Sciences Research Council (UK). http://www.theochem.ru.nl/molscat/TOC.html

14. J. Loreau, P. Zhang and A. Dalgarno, *J. Chem. Phys.* **135**, 174301(2011).

15. G. Sarma, C. Yang, A. Saha, David H. Parker, and L. Wiesenfeld, *J. Chem. Phys.*

138, 024314 (2013).

16. J. Loreau, P.Zhang and A. Dalgarno, *J. Chem. Phys.* **136**, 164305 (2012).

17. T.-G. Lee, N. Balakrishnan, R. C. Forrey, P. C. Stancil, D. R. Schultz, and G. J. Ferland, *J. Chem. Phys.* **125**, 114302 (2006).

18. J. Brudermann, C. Steinbach, U. Buck, K. Patkowski, and R. Moszynski*, J. Chem. Phys.* **117**, 11166 (2002).

19. M.-L. Dubernet, P. A. Tuckey, G. Jolicard, X. Michaut, and H. Berger Resen,*J. Chem. Phys.* **114**, 1286 (2001).

20. B. H. Yang, P. C. Stancil, N. Balakrishnan, and R. C. Forrey, *J. Chem. Phys.* **124**, 104304 (2006).

21. M.-L. Dubernet, F. Daniel, A. Grosjean, and C. Y. Lin, *Astron. & Astrophys.* **497**, 911 (2009).

22. F. Daniel, M.-L. Dubernet, F. Pacaud and A. Grosjean, *Astron. & Astrophys.* **517**, A13 (2010).

23. F. Daniel, M.-L. Dubernet, and A. Grosjean, *Astronomy & Astrophysics,* **536**, A76 (2011).

24. L. Wiesenfeld, Y. Scribano, and A. Faure, *Phys. Chem. Chem. Physics* **13**, 8230 (2011).

25. C. H. Yang, G. Sarma, D. H. Parker, J. J. ter Meulen, and L. Wiesenfeld, *J. Chem. Phys*. **134**, 20 (2011).

26. A. Faure, K. Szalewicz and L. Wiesenfeld, *J. Chem. Phys.* **135**, 24301 (2011).

27. G. D. Billing, *Chem. Phys*. **9**, 359 (1975).

28. G. D. Billing, *J. Chem. Phys***. 57**, 5241 (1972).

29. G. D. Billing, *Chem. Phys*. **107**, 39 (1986).

30. G. D. Billing, *Comp. Phys. Rep*. **1**, 237 (1984).

31. G. D. Billing, "The Quantum-Classical Theory", Oxford University Press (2002).

32. J.B. Delos, W. R. Thorson and S. K. Knudson, *Phys. Rev. A* **6**, 709 (1972).

33. A. Semenov and D. Babikov, *J. Chem. Phys.* **138**, 164110 (2013).

34. A. Semenov, M. Ivanov and D. Babikov, *J. Chem. Phys*. **139**, 74306 (2013).

35. M. Ivanov and D. Babikov, *J. Chem. Phys*. **134**, 144107 (2011).

36. M. Ivanov and D. Babikov, *J. Chem. Phys*. **134**, 174308 (2011).

37. M. Ivanov and D. Babikov, *J. Chem. Phys*. **136**, 184304 (2012).

38. M. Ivanov and D. Babikov, *PNAS.* **110**,17708–17713(2013).

39. A. Semenov and D.Babikov, *J. Phys. Chem. Lett.*, **5** (2), 278 (2014)

40. D. J. Tannor, Introduction to Quantum Mechanics: A Time-dependent Perspective University Science Books, (2007).

41. R. T Pack, *J. Chem. Phys*. **60**, 633 (1974).

42. J. J. Griffin, *Group Theory and its Application to the Quantum Mechanics of Atomic Spectra*, New York: Academic Press (1959).

43. D. A. Varshalovich, A. N. Moskalev, V. K. Khersonskii, *Quantum Theory of Angular Momentum,*World Scientific, Singapore (1988).

44. F. Lique, A. Spielfiedel, M.-L. Dubernet, and N. Feautrier,*J. Chem. Phys.* **123**, 134316 (2005)**.**

45. F. Dumouchel, J. Kłos, R. Toboła, A.Bacmann, S. Maret, P.Hily-Blant, A. Faure, and F. Lique. *J. Chem. Phys.* **137**, 114306 (2012).

46. R. Z. Martinez, J. L. Domenech, D. Bermejo, F. Thibault, J.-P. Bouanich, and C. Boulet, *J. Chem. Phys.* **119**, 10563 (2003).

CHAPTER 3. MIXED QUANTUM/CLASSICAL CALCULATIONS OF TOTAL AND DIFFERENTIAL ELASTIC AND ROTATIONALLY INELASTIC SCATTERING CROSS SECTIONS FOR LIGHT AND HEAVY REDUCED MASSES IN A BROAD RANGE OF COLLISION ENERGIES

3.1 Mixed Quantum/Classical Theory for Rotationally Inelastic Scattering

The main goal of this part of the work is to explore the limits of validity of the mixed quantum/classical theory (MQCT) for rotationally-inelastic atom + molecule scattering [1].

Foundations of MQCT were laid by Gert Billing in 1980's, but the main body of his work belongs to *vibrationally-inelastic* scattering and development of the method in which vibration of the molecule is treated quantum mechanically, while its rotation and the scattering process are treated classically [2,3]. In recent years such methods have been revived and improved [4-6], and applied to complicated problems, such as recombination reactions [7-9].

For description of *rotationally-inelastic* scattering Billing proposed another version of MQCT, in which the rotational motion is treated quantum mechanically, and only the translational motion is treated classically [2,3]. He applied this theory to one system, He + H_2, at two relatively high values of scattering energies: E = 0.1 and 0.9 eV [10]. Those ground-breaking results were included into a review paper [2] and a book [3] but, surprisingly, remained the only example of MQCT treatment of rotationally-inelastic scattering.

Detailed analysis of Billing's work reveals that he employed only an approximate version of MQCT, known as coupled-states (CS) approximation, where transitions between different *m*-states, within the same rotational energy level *j*, are entirely neglected. We also found that the equations Billing used are applicable only to the simplest case, when the initial rotational wave function has cylindrical symmetry (*i.e.*, describes pure eigenstate). Such equations can't be employed to handle a general case, when the initial rotational wave function corresponds to an arbitrary superposition of eigenstates (a wave packet).

In a recent theory paper [1] we presented a general and fully-coupled version of MQCT for rotationally-inelastic scattering, formulated in both laboratory-fixed and body-fixed (BF) reference frames, and tested it using a model system. Here we present results of calculations for two real systems, Na + N_2 and He + H_2, carried out in a broad range of scattering energies. For our best knowledge this is the first systematic and rigorous study of MQCT for rotationally-inelastic scattering. Our choice of the benchmark systems was based on the following arguments. First of all, accurate full-quantum coupled-channel (CC) results for these systems are available from recent literature [11-13], as well as potential energy surfaces (PES) used in those studies. Second, all atoms in Na + N_2 are relatively heavy, while they are light in the He + H_2. This gives opportunity to observe the effect of reduced mass of the scattering partners – an important aspect for the method where scattering is treated classically. Third, the rotational quanta in heavy N_2 and light H_2 are very different, spanning the range of transition energies ΔE from ~12 cm^{-1} to ~813 cm^{-1}, which allows testing applicability of second Delos criterion [14]. Namely, based on this criterion, it is sometimes argued that any mixed quantum/classical method

is accurate only when the classical collision energy E is much larger than the energy change ΔE associated with quantum transition between the internal states [14]. However, for MQCT treatment of rotationally inelastic scattering this criterion has never been tested and our results indicate that MQCT remains accurate in a broader range than predicted by this criterion.

Another aspect that, to our best knowledge, has not been addressed before within MQCT framework is calculation of the elastic scattering cross section and the differential (over scattering angle) cross section. It is well known that classical scattering theory is deficient in these two respects. At large impact parameters and small scattering angles the classical scattering cross section diverges, due to the lack of phase information. Only at scattering angles larger than the "rainbow" angle (small impact parameters) the process of scattering is classical. Interestingly, we found a way to compute the scattering phase using MQCT, and use it to compute accurate differential cross section at small scattering angles, *i.e.*, in the quantum scattering regime when interference is important.

The chapter is organized as follows: In Sec. 3.2 we review major equations of the fully-coupled general MQCT, its simplified version, and the approximate CS version, and also present the method of computing cross sections. In Sec. 3.3 we report numeric results for the integral rotationally-inelastic scattering cross sections for two benchmark systems and compare them with full quantum CC results, as well as with complementary classical trajectory simulations, in a broad range of collision energies. Subsection 3.3.4 is devoted to elastic scattering cross sections and differential cross sections computed by MQCT. Major findings are summarized in Sec. 3.5.

3.2 Theoretical Framework

3.2.1 General and Fully-Coupled MQCT

From the computational performance point of view the most efficient formulation of MQCT is that in the BF reference frame [1]. In order to simplify notations, in this chapter we use jm and $j'm'$ to label the initial and final rotational sates of the molecule, instead of $j'm'$ and $j''m''$ used in Ref. [1], and we also use φ instead of φ' used in Ref. [1]. Rotational and vibrational motion of the diatomic molecule is described by coordinates $\mathbf{q} = (r, \gamma, \varphi)$. These are quantum degrees of freedom; their evolution is determined by wave function $\psi(r, \gamma, \varphi)$. Scattering of the quencher atom is described by spherical polar coordinates $\mathbf{Q} = (R, \Theta, \Phi)$. These are classical degrees of freedom; their evolution is determined by conjugate momenta P_R, P_Θ and P_Φ. Interaction potential does not depend on classical angles and angle φ due to symmetry, so, potential is a function of Jacobi variables $V = V(R, r, \gamma)$. Definition of these coordinates in the BF reference frame is illustrated in Fig. 2 of Ref. [1]. The MQCT equations of motion for classical variables are [1]:

$$\dot{R} = \frac{P_R}{\mu}, \tag{1}$$

$$\dot{\Theta} = \frac{P_\Theta}{\mu R^2}, \tag{2}$$

$$\dot{\Phi} = \frac{P_\Phi}{\mu R^2 \sin^2 \Theta}, \tag{3}$$

$$\dot{P}_R = -\frac{\partial \widetilde{V}(R)}{\partial R} + \frac{P_\Theta^2}{\mu R^3} + \frac{P_\Phi^2}{\mu R^3 \sin^2 \Theta}, \tag{4}$$

$$\dot{P}_{\Theta} = \sum_{n'j'm'} \sum_{njm} a^{*}_{n'j'm'} a_{njm} \exp\{i(E_{n'j'} - E_{nj})t/\hbar\} \left[\mathbf{M},\mathbf{U}\right]^{n'j'm'}_{njm} + \frac{P_{\Phi}^{2}\cos\Theta}{\mu R^{2}\sin^{3}\Theta}, \tag{5}$$

$$\dot{P}_{\Phi} = -i \sum_{n'j'm'} \sum_{njm} a^{*}_{n'j'm'} a_{njm} \exp\{i(E_{n'j'} - E_{nj})t/\hbar\} \sin\Theta \left[\mathbf{M},\mathbf{V}\right]^{n'j'm'}_{njm}. \tag{6}$$

Here we introduced the mean-field potential $\tilde{V}(R) = \left\langle \psi(r,\gamma,\phi) \middle| V(R,r,\gamma) \middle| \psi(r,\gamma,\phi) \right\rangle$ and the commutators $\left[\mathbf{M},\mathbf{U}\right]$ and $\left[\mathbf{M},\mathbf{V}\right]$ of the matrices introduced below. Expansion of wave function over the basis set of ro-vibrational eigenstates with time-dependent coefficients $a_{njm}(t)$ and substitution into Schrodinger equation leads to [1]:

$$i\hbar \frac{\partial a_{njm}}{\partial t} = \sum_{n'j'} a_{n'j'm} \exp\{i(E_{nj} - E_{n'j'})t/\hbar\} \; M^{n'j'}_{nj}(R) - i\hbar \sum_{m'} a_{njm'} W^{m'}_{m}. \tag{7}$$

Structure of these coupled equations is such that the state-to-state transition matrix $M^{n'j'}_{nj}$, introduced for every m as

$$M^{n'j'}_{nj}(R) = A_{j'm,jm} \left\langle \phi_{nj}(r) P_{jm}(\cos\gamma) \middle| V(R,r,\gamma) \middle| \phi_{n'j'}(r) P_{j'm}(\cos\gamma) \right\rangle, \tag{8}$$

describes only transitions from (nj) to $(n'j')$, within the same value of m. In contrast, the matrix $W^{m'}_{m}$, introduced for every j, describes transitions between m and $m' = m \pm 1$, within the same energy level (nj). Elements of this matrix,

$$W^{m'}_{m} = U^{m'}_{m} \, \dot{\Theta} + i \, (\sin\Theta V^{m'}_{m} - m' \cos\Theta \delta_{m,m'}) \, \dot{\Phi}, \tag{9}$$

are expressed through elements of two simpler matrices [1]:

$$U^{m'}_{m} = \frac{1}{2}\left[\sqrt{j(j+1) - m'(m'-1)}\,\delta_{m,m'-1} - \sqrt{j(j+1) - m'(m'+1)}\,\delta_{m,m'+1}\right] \tag{10}$$

and

$$V_m^{m'} = \frac{1}{2}\left[\sqrt{j(j+1)-m'(m'-1)}\,\delta_{m,m'-1} + \sqrt{j(j+1)-m'(m'+1)}\,\delta_{m,m'+1}\right]. \qquad (11)$$

Matrices **M**, **U** and **V** are all real-valued, sparse and time-independent (should be computed only once). Note that elements of the matrix **M** and the mean-field potential $\widetilde{V}$ depend on *R* only.

3.2.2 A Simplified Version of MQCT

If the initial rotational wave function exhibits cylindrical symmetry around the atom-molecule axis (*i.e.*, corresponds to rotational eigenstate, rather than rotational wave packet) the classical trajectory remains in the same plane during the course of entire collision event. In such cases we can restrict our calculations to one plane, for example, $\Theta = \pi/2$ and set $P_\Theta = 0$. Equations (2-5) simplify to

$$\dot{\Theta} = 0\,, \qquad (2')$$

$$\dot{\Phi} = \frac{P_\Phi}{\mu R^2}\,, \qquad (3')$$

$$\dot{P}_R = -\frac{\partial \tilde{V}(R)}{\partial R} + \frac{P_\Phi^2}{\mu R^3}\,, \qquad (4')$$

$$\dot{P}_\Theta = 0\,. \qquad (5')$$

Clearly, equations (2′) and (5′) are obsolete and there is no need to propagate them. Equation (6) becomes

$$\dot{P}_\Phi = -i\sum_{n'j'm'}\sum_{njm} a^*_{n'j'm'}a_{njm}\exp\{i(E_{n'j'}-E_{nj})t/\hbar\}\left[\mathbf{M},\mathbf{V}\right]^{n'j'm'}_{njm}. \qquad (6')$$

3.2.3 An Approximate CS Version of MQCT

The coupled-states (CS) approximation is easily formulated within MQCT by setting $W_m^{m'} = 0$ in Eq. (7) for wave function evolution. It becomes:

$$i\hbar \frac{\partial a_{nj}}{\partial t} = \sum_{n'j'} a_{n'j'} \exp\{i(E_{nj} - E_{n'j'})t/\hbar\}\, M_{nj}^{n'j'}(R), \qquad (7'')$$

and should be solved for every value of *m* separately. Classical equations of motion (5-6) also simplify significantly, because the commutator matrices vanish: $[\mathbf{M},\mathbf{U}] = 0$ and $[\mathbf{M},\mathbf{V}] = 0$. If this CS-approximation is used together with simplification of Sec. II.B (cylindrical symmetry), then Eqs. (5,6) convert into:

$$\dot{P}_\Theta = 0\,, \qquad (5'')$$

$$\dot{P}_\Phi = 0\,. \qquad (6'')$$

Again, these equations are trivial and there is no need to propagate them.

In this form the MQCT becomes rather simple and similar to the method of Billing [2], with only one distinction. Billing has chosen to restrict his trajectories to $\Phi = 0$ plane and set $P_\Phi = 0$. In principle this is equivalent, but in practice our version is better, because fixing $\Theta = \pi/2$ permits to avoid singularity at $\Theta = 0$, which affects equations (3), (4) and (5). Equation (1) remains in its original form in any version of MQCT.

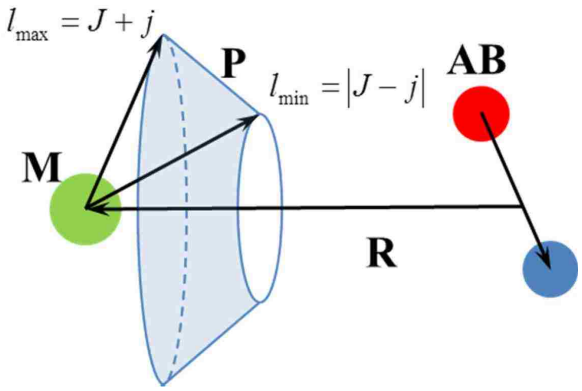

Figure 1. Sampling of initial conditions for atom-molecule collision in space-fixed (SF) reference frame. Shaded area on the surface of the sphere of radius $|\mathbf{P}|$ determines all possible directions of classical vector $\mathbf{P}$. Different directions correspond to different values of impact parameter, with largest impact parameter obtained in the case of $l_{\max}$ and smallest impact parameter in the case of $l_{\min}$.

3.2.4 Sampling of Initial Conditions

The exact quantum expressions for (integral) scattering cross section are [15]:

$$\sigma_{j\to j'} = \frac{1}{(2j+1)} \sum_{m=-j}^{j} \sum_{m'=-j'}^{j'} \sigma_{jm\to j'm'} \ , \tag{8}$$

$$\sigma_{jm\to j'm'} = \frac{\pi}{k_j^2} \sum_{J=0}^{\infty} \sum_{l=|J-j|}^{J+j} \sum_{l'=|J-j'|}^{J+j'} (2J+1) \left| \delta_{jj'}\delta_{ll'}\delta_{mm'} - S^J_{jj',ll',mm'} \right|^2 \ , \tag{9}$$

where $S^J_{jj',ll',mm'}$ is the scattering matrix in BF system . MQCT treatment is most straightforward for *inelastic* scattering channels, when $\delta_{jj'} = 0$ and the probability amplitudes $a_{j'm'}$ from Eq. (7) at the final moment of time can be used to compute

transition probability as $\left|\delta_{jj'}\delta_{ll'}\delta_{mm'} - S^{J}_{jj',ll',mm'}\right|^2 = \left|a_{j'm'}\right|^2$. Transformation to MQCT treatment is achieved by making the total angular momentum J a continuous (classical) variable, while keeping the values of j and m integer and quantized. This imposes certain restrictions onto the values of continuous classical variable $\ell = |\mathbf{l}|$, namely: $|J - j| \le \ell \le J + j$. Figure 1 explains sampling of initial conditions, including illustration of the allowed values for classical vector of orbital angular momentum $\mathbf{l}$, related closely to the collision impact parameter *b* through $\ell(\ell+1) = k^2 b^2$ and $\mathbf{k} = \mathbf{P}/\hbar$. Absolute value of the initial momentum $\mathbf{P}^2 = P_R^2 + (P_\Phi^2/\sin^2\Theta + P_\Theta^2)/R^2$ is determined by incident energy of collision, while various possible *directions* of $\mathbf{P}$ in space correspond to different values of $\ell = |\mathbf{l}|$, where $\mathbf{J} = \mathbf{l} + \mathbf{j}$. In a general situation (without cylindrical symmetry, $\Theta \neq const$) the range of possible directions of $\mathbf{P}$ is represented by a segment of spherical surface illustrated in Fig. 1. If the simplified version of theory (cylindrical symmetry) is appropriate, this range shrinks to a one-dimensional section of this surface by $\Theta = \pi/2$ plane.

Following these arguments, the triple sum in quantum Eq. (9) is replaced by classical integral:

$$\sigma_{jm\to j'm'} = \frac{\pi}{k_j^2}\int_0^\infty (2J+1)dJ \int_{\mathbf{J}=\mathbf{l}+\mathbf{j}} \left|a_{j'm'}\right|^2 d\,\mathbf{l}\,. \tag{10}$$

In practice, this integral is estimated using the Monte-Carlo sampling technique. First, the value of J is sampled randomly and uniformly between zero and $J_{\max} = k\hbar b_{\max}$. Next, for a chosen initial j, the value of ℓ is sampled randomly and uniformly in the range

$|J-j| \le \ell \le J+j$, and is used to define the initial classical momentum $P_\Phi = \hbar\sqrt{\ell(\ell+1)}$ in Eq. (3-5). This procedure is repeated for *N* classical trajectories (labeled by i) and the inelastic scattering integral cross section is determined numerically as:

$$\sigma_{jm\to j'm'} = \frac{\pi}{k^2}\frac{J_{\max}}{N}\sum_i (2J^{(i)}+1)\left|a^{(i)}_{j'm'}\right|^2. \qquad (11)$$

Quantum equation (8) is used in MQCT without modifications; it describes sum over the final values m' and average over the initial values m.

It may also be instructive to consider the trivial case of $j=0$, when $J=\ell$ and the range of possible directions of vector **P** shrinks to a single point. In this case no sampling over ℓ is needed at all, the integral in Eq. (10) becomes one-dimensional, $\sigma_{jm\to j'm'} = \pi/k_j^2 \int (2J+1)\left|a_{j'm'}\right|^2 dJ$, which can be easily evaluated using any structured grid method (no Monte-Carlo needed). However, when $j>0$, it is advantageous to use the two-dimensional Monte-Carlo sampling over J and ℓ, for faster convergence.

3.2.5 Phases and Elastic Scattering Cross Sections

For the elastic scattering channel the phase of the corresponding diagonal element of scattering matrix S in Eq. (9) becomes important, but there are two contributions to the overall phase. One contribution is phase of rotational (or ro-vibrational, internal) wave function. It is contained in the complex-valued transition amplitude a_{jm}, which is accurately computed within MQCT by propagating Eq. (7). We will denote this phase δ_j and compute it as $\delta_j = \arg a_{jm}$. Second contribution is phase shift of the partial wave,

δ_ℓ, which is missing in MQCT because scattering is treated classically. However, classical treatment of scattering provides classical deflection function $\Theta(\ell)$. The deflection function can't really be used directly to compute cross section at angles smaller than the rainbow angle (see for example, Ref. [16]), but we found it possible to recover the value of δ_ℓ from the $\Theta(\ell)$ dependence. Namely, in the semi-classical treatments of scattering it is assumed that deflection is determined by the total phase shift (see Appendix A):

$$\Theta(\ell) = \frac{d\left(\delta_\ell + \delta_j(\ell)\right)}{d\ell}. \tag{12}$$

If the $\Theta(\ell)$ and $\delta_j(\ell)$ dependencies are both known, this expression can be used as a differential equation for $\delta_\ell(\ell)$ with boundary condition $\delta_\ell(\infty) = 0$, which corresponds to no scattering at large impact parameters. Solving this equation numerically allows reconstructing the $\delta_\ell(\ell)$ dependence and expressing transition probability in Eq. (9) for the elastic channel as: $\left|\delta_{jj'}\delta_{ll'}\delta_{mm'} - S^J_{jj',ll',mm'}\right|^2 = \left|1 - a_{jm}\exp(i\delta_\ell)\right|^2$. Finally, this probability is averaged over *N* trajectories using the Monte-Carlo method, just like in Eq. (11):

$$\sigma_{jm\to jm} = \frac{\pi}{k^2}\frac{J_{\max}}{N}\sum_i (2J^{(i)}+1)\left|1 - a^{(i)}_{jm}\exp(i\delta_\ell)\right|^2, \tag{13}$$

where the phase shift is computed from

$$\delta_\ell = -\int_\infty^\ell \Theta(s)ds - \delta_j(\ell), \tag{14}$$

where *s* is a dummy variable introduced for integration over ℓ.

3.2.6 Differential Cross Sections

For simplicity of presentation, we will focus on differential cross section for the elastic channel ($j \to j$), but the procedure and conclusions are general and applicable to inelastic scattering as well. Scattering amplitude

$$f_{jm\to jm}(\theta) = \frac{i}{k}\sum_{l=0}^{\infty}(2l+1)(1-S^{J}_{jj,ll,mm})P_l(\cos\theta) \tag{15}$$

is used to compute the differential cross section (averaged over the initial states *m*):

$$\frac{d\sigma_{j\to j}(\theta)}{d\Omega} = \frac{1}{(2j+1)}\sum_{m'=-j}^{j}\sum_{m=-j}^{j}\left|f_{jm\to jm'}(\theta)\right|^2 . \tag{16}$$

In MQCT, the sum of Eq. (15) is replaced by a semi-classical integral over continuous distribution of ℓ , and the phase δ_ℓ is introduced (as above), which leads to:

$$f_{jm\to jm}(\theta) = \frac{i}{k}\int_0^{\infty}(2\ell+1)(1-a_{jm}\exp(i\delta_\ell))P_l(\cos\theta)d\ell . \tag{17}$$

Using Monte-Carlo approach this integral is computed as:

$$f_{jm\to jm}(\theta) = \frac{i}{k_j}\frac{J_{\max}}{N}\sum_{i}(2\ell+1)(1-a^{(i)}_{jm}\exp(i\delta_\ell))P_l(\cos\theta) . \tag{18}$$

3.2.7 Numerical Approach

As in full-quantum calculations, we used the potential energy surface expanded in terms of Legendre polynomials: $V(R,r,\gamma) = \sum V_k(R,r)P_k(\cos\gamma)$. For Na + N_2(v=0) system we included all even terms up to $k=8$ and used the *R*-dependent expansion coefficients V_k from Ref. [10]. For He + H_2 system we included terms up to $k=8$. Equations (1-7) were solved numerically altogether using Runge-Kutta method of 4th

order. The initial molecule-quencher separation was close to $R = 28.2a_0$ in the case of Na + N_2 system and about $R = 24a_0$ in the case of He + H_2. Classical impact parameter, determined by convergence studies, was $b_{\max} = 24\,a_0$ in the case of Na + N_2 and $b_{\max} = 15\,a_0$ in the case of He + H_2. The magnitude of classical momentum is chosen as prescribed by the symmetrized average-velocity approach [4], which takes into account microscopic reversibility of state-to-state transitions. In calculations with small j the rotational basis set included all eigenstates up to $j = 14$ in the case of Na + N_2 system and up to $j = 12$ in the case of He + H_2. In one case, quenching of $j = 22$ in He + H_2, we included all rotational states up to $j = 32$ and two vibrational states $v = 0$ and $v = 1$.

An important practical aspect is how to generate $P_l(\cos\theta)$ when ℓ is a continuous variable. In principle, one should replace a set of Legendre polynomials by their continuous analogue -- the hyper-geometric function [17]. A FORTRAN routine from the package POLPAK for computation of the hyper-geometric functions worked fine for $\ell < 25$ but crashed at larger values of ℓ. We also tried to compute hyper-geometric function using MATLAB, but at large ℓ this was inconveniently slow. As an alternative, we tried to round the value of ℓ to the closest integer and use polynomials, since they are fast to compute at any values of ℓ. For the moderate values of ℓ the difference between the two methods was small, and we finally adopted this approach.

In general, using a standard expansion of the PES in Jacobi coordinates $V(R,r,\gamma) = \sum V_k(R,r)P_k(\cos\gamma)$, one can evaluate matrix elements $M_{nj}^{n'j'}(R)$ as follows:

$$M_{n\,j}^{n'j'}(R)=\left\langle \phi_{nj}(r)\middle|V_k(R,r)\middle|\phi_{n'j'}(r)\right\rangle \begin{pmatrix} j' & k & j \\ -m & 0 & m \end{pmatrix}\begin{pmatrix} j' & k & j \\ 0 & 0 & 0 \end{pmatrix}\sqrt{(2j'+1)(2j+1)}(-1)^m . \qquad (19)$$

A FORTRAN routine W3JS [18] was used to compute Wigner 3j symbols. Note that matrix elements $\left\langle \phi_{nj}(r)\middle|V_k(R,r)\middle|\phi_{n'j'}(r)\right\rangle$ do not depend on m. Their values were computed on a grid of 400 points for along $2.0<R<25.0\,a_0$. In order to calculate derivatives in Eq. (4) a cubic spline was prepared for each such matrix element. Vibrational wave functions $\phi_{nj}(r)$ were calculated as prescribed in Ref. [4] using package ARPACK on an optimized grid of 128 points along $0.2<r<5.0a_0$.

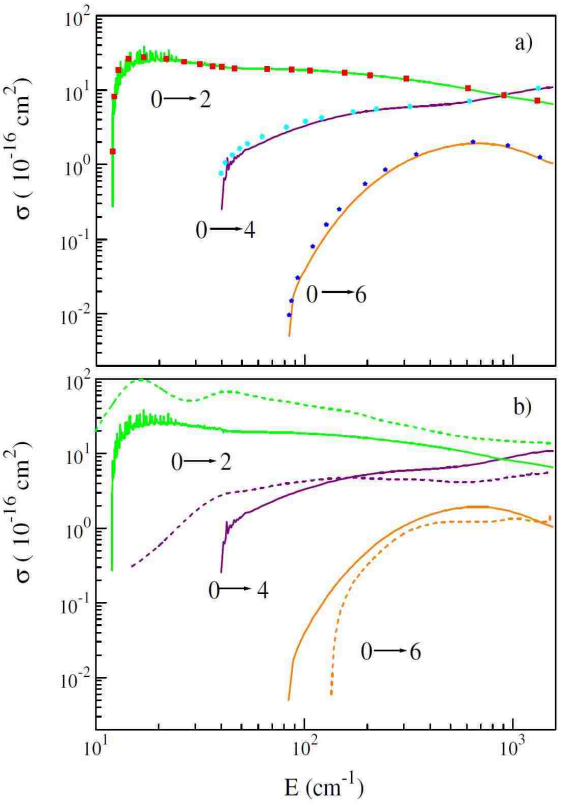

Figure 2. Energy dependence of excitation cross sections for Na + N_2 system in the ground rotational state $j=0$. Three allowed rotationally-inelastic channels are shown for transitions into the excited states $j=2$, $j=4$ and $j=6$. MQCT results are shown by symbols in frame (a), while classical trajectory results are shown by dashed lines in frame (b). Full-quantum data from Ref. [11] are shown by solid lines in both frames for comparison.

3.3 Numerical Results

3.3.1 Tests of Fully Coupled MQCT Method

Inelastic scattering calculations for Na + N_2 system were carried out in order to test accuracy of MQCT method in the case of reasonably heavy atomic masses. Full quantum CC results for this system are available from Ref. [11]. Figure 2(a) summarizes data for excitation of the

ground rotational state $j = 0$. Excitation cross sections were computed in a broad range of collision energies, $10 \le E \le 1100\ \mathrm{cm}^{-1}$. Recall that for homo-nuclear N_2 in the initial state $j = 0$ the allowed transitions are: $0 \to 2,\ 0 \to 4,\ 0 \to 6$, *etc*. Analysis of Fig. 2(a) indicates that all these excitation processes are accurately reproduced by MQCT in a broad range of collision energies, and through four-orders-of-magnitude range of cross section values. Interestingly, as energy E increases, the value of cross section for $0 \to 2$ slightly decreases, while it increases slightly for $0 \to 4$, and it passes through a pronounced maximum in the case of $0 \to 6$ transition. All these major features are reproduced well by MQCT (see Fig. 2(a)). But even less significant features, such as slight ondulations of the $\sigma(E)$ dependencies, are also reproduced by MQCT. Importantly, even the channel thresholds are correctly predicted.

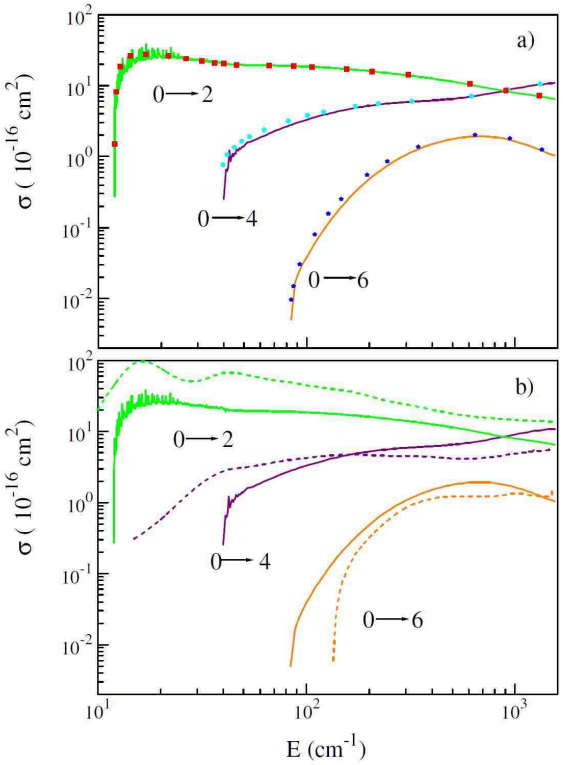

Figure 3. Energy dependence of inelastic cross sections for Na + N_2 system in the excited rotational state $j = 5$. Two excitation channels correspond to allowed transitions into $j = 7$ and $j = 9$. Two quenching channels correspond to allowed transitions into $j = 1$ and $j = 3$. MQCT results are shown by symbols in frame (a), while classical trajectory results are shown by dashed lines in frame (b). Full-quantum data from Ref. [11] are shown by solid lines in both frames for comparison

In Fig. 3(a) we summarized results for the inelastic transition processes that originate in the excited rotational state $j = 5$, located at energy $E = 59.7\ \mathrm{cm}^{-1}$ above the

ground rotational state. In this case the allowed excitation processes are: $5\to7$, $5\to9$, *etc.*, while the allowed quenching processes are $5\to3$ and $5\to1$. In all these cases MQCT reproduced quantum results very accurately in a broad range of collision energies and through five-orders-of-magnitude range of cross section values. Again, even small oscillations of $\sigma(E)$ dependencies for the processes $5\to3$ and $5\to1$ are correctly reproduced.

Inelastic scattering calculations for He + H_2 system were carried out in order to test accuracy of MQCT method in the limit of lightest atomic masses. This example is often thought of as an essentially non-classical system, the worst-case scenario for, and the stringent possible test of, the mixed quantum/classical method. Full quantum benchmark data for this system are available from Refs [12,13]. Figure 4 summarizes results for quenching or two lowest excited rotational states, the processes $2\to0$ and $4\to2$, at collision energies in the range $1 \le E \le 10000\ \mathrm{cm}^{-1}$. We see that, indeed, in this light system the deviations of MQCT from quantum benchmark are more noticeable, and occur in a somewhat larger range of collision energies, compared to more classical Na + N_2 system. However, the values of these deviations are still relatively small. For example, at $E = 25\ \mathrm{cm}^{-1}$ the deviations are only 15% and 25% for processes $2\to0$ and $4\to2$,

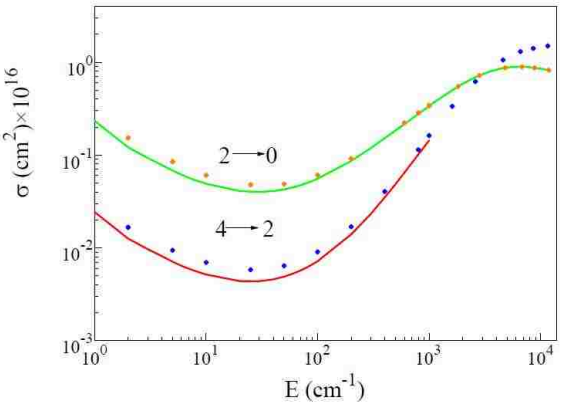

Figure 4. Energy dependence of quenching cross sections for He + H_2 system. Two transitions are shown, one from $j=4$ into $j=2$, and the other from $j=2$ into $j=0$. MQCT results are shown by symbols. Full-quantum data from Ref. [12], where available, are shown by solid lines for comparison.

respectively. Interestingly, at even lower collision energies, the accuracy of MQCT remains about the same, it does not worsen significantly even at $E = 2\ \mathrm{cm}^{-1}$. But, as energy increases, MQCT results merge monotonically with full quantum results. For $2 \rightarrow 0$ excellent agreement is found above $E = 100\ \mathrm{cm}^{-1}$. For $4 \rightarrow 2$ the agreement improves significantly when collision energy approaches $E = 200\ \mathrm{cm}^{-1}$. Note that the dependence of cross section in Fig. 4 goes through minimum and maximum and those features are reproduced well by MQCT. Thus, MQCT is applicable even to this light and highly non-classical system, and it remains reasonably accurate even at low collision energies.

3.3.2 Test of CS-Approximation

Figure 5 shows the same data as in Fig. 2(a), but obtained using the approximate CS-version of MQCT, derived in Sec. II.C. Overall, the quality of these data is very reasonable. Deviations from the full quantum benchmark are observed for all three processes: $0 \rightarrow 2$, $0 \rightarrow 4$ and $0 \rightarrow 6$, but typically they do not exceed 25% (somewhat more near the channel threshold). Overall, one should admit that the fully-coupled version of MQCT is in much better and more detailed agreement with exact quantum results (compare Fig. 5 *vs.* Fig. 2(a)).

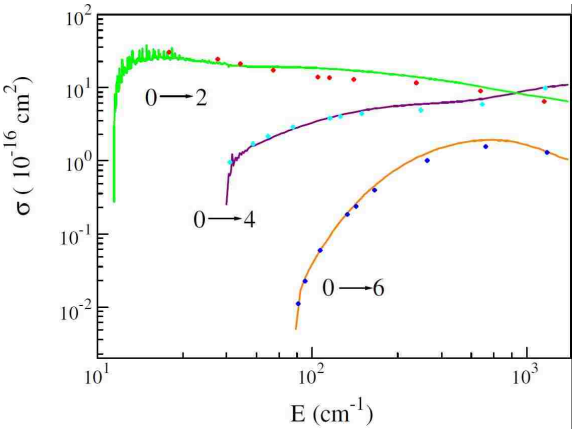

Figure 5. Same as in Fig. 2(a), but using an approximate CS-version of MQCT.

For Na + N_2 system the CS-version of theory was faster, but not by much, just by a factor of ×3. For more complicated systems (triatomic + atom, or triatomic + diatomic) the computational speed up may be more substantial, but one should keep in mind that accuracy of CS approximation is non-uniform. For example, we found that for $0 \rightarrow 2$ transition at lower collision energies the value of CS cross section is larger, while at higher collision energies it is smaller, compared to the fully-coupled MQCT data and quantum benchmark data. The switching occurs near $E = 50\ \mathrm{cm}^{-1}$, which produces an artificial oscillation of the CS cross section, quite different from the benchmark data. In contract, the fully-coupled version of MQCT gives detailed and uniformly reliable description through the entire range of collision energies.

Full quantum calculations are very demanding at high collision energies and for highly excited rotational states. At such conditions the exact CC-method is almost never used, and the CS-approximation is usually adopted. For He + H_2 system at high levels of rotational excitations such (full quantum but approximate) CS results are available from literature [12,13] and web site of one of the authors [19]. We carried out similar calculations using MQCT. Figure 6 presents our MQCT-CS results for rotational quenching of $j = 22$ in comparison with quantum benchmark data. The dominant process is $22 \rightarrow 20$, and the corresponding transition

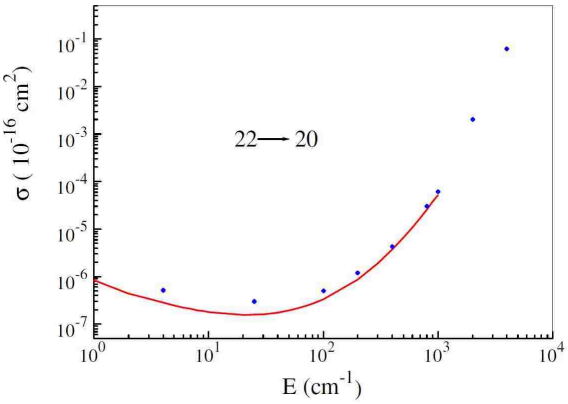

Figure 6. Energy dependence of cross section for quenching of $j = 22$ into $j = 20$ in He + H_2 system. CS-version of MQCT is used (symbols) and compared to full-quantum CS method (solid line) from Ref. [13], where available.

energy is huge, $\Delta E = 2{,}967.6\ \mathrm{cm}^{-1}$. Results of MQCT are accurate at collision energies above $350\ \mathrm{cm}^{-1}$. For this transition, no quantum CS results are available above $E = 1{,}000\ \mathrm{cm}^{-1}$, but we easily computed few points up to $E = 10{,}000\ \mathrm{cm}^{-1}$. Moreover, it should be noted that in the He + H_2 system in $j = 22$ and at this collision energy the *vibrational* state-to-state transitions become important and should also be included, in addition to rotational state-to-state transitions. The calculations we did were such ro-vibrational calculations. However, in present work we prefer to restrict discussion to *rotational* transitions only.

3.3.3 Criterion of Accuracy

According to Delos criterion for atom-atom collisions [14], and by analogy with our earlier findings from MQCT calculations of *vibrational* quenching [5], the MQCT method is expected to be more accurate when the energy change ΔE associated with quantum state-to-state transition is small. Similar conclusion can be deduced from our data for Na + N_2 system presented in Fig. 2(a). For example, the transition $0 \to 2$, which has smallest value of $\Delta E = 11.9\ \mathrm{cm}^{-1}$, is reproduced by MQCT particularly well. For this process the deviation from full quantum result is observed only near the channel threshold, and this discrepancy vanishes quickly as collision energy is increased. If we look at transitions $0 \to 4$ and $0 \to 6$, where the values of energy quantum rise to $\Delta E = 39.8\ \mathrm{cm}^{-1}$ and $83.5\ \mathrm{cm}^{-1}$, respectively, we start seeing some deviations from full quantum results slightly further from the channel threshold. This behavior is understood and even expected near the channel threshold, where $E \approx \Delta E$. Roughly, results of Fig.

2(a) show that MQCT becomes very accurate at collision energies $E > 2\Delta E$. But even in the energy range $\Delta E < E < 2\Delta E$ the results of MQCT are quite reasonable.

Most interestingly, we found that MQCT is particularly accurate for the rotationally excited states. This makes sense, since excited states are more classical. For example, the four sets of data presented in Fig. 3(a) still correspond to relatively large values of ΔE: $35.8\,\mathrm{cm}^{-1}$, $51.7\,\mathrm{cm}^{-1}$, $55.7\,\mathrm{cm}^{-1}$ and $119.4\,\mathrm{cm}^{-1}$. Nevertheless, the excitation cross sections computed by MQCT for $5 \to 7$ and $5 \to 9$ are very accurate (even at the channel threshold, $E = \Delta E$), and the quenching cross for $5 \to 3$ and $5 \to 1$ are accurate at *any* energies we considered, down to $E = 5\,\mathrm{cm}^{-1}$ (because there is no threshold for quenching). No any obvious criterion can be formulated or needed here. MQCT data are simply almost as accurate as the full quantum data.

In the case of He + H_2 system the state-to-state transition energies ΔE are large: $384\,\mathrm{cm}^{-1}$ and $813\,\mathrm{cm}^{-1}$ for the processes $2 \to 0$ and $4 \to 2$, respectively. From one side, this explains why deviations of MQCT results from quantum benchmark are larger in this system than in Na + N_2. But from another side, this also means that the criterion for validity of MQCT may be less stringent. Namely, for He + H_2, MQCT is rather accurate at collision energies above $E = 100\,\mathrm{cm}^{-1}$ for transition $2 \to 0$

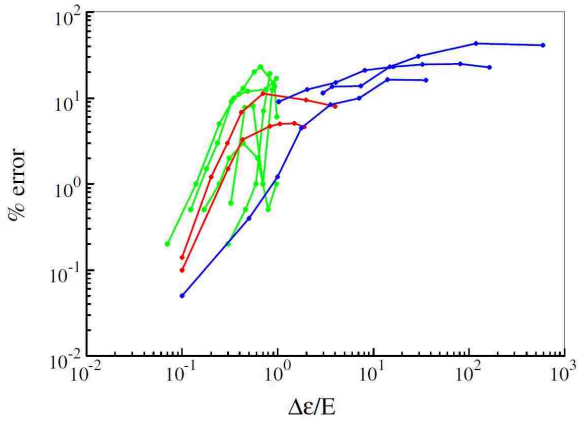

Figure 7. Percent error of MQCT method for all calculations of this chapter. The value of error correlates with the ratio of transition energy to scattering energy. Quenching processes for Na + N_2 are plotted using red solid lines, while excitation processes are plotted using green lines . The data for He + H_2 are blue.

, and above $E = 200$ cm^{-1} for transition $4 \rightarrow 2$. Roughly, this corresponds to $E > \Delta E / 4$. And again, this is for the lower, most quantum mechanical states. Excited rotational states are more classical. For transition $22 \rightarrow 20$ we have $\Delta E = 2{,}967.6$ cm^{-1} and MQCT is accurate above 350 cm^{-1} which, in fact, is much better than $\Delta E / 4$ (this is closer to $\Delta E / 8$). This example gives clear indications where the range of applicability and the predictive power of MQCT approach are.

For all integral cross sections discussed above and both benchmark systems studied here we computed relative errors of MQCT method (% of the full-quantum result) and collected them all together in Fig. 7. Only a few outlying points were not included into this graph. Both excitation and quenching processes were included. Horizontal axis gives the ratio $\Delta E / E$, and the range of its values is rather large, $10^{-2} < \Delta E / E < 10^{3}$. More accurate corner of this graph corresponds to low ΔE and high E, while less accurate corner corresponds to high ΔE and low E. Despite some spread of points present in these data, the plot in Fig. 7 shows clear correlation between accuracy and the value of $\Delta E / E$. We found that the data for He + H_2 and for Na + H_2 complement each other, following very similar trends. Thus, we conclude that this dependence is rather general and we recommend using this picture to estimate the error of MQCT method before applying it to new systems. For example, consider rotational quenching from the first excited rotational state to the ground state in H_2O, NH_3 and in $HCOOCH_3$ (methyl formate, small organic molecule important for astrophysics). Rotational quanta in these molecules are $\Delta E =$ 18.6 cm^{-1}, 16.3 cm^{-1} and 0.41 cm^{-1} respectively. Neither of these systems was studied using MQCT, but we plan doing such calculations in the

future. From Fig. 7 one can expect that at energy of collision $E = 100\,\mathrm{cm}^{-1}$ an error of MQCT should be no more than 2% for H_2O and NH_3, and no more than 0.5% for methyl formate. At higher collision energies the errors are expected to be smaller. When MQCT results for these new molecules become available, they can be added to this graph, in order to improve predictive capability of the method.

One can also notice that the full quantum data for Na + N_2 system (from Ref. [11], used here as a benchmark) exhibit some resonances just above threshold, especially in the case of $0 \to 2$ transition shown in Fig. 2(a). It is an interesting general question whether MQCT can be used to treat these purely quantum features of cross section. For example, classical trajectory capture is analog of quantum scattering resonance, and we saw that at energies close to threshold many trajectories were captured in the interaction region. Analysis of these trajectories may give some useful information about scattering resonances, but we decided to postpone exploration of this topic to future work, and do that for a different system, with fewer isolated resonances. Here, we restricted our analysis to non-resonant cross sections only, and simply zeroed all trajectories that exhibited resonant behavior.

3.3.4 Differential Cross Sections

Figure 8 presents differential cross section for the elastic scattering channel of Na + N_2 ($j = 0$) system at relatively low collision energy $E = 50\ \mathrm{cm}^{-1}$. Figures 8(a) and 8(b) show the same for higher collision energies, $E = 100\ \mathrm{cm}^{-1}$ and $E = 700\ \mathrm{cm}^{-1}$, respectively. In all these cases the full quantum benchmark data are available from Ref. [11]. We see that dependence of cross section on scattering angle is highly oscillatory (non-classical) but MQCT method reproduces every single oscillation of this dependence very accurately. To our best knowledge this is the first application of mixed quantum/classical theory to calculation of differential scattering cross section.

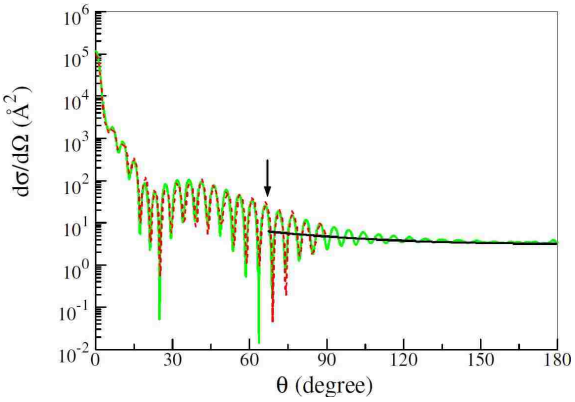

Figure 8. Differential cross section for the elastic scattering channel of Na + N_2($j = 0$) system at collision energy $E = 50\ \mathrm{cm}^{-1}$. MQCT results are shown by red dashed line. Full-quantum data from Ref. [11] are shown by green solid line for comparison. Classical rainbow angle is indicated by arrow. A pseudo-classical (see text) cross section is shown by black solid line in the range of angles beyond the rainbow.

Recall that classical scattering theory works only at large scattering angles, beyond the classical rainbow angle (small impact parameters, backscattering). At the rainbow angle the classical scattering cross section diverges (see Appendix A), and it is poorly defined at angles smaller than the rainbow angle (large impact parameters). Various versions of semi-classical treatment of scattering exist, capable of removing singularity at the rainbow angle [18], and expanding the range of validity of the classical scattering theory slightly into the quantum scattering regime (vicinity of the rainbow angle). No semi-classical treatment of scattering is expected to work at small scattering angles, in the quantum scattering regime.

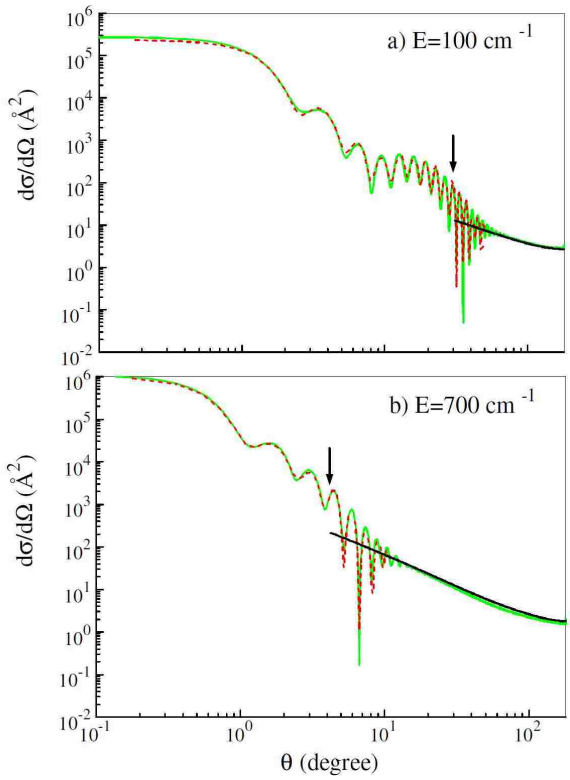

Figure 9. Differential cross section for the elastic scattering channel of Na + N_2($j=0$) system at collision energies $E=100\text{cm}^{-1}$ and $700\,\text{cm}^{-1}$ in frames (a) and (b), respectively. MQCT results are shown by red dashed line. Full-quantum data from Ref. [11] are shown by green solid line for comparison. Classical rainbow angle is indicated by arrow. A pseudo-classical (see text) cross section is shown by black solid line in the range of angles beyond the rainbow. This figure emphasizes small scattering angles (note logarithmic scale in the horizontal axis).

It is encouraging that MQCT is very accurate at small scattering angles, in the quantum scattering regime. Note that in Fig. 9 logarithmic scale is applied to the horizontal axis, in order to emphasize the small scattering angle part of cross section dependence. The

rainbow angle is also marked in Figs. 8-9, and we see that in its vicinity the dependence of MQCT cross section is regular, just as quantum benchmark data, and is very accurate.

Unexpectedly, we found that differential cross sections computed by MQCT exhibit unphysical behavior at *large* scattering angles (not shown here), in the classical scattering regime, where even a simple classical mechanics is expected to work! This behavior is not yet completely understood, and most probably is due to some technical issue, but we found a temporary fix for it. In Figs. 8-9 we also plotted a pseudo-classical cross section, obtained simply by differentiating the classical deflection function $\Theta(\ell)$ derived from MQCT calculations (see Eq. (A15) in Appendix A). At scattering angles larger than rainbow angle such cross section is well defined and comparison with full quantum data shows that it sets up accurately the asymptotic trend (see Figs. 8-9). Thus, at large scattering angles one can easily switch to this pseudo-classical cross section.

Finally, the integral elastic scattering cross section, obtained by integrating the differential cross sections discussed above, is presented in Fig. 10. The agreement with quantum benchmark data is rather good, down to collision energies $E = 50\ \mathrm{cm}^{-1}$ or so. At even lower energies we start seeing deviations, but the overall trend of dependence is captured well by MQCT: it goes through maxima and minima several times and these

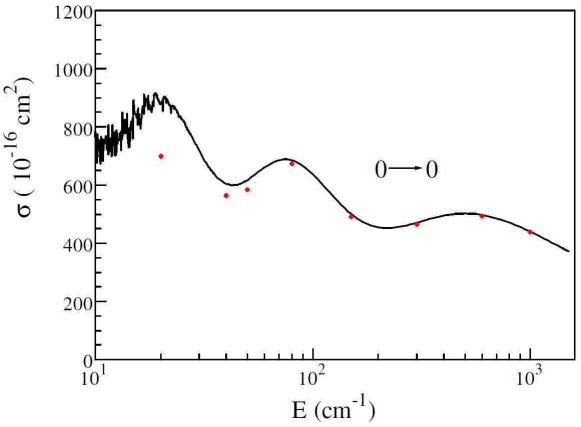

Figure 10. Energy dependence of integral cross section for the elastic scattering channel of Na + N_2 system in the ground rotational state $j = 0$. MQCT results are shown by symbols. Full-quantum data from Ref. [11] are shown by solid line for comparison.

quantum oscillations are all reproduced. Recall that classical scattering theory can't predict the elastic scattering cross section, because the maximum impact parameter is impossible to define rigorously. In contrast, MQCT uses phase information (just as full quantum method) which avoids the problem. In the range of collision energies where MQCT is accurate it can be used to predict the elastic scattering cross sections reliably.

As discussed in the theory section above, calculations of differential cross sections and elastic scattering cross sections use phase information and quantum interference. These phenomena are very sensitive to errors and when MQCT becomes less accurate overall (at lower scattering energies) these cross sections suffer the most. For example, we also calculated the differential cross section at low collision energy $E = 15\ \mathrm{cm}^{-1}$ (in the region of scattering resonances), but in this case we found larger discrepancies between MQCT results and the full quantum benchmark data. So, at very low collision energies one should be careful using MQCT to predict differential cross sections or the elastic scattering cross sections.

3.3.5 Purely Classical Trajectories

In MQCT formalism of rotational quenching the classical mechanics is used only for description of scattering, while quantum mechanics is used for rotational state-to-state transitions. Why not to get rid of the quantum mechanics entirely, and treat all degrees of freedom classically? This was attempted in the past and, in particular, it was shown that for the He + H_2 system at collision energies close to $E = 1000\ \mathrm{cm}^{-1}$ the value of cross section for transition $2 \to 0$ is underestimated by an order of magnitude or so [12]. At collision energies lower than $E = 1000\ \mathrm{cm}^{-1}$ it is expected to be even worse.

Performance of the classical trajectory method for He + H_2 system improves only when the collision energy reaches $E = 4000\ \mathrm{cm}^{-1}$ or so, but the agreement with full quantum method still remains rather rough [12].

For heavy atoms classical mechanics is expected to work somewhat better, and we decided to run the purely classical trajectory simulations for Na + N_2 system. We tried several known methods of the final state analysis but we found that, when applied to various needed state-to-state cross sections in a broad range of energies, neither method works consistently better than others (although, we did not attempt the Gaussian binning [20]). Results presented below were obtained using the prescription of Bowman [21], which worked slightly better. Furthermore, since N_2 is symmetric, we had to introduce an *ad hoc* factor of ×1/2 (which would be hard to justify in the case of different isotopes). Only then the results of classical trajectory simulations for Na + N_2 fall into the right order of magnitude range.

Our classical results are summarized in Figs. 2(b) and 3(b). They can be conveniently compared to the full quantum benchmark data and to our MQCT results as well, shown in Figs. 2(a) and 3(a). We see that although not all, but many $\sigma(E)$ dependencies are similar. However, the quality of agreement is qualitative (at best), rather than quantitative. Some of the classical state-to-state cross sections are higher while others are lower compared to quantum results. Large deviations by a factor of 2 to 4 are typical. Moreover, near the channel thresholds (for excitation processes) and at lower collision energy (for quenching processes) the deviations are particularly large and often reach two orders of magnitude. In terms of accuracy for rotational state-to-state transition cross sections, the classical trajectory method is not even close to MQCT.

Finally, we found that, from the computational standpoint, the classical trajectory simulations are even *more* demanding than MQCT. This seems surprising first, but has simple explanation. It appears that at low collision energy, when the value of transition cross section is small (and many cross sections in Figs. 2(a) and 3(a) are very small) one needs to sample literally hundreds of thousands of classical trajectories, in order to find that rare event (special collision arrangement) that makes non-zero contribution to cross section. In addition to everything said above, the classical cross sections at low energies are typically poorly converged and very expensive computationally. MQCT is the method of choice. It is almost as accurate as the full quantum method, and is computationally cheaper than the classical trajectory method.

3.4 Conclusions for Chapter 3

In this chapter we carried out the first extensive benchmarking of accuracy of the MQCT treatment of rotationally inelastic scattering processes. Two molecular systems were considered, one of which contained all light atoms (He + H_2), while the other one contained all reasonably heavy atoms (Na + N_2). A broad range of classical collision energies was explored: $1 < E < 10{,}000\ \text{cm}^{-1}$. The values of quantum state-to-state transition energies studied here also covered a wide range: $10 < \Delta E < 3{,}000\ \text{cm}^{-1}$. The amount of initial rotational excitation varied from $j = 0$ to $j = 22$. The values of obtained scattering cross sections varied from 10^{-23} to $10^{-13}\ \text{cm}^2$. In addition to energy dependence of integral cross sections, we also looked at the differential (over scattering angle) cross sections. Both elastic and inelastic scattering channels were studied. In all

these cases a detailed comparison of MQCT against the full quantum method was carried out.

We found that in many of these cases the results of MQCT are hard to distinguish from the full quantum (CC) results. We also saw that in some unfavorable cases (low mass, low collision energy and large transition energy) MQCT becomes less accurate, but we never really saw it failing. For example, in the worst-case situations the values of MQCT cross sections were overestimated by 25% or so, which still can be characterized as a semi-quantitative agreement. And this is in the lightest possible system, He + H_2. In all other chemically relevant molecular systems, at thermal collision energies, MQCT is expected to be much more accurate than this.

As a rule of thumb, one can probably use the following criterion for rotational quenching processes: *When* $E > \Delta E / 4$ *the results of MQCT become accurate to within few percent, compared to full quantum data.* Most importantly is that MQCT results approach the full quantum results monotonically, in a predictable way. Above $E = \Delta E / 4$ they are very accurate, below $E = \Delta E / 4$ they start deviating from the full quantum data, but this deviation does not increase rapidly. We saw that MQCT always produces reasonable data, even in unfavorable situations, when it is less accurate.

It seems that this method represents a useful alternative to the full quantum methods in situations when collisional energies are high, rotational excitation is significant, masses are large and the densities of states are large (small state-to-state transition energies). These cases are hard to handle numerically using the full quantum methods, such as CC, but MQCT becomes very accurate in these same situations. Of course, larger number of states involved in expansion of wave function will make any

calculations more demanding, both CC and MQCT, but overall the mixed quantum/classical approach is much more affordable.

The computational cost of MQCT is really low. For small values of *j* in both systems considered here, only about 1 minute on single processor was spent per energy point. It is still hard to say how this will grow with size of the molecule, since we only start applying this theory to triatomic + atom systems. However, we want to stress that MQCT calculations for different trajectories are entirely independent (sampling over ℓ), which makes this method intrinsically and embarrassingly parallel. One can easily spread MQCT trajectories onto hundreds of processors with zero communication overlap. With this capability, MQCT calculations are expected to be affordable even for polyatomic molecules, with large number of states included, and even without the CS-approximation involved. It is also important to note that propagation of MWCT trajectories is computationally faster at higher collision energies, which makes this method appealing for high temperature applications.

One more appealing aspect of MQCT methodology is that it offers a unique time-dependent insight into mechanism of the process. Indeed, although the standard time-independent scattering theory provides the transition matrix and characterizes completely the outcome of molecular collision, it tells us nothing about the course of the process, how wave function of the system evolves in time and space. In our MQCT approach and other related time-dependent methods [22-23] one can monitor how state populations $a^2_{j'm'}$ change as collision progresses along the trajectory. Do the populations change monotonically and describe direct transitions, or there is a temporary population transfer

to some intermediate states? And what is the time scale of the process? These opportunities will be explored in the near future.

Appendix 3A: Semi-classical Theory of Scattering

Figure 11 represents example of classical scattering function $\Theta(\ell)$ and deflection function $\Theta(\ell)$ obtained from MQCT calculations for Na + N_2 ($j = 0$) system at collision energy $E = 50\ \mathrm{cm}^{-1}$. The "rainbow" angle is observed at 67.5 deg. At scattering angles larger than rainbow angle only one branch of the $\Theta(\ell)$ dependence contributes to the differential cross section and the scattering is classical (small values of ℓ, small impact parameters). At angles smaller than rainbow angle several branches contribute (three in Fig. 11), producing interference. So, small scattering angles correspond to quantum scattering regime (large values of ℓ, large impact parameters).

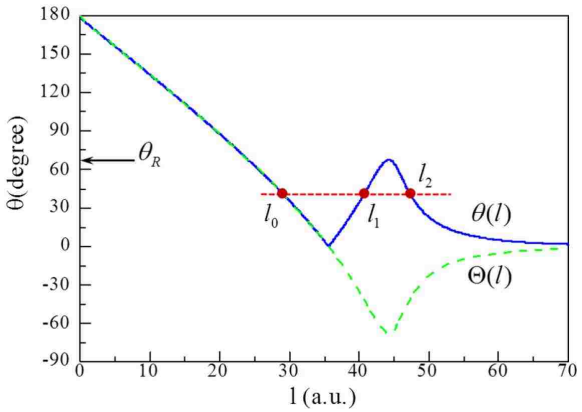

Figure 11. Pseudo-classical deflection and scattering functions from MQCT calculations. Scattering function $\theta(\ell)$ is always positive (solid line), while deflection function $\Theta(\ell)$ is always smooth (dashed line). Classical rainbow angle is indicated. At angles below this value three branches of scattering function contribute and interfere (quantum scattering regime). At angles above this value only one branch contributes and scattering is classical.

When $(l+1/2)\sin\theta >> 1$ it is usual to approximate Legendre polynomials in Eq. (17) by the following expression [16]:

$$P_l(\cos\theta) \approx -\frac{i}{\sqrt{2\pi\, l \sin\theta}}\left[\exp\left\{i\left(\left(l+\frac{1}{2}\right)\theta+\frac{\pi}{4}\right)\right\}-\exp\left\{i\left(-\left(l+\frac{1}{2}\right)\theta-\frac{\pi}{4}\right)\right\}\right]. \qquad (3A1)$$

Also, as explained in Sec. 3.2.4, the elastic element of transition matrix is $1-a(l)\exp\{i\delta_l\}=1-|a(l)|\exp\{i(\delta_j+\delta_l)\}$, where, in order to simplify notations, we omitted subscripts in $a(l)$. Using these expressions the integral of Eq. (17), we can split it onto three terms:

$$f(\theta)=\frac{1}{2k}\int_0^\infty\frac{(2l+1)|a(l)|}{\sqrt{2\pi l\sin\theta}}\exp\left\{i\left(\delta_l+\delta_j-\left(l+\frac{1}{2}\right)\theta-\frac{\pi}{4}\right)\right\}dl$$
$$-\frac{1}{2k}\int_0^\infty\frac{(2l+1)|a(l)|}{\sqrt{2\pi l\sin\theta}}\exp\left\{i\left(\delta_l+\delta_j+\left(l+\frac{1}{2}\right)\theta+\frac{\pi}{4}\right)\right\}dl \qquad (3A2)$$
$$+\frac{1}{2ik}\int_0^\infty(2l+1)P_l(\cos\theta)dl.$$

The last term is equal to zero and does not affect the differential cross section. The first two terms are estimated using the stationary phase approximation. Namely, the main contribution to the first integral is given by small ℓ (repulsive short range interaction) where the phase reaches a local maximum [16]. In other words

$$\frac{d}{dl}\left(\delta_l+\delta_j-\left(l+\frac{1}{2}\right)\theta-\frac{\pi}{4}\right)=0\,, \qquad (3A3)$$

which gives us the condition:

$$\frac{d\left(\delta_l+\delta_j\right)}{dl}=+\theta\,. \qquad (3A4)$$

Similar arguments for the second term in (3A2) give us:

$$\frac{d\left(\delta_l+\delta_j\right)}{dl}=-\theta\,. \qquad (3A5)$$

Combining these two expressions, we have:

$$\frac{d\left(\delta_l+\delta_j\right)}{dl}=\pm\theta=\Theta(l)\,. \qquad (3A6)$$

In semi-classical treatment $\Theta(l)$ is assumed to be the classical deflection function. This finalizes derivation of Eq. (12) used in Sec. 3.2.4.

Note that in our MQCT calculations of differential cross sections we neither use the approximation of Eq. (3A1) for $P_l(\cos\theta)$, nor we estimate $f(\theta)$ from Eq. (3A2). Instead, we use Eq. (3A6) only to recover the value of scattering phase δ_l (see Eq. 14), and then we substitute δ_l into the exact Eq. (17), without any approximations. This must be the reason why MQCT treatment works well even at small scattering angles, where the usual semi-classical theory of scattering (outlined below) does not work.

In order to continue manipulations with Eq. (3A2), for given θ we can find a stationary point l_0 (or, in the quantum regime, several such points: l_0, l_1 and l_2) and expand the argument in its vicinity using Taylor series to 2nd order. First derivative is equal to zero since l_0 is extremum. Second derivative:

$$\frac{\partial^2}{\partial l^2}\left(\delta_l+\delta_j-\left(l+\frac{1}{2}\right)\theta-\frac{\pi}{4}\right)=\frac{\partial^2}{\partial l^2}\left(\delta_l+\delta_j\right)=\frac{\partial\Theta(l)}{\partial l}, \tag{3A7}$$

where we used Eq. (12). The expansion is:

$$\begin{aligned}\delta_l+\delta_j-\left(l+\frac{1}{2}\right)\theta-\frac{\pi}{4}&\approx\delta_l(l_0)+\delta_j(l_0)-\left(l_0+\frac{1}{2}\right)\theta-\frac{\pi}{4}+\frac{\partial\Theta(l_0)}{\partial l}\frac{(l-l_0)^2}{2}=\\&=-\int_{\infty}^{l_0}\Theta(s)ds-\left(l_0+\frac{1}{2}\right)\theta-\frac{\pi}{4}+\frac{\partial\Theta(l_0)}{\partial l}\frac{(l-l_0)^2}{2},\end{aligned} \tag{3A8}$$

where we used Eq. (14). Substitution of this argument into the first integral in Eq. (A2) gives:

$$\begin{aligned}&\frac{1}{k}\int_{-\infty}^{\infty}\frac{\left(l_0+\frac{1}{2}\right)\left|a(l_0)\right|}{\sqrt{2\pi\, l_0\sin\theta}}\exp\left\{i\left(-\int_{\infty}^{l_0}\Theta(s)ds-\left(l_0+\frac{1}{2}\right)\theta-\frac{\pi}{4}+\frac{\partial\Theta(l_0)}{\partial l}\frac{(l-l_0)^2}{2}\right)\right\}dl\\&=\frac{\left(l_0+\frac{1}{2}\right)\left|a(l_0)\right|}{k\sqrt{2\pi\, l_0\sin\theta}}\exp\left\{i\left(-\int_{\infty}^{l_0}\Theta(s)ds-\left(l_0+\frac{1}{2}\right)\theta-\frac{\pi}{4}\right)\right\}\int_{-\infty}^{\infty}\exp\left\{i\left(\frac{\partial\Theta(l_0)}{\partial l}\frac{(l-l_0)^2}{2}\right)\right\}dl.\end{aligned} \tag{3A9}$$

The last factor here can be computed using Fresnel's integral:

$$\int_{-\infty}^{\infty} \exp\left\{ i \left(\frac{\partial \Theta(l_0)}{\partial l} \frac{(l-l_0)^2}{2} \right) \right\} dl = \sqrt{\frac{2\pi}{\frac{\partial \Theta(l_0)}{\partial l}}} \exp\left\{ i \frac{\pi}{4} \right\}. \tag{3A10}$$

Substitution of this result into Eq. (3A9) leads to:

$$\begin{aligned}
&\frac{\left(l_0 + \frac{1}{2}\right)|a(l_0)|}{k\sqrt{2\pi\, l_0 \sin\theta}} \exp\left\{ i \left(-\int_{\infty}^{l_0} \Theta(s) ds - \left(l_0 + \frac{1}{2}\right)\theta - \frac{\pi}{4} \right) \right\} \sqrt{\frac{2\pi}{\frac{\partial \Theta(l_0)}{\partial l}}} \exp\left\{ i \frac{\pi}{4} \right\} = \\
&= \frac{\left(l_0 + \frac{1}{2}\right)|a(l_0)|}{k\sqrt{l_0 \sin\theta \frac{\partial \Theta(l_0)}{\partial l}}} \exp\left\{ i \left(-\int_{\infty}^{l_0} \Theta(s) ds - \left(l_0 + \frac{1}{2}\right)\theta \right) \right\} \\
&= \frac{\left(\sqrt{l_0} + \frac{1}{2\sqrt{l_0}}\right)|a(l_0)|}{k\sqrt{\sin\theta \frac{\partial \Theta(l_0)}{\partial l}}} \exp\left\{ i \left(-\int_{\infty}^{l_0} \Theta(s) ds - \left(l_0 + \frac{1}{2}\right)\theta \right) \right\} \\
&\approx \frac{\sqrt{l_0}\,|a(l_0)|}{k\sqrt{\sin\theta \frac{\partial \Theta(l_0)}{\partial l}}} \exp\left\{ i \left(-\int_{\infty}^{l_0} \Theta(s) ds - \left(l_0 + \frac{1}{2}\right)\theta \right) \right\}.
\end{aligned} \tag{3A11}$$

Here we assumed that $l_0 >> 1$. This is the final result for the first integral in Eq. (3A2).

Similar considerations are applicable to the second integral in Eq. (3A2), but in the classical scattering regime (single branch of the deflection function, single extremum l_0) the second integral is always oscillatory and makes no contribution to $f(\theta)$. However, in the quantum scattering regime, each additional branch of the deflection function produces one additional extremum (l_1 and l_2 in Fig. 11). At such conditions the second integral in Eq. (3A2) gives

$$\frac{\sqrt{l_1}\,|a(l_1)|}{k\sqrt{\sin\theta\left|\frac{\partial\Theta(l_1)}{\partial l}\right|}}\exp\left\{i\left(-\int_{\infty}^{l_1}\Theta(s)ds+\left(l_1+\frac{1}{2}\right)\theta\right)\right\} \tag{A12}$$

for l_1, and similar for l_2. Combining all branches of the deflection function and using $\pm\theta=\Theta$, we finally obtain a semi-classical expression for scattering amplitude:

$$f(\theta)=\sum_q\frac{\sqrt{l_q}\,|a(l_q)|}{k\sqrt{\sin\theta\left|\frac{\partial\Theta(l_q)}{\partial l}\right|}}\exp\left\{i\left(-\int_{\infty}^{l_q}\Theta(s)ds-\left(l_q+\frac{1}{2}\right)\Theta(l_q)\right)\right\}, \tag{3A13}$$

where the sum is over *q* branches of the deflection function $\Theta(l)$ (*e.g.*, three in Fig. 11).

We tried this semi-classical method for differential cross section and found that indeed the Eq. (3A13) allows removing singularity at the rainbow point and gives correct asymptotic value of cross section at large scattering angles (as $\theta\to\pi$, backscattering, classical regime). However, it fails to reproduce quantum oscillations of cross section seen in Figs. 7 and 8. Also, it is rather inaccurate at small scattering angles and diverges at $\theta\to 0$. Overall, the standard semi-classical approach reviewed in this Appendix is inferior to the MQCT treatment proposed in this chapter, and from our point of view is not particularly useful (except Eq. (3A6), used to compute the scattering phase δ_l).

In the case of a single branch, *i.e.*, outside of the rainbow point, in the classical scattering regime, one can substitute

$$f(\theta)=\frac{\sqrt{l_0}\,|a(l_0)|}{k\sqrt{\sin\theta\,\frac{\partial\Theta(l_0)}{\partial l}}}\exp\left\{i\left(-\int_{\infty}^{l_0}\Theta(s)ds-\left(l_0+\frac{1}{2}\right)\Theta\right)\right\} \tag{3A14}$$

into Eq. (16), which yields classical expression for differential cross section:

$$\frac{d\sigma(\theta)}{d\Omega} = \frac{l_0 \left| a(l_0) \right|^2}{k^2 \sin\theta \left| \frac{\partial \Theta(l_0)}{\partial l} \right|}. \tag{3A15}$$

In the body of the chapter we called this version a pseudo-classical cross section, since the expression itself is classical, but the input data for probability $\left|a(l)\right|^2$ and the deflection function $\Theta(l)$ are obtained from MQCT calculations.

BIBLIOGRAPHY for Chapter 3

1. A. Semenov and D. Babikov, *J. Chem. Phys.* **139**, 174108 (2013).
2. G. D. Billing, *Comp. Phys. Rep.* **1**, 237 (1984).
3. G. D. Billing, "The Quantum-Classical Theory", Oxford University Press (2002).
4. M. Ivanov and D. Babikov, *J. Chem. Phys.* **134**, 144107 (2011).
5. A. Semenov, M. Ivanov and D. Babikov, *J. Chem. Phys*. **139**, 74306 (2013).
6. A. Semenov and D. Babikov, *J. Chem Phys.***138**,164110 (2013).
7. M. Ivanov and D. Babikov, *J. Chem. Phys*. **134**, 174308 (2011).
8. M. Ivanov and D. Babikov, *J. Chem. Phys.* **136**, 184304 (2012).
9. M. Ivanov and D. Babikov, *Proc. Natl. Acad. Sci*. **110**, 17708 (2013).
10. G. D. Billing, *J. Chem. Phys*. **57**, 5241 (1972).
11. J. Loreau, P. Zhang and A. Dalgarno, *J. Chem. Phys*. **135**, 174301 (2011).
12. A. Mack, T. K. Clark, R. C. Forrey, N. Balakrishnan, T.-G. Lee, and P. C. Stancil, *Phys. Rev. A* **74**, 052718 (2006).
13. N. Balakrishnan, M. Vieira, J. F. Babb, A. Dalgarno, R. C. Forrey, and S. Lepp, *Astrophysical Journal* **524**, 1122 (1999).
14. J. B. Delos, W. R. Thorson and S. K. Knudson, *Phys. Rev. A* **6**, 709 (1972).
15. P. McGuir and D. J. Kouri, *J. Chem. Phys.* **60**, 2488 (1974).
16. J. Ross,"Molecular beams", *Adv. in Chem. Phys.* **X**, (1966).
17. M. Abramowitz and I. Stegun, "Handbook of Mathematical Functions with Formulas, Graphs, and Mathematical Tables", New York: Dover (1965).
18. E. L. Degl'Innocenti,"Polarization in Spectral Lines", Springer (2006).
19. Full quantum results of R. Forrey can be found at http://physics.bk.psu.edu/sigma/index.html
20. R. Conte, B. Fu, E. Kamarchik and J. M. Bowman, *J. Chem. Phys*. **139**, 044104 (2013).
21. J. M. Bowman and S. C. Park, *J. Chem. Phys*. **77**, 5441 (1982).

22. D. E. Manolopoulos and M. H. Alexander, *J. Chem. Phys*. **97**, 2527 (1992).

23. M. H. Alexander, C. Rist and D. E. Manolopoulos, *J. Chem. Phys.* **97**, 4836 (1992).

CHAPTER 4. MIXED QUANTUM/CLASSICAL THEORY FOR INELASTIC SCATTERING OF SYMMETRIC/ASYMMETRIC-TOP-ROTOR + ATOM IN THE BODY-FIXED REFERENCE FRAME AND APPLICATION TO THE H_2O + HE AND CH_3OOCH +HE SYSTEMS

4.1 Rotationally Inelastic Scattering of Polyatomic Molecules

Quantum mechanical treatment of rotationally and vibrationally inelastic scattering remains a computationally challenging task [1-6]. This is particularly so for heavier collision partners and at higher collision energies, when the number of internal quantum states accessed by state-to-state transitions and the number of partial waves involved into scattering are both large. Thus, it is desirable to develop an alternative (or complimentary) approach that would allow circumventing the computational difficulties by employing some kind of approximation.

It is an old idea to use a classical approximation for scattering degrees of freedom (the relative motion of two collision partners), keeping quantum mechanics for the internal degrees of freedom only (rotation and/or vibration of one or both partners), and linking the two components of the problem through an effective mean-filed potential [7]. Such approach is expected to be accurate when the collision partners are heavy and when the spectrum of internal states is dense. Importantly, this is the same regime when the full-quantum calculations becomes computationally demanding. In this sense, the mixed quantum/classical approach may be considered as a method *complementary* to the full-quantum method. Namely, at low collision energies one may want to do the full-quantum scattering calculations because they are affordable and because quantum features, like scattering resonances, are important. However, at higher collision energies, when the full-

quantum calculations become unaffordable (and, in fact, unnecessary) one may want to switch to the mixed quantum/classical approach.

Although physically sound and methodologically appealing this approach has never been fully developed and properly tested, and, at some point, was basically abandoned. Recently, we took a fresh look at this problem and worked out a mixed quantum/classical theory (MQCT) for the simplest case -- collision of a diatomic molecule with an atom [8]. We extensively tested MQCT by doing calculations on several diatomic + atom systems and comparing results again the full-quantum benchmarks in a broad range of collision energies, through several orders of magnitude of cross section values, for heavy and light masses of collision partners, with low and high levels of rotational excitation [9-10]. We found that MQCT reproduces all major features of inelastic collisions, including differential cross sections, both excitation and quenching pathways, and gives reasonable results even at low collision energies. For heavier collision partners and at high collision energies MQCT results are very close to the full-quantum data. The systems studied so far include N_2 + Na [9] and H_2 + He [10]. Calculations for CO + He (heteronuclear diatomic) and for CH_3 + He (oblate symmetric top) are ongoing and will be reported elsewhere.

The next logical step is extension of MQCT onto larger and more complicated systems, like an asymmetric-top rotor + atom, and the first step in this direction has already been made [11]. Very recently, we used MQCT (formulated in the space-fixed reference frame, SF) to compute cross sections of rotational quenching in H_2O + He collisions, for several most important states of *para*- and *ortho*-water. We found that MQCT reproduces major features of state-to-state cross sections with reasonable

accuracy, which is very encouraging. However, we realized that the SF version of MQCT is inefficient numerically because it operates with a dense state-to-state transition matrix, whose elements are complex-valued [11]. Worst of all is that each such matrix element (used in the quantum part of calculations) depends on three classical variables (that change along trajectory), which makes the numerical procedure of splining very costly [11].

One goal of this chapter is to formulate MQCT for a general case of an asymmetric-top rotor + atom in the body-fixed reference frame (BF), where the elements of state-to-state transition matrix are real and depend on one variable only, while the matrix itself is sparse and dominated by the near-diagonal terms. The second goal is to apply this theory to H_2O + He system to (i) assess its accuracy and (ii) numerical performance, in comparison with the full-quantum approach.

4.2 Theory

4.2.1 General MQCT Equations

In MQCT the time-dependent rotational wave function of the system $\psi(\alpha',\beta',\gamma',t)$ is expanded over basis set of rotational eigenstates $\Psi_{m'n}(\alpha',\beta',\gamma')$ using the time-dependent coefficients $a_{m'n}(t)$ as follows:

$$\psi(\alpha',\beta',\gamma',t) = \sum_{m'n} a_{m'n}(t)\Psi_{m'n}(\alpha',\beta',\gamma')\exp\{-iE_n t/\hbar\}\,. \qquad (1)$$

Primed Euler angles (α',β',γ') define position of the molecule in the BF reference frame, where axis *z* is aligned along the molecule-atom direction (accurate definition of the BF reference frame is given in Appendix). Index *n* is a composite index that labels

states and its meaning depends on the system. For a diatomic molecule we have simply $n \equiv \{j\}$ and $\Psi_{m'n} \equiv \Psi^{j}_{m'}$. For a symmetric top rotor (oblate or prolate) we have $n \equiv \{j,k\}$ and $\Psi_{m'n} \equiv \Psi^{j}_{m'k}$. In the general case of an asymmetric top rotor we should set $n \equiv \{j,k_a,k_c\}$ and $\Psi_{m'n} \equiv \Psi^{j}_{m'k_ak_c}$. In either case, the energy E_n of an eigenstate depends on n only, and does not depend on m', which is projection of angular momentum j of the molecule onto *z*-axis in the BF reference frame. Note that although we neglect the vibrational excitation and focus on rotational transitions only, inclusion of vibrational eigenstates into the basis set expansion is rather straightforward [8].

Starting with expansion (1) and following the derivations outlined in Ref. [8], one can derive the general MQCT equations for time-evolution of probability amplitudes $a_{m'n}(t)$ (quantum part of the system) and for time-evolution of the classically treated degrees of freedom in the problem $\{R,\Phi,\Theta\}$. These coordinates define the molecule-atom separation and the direction of the atom-molecule axis (which is the BF *z*-axis) with respect to the laboratory reference frame. Here, we present just the final equations, adopted to the case when the initial rotational wave function $\psi(\alpha',\beta',\gamma',t)$ is a rotational eigenfunction, rather than a general rotational wave packet. In this special case the rotational wave function possesses cylindrical symmetry and the classical trajectory of motion $\{R(t),\Phi(t),\Theta(t)\}$ is restricted to one plane. One can choose this plane to be the equatorial plane $\Theta = \pi/2$, which greatly simplifies both classical and quantum equations of motion. In this case the time-dependent Schrodinger equation for atom-molecule scattering is reduced to the following system of coupled equations for probability amplitudes:

$$i\hbar \frac{\partial a_{m'n}}{\partial t} = \sum_{n'} a_{m'n'} \exp\{i(E_n - E_{n'})t / \hbar\} M_n^{n'} + \hbar \sum_{m''} a_{m''n} V_{m'}^{m''} \dot{\Phi} . \quad (2)$$

Here the matrix **V** describes transitions between m'-components of j in the BF reverence frame. It is computed analytically for every *j* as follows:

$$V_{m'}^{m''} = \frac{1}{2}\left[\sqrt{j(j+1) - m''(m''-1)}\delta_{m',m''-1} + \sqrt{j(j+1) - m''(m''+1)}\delta_{m',m''+1}\right]. \quad (3)$$

The last term in Eq. (2) occurs in the BF formalism only [8], not in the SF formalism, and the coupled-states approximation is obtained readily by neglecting this term [10]. Note that matrix **V** is time-independent (should be computed only once) and is analytic. It doesn't involve any interaction potential. In contrast, matrix **M** in Eq. (2) describes transitions between states *n*, and is computed for every m'-component of j as follows:

$$M_n^{n'}(R) = \left\langle \Psi_{m'n}(\alpha', \beta', \gamma') \middle| V(R, \alpha', \beta', \gamma') \middle| \Psi_{m'n'}(\alpha', \beta', \gamma') \right\rangle . \quad (4)$$

This is a potential coupling matrix. Its elements include the interaction potential and should be computed numerically. Elements of **M** are real and depend on *R* only.

Differential equations for classical degrees of freedom also include matrixes **M** and **V**, as a commutator [8-10]:

$$\dot{R} = \frac{P_R}{\mu} \quad (5)$$

$$\dot{\Phi} = \frac{P_\Phi}{\mu R^2} \quad (6)$$

$$\dot{P}_R = -\frac{\partial \tilde{V}(R)}{\partial R} + \frac{P_\Phi^2}{\mu R^3} \quad (7)$$

$$\dot{P}_{\Phi} = -i \sum_{m''n''} \sum_{m'n'} a^{*}_{m''n''} a_{m'n'} \exp\{i(E_{n''} - E_{n'})t/\hbar\} \left[\mathbf{M},\mathbf{V}\right]^{m''n''}_{m'n'} . \quad (8)$$

As we showed in Appendix C of Ref. [8], the expressions in the right-hand sides of Eqs. (7-8) are real-valued, leading to the real-valued classical momenta and their time-derivatives. Such equations can be easily propagated numerically, just as classical trajectories of motion. Derivative in Eq. (7) is computed by cubic spline of the mean-field potential itself, computed as:

$$\tilde{V}(R) = \sum_{m''n''} \sum_{m'n'} a^{*}_{m''n''} a_{m'n'} M^{n'}_{n}(R) .$$

Sampling of the classical initial conditions, and the final analysis of transition amplitudes $a_{m'n'}(t = +\infty)$ to compute cross sections, are both nontrivial and, in fact, closely interconnected issues [10]. Absolute value of the initial momentum $\mathbf{P}$ is determined by incident energy of collision, $|\mathbf{P}| = \sqrt{2\mu E}$, while various possible directions of $\mathbf{P}$ in space correspond to different values of $\ell = |\mathbf{l}|$ and $J = |\mathbf{J}|$, where $\mathbf{l}$ is the orbital angular momentum, and $\mathbf{J} = \mathbf{l} + \mathbf{j}$ is the total angular momentum. In order to determine two components of $\mathbf{P}^2 = P_R^2 + P_{\Phi}^2 / R^2$, first, the value of J is sampled randomly and uniformly between $J = 0$ and $J_{\max}$. Next, for a chosen initial j, the value of ℓ is sampled randomly and uniformly in the range $|J - j| \le \ell \le J + j$, and is used to define the initial classical momentum $P_{\Phi} = \hbar\sqrt{\ell(\ell+1)}$ in Eq. (6-7). The value of ℓ is closely related to the collision impact parameter b through $\ell(\ell+1) = k^2 b^2$ and $\mathbf{k} = \mathbf{P}/\hbar$. The value of P_R to use in Eq. (5) is computed from $P_R = \sqrt{\mathbf{P}^2 - P_{\Phi}^2 / R^2}$. This procedure

is repeated for $\aleph$ classical trajectories (labeled by i) and the inelastic scattering cross section is determined numerically as:

$$\sigma_{nm\to n'm'} = \frac{\pi}{k^2}\frac{J_{\max}}{\aleph}\sum_i (2J^{(i)}+1)\left|a^{(i)}_{n'm'}(t=+\infty)\right|^2 .$$

More detailed description of this procedure can be found in Sec. 3.2.4. of Ref. [10].

We want to emphasize that MQCT trajectories are not binned into any "boxes" at the final moment of time. Each MQCT trajectory, started in a given initial state nm, makes contribution to every final state $n'm'$, according to the values of $a_{m'n'}(t=+\infty)$. This feature results in favorable convergence properties of the method and requires only a moderate number of MQCT trajectories.

4.2.2 Matrix Elements for a Symmetric Top

First, we will consider a simpler case of a symmetric top + atom. Rotational eigenfunctions in the BF the can be re-expressed through the SF basis functions $\Psi^j_{mk}(\alpha,\beta,\gamma)$ and the Wigner rotation functions as follows [8,12]:

$$\Psi^{\,j}_{m'k}(\alpha',\beta',\gamma') = \sum_m D^{\,j}_{mm'}(\Phi,\Theta,0)\,\Psi^{\,j}_{mk}(\alpha,\beta,\gamma), \tag{9}$$

$$\Psi^j_{m'k}(\alpha',\beta',\gamma') = \sqrt{\frac{2j+1}{8\pi^2}}D^j_{m'k}(\alpha',\beta',\gamma'), \tag{10}$$

where Euler angles (α,β,γ) describe position of the symmetric top in the SF reference frame and indexes j,m,k are quantum numbers that correspond to the total angular momentum, its projection onto z-axis of SF, and its projection onto the symmetric-top axis, respectively.

In the BF reference frame the molecule-atom interaction potential can be expressed in the following form [13]:

$$V(\alpha',\beta',\gamma') = \sum_{\lambda,\mu} \sqrt{\frac{2\lambda+1}{4\pi}} c_{\lambda\mu}(R)\left(1+\delta_{0\mu}\right)^{-1}\left[D^{\lambda}_{0\mu}(\alpha',\beta',\gamma') + (-1)^{\mu} D^{\lambda}_{0-\mu}(\alpha',\beta',\gamma')\right], \tag{11}$$

and it can be shown that (see Appendix):

$$V(\alpha',\beta',\gamma') = V(\theta,\phi) = \sum_{\lambda,\mu} c_{\lambda\mu}(R)\left(1+\delta_{0\mu}\right)^{-1}\left[Y_{\lambda\mu}(\theta,\phi) + Y_{\lambda-\mu}(\theta,\phi)\right], \tag{12}$$

where $c_{\lambda\mu}$ is the same set of radial expansion coefficients. Azimuthal and polar angles (θ,φ) describe position of the atom in the Cartesian reference frame associated with the principal axis of inertia of the molecule. Note that $V(\alpha',\beta',\gamma')$ does not depend on α' because:

$$D^{\lambda}_{0\mu}(\alpha',\beta',\gamma') = d^{\lambda}_{0\mu}(\beta')\exp(-\mu\gamma'). \tag{13}$$

Physical meaning of this property is that the atom is structureless, so, the rotation around z-axis does not change the interaction energy. Substitution of Eqs. (11) and (10) into (6) leads to the following final formula [12,13]:

$$\begin{aligned} M^{j'k'}_{jk}(R) = \sum_{\lambda,\mu} & \sqrt{\frac{2j+1}{8\pi^2}}\sqrt{\frac{2j'+1}{8\pi^2}}\sqrt{\frac{2\lambda+1}{4\pi}} c_{\lambda\mu}(R)\left(1+\delta_{0\mu}\right)^{-1} \\ & \times\left[\left\langle D^{j}_{m'k}(\alpha',\beta',\gamma')\middle| D^{\lambda}_{0\mu}(\alpha',\beta',\gamma')\middle| D^{j'}_{m'k'}(\alpha',\beta',\gamma')\right\rangle\right. \\ & \left. + (-1)^{\mu}\left\langle D^{j}_{m'k}(\alpha',\beta',\gamma')\middle| D^{\lambda}_{0-\mu}(\alpha',\beta',\gamma')\middle| D^{j'}_{m'k'}(\alpha',\beta',\gamma')\right\rangle\right] \\ = \sum_{\lambda,\mu} & \sqrt{2j+1}\sqrt{2j'+1}\sqrt{\frac{2\lambda+1}{4\pi}}(-1)^{-m'-k} c_{\lambda\mu}(R)\left(1+\delta_{0\mu}\right)^{-1} \\ & \times\left[\begin{pmatrix} j' & \lambda & j \\ m' & 0 & -m' \end{pmatrix}\begin{pmatrix} j' & \lambda & j \\ k' & -\mu & -k \end{pmatrix} + (-1)^{\mu}\begin{pmatrix} j' & \lambda & j \\ m' & 0 & -m' \end{pmatrix}\begin{pmatrix} j' & \lambda & j \\ k' & \mu & -k \end{pmatrix}\right]. \end{aligned} \tag{14}$$

Non-zero elements in this matrix (allowed transitions) correspond only to $k = k' + \mu$. Different values of λ drive transitions between different j, while different values of μ drive transitions between different k.

4.2.3 Matrix Elements for a Diatomic Molecule

The case of $k' = 0$ and $\mu = 0$ corresponds to a diatomic molecule, when

$$\begin{pmatrix} j & \lambda & j' \\ -k & \mu & k' \end{pmatrix} = \begin{pmatrix} j & \lambda & j' \\ 0 & 0 & 0 \end{pmatrix}. \tag{15}$$

For this simpler case the matrix elements are [8]:

$$M_j^{j'}(R) = \sum_{\lambda} \sqrt{2j+1}\sqrt{2j'+1}(-1)^{m'} c_{\lambda}(R) \begin{pmatrix} j' & \lambda & j \\ 0 & 0 & 0 \end{pmatrix} \begin{pmatrix} j' & \lambda & j \\ m' & 0 & -m' \end{pmatrix}. \tag{16}$$

4.2.4 Matrix Elements for an Asymmetric Top

Now consider a general case of an asymmetric-top-rotor. Instead of Eq. (10) we have to expand wave function as follows:

$$\Psi^{j}_{m'k_a k_c}(\alpha', \beta', \gamma') = \sqrt{\frac{2j+1}{8\pi^2}} \sum_{k=-j}^{j} b^{k}_{j k_a k_c} D^{j}_{m'k}(\alpha', \beta', \gamma'), \tag{17}$$

where the coefficients $b^{k}_{j k_a k_c}$ are obtained by numerical diagonalization of the rotational Hamiltonian of the molecule. The state-to-state potential coupling matrix is larger in this case:

$$M^{j'k'_ak'_c}_{jk_ak_c}(R)=\sum_{\lambda,\mu}\sum_{k,k'}\sqrt{\frac{(2j+1)(2j'+1)(2\lambda+1)}{4\pi}}(-1)^{-m'-k}\left(1+\delta_{0\mu}\right)^{-1}b^{k}_{jk_ak_c}b^{k'}_{j'k'_ak'_c}c_{\lambda\mu}(R)$$
$$\times\left[\begin{pmatrix}j'&\lambda&j\\m'&0&-m'\end{pmatrix}\begin{pmatrix}j'&\lambda&j\\k'&-\mu&-k\end{pmatrix}+(-1)^{\mu}\begin{pmatrix}j'&\lambda&j\\m'&0&-m'\end{pmatrix}\begin{pmatrix}j'&\lambda&j\\k'&\mu&-k\end{pmatrix}\right], \tag{18}$$

but it still remains a real-valued.

4.3 Numerical Implementation

The sampling MQCT trajectories over J and ℓ is similar to sampling of purely classical trajectories over impact parameter, since $J_{\max}=k\hbar b_{\max}$. In this work, the maximum value of impact parameter determined by convergence studies was b_{max} = 10 a_0, sufficient even at low collision energies, and more than sufficient at high collision energies. The initial molecule-atom separation R was 18 a_0. The total number of classical trajectories was around 500 at each scattering energy, providing convergence of cross section with respect to this parameter on order of 1-2%. This number of trajectories is not particularly large because we only have to sample over J and ℓ, as explained in Sec. 4.2.1 above. The number of channels needed for MQCT calculations was also checked by convergence studies and happened to be very similar to the number of channels in the full quantum calculations (see below). Typically, 5 to 10 closed channels, in addition to all open (energetically accessible) channels, were included at each scattering energy.

The exponential terms in Eq. (8) cause no numerical problems, since they are always multiplied by the probability amplitudes. For example, if the final state n'' is energetically far from the initial state n' (a situation in which one could expect fast oscillations of the exponential term), the corresponding transition amplitude is usually

small, so that the effect of oscillations is damped. Only for energetically close states the transition amplitudes are significant, but in those cases the oscillations of the exponential terms are manageable. Same is true for the exponential terms in Eq. (2).

The full-quantum scattering calculations were performed using modified versions of both the sequential and parallel versions of the MOLSCAT code [14,15] using the Airy propagator [16]. The water molecule is described by a version of the effective Hamiltonian of Kyro [17], compatible with the symmetries of the PES. We use the molecular constants from Table I of Kyro and our calculated rotational levels of $H_2{}^{16}O$ are identical to those of Green [18]. Close coupling calculations are carried out up to collision energy 8000 cm^{-1}. The rotational basis set includes, in addition to open channels, 10 closed channels for all total energies up to 2000 cm^{-1}, and is reduced to 5 closed channels for higher energies. State-to-state transition cross sections were converged to better than 1%. Our rate coefficients for quenching can be compared to those of Yang *et al.* [19,20] obtained with roughly the same methodology and using the same potential energy surface. For example, for transition from $1_{1,1}$ to $0_{0,0}$ in the temperature range 5–800 K the difference is below or about 1% [19-21].

4.4 Results and Discussion for H_2O + He System

In Fig. 1, we report results for quenching of several excited states of para-water onto the ground rotational state $0_{0,0}$. For these four transitions the value of state-to-state energy difference ΔE varies from −37.14 to −136.26 cm^{-1}. Consequently, the magnitude of quenching cross section also varies significantly, within three orders of magnitude. In Fig. 1 each cross section is shown as a function of collision energy (kinetic energy of scattering partners in the center-of mass reference frame), and each transition

demonstrates a unique dependence. Most dramatic changes are observed for transition $2_{1,1} \rightarrow 0_{0,0}$. Cross section of this process first increases, then decreases, showing a maximum and a minimum in the energy range $1.0 < E < 10{,}000$ cm^{-1} (see Fig. 1). For other three processes the dependencies of cross sections on collision energy are more monotonic. For all of these transitions MQCT results are in very good agreement with full-quantum results in the entire range of considered energies.

In Fig. 2 we report results for three transitions between different states with $j = 2$. For these, the values of ΔE are −25.08, −40.98 and −66.07 cm^{-1}. Again, the full-quantum behavior of scattering cross sections is rather involved, but it is reproduced reasonably well by MQCT, particularly at higher energies. At lower collision energies we see some systematically increasing deviations.

In Fig. 3 we collected the data for quenching of several $j = 2$ states onto the first excited state $1_{1,1}$. Here the values of ΔE are −32.85, −57.93 and −98.92 cm^{-1}. These transitions exhibit comparable cross sections and are shown in different frames of Fig. 3 for clarity. One can see that the largest discrepancies between MQCT and the full-quantum results are observed for transition $2_{0,2} \rightarrow 1_{1,1}$.

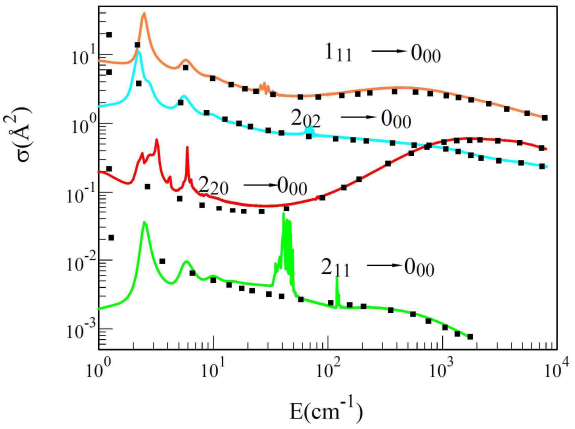

Figure 1. Inelastic cross sections for quenching of several rotationally excited states of H_2O onto its ground state in collisions with He. Results of full-quantum calculations are shown by solid lines, MQCT results are shown by symbols.

These and all other discrepancies seen in Figs. 1-3 are analyzed altogether in Fig. 4, in order to quantify the accuracy of MQCT. In this figure, the percent-errors for quenching cross sections are plotted as a function of collision energy *E*, together for all transitions discussed above, regardless of transition intensity. These data show that at scattering energies above 2,000 cm^{-1} the errors are consistently small, in the range of 1-2% (which is basically our convergence criterion with respect to the number of trajectories), for all considered transitions. This is very encouraging. However, at lower collision energies the errors are somewhat larger, and the magnitude of the error depends on transition. One group of transitions shows errors up to 12%, with average error close to 3% (red points in Fig. 4). Another group of transitions shows errors up to 17%, with average error close to 8% (blue points in Fig. 4).

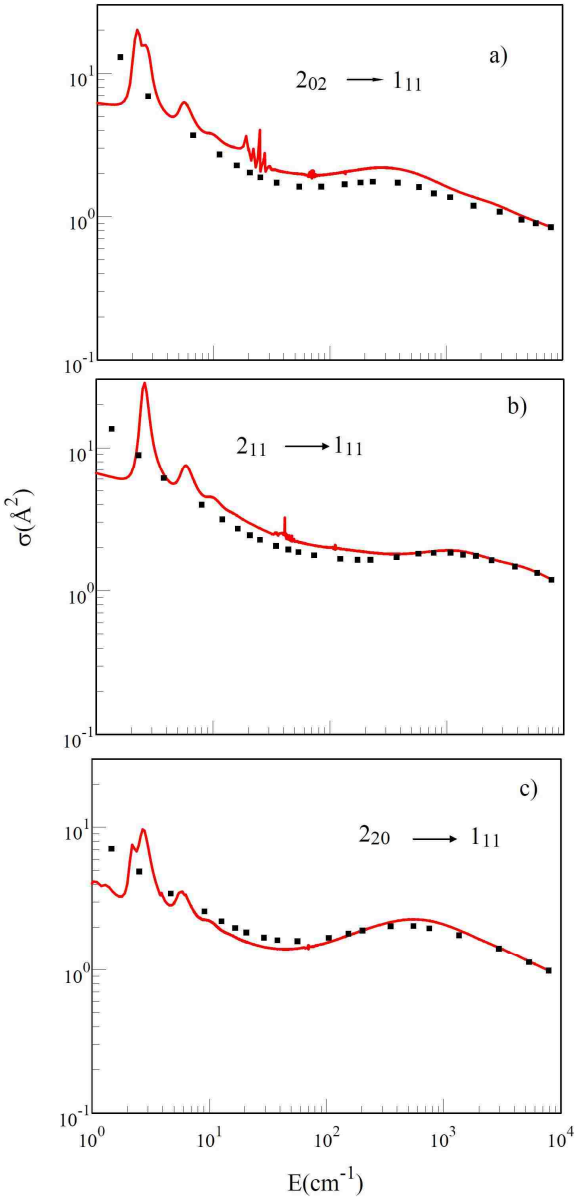

Figure 2. Inelastic cross sections for transitions between several $j = 2$ states of H_2O in collisions with He. Results of full-quantum calculations are shown by solid lines, MQCT results are shown by symbols.

We noticed that all transitions of this last group, described less accurately by MQCT, are induced by $c_{10}(R)$ term of the potential expansion in Eq. (12). This includes several transitions with $\Delta j = 1$, namely: $2_{0,2} \rightarrow 1_{1,1}$, $2_{1,1} \rightarrow 1_{1,1}$, $2_{2,0} \rightarrow 1_{1,1}$ and, finally, $1_{1,1} \rightarrow 0_{0,0}$. Transitions $2_{2,0} \rightarrow 2_{1,1}$, $2_{1,1} \rightarrow 2_{0,2}$ and $2_{2,0} \rightarrow 2_{0,2}$ with $\Delta j = 0$ are also affected by $c_{10}(R)$, but less. At this point we don't entirely understand why this happens, but it looks like *longer range* anisotropy of the potential leads to less accurate MQCT results, while *shorter range* anisotropy leads to more accurate MQCT results. This question requires further attention and, ideally, a joint analysis of MQCT results obtained for several different systems, which will be pursued in the near future and reported elsewhere.

It is worth noting that MQCT method produces reasonable results even at low scattering energies, $1.0 < E < 30$ cm^{-1}, where the quantum scattering resonances are predicted by the full-quantum scattering calculations. Strictly speaking, MQCT does not reproduce resonances, but we found that when resonances are broad and isolated the MQCT results reproduce quantum cross sections on average. In contrast, when resonances are narrow, numerous and overlapping, the MQCT method describes well the non-resonant (background) behavior, and "doesn't see" such resonances. Multiple examples of both of these behaviors can be found in Figs.

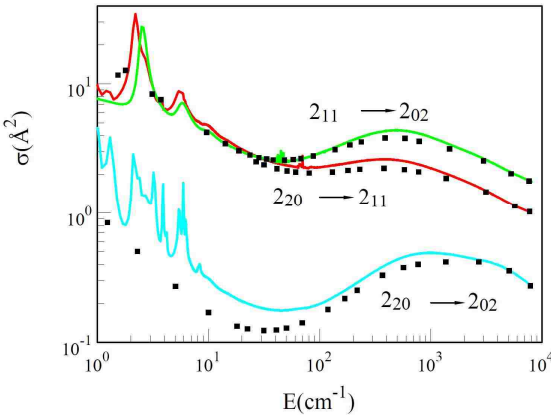

Figure 3. Inelastic cross sections for quenching of several $j = 2$ states of H_2O onto its first excited state in collisions with He. Results of full-quantum calculations are shown by solid lines, MQCT results are shown by symbols.

1-3, and this is also consistent with our previous observations [11]. Importantly, MQCT never fails miserably. Even in the quantum regime, when MQCT is less accurate, it remains quite dependable.

In order to quantify the numerical performance of MQCT we plotted in Fig. 5 the CPU time as a function of total number of states in the calculations (including m'-components of j), which grows significantly as collision energy increases. Fitting of these data shows that they are described by an $N^{1.32}$ dependence. Thus, overall, our method scales as $N^{1.32}$, where N is the total number of *states* in MQCT calculations. In order to make a meaningful comparison with full quantum calculations we also analyzed correlation between CPU time and the number of *channels* n, which is the size of matrix **M**. Note that $n < N$ because m'-components of j are not included (same as in the full-quantum calculations). Correlation analysis of such dependence shows that it is nearly quadratic, $n^{1.98}$. Still, this is a more favorable scaling low, compared to the full-quantum CC approach, which scales as n^3 with respect to the number of channels. In this sense, MQCT is expected to outperform the full-quantum calculations at high energies and for molecules with dense spectra.

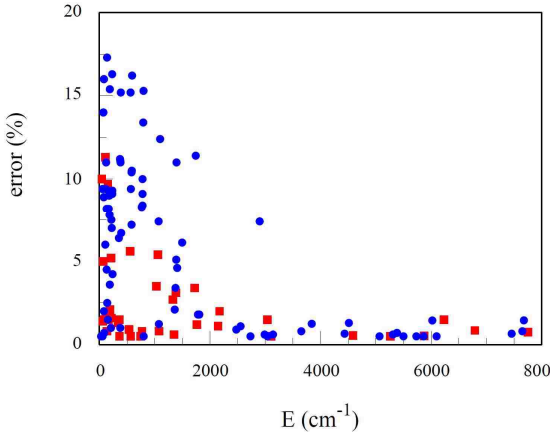

Figure 4. Error of MQCT calculations, determined by comparison with full-quantum results, for all transitions presented in Figs. 1-3. Blue symbols correspond to transitions affected by the $j = 2$ term of potential expansion. Red dots are used for all other transitions. See text for discussion.

In present calculations for H_2O + He we did not really try to optimize our MQCT code, and did not try to reduce the CPU

cost of MQCT, because it was quite affordable anyway. For example, at lower energies calculations took about 0.5 minutes per energy point. At higher energies they took about 15 hours per point. These numbers can be improved by optimization of the code, by slightly increasing (or varying) step size of numerical integration, or by trying a different integrator. For example, for solving both quantum (2) and classical (7-8) equations we used the 4^{th} order constant step-size Runge-Kutta code from Numerical Recipes, known to be not particularly efficient. But code optimization was not our goal here. We rather focused on the fundamental scaling law.

The most intense part of MQCT calculations is to compute, several times per time step, the right-hand-side parts of the differential equations for numerical integration (by the Runge-Kutta method, in our code). This includes the system of quantum equations (2) and the classical equations (7-8). For the system of Eq. (2) we are computing a single-sum for each state (which is basically a matrix×vector multiplication), while for Eqs. (7) and (8) we are computing a double-sum (basically a vector×matrix×vector multiplication). We have not yet tried to optimize these procedures for speed. At this point they are computed simply by using multiple loops, and this is where the quadratic scaling may originate. But in principle, such calculations could be done more efficiently using optimized mathematical libraries for linear algebra, such as BLAS, which could further facilitate the MQCT calculations.

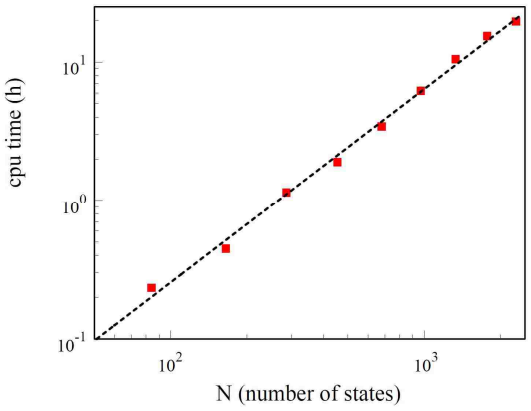

Figure 5. Numerical performance of MQCT approach. Dashed line shows a fit by quadratic function. Note that log scale is used for both horizontal and vertical axes.

It should also be mentioned that MQCT is easily and efficiently parallelizable by computing different trajectories on different processors. Such calculations do not need to pass messages from one processor to another, at all. Since the number of trajectories is on order of few hundred, the wall clock time is easily reduced by an order of 100, placing just few trajectories per processor.

Formalism of the mixed quantum/classical theory for inelastic scattering was developed to treat any molecule-atom collisions, including the simplest diatomic + atom case, a more complicated case of a symmetric-top molecule + atom, and finally a general case of an asymmetric-top rotor + atom. Transition matrix elements are given for each case and, from the theory standpoint, those represent the only difference between the three cases. The equations of motion for classical variables (responsible for the relative molecule + atom motion) and the coupled equations for evolution of populations of the internal (rotational, vibrational) states are always the same.

As for numerical performance, the BF formulation presented here is computationally efficient, unlike the SF formulation published earlier (which happened to be extremely inefficient). In present formulation the transition matrix is real-valued, simply structured and dominated by the near-diagonal terms. Each matrix element depends on one variable only -- the molecule-atom distance R. The H_2O + He system is complex enough to benchmark performance of MQCT and determine its scaling law. We found that the cost of MQCT scales only as n^2, where n is the number of channels. Furthermore, the calculations are straightforward to parallelize without any message-passing overhead, which makes this approach very practical.

As for accuracy, we found that for H_2O + He system at collision energies above 2,000 cm^{-1} the MQCT method basically repeats results of the full-quantum CC calculations, for all transitions considered here. At lower energies the method is still reliable, although it is less accurate. For example, the errors of inelastic cross sections on order of 10% are not unusual at collision energies below 1,000 cm^{-1}, although average errors are smaller, 3-8%. This accuracy may be well sufficient for many applications. Importantly, we never saw MQCT method failing for any transition at any collision energy. It always produces reasonable results, although it should be mentioned that at lower collision energies *some* of transitions are treated less accurately than others. This feature is important to understand, in order to formulate transparent criteria for general applicability of the MQCT approach.

4.5 Rotational Inelastic Scattering for CH_3OOCH + He.

To the present day more than 200 molecular species have been detected in space, including some complex organic molecules and long carbon chains [21,23-27]. For quantitative interpretation of their observed spectra the inelastic state-to-state transition cross sections for these molecules collided with background gasses (H_2 and He in the interstellar medium, or H_2O in cometary environment) are needed, often in a broad range of collision energies. This information, however, is largely missing and there is no simple way of determining it from experiments. Collisional cross sections could be computed within quantum mechanical framework [13,28], by numerically solving the Schrödinger equation for nuclear motion of colliding partners, but such brute-force calculations are computationally affordable only for some of the smallest molecules, and only at low

energies of collision [23,29]. For example, quantum calculations of $H_2O + H_2$ in the required range of collision energies (up to T = 1,500 K) have been achieved just recently [1], and represent the state-of-the-art in the field. Calculations for $HCOOCH_3$ + He have been attempted [22], but were shown to be computationally affordable only for collision energies below 30 cm^{-1}. Such important process as scattering of $H_2O + H_2O$ in the desired energy range (up to T ~ 300 K) is also beyond the reach of theorists. This is quite demonstrative, since many astrophysically important molecules are larger than H_2O, e.g.: CH_3CHO, CH_3OCH_3, C_2H_5CN, C_6H_2, CH_3C_4H and HC_5N [22,23,30,31]. One should admit, that although a significant progress has been made on inelastic scattering calculations for small molecules and at low collision energies [21, 23], the standard full-quantum approach is, basically, stuck, when the molecules are heavy and the collision energy is large, or when molecule-molecule collisions are important, or, when in addition to rotation the vibrational motion (torsion, bending) has to be taken into account. Thus, it is desirable to develop an alternative or complimentary approach that would allow circumventing the computational difficulties by employing some kind of approximation.

Recently we developed a Mixed Quantum/Classical Theory (MQCT) for inelastic scattering [8, 32] where the internal motion of the molecule is still treated quantum mechanically, while the scattering of the atom is described approximately using classical mechanics (Newtonian trajectories), which reduces the computational cost dramatically. We rigorously tested this theory by applying it to CO + He [33], H_2 + He [9], N_2 + Na [10] and H_2O + He [34], and obtained very good agreement with the standard full-quantum treatment in a broad range of collision energies (computationally affordable for these simpler molecules). We found that MQCT gives a detailed description of the

scattering process, even at the level of differential cross sections in the forward scattering quantum regime [9, 10], which is a known unresolved issue for all semi-classical methods [35]. At higher collision energies it reproduces the full-quantum results almost exactly, but even at low collision energies the predictions of MQCT are reasonable [9,10,33,34]. The only feature that MQCT does not reproduce is scattering resonances at very low collision energies, near threshold of the excitation process. In the last decade, a family of closely related theoretical methods have been developed using the quantized Hamiltonian dynamics (QHD) approach [36-38]. They also utilize the mixed quantum/classical ideas based on the Ehrenfest mean-field potential, but in a different fashion.

It is interesting that foundations of this theory were laid out by Billing in 80's and 90's [7,39], but then it was largely abandoned, without been properly tested. Our recent progress on diatomics and triatomics was rapid [8-10,32-34], which demonstrated that MQCT can be used as an efficient predictive computational tool for small molecules. However, it is often a challenge to extend an approximate method onto the complex systems. New problems may appear, such as difficulty of accurate representation of the potential energy surface, density of rotational spectrum of a heavy asymmetric-top rotor, and higher costs of numerical calculations, to name just a few. Our goal nowadays is to apply MQCT to several complicated problems, such as small organic molecules of astrophysical importance, which would represent a major step forward.

In this section we report MQCT results for rotational excitation of $HCOOCH_3$ (methyl formate) by He in the range of collision energies up to 1000 cm^{-1}, typical for warm star-forming regions. To our best knowledge this is the largest molecule ever

considered for the inelastic scattering calculations [23]. The full-quantum scattering results (available for this process at low energy only [22]) serve as a benchmark and demonstrate that our approach is accurate. Our general conclusion is that at medium and higher collision energies, when quantum scattering resonances are not important, MQCT can confidently replace the full-quantum scattering approach. MQCT remains computationally affordable and enables theoretical predictions of inelastic cross sections for larger molecules and at higher collision energies than was possible before, in particular for the processes of astrochemical importance.

The details of our theory are given in section 4.2. In a nutshell, we propagate batches of MQCT trajectories to sample the classical impact parameter for collisions between He and $HCOOCH_3$. Such trajectories are driven by the mean-field potential, averaged over the rotational wave function of the molecule. Typically, the number of trajectories on order of a hundred is sufficient to capture the dependence of transition probability on the impact parameter, as shown in Fig. 6. As trajectory progresses, the evolution of rotational wave function of the molecule is determined by the system of coupled differential equations that includes elements of the transition matrix, due to interaction with the atom. In this way, the scattering motion of the atom and the rotational motion of

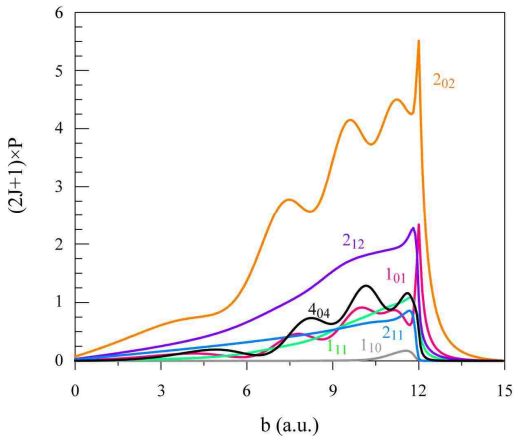

Figure 6. Dependence of quantum transition probability on classical impact parameter for excitation (by He collision) of $HCOOCH_3$ from its ground rotational state $0_{0,0}$ into several final rotational states. The collision energy is 17 cm^{-1}. The color of state-labels corresponds to the color of curves.

the molecule affect each other, and the quantum and classical degrees of freedom are treated self-consistently. The energy is exchanged between translation and rotation, while the total energy is conserved. Figure 7 illustrates evolution of state populations along a typical MQCT trajectory. In this picture the atom-molecule encounter occurs in the short time interval between $t \sim 70$ and 100×10^3 a.u. Two scenarios of rotational excitations can be identified. For majority of states the population start growing exponentially on the pre-collisional stage, and remains almost constant on the post collisional stage. Examples are 2_{02}, 2_{12}, 4_{04}, 1_{11}, and 1_{01}. However, for some states the population starts growing much later, basically during the collision, and continues evolving at the post-collisional stage. Examples are 2_{11} and 1_{10}. This difference comes from the fact that the first group of states is populated by transitions directly from the ground state 0_{00} due to *potential coupling*. The second group of states is populated due to *centrifugal coupling* with other excited states, indirectly, and only after those intermediate states receive enough population. This leads to a later start, longer time evolution, and lower transition probabilities (see Fig. 7). As discussed below, such transitions are often neglected by the coupled-states (or centrifugally-sudden) approximation, but they are included in MQCT calculations. In either case, the

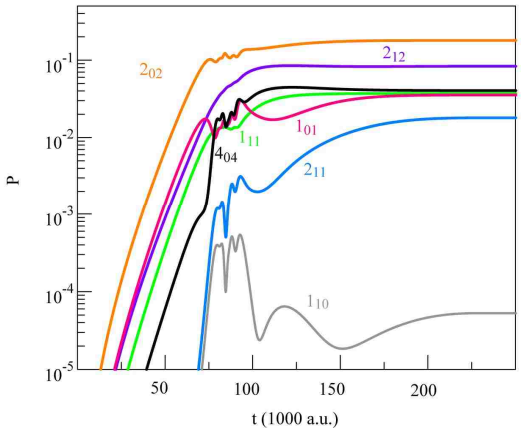

Figure 7. Evolution of state populations in $HCOOCH_3$ along a typical MQCT trajectory that describes its collision with He. The collision energy is 17 cm^{-1}, the impact parameter is 10.5 a_0. The color of state-labels corresponds to the color of curves.

populations of rotational states of the molecule at the end of trajectories are used to compute the state-to-state transition cross sections [33].

In Fig. 8 we compare our MQCT results against the available full-quantum results from Ref. [22] for rotational excitation of the ground state 0_{00} of $HCOOCH_3$ to several low-lying rotationally excited states, using the same potential energy surface. For the most important states (large cross sections) the agreement is excellent: In the energy range 15-30 cm^{-1}, where quantum resonances level off, the typical differences are on order of only 5%. For the less important state $1_{1,0}$ (small cross section) the difference is somewhat larger near, but it should be stressed that our MQCT results are fully converged with respect to the number of partial waves (J_{max} = 20), while convergence of the full-quantum data from Ref. [22] for the state $1_{1,0}$ was reported as around 20% (i.e., not entirely converged, due to high computational cost of better calculations), which explains larger difference obtained for this state. In order to make comparison meaningful, the rotational basis set size in our MQCT calculations was taken the same as in Ref. [22], namely j_{max} = 14 (225 channels).

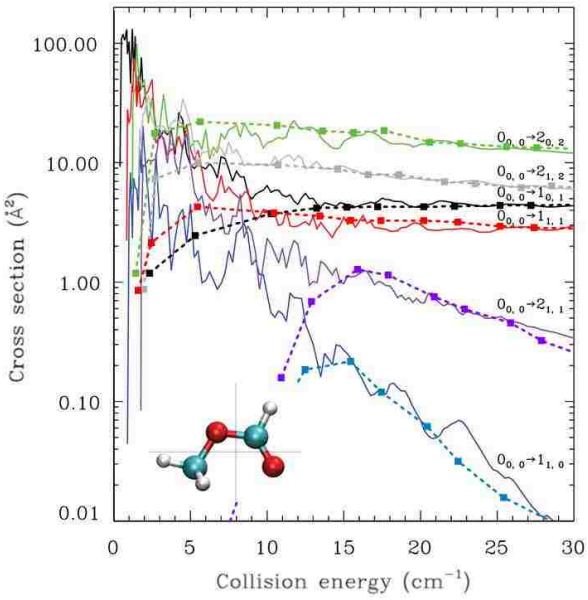

Figure 8. Inelastic cross sections for excitation of several rotationally excited states of $HCOOCH_3$ from its ground state in collisions with He at low scattering energies. Results of the full-quantum calculations from Ref. [22] are shown by solid lines (Reproduced with permission from A. Faure, K. Szalewicz and L. Wiesenfeld, *J. Chem. Phys.* 135, 024301 Copyright 2011 AIP Publishing LLC), our MQCT results are shown by symbols of the same color (connected by dashed-lines for clarity). The insert shows molecular structure of methyl formate.

In the lower energy range, 5-15 cm^{-1} in Fig. 8, the results of MQCT for the most important transitions are still reasonable. The accuracy of MQCT drops significantly only at collision energies below 5 cm^{-1}, where quantum resonances dominate. At these low collision energies many trajectories describe orbiting of the He atom around the molecule, which is classical analogue of quantum resonance. A good recipe for analysis of such trajectories is yet to be found. For now, we simply removed them from consideration, focusing on non-resonant contribution to the process.

Overall, Fig. 8 demonstrates that at collision energies near 30 cm^{-1} the MQCT method gives an accurate description of the inelastic $HCOOCH_3$ + He collisions. Our prior experience with MQCT applied to four different systems in a broad energy range [9,10,33,34] shows that its accuracy always improves as collision energy is raised. So, based on results of Fig. 8, we can expect that at energies above 30 cm^{-1} (where there are no quantum data available) our MQCT predictions of the inelastic scattering cross sections would be reliable, with errors less than 5%. In Fig. 4 we present the MQCT predictions for excitation of the twenty most important rotational states of $HCOOCH_3$, starting from the ground state 0_{00}, in the

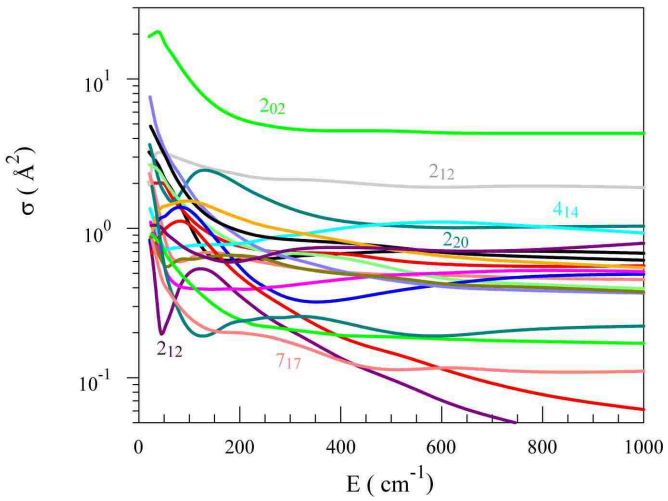

Figure 9. Inelastic cross sections for excitation of 20 most important rotationally excited states of $HCOOCH_3$ from its ground state computed by MQCT for a broad range of collision energies. Some of the final states are labeled, others are listed in the text.

collisional energy range expanded by a factor of more than 30, up to 1000 cm^{-1}. These states are: 1_{01}, 1_{11}, 2_{02}, 2_{12}, 2_{22}, 2_{21}, 3_{03}, 3_{13}, 3_{21}, 3_{31}, 4_{04}, 4_{14}, 4_{22}, 4_{40}, 5_{05}, 5_{33}, 5_{33}, 5_{41}, 6_{16}, 6_{24} and 7_{17}. The dependencies in Fig. 9 are rather smooth, although some of them are not entirely monotonic and the overall picture is rather complicated. The reason for this is that $HCOOCH_3$ is a heavy rotor and the spectrum of its states is rather dense, with many state-to-state transitions accessible and participating actively in the energy transfer. In these MQCT calculations the number of rotational channels was around 1130, with typical values of J_{max} around 120. This is a very large number of channels. The full-quantum calculations with such number of channels would not be practical. For all calculations in this section we used the potential energy surface from Ref. [22]. This surface is based on high-level *ab initio* electronic structure calculations (CCSD(T)/aug-cc-pVTZ), employs fitting of 476 data points by an analytic function, and is expected to be accurate up to collision energy of 1000 cm^{-1}. Note that we did not employ expansion of the PES over the basis set of spherical harmonics. This procedure, standard for small and simple molecules, does not work well for larger and complicate molecules [22], such as methyl formate. Elements of the potential coupling matrix were computed numerically by integrating over Euler's angles β' and γ' using a Legendre-Gauss quadrature on a two-dimensional 50×50 grid, determined by convergence studies. One known way to make the full-quantum scattering calculations more affordable is the coupled-states (CS) approximation [40], in which some transitions (between states with different values m of projection of the angular momentum *j*) are neglected to ease calculations. The CS-method is usually employed at higher collision energies. Interestingly, within MQCT one can also formulate the CS-approximation, and test it by comparing its results against the fully-

coupled MQCT, which we will now call CC-MQCT [9]. Results of such CS-MQCT calculations are presented in Fig. 10. Comparison of these data against CC-MQCT (presented in Fig. 8) shows that although the general behavior of energy dependence is similar, the absolute values of CS cross sections are often different (e.g., by a factor of up to ×1.8 for state 2_{20}, by a factor of up to ×2.1 for state 4_{12} and by a factor of up to ×1.4 for state 2_{02}). For some transitions these differences vanish as collision energy reaches 1000 cm^{-1}, but for several other state-to-state transitions large differences survive even at higher energies. Needless to say that some transitions don't happen at all within the CS-approximation (e.g., excitation of states 1_{10} and 2_{11}). One important conclusion is that the CS approximation is not particularly accurate for the $HCOOCH_3$ + He system in the considered energy range. One should not expect that the quantum CS calculations for this molecule will be accurate. Thus, the fully-coupled version of MQCT is, perhaps, the only practical way of doing accurate calculations for this and other similar organic molecules of astrophysical relevance.

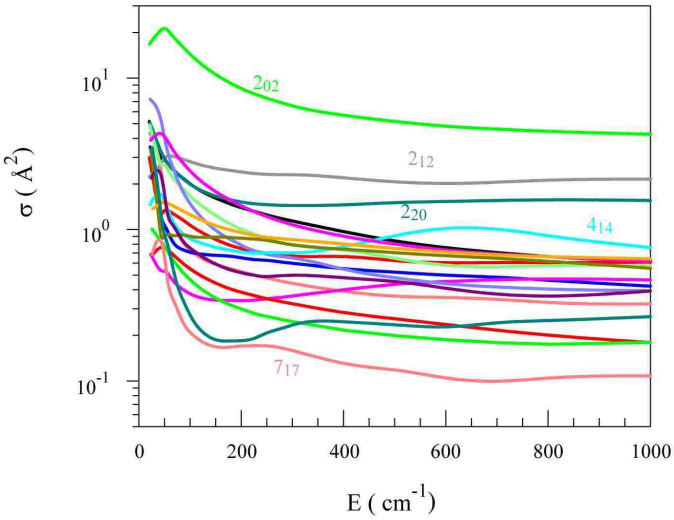

Figure 10. Same as in Fig. 4, but computed using CS-approximation within MQCT framework.

The numerical cost of our MQCT calculations is represented by Fig. 11. The CS version of MQCT is faster than the fully-coupled MQCT, by a factor of roughly 20. The scaling law (computational cost vs. number of included channels) is $n^{2.4}$ for the fully-coupled MQCT and is n^2 for CS-MQCT. These numbers are taken directly from calculations presented in Figs. 8-9, and represent a practical measure of the computational cost of the method in a range of collision energies. We also did run an idealized test of performance, when MQCT calculations were done at one representative collision energy, while the number of included channels was varied in a broad range. In such tests the scaling law of the fully coupled MQCT was $n^{2.5}$. For comparison, the full-quantum calculations (e.g., using Hibridon or MOLSCAT [41, 14] are usually said to scale as n^3 with respect to the number of channels, but the cost of converging the quantum calculations with respect to the number of partial waves (which depends on collision energy and the reduced mass) should be added to that, leading, in practice, to the total cost on the order of n^5 or n^6. In contrast, MQCT has no such "overhead", since scattering of the atom is treated classically. Thus, the scaling properties of MQCT are more favorable than those of the full-quantum method, and the advantages are particularly

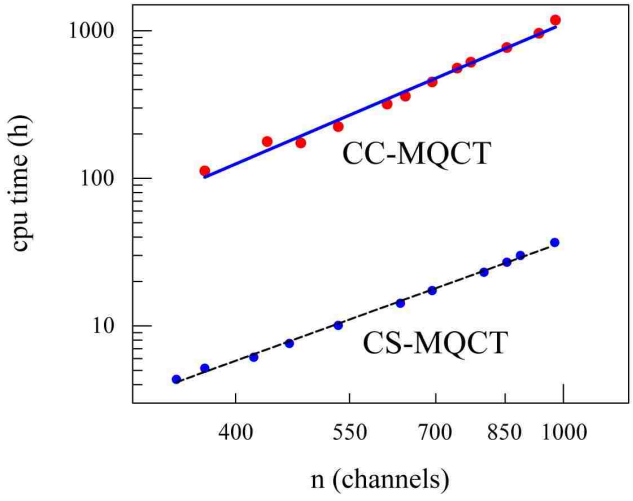

Figure 11. Numerical performance of MQCT, observed for its fully-coupled CC-version and for the approximate CS-version. Logarithmic scale is used for both horizontal and vertical axes. Dashed lines show fits by two different power functions.

significant for heavier collision partners and at higher collision energies. However, it should also be mentioned that at this point we have only undertaken some basic optimizations of our code. Development of an efficient computer program should reduce the computational costs of MQCT even further.

In conclusion, we carried out the rotationally-inelastic scattering calculations for collision of methyl formate with helium atom, within framework of the mixed quantum/classical theory. First, we compared our results against the full-quantum results available at low collision energies and found a very good agreement in the range between 15 and 30 cm^{-1}. Next, we significantly expanded the range of collision energies (by a factor of more than 30, up to 1000 cm^{-1}), covering a practically useful scattering regime. Importantly, the standard full-quantum calculations are computationally unaffordable for such a large molecule in this scattering regime. One can look at MQCT as a method that is complementary to the standard full-quantum method. Namely, at low collision energies one may want to do the full-quantum scattering calculations because they are affordable and because some quantum features, like scattering resonances, may be important. However, at higher collision energies, when the full-quantum calculations become unaffordable (and, in fact, unnecessary) one may want to switch to the mixed quantum/classical theory. It is feasible to apply MQCT to a number of complicated processes of astrophysical relevance, such as collisions of complex organic molecules (CH_3CHO, CH_3OCH_3, C_2H_5CN and $HCOOCH_3$) or linear carbon chains (C_6H_2, CH_3C_4H and HC_5N) with He.

It is possible to extend MQCT onto the case of two coupled rotors, which would permit inelastic scattering calculations of molecule + molecule collisions. Such

developments are in progress. The relevant applications will include excitation/quenching of complex organic molecules and linear carbon chains by H_2, but also collisions between two water molecules (including their isotopomers) and several other triatomic + triatomic systems of astrophysical relevance, way too complicated for the full-quantum treatment. Our estimates suggest that calculations for all of these processes are affordable within the framework of MQCT.

Although less relevant to astrophysics, another useful extension of MQCT is toward the high pressure regime, where the multiple collisions of a molecule with bath gas atoms/molecules can't be treated independently, similar to the fall-off regime of recombination kinetics where the three-body collisions are important. The time-dependent formulation of MQCT should allow simulations in which the molecule would interact successively or simultaneously with two or more quenchers along one trajectory. Such theory would have numerous applications in the high-pressure combustion.

4.6 Conclusions for CHAPTER 4

Formalism of the mixed quantum/classical theory for inelastic scattering was developed to treat any molecule-atom collisions, including the simplest diatomic + atom case, a more complicated case of a symmetric-top molecule + atom, and finally a general case of an asymmetric-top rotor + atom. Transition matrix elements are given for each case and, from the theory standpoint, those represent the only difference between the three cases. The equations of motion for classical variables (responsible for the relative

molecule + atom motion) and the coupled equations for evolution of populations of the internal (rotational, vibrational) states are always the same.

As for numerical performance, the BF formulation presented here is computationally efficient, unlike the SF formulation published earlier (which happened to be extremely inefficient). In present formulation the transition matrix is real-valued, simply structured and dominated by the near-diagonal terms. Each matrix element depends on one variable only -- the molecule-atom distance R. The H_2O + He system is complex enough to benchmark performance of MQCT and determine its scaling law. We found that the cost of MQCT scales only as n^2, where n is the number of channels. Furthermore, the calculations are straightforward to parallelize without any message-passing overhead, which makes this approach very practical.

As for accuracy, we found that for H_2O + He system at collision energies above 2,000 cm^{-1} the MQCT method basically repeats results of the full-quantum CC calculations, for all transitions considered here. At lower energies the method is still reliable, although it is less accurate. For example, the errors of inelastic cross sections on order of 10% are not unusual at collision energies below 1,000 cm^{-1}, although average errors are smaller, 3-8%. This accuracy may be well sufficient for many applications. Importantly, we never saw MQCT method failing for any transition at any collision energy. It always produces reasonable results, although it should be mentioned that at lower collision energies *some* of transitions are treated less accurately than others. This feature is important to understand, in order to formulate transparent criteria for general applicability of the MQCT approach.

The significant attempt has been made to extent the MQCT to practical use where the full quantum treatment is impossible in practice. The calculations for inelastic rotationally scattering were carried out for CH_3OOCH + He. At low collision energies where the full quantum results are available (< 30 cm^{-1}) the agreement between CC data and MQCT is excellent. Also we extended the accessible range of collisional energy 10 times to 300 cm^{-1} and using MQCT framework. This data can be already used for practical purposes in astrochemical applications. It is the first time when scattering cross section were computed for such complicated scattering system and for complex organic molecule and in a broad range of energies. The benchmarks study in the range where the full quantum data is available and the previous studies for other systems makes us believe that MQCT reproduces the scattering phenomena in the full range of collisional energies. This is a large impact in both fields of studies: in collisional dynamics as a new fundamental theory and in astrochemistry as a new practical tool which completes the existing quantum codes and can even replace them for complicated cases such large molecules and high energy of collisions.

Appendix 4A: BF Reference Frame, Euler and Spherical Angels

We have to demonstrate that for a molecule + atom system [12]:

$$\sqrt{\frac{2\lambda+1}{4\pi}}D^{\lambda}_{0\mu}(\alpha',\beta',\gamma') = Y_{\lambda\mu}(\beta',\gamma') = Y_{\lambda\mu}(\theta,\varphi)\,.$$

This can be done graphically, by establishing correspondence between the Euler angles (α',β',γ') used by MQCT formalism and the spherical angles (θ,φ) used in the full-quantum CC calculations.

Thus, in MQCT calculations the *z*-axis of the BF reference frame (X',Y',Z') points from the molecule's center-of-mass to the atom. Euler angles (α',β',γ') are used to define position of the molecule with respect to this SF reference frame using three rotations, as shown in Fig. 8. As the molecule-atom scattering progresses along the classical trajectory of motion, the BF reference frame rotates with respect to SF reference frame frozen in the lab and this process is described by two classically treated angles (Θ,Φ), as discussed in the chapter 4th .

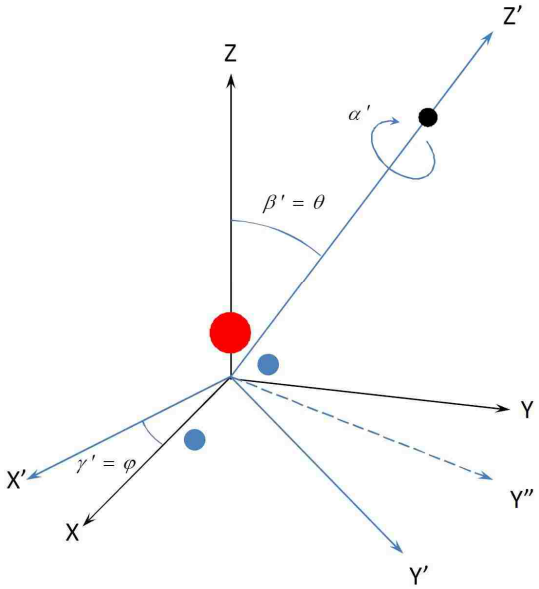

Figure 12. Explanation of angles in the BF and SF reference frames used in MQCT and full-quantum calculations. See Appendix for details.

As for expansion of potential, a Cartesian reference frame (X,Y,Z) is defined by the principal axes of inertia of the molecule and is permanently fixed on the molecule itself, regardless of position of the colliding atom. Position of the atom is defined by azimuthal and polar angles (θ,φ) relative to this Cartesian reference frame (see Fig. 8).

The origin of angles β' and γ' can be chosen such that rotation of the molecule by β' and then by γ' with respect to BF reference frame would place molecule into the conventional position in the SF reference frame, as shown in Fig. 8. This can always be done. Furthermore, the origin of α' is arbitrary since in the molecule + atom system the interaction potential does not depend on α'. Indeed, as can be seen from Fig. 6, rotation

by α' corresponds to rotation around Z' axis. Without loss of generality we can set $\alpha' = 0$. Most importantly, Fig. 12 demonstrates that $\beta' = \theta$ and $\gamma' = \varphi$.

BIBLIOGRAPHY FOR CHAPTER 4

1. F. Daniel, M.-L. Dubernet, F. Pacaud, A. Grosjean, *Astron. Astrophys*. **536,** A76 (2011).
2. L. Wiesenfeld, Y. Scribano, and A. Faure, *Phys. Chem. Chem. Phys*. **13**, 8230 (2011).
3. F. Lique, J. Kłos and M. Hochlaf, *Phys. Chem. Chem. Phys*. **12**, 15672 (2010).
4. P. J. Dagdigian and M. H. Alexander, *J. Chem. Phys*. **135**, 064306 (2011).
5. S. Fonseca dos Santos, N. Balakrishnan, S. Lepp, G. Quéméner, R. C. Forrey, R. J. Hinde and P. C. Stancil, *J. Chem. Phys*. **134**, 214303 (2011).
6. S. Fonseca dos Santos, N. Balakrishnan, R. C. Forrey and P. C. Stancil, *J. Chem. Phys.* **138**, 104302 (2013).
7. G. D. Billing, *The Quantum-Classical Theory* (Oxford University Press, 2002).
8. A. Semenov and D. Babikov, *J. Chem. Phys*. **139**, 174108 (2013).
9. A. Semenov and D. Babikov, *Phys. Chem. Lett.* **5**, 275 (2014).
10. A. Semenov and D. Babikov, *J. Chem. Phys*. **140**, 044306 (2014).
11. M. Ivanov, M.-L. Dubernet, and Dmitri Babikov, *J. Chem. Phys.* **140**, 134301 (2014).
12. D. A. Varshalovich, A. N. Moskalev, and V. K. Khersonskii, *Quantum Theory of Angular Momentum* (World Scientific, Singapore, 1988).
13. S. Green, *J. Chem. Phys*. **64**, 3463 (1976).
14. J. M. Hutson and S. Green, MOLSCAT computer code, version 14, Collaborative Computational Project No. 6 Science and Engineering Research Council, United Kingdom (1994).
15. G. McBane, MOLSCAT computer code, parallel version (2004).
16. M. H. Alexander and D. E. Manolopoulos, *J. Chem. Phys*. **86**, 2044 (1987).
17. E. Kyro, *J. Mol. Spectrosc.* **88**, 167 (1981).
18. S. Green, S. Maluendes, and A. D. McLean*, Astrophys. J. Suppl. Ser*. **85**, 181 (1993).
19. B. H. Yang and P. C. Stancil, *J. Chem. Phys*. **126**, 154306 (2007).
20. B. Yang, M. Nagao, W. Satomi, M. Kimura, and P. C. Stancil, *Astrophys. J.* **765**, 77 (2013).

21. M.-L. Dubernet, M. H. Alexander, Y. A. Ba, N. Balakrishnan *et al*, *Astron. Astrophys.* **553**, A50 (2013).

22. A.Faure , K. Szalewicz and L. Wiesenfeld, *J. Chem. Phys* **135**, 024301 (2011).

23. E. Roueff, F. Lique, *Chem. Rev*. **113**, 8906- 8938 (2013).

24. A.G. Tielens, *The Physics and Chemistry of the Interstellar Medium*, CUP(2006).

25. P. Caselli, C. Ceccarelli, *Astron. Astrophys. Rev*. **20:56**, 1-68, (2012)

26. N. Sakai, S.Yamamoto, *Chem. Rev*. **113**, 8981–9015, (2013).

27. T. Henning, D. Semenov, *Chem. Rev*. **113**, 9016–9042, (2013).

28. A.M. Arthurs, A. Dalgarno, *Proceedings of the Royal Society*, **A256**, 540-551(1960).

29. M. Wernli, L. Wiesenfeld; A. Faure; P. Valiron, *Astron. Astrophys*. **464**, 1147-1154, (2007).

30. D.Rabli, D.R. Flower, *Mon. Not. R. Astron. Soc.* **406**, 95, (2010).

31. N. Troscompt, A. Faure, L.Wiesenfeld, C.Ceccarelli, P.Valiron, *Astron. Astrophys*. **493**, 687-696, (2009).

32. A. Semenov, D. Babikov, *J. Chem. Phys.* **138**, 164110, (2013).

33. A. Semenov, M.V. Ivanov, D. Babikov, *J. Chem. Phys*. **139**, 074306, (2013).

34. A. Semenov, M.-L. Dubernet, D. Babikov*, J. Chem. Phys.* **141**, 114304, (2014).

35. R.D. Levine, *Quantum Mechanics of Molecular Rate Processes*, Oxford University Press (1969).

36. O.V. Prezhdo, *Theor. Chem. Acc.* **116**, 206–218, (2006).

37. O.V. Prezhdo, Y.V. Pereverzev, *J. Chem. Phys*. **113**, 6557, (2000).

38. C. Booksby, O.V. Prezhdo*, Chem. Phys. Lett*. **346**, 463–469, (2001).

39. G.D. Billing, *Comp. Phys. Rep*. **1**, 237-296, (1984).

40. P. McGuire, D.J. Kouri, *J. Chem. Phys.* **60**, 2488-2499 (1974).

41. M.H. Alexander, D.E. Manolopoulos, H.J. Werner, P.F. Vohralik, D. Lemoine; G.Corey, Gordon, R.; B.Johnson, T. Orlikowski, A. Berning, *et.al.* Hibridon. University of Maryland: College Park, MD, (2011).

CHAPTER 5. MIXED QUANTUM/CLASSICAL THEORY FOR MOLECULE-MOLECULE INELASTIC SCATTERING: DERIVATIONS OF EQUATIONS AND APPLICATION TO N_2 + H_2 AND H_2+H_2 SYSTEMS

5.1 Molecule – Molecule Scattering

Inelastic scattering of two gas-phase molecules is a fundamental physical process important in the atmosphere [1], combustion [2], laboratory experiments, [3] and in the outer space [4]. The simplest version of the process is a rotationally inelastic collision where just the rotational state of one collision partner change (rotational excitation or quenching), but the processes where the rotational states of both partners change (quasi-resonant energy transfer) are also important [5]. Often, the low-energy vibrational states (bending, torsion) participate in the process too, leading to the coupled ro-vibrational transitions [6]. In the processes where the collision energy is high, so that the vibrational excitation is significant, the collision-induced dissociation of the molecule may occur [7] which is also an example (the limiting case) of the inelastic scattering.

Theoretical and computational description of these processes is a challenging task. The exact quantum mechanical treatment of rotational transitions usually employs the coupled-channel (CC) formalism developed in 1960th [8]. This approach had great success in simple systems. Thus, CC calculations for collision of a diatomic molecule with an atom are very efficient and computationally affordable, even at higher energies and for heavier molecules and quenchers [9]. However, CC calculations for a triatomic molecule + atom are much more demanding [10]. The diatomic + diatomic [11] and the triatomic + diatomic [5] calculations are computationally challenging, especially for heavy molecules and at higher energies [12]. In order to make them more affordable the

coupled-states (CS) approximation is often employed [10] which neglects transitions between different m-states, within the same rotational energy level. Still, the quantum CC calculations for rotational transitions in triatomic + triatomic systems, such as H_2O + H_2O collisions at room temperature, remain computationally unaffordable. Inclusion of vibrational states (in addition to the rotational states) is possible within the CC formalism [13], but such ro-vibrational calculations are even more demanding.

Thus, the range of applications of the quantum approach remains limited to simple molecules (small number of internal quantum states), light masses and low collision energies (small number of the partial scattering waves). The classical trajectory method, on the other side, is applied to larger systems at high scattering energies to study the collisional energy transfer [14]. This method is quite affordable computationally, but several flaws of the purely classical approach are also well known. Among them are zero-point energy leakage [15], inability to incorporate symmetry restrictions into state-to-state transitions [16], absence of tunneling [17] or scattering resonances [18].

It is an old idea to combine classical mechanics with quantum mechanics in a mixed (or hybrid) approach to the inelastic scattering in order to use benefits offered by both classical and quantum frameworks, and trying to avoid the disadvantages of both. It would be attractive to use quantum description of the internal quantized states of the molecules (the vibrational and/or rotational motion), while the classical mechanics is employed for description of the translational motion of collision partners (the scattering process). In this way, the quantum treatment of continuum motion is avoided, leading to significant computational advantage, but the state-to-state transitions are described rather

rigorously, including many quantum effects, such as level quantization, zero-point energy, symmetry of wave functions and associated selection rules, etc.

Some early references on implementations of these ideas date back to the work of McCann and Flannery in 1970th [19,20] but the most popular and noticeable quantum/classical approach appeared in 1980th and 90th due to the work of Billing [21,22]. He introduced two different versions of the quantum/classical theory. His major focus was on the method for description of ro-vibrational processes, where quantum mechanics is used for description of the vibrational motion only, while classical mechanics is used for both the translational motion of the collision partners and for their rotational motion. When thinking about this approach, a useful parallel with statistical mechanics can be drawn. Namely, for statistical description of molecular processes the translational and rotational partition functions are normally computed in the high-temperature limit (equivalent to the classical limit), while the vibrational partition function is always a sum over quantized states. Thus, the mixed quantum/classical approach of Billing is well justified for many molecular systems in a broad range of collision conditions. It was applied to several model systems and several simple real systems [22], and showed great promise. Unfortunately, due to a tragically early death of Billing in 2002 [23] the quantum/classical approach remained not fully developed and this research direction was, basically, abandoned, for a while.

The opportunity of using a mixture of quantum and classical mechanics was called to memory only recently [24-26] for the studies of ozone formation reaction O + O_2 + Ar, which is a recombination reaction that includes formation and stabilization of highly excited ro-vibrational states of O_3, or scattering resonances – a very complex

process for which no standard approach or well-developed method exist. This interesting application stimulated a new round of theory developments [27,28], including the second version of quantum/classical theory, with emphasis on quantum treatment of rotation [29]. In his early work Billing also developed a method where the rotation of a diatomic molecule (treated as rigid rotor, no vibration) was described quantum mechanically, while the scattering of an atom off the diatomic was treated classically [30]. Surprisingly, one can find very limited applications of this method in the literature. Billing himself applied it to just one simplest system, He + H_2, at just two scattering energies, looking at transitions between the lowest energy levels only [22,30]. Although his results were encouraging, more detailed studies have never been pursued, to the best of our knowledge. One reason for this could be that at that time the full-quantum scattering calculations (to compare with) were also quite limited. In any case, this second mixed quantum/classical method, focused on the quantum treatment of rotation, was abandoned as well.

The mixed quantum classical theory (MQCT) we developed recently is similar to this second method of Billing in many respects. We also describe the rotational motion quantum mechanically, by expanding the rotational wave function over the basis set of rotational eigenstates with time-dependent expansion coefficients, and, we also describe scattering of collision partners using classical trajectories, driven by the mean-field potential. However, we went much further in theory development, testing and applications. First of all, we worked out the MQCT formalism in both the space-fixed (SF) reference frame and the body-fixed (BF) reference frame [29], and carried out calculations on a model system in order to demonstrate that both versions are physically

equivalent and both theories, equations and computer codes are correct. We quickly learned that the SF version of MQCT is numerically inefficient [31], because the corresponding state-to-state transition matrix (which governs evolution of the rotational wave function) is complex-valued with dense structure and each matrix element dependent on three classical variables (that evolve along the collision trajectory). Luckily, we found that the BF version of MQCT, in contrast, involves a real-valued sparse state-to-state transition matrix with simple bock-diagonal structure, and each element is dependent on the molecule-quencher separation only -- just one classical variable [29]. In the work that followed [32-35] we demonstrated that this BF version of MQCT is numerically efficient.

For example, for the fully-coupled MQCT the scaling law, which is computational cost vs. number of channels, is $n^{2.5}$, and this is only slightly better than n3 scaling of the full-quantum CC calculations [34,35]. Note, however, that here n is the number of included rotational energy levels at one representative collision energy, and it should not be forgotten that the cost of converging the full-quantum calculations with respect to the number of partial waves also increases when the collision energy is raised, leading in practice to the total cost in the range of n^5 to n^6. In contrast, MQCT has no such “overhead”, since scattering of the quencher is treated classically. Thus, the scaling properties of MQCT are superior, and the advantages are particularly significant for heavier collision partners and at higher collision energies. Interestingly, within MQCT one can also formulate the CS approximation [33], which gives another source of speed-up, by a factor of roughly ×20 [35]. It is worth noting that Billing used only such CS version of his quantum classical theory, while our focus is on the fully-coupled MQCT

approach, which appears to be surprisingly accurate when compared to the full-quantum CC method.

In order to access the accuracy of MQCT, we conducted a very detailed and hierarchical benchmark studies for several real molecules + atom systems. We applied it to heavy and light collision partners, at low and high scattering energies in a broad range, to study rotational excitation and quenching, of the low-lying and highly excited rotational states, computing total and differential, elastic and inelastic cross sections, and we even looked at the simplest ro-vibrational transitions. We started with diatomic + atom systems and studied N_2 + Na [32,33] and H_2 + He [33]. Then we moved to the symmetric top rotors, such as CH_3 radical and NH_3 collided with He (unpublished), and, finally, extended MQCT to treat the general case of an asymmetric top rotor + atom. This was applied to H_2O + He [34], and, most impressively, to $HCOOCH_3$ + He [35], which is the largest molecule (methyl formate) ever considered for the inelastic scattering calculations. In all these systems we saw that at higher collision energies MQCT gives results nearly identical to the full-quantum results and remains computationally cheap (e.g., up to collision energies of 10,000 cm^{-1} in the case of H_2O + He).34 At low collision energies the excitation thresholds are predicted correctly (e.g., in N_2 + Na) [32,33] and, the results of MQCT remain reasonably accurate down to collision energies of just few wavenumbers. We also learned how to use phase information to reproduce quantum interference and construct the differential over scattering angle cross sections (e.g., in N_2 + Na) [32,33], but still have to find a way how to describe scattering resonances. This seems to be feasible, [36] but at present we simply remove the orbiting trajectories, and

focus on non-resonant contribution to cross sections (e.g., in $HCOOCH_3$ + He)[35]. Importantly, we never saw MQCT failing miserably.

This Chapter is focused on another important development of MQCT – its extension onto the molecule + molecule systems, the case that is particularly demanding to treat computationally using the full-quantum approach. There are many important molecule + molecule systems that could be studied using MQCT, including small organic molecules and linear carbon chains relevant to astrophysical environments collided with H_2[4], small polyatomic molecules in the atmosphere collided with O_2 and N_2, and triatomic molecules collided with H_2O, including water-water collisions.

The chapter is organized as follows. In Section 5.2 we outline the theory for MQCT calculations of scattering of two non-identical diatomic molecules. In Section 5.3 we present numerical results for N_2 + H_2 system. In Section 5.4 we discuss importance of identical particle treatment and the theory for MQCT calculations of identical particles is described in Section 5.5. In Section 5.6 we present the MQCT results for H_2+H_2 and compare them with the data obtained using different quantum methods. The conclusions are given and future research directions are discussed in Section 5.7.

5.2 Theoretical Framework for Molecule - Molecule Scattering

5.2.1 Quantum and Classical Degrees of Freedom

Consider collisions of two molecules: Molecule 1 is AB and molecule 2 is CD, as shown in Fig. 1. Classical variables that describe molecule-molecule scattering are three coordinates (R,Θ,Φ) of the vector $\mathbf{Q}$ that connects centers of mass of two molecules. Quantum degrees of freedom are four angles $(\theta_1,\theta_2,\phi_1',\phi_2')$ needed to describe positions

of two diatomics with respect to vector $\mathbf{Q}$ (*i.e.*, in the BF reference frame). As in the earlier paper [29], we use *primed* variables and indexes for the BF reference frame (*e.g.*: ϕ', m'), in order to distinguish from those in the SF reference frame. The interatomic distances r_1 and r_2 are considered to be fixed for simplicity (rigid rotors), but they can be easily introduced into the formalism for description of ro-vibrational processes, just as it was done in our earlier work on the molecule-atom systems[29].

Rotation of each molecule is quantized and is described by the corresponding rotational eigenfunction, $Y_{j_1}^{m_1'}(\theta_1,\phi_1')$ and $Y_{j_2}^{m_2'}(\theta_2,\phi_2')$ for molecules 1 and 2, respectively (spherical harmonics in the BF). The total angular momentum of two molecules $\mathbf{j}_{12}=\mathbf{j}_1+\mathbf{j}_2$ is also quantized. The corresponding eigenfunctions can be expressed through spherical harmonics as follows [37]

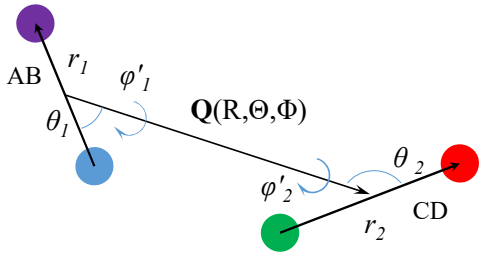

Figure 1. Classical and quantum variables for description of inelastic collision of two diatomic molecules in the body-fixed reference frame.

$$\Upsilon_{j_{12}j_1j_2}^{m_{12}'}(\theta_1,\theta_2,\phi_1',\phi_2') = \sum_{m_1'm_2'} \left\langle j_1m_1'j_2m_2' \middle| j_{12}m_{12}' \right\rangle Y_{j_1}^{m_1'}(\theta_1,\phi_1')Y_{j_2}^{m_2'}(\theta_2,\phi_2'). \qquad (1)$$

The total time-dependent wave function for the quantum part of the system can be expressed as

$$\psi(\theta_1,\theta_2,\phi_1',\phi_2',t) = \sum_{j_{12}m_{12}'j_1j_2} a_{j_{12}j_1j_2}^{m_{12}'}(t)\Upsilon_{j_{12}j_1j_2}^{m_{12}'}(\theta_1,\theta_2,\phi_1',\phi_2')\exp\{-iE_{j_1j_2}t\} \qquad (2)$$

where $a_{j_{12}j_1j_2}^{m_{12}'}$ are time-dependent expansion coefficients, and atomic units are used for energy. The range of values of j_1 and j_2 in this sum defines the basis set size for description of two quantized rotors (*e.g.*, $0\le j_1\le j_1^{\max}$ and $0\le j_2\le j_2^{\max}$). It depends on

physical properties of the system and is a convergence parameter. The value of j_{12} varies in the range $|j_1 - j_2| \le j_{12} \le j_1 + j_2$. The value of m'_{12} varies in the range $-j_{12} \le m'_{12} \le j_{12}$.

In order to avoid confusion, we want to emphasize that $\mathbf{j}_{12}$ is *not* the orbital angular momentum of the motion of one molecule with respect to the other. The orbital motion (scattering) is described classically in this formalism and is not quantized. It should also be stressed that the four-dimensional functions $\Upsilon^{m'_{12}}_{j_{12} j_1 j_2}(\theta_1, \theta_2, \phi'_1, \phi'_2)$ play an accessory role only, and don't enter into any final equations of motion (derived below). But, if needed, they can be obtained from Eq. (1) using spherical harmonics and Clebsch-Gordan coefficients, and visualized as we have done in Fig. 2, which represents the component $j_{12} = 2$, $m_{12} = 0$ for the collision of AB($j_1 = 2$) with CD($j_2 = 0$).

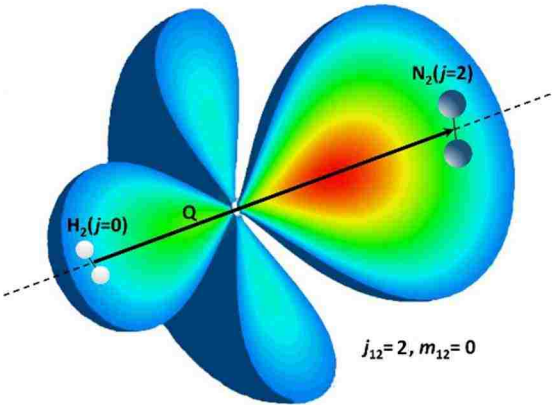

Figure 2. Density probability for the state with j_{12}=2, m_{12}=0.

5.2.2 BF Transformation of Wave Functions

The key point of the BF formulation of MQCT is to describe how the function (2) evolves due to rotation of the intermolecular axis, described by $\mathbf{Q}$, in the course of molecule-molecule scattering. For this, we express rotational eigenstates of the molecules 1 and 2 in the BF frame through the rotational eigenstates in the SF frame using Wigner *D*-matrixes (see Eq. (17) in Ref. 29)

$$Y_{j_1}^{m_1'}(\theta_1,\phi_1') = \sum_{m_1} D^{j_1}_{m_1 m_1'}(\Phi,\Theta,0) Y_{j_1}^{m_1}(\theta_1,\phi_1) \qquad (3a)$$

$$Y_{j_2}^{m_2'}(\theta_2,\phi_2') = \sum_{m_2} D^{j_2}_{m_2 m_2'}(\Phi,\Theta,0) Y_{j_2}^{m_2}(\theta_2,\phi_2) \qquad (3b)$$

Here, as in the earlier paper [29] we use *unprimed* variables and indexes for the SF reference frame (*e.g.*: θ, m). Substitution of (3a) and (3b) into (1) gives

$$\Upsilon^{m_{12}'}_{j_{12} j_1 j_2}(\theta_1,\theta_2,\phi_1',\phi_2') = \sum_{m_1' m_2', m_1 m_2} \left\langle j_1 m_1' j_2 m_2' \middle| j_{12} m_{12}' \right\rangle D^{j_1}_{m_1 m_1'}(\Phi,\Theta,0) D^{j_2}_{m_2 m_2'}(\Phi,\Theta,0) Y_{j_1}^{m_1}(\theta_1,\phi_1) Y_{j_2}^{m_2}(\theta_2,\phi_2).$$

(4).

The product of two Wigner *D*-functions in this formula can be simplified as follows (see Eq. 4.4.1 in Ref. 38):

$$D^{j_1}_{m_1 m_1'}(\Phi,\Theta,0) D^{j_2}_{m_2 m_2'}(\Phi,\Theta,0) = \sum_{j=|j_2-j_1|}^{j_2+j_1} \sum_{m=-j}^{j} \sum_{k=-j}^{j} \left\langle j_1 m_1' j_2 m_2' \middle| j m \right\rangle \left\langle j_1 m_1 j_2 m_2 \middle| j k \right\rangle D^{j}_{km}(\Phi,\Theta,0)$$

. (5)

Substitution of (5) into (4) gives

$$\Upsilon^{m_{12}'}_{j_{12} j_1 j_2}(\theta_1,\theta_2,\phi_1',\phi_2') = \sum_{m_1' m_2', m_1 m_2} \left\langle j_1 m_1' j_2 m_2' \middle| j_{12} m_{12}' \right\rangle \times \sum_{j=|j_2-j_1|}^{j_2+j_1} \sum_{m=-j}^{j} \sum_{k=-j}^{j} \left\langle j_1 m_1' j_2 m_2' \middle| j m \right\rangle \left\langle j_1 m_1 j_2 m_2 \middle| j k \right\rangle D^{j}_{km}(\Phi,\Theta,0) Y_{j_1}^{m_1}(\theta_1,\phi_1) Y_{j_2}^{m_2}(\theta_2,\phi_2)$$

(6)

Note that in the SF reference frame one could write an expression analogous to Eq. (1), written for the BF reference frame, namely

$$\Upsilon^{k}_{j j_1 j_2}(\theta_1,\theta_2,\phi_1,\phi_2) = \sum_{m_1 m_2} \left\langle j_1 m_1 j_2 m_2 \middle| j k \right\rangle Y_{j_1}^{m_1}(\theta_1,\phi_1) Y_{j_2}^{m_2}(\theta_2,\phi_2) \qquad (7)$$

Comparing (6) and (7) we can establish transformation of the total wave functions Υ between the BF and SF reference frames:

$$\Upsilon^{m'_{12}}_{j_{12}j_1j_2}(\theta_1,\theta_2,\phi'_1,\phi'_2) = \sum_{m'_1m'_2} \langle j_1m'_1j_2m'_2 \,|\, j_{12}m'_{12}\rangle \times \sum_{j=|j_2-j_1|}^{j_2+j_1} \sum_{m=-j}^{j} \sum_{k=-j}^{j} \langle j_1m'_1j_2m'_2 \,|\, jm\rangle D^j_{km}(\Phi,\Theta,0)\Upsilon^k_{j\,j_1j_2}(\theta_1,\theta_2,\phi_1,\phi_2) = \sum_{j=|j_2-j_1|}^{j_2+j_1} \sum_{m=-j}^{j} \sum_{k=-j}^{j} D^j_{km}(\Phi,\Theta,0)\Upsilon^k_{j\,j_1j_2}(\theta_1,\theta_2,\phi_1,\phi_2) \sum_{m'_1m'_2} \langle j_1m'_1j_2m'_2 \,|\, j_{12}m'_{12}\rangle\langle j_1m'_1j_2m'_2 \,|\, jm\rangle.$$

(8)

The last term of this expression can be simplified using closure relation

$$\sum_{m'_1m'_2} \langle j_1m'_1j_2m'_2 \,|\, j_{12}m'_{12}\rangle\langle j_1m'_1j_2m'_2 \,|\, jm\rangle = \langle j_{12}m'_{12}|\, jm\rangle,$$

which converts Eq. (8) into the following form

$$\Upsilon^{m'_{12}}_{j_{12}j_1j_2}(\theta_1,\theta_2,\phi'_1,\phi'_2) = \sum_{j=|j_2-j_1|}^{j_2+j_1} \sum_{m=-j}^{j} \sum_{k=-j}^{j} D^j_{km}(\Phi,\Theta,0)\Upsilon^k_{j\,j_1j_2}(\theta_1,\theta_2,\phi_1,\phi_2)\langle j_{12}m'_{12}|\, jm\rangle = \sum_{j=|j_2-j_1|}^{j_2+j_1} \sum_{m=-j}^{j} \sum_{k=-j}^{j} D^j_{km}(\Phi,\Theta,0)\Upsilon^k_{j\,j_1j_2}(\theta_1,\theta_2,\phi_1,\phi_2)\delta^{j_{12}}_j\delta^{m'_{12}}_k \quad (8') = \sum_{k=-j_{12}}^{j_{12}} D^{j_{12}}_{km'_{12}}(\Phi,\Theta,0)\Upsilon^k_{j_{12}j_1j_2}(\theta_1,\theta_2,\phi_1,\phi_2).$$

To simplify notation, we can leave out the range of the index *k*, which gives the following final formula

$$\Upsilon^{m'_{12}}_{j_{12}j_1j_2}(\theta_1,\theta_2,\phi'_1,\phi'_2) = \sum_k D^{j_{12}}_{km'_{12}}(\Phi,\Theta,0)\Upsilon^k_{j_{12}j_1j_2}(\theta_1,\theta_2,\phi_1,\phi_2). \quad (8'')$$

Notice that qualitatively, this expression is similar to Eqs. (3a-b), which is understood: transformation of rotational wave function in space due to its rotation should not depend on how this wave function is constructed; it should transform just as the corresponding angular momentum, which gives the physical meaning of Eq. (8″).

5.2.3 Equations of Motion

Equations of motion for time-evolution of the expansion coefficients $a^{m'_{12}}_{j_{12}j_1j_2}$ are obtained by substituting Eq. (2), with $\gamma^{m'_{12}}_{j_{12}j_1j_2}$ expressed by Eq. (8″), into the time-dependent Schrödinger equation. Derivations are very similar to those in the molecule + atom case, outlined in Eq. (18-21) of our earlier paper, Ref. 29. For the sake of brevity, we will not repeat them here, and will only present the result

$$\frac{\partial a^{m'_{12}}_{j_{12}j_1j_2}}{\partial t} = -i \sum_{j'_{12}m''_{12}j'_1j'_2} a^{m''_{12}}_{j'_{12}j'_1j'_2} M^{j_{12}m'_{12}j_1j_2}_{j'_{12}m''_{12}j'_1j'_2}(R) \exp\{i(E_{j_1j_2} - E_{j'_1j'_2})t\} - \sum_{m''_{12}} a^{m''_{12}}_{j_{12}j_1j_2} W^{m'_{12}}_{m''_{12}} . \qquad (9)$$

We see that besides phase factors, time-evolution of the expansion coefficients is driven by two transition matrixes. Matrix $W^{m'_{12}}_{m''_{12}}$ is responsible for transitions between different (energetically degenerate) projection states of the total angular momentum j_{12}. It can be expressed as

$$W^{m'_{12}}_{m''_{12}} = U^{m'_{12}}_{m''_{12}} \dot{\Theta} + i(\sin\Theta V^{m'_{12}}_{m''_{12}} - m''_{12}\cos\Theta\delta_{m'_{12},m''_{12}})\dot{\Phi}, \qquad (10)$$

where for convenience we introduced two time-independent matrixes

$$U^{m'_{12}}_{m''_{12}} = \frac{1}{2}\left[\sqrt{j_{12}(j_{12}+1) - m''_{12}(m''_{12}-1)}\,\delta_{m'_{12},m''_{12}-1} - \sqrt{j_{12}(j_{12}+1) - m''_{12}(m''_{12}+1)}\,\delta_{m'_{12},m''_{12}+1}\right],$$

(11a)

$$V^{m'_{12}}_{m''_{12}} = \frac{1}{2}\left[\sqrt{j_{12}(j_{12}+1) - m''_{12}(m''_{12}-1)}\,\delta_{m'_{12},m''_{12}-1} + \sqrt{j_{12}(j_{12}+1) - m''_{12}(m''_{12}+1)}\,\delta_{m'_{12},m''_{12}+1}\right].$$

(11b)

Matrixes $U^{m'_{12}}_{m''_{12}}$ and $V^{m'_{12}}_{m''_{12}}$ have to be computed only once, for every value of j_{12}, but they don't depend on j_1 or j_2. They are computed analytically and don't include the

interaction potential. Physical meaning of the last term in Eq. (9) is the centrifugal coupling effect. Allowed transitions are $\Delta m'_{12} = \pm 1$. Neglecting this term leads to CS-approximation within MQCT framework, with no transitions allowed between the m'_{12} states. Here we don't follow this path and focus on the fully-coupled MQCT. However, Eq. (10) can be simplified in the case when the initial state of the system is an eigenstate (rather than a wave packet) and the interaction potential is cylindrically symmetric. In this case the trajectory of relative molecule-molecule scattering stays in one plane, which can be chosen as the equatorial plane, $\Theta = \pi / 2$, without loss of generality. With this choice, as collision progresses, the classical vector $\mathbf{Q}$ rotates in the equatorial plane, which is described by time evolution of classical variables $R(t)$ and $\Phi(t)$, as one can see in Fig. 1. Since $\sin\Theta = 1$, $\cos\Theta = 0$ and $\dot{\Theta} = 0$, Eq. (10) simplifies significantly, giving

$$W_{m''_{12}}^{m'_{12}} = i V_{m''_{12}}^{m'_{12}} \dot{\Phi} . \tag{12}$$

This formula shows clearly that although $V_{m''_{12}}^{m'_{12}}$ is time-independent, the entire matrix $W_{m''_{12}}^{m'_{12}}$ evolves in time, according to the angular speed $\dot{\Phi}$ of the vector $\mathbf{Q}$ (see below).

The second matrix in Eq. (9) is the potential coupling matrix $M_{j'_{12} m''_{12} j'_1 j'_2}^{j_{12} m'_{12} j_1 j_2}$ that should be computed numerically, using the potential energy surface $V(R, \gamma_1, \gamma_2, \phi'_1, \phi'_2)$, as:

$$M_{j'_{12} m''_{12} j'_1 j'_2}^{j_{12} m'_{12} j_1 j_2}(R) = \left\langle \Upsilon_{j_{12} j_1 j_2}^{m'_{12}}(\gamma_1, \gamma_2, \varphi'_1, \varphi'_2) \middle| V(R, \gamma_1, \gamma_2, \varphi'_1, \varphi'_2) \middle| \Upsilon_{j'_{12} j'_1 j'_2}^{m''_{12}}(\gamma_1, \gamma_2, \varphi'_1, \varphi'_2) \right\rangle . \tag{13}$$

Notice that each matrix element is a function of molecule-molecule separation *R*, which is the length of the vector $\mathbf{Q}$, that itself evolves during the collision (see below). In

practice, a useful expression for matrix elements is obtained by expanding the interaction potential over basis set of spherical harmonics [39]

$$V(R,\theta_1,\theta_2,\phi_1',\phi_2') = \sum_{l\,l_1 l_2} \sqrt{\frac{2l+1}{4\pi}} A_{l\,l_1 l_2}(R) \sum_{m} \left\langle l_1 m l_2 - m \middle| l 0 \right\rangle Y_{l_1}^{m}(\theta_1,\phi_1') Y_{l_2}^{-m}(\theta_2,\phi_2'). \qquad (14)$$

This is a formal mathematical expansion of the (real-valued) potential energy function. Here, for two chosen values of l_1 and l_2 the value of l varies in the range $|l_1 - l_2| \le l \le l_1 + l_2$. The basis set size depends on physical properties of the system and is a convergence parameter (*e.g.*, $0 \le l_1 \le l_1^{\max}$ and $0 \le l_2 \le l_2^{\max}$). The value of m varies in the range $-\min(l_1,l_2) \le m \le \min(l_1,l_2)$. However, using Eq. (1) the sum over *m* in this expression can be eliminated. Substitution of the result into Eq. (13) gives:

$$\begin{aligned} M_{j'_{12} m''_{12} j'_1 j'_2}^{j_{12} m'_{12} j_1 j_2}(R) = & \sum_{l\,l_1 l_2} \sqrt{\frac{2l+1}{4\pi}} A_{l\,l_1 l_2}(R) \\ & \times \left\langle \Upsilon_{j_{12} j_1 j_2}^{m'_{12}}(\theta_1,\theta_2,\phi_1',\phi_2') \middle| \Upsilon_{l\,l_1 l_2}^{0}(\theta_1,\theta_2,\phi_1',\phi_2') \middle| \Upsilon_{j'_{12} j'_1 j'_2}^{m''_{12}}(\theta_1,\theta_2,\phi_1',\phi_2') \right\rangle. \end{aligned} \qquad (15)$$

In fact, even from here one may see that matrix elements are non-zero only if $m'_{12} = m''_{12}$. This property can be derived in more rigorous way, by using Eq. (1) in Eq. (15) three times (for each of the four-dimensional functions Y), and splitting the four-dimensional integral onto two two-dimensional integrals, as follows:

$$\begin{aligned} M_{j'_{12} m''_{12} j'_1 j'_2}^{j_{12} m'_{12} j_1 j_2}(R) = & \sum_{l\,l_1 l_2} \sqrt{\frac{2l+1}{4\pi}} A_{l\,l_1 l_2}(R) \\ & \times \sum_{m'_1 m'_2 m''_1 m''_2 m} \left\langle l_1 m l_2 - m \middle| l 0 \right\rangle \left\langle j_1 m'_1 j_2 m'_2 \middle| j_{12} m'_{12} \right\rangle \left\langle j'_1 m''_1 j'_2 m''_2 \middle| j'_{12} m''_{12} \right\rangle \\ & \times \left\langle Y_{j_1}^{m'_1}(\theta_1,\phi_1') \middle| Y_{l_1}^{m}(\theta_1,\phi_1') \middle| Y_{j'_1}^{m''_1}(\theta_1,\phi_1') \right\rangle \left\langle Y_{j_2}^{m'_2}(\theta_2,\phi_2') \middle| Y_{l_2}^{-m}(\theta_2,\phi_2') \middle| Y_{j'_2}^{m''_2}(\theta_2,\phi_2') \right\rangle. \end{aligned}$$

(16)

This formula allows seeing that matrix elements are non-zero only if $m_1' = m_1'' + m$ and $m_2' = m_2'' - m$ (from the integrals), but also only if $m_{12}' = m_1' + m_2'$ and $m_{12}'' = m_1'' + m_2''$ (from the Clebsch-Gordan coefficients). All these conditions can be satisfied simultaneously only if $m_{12}' = m_{12}''$. So, the matrix M is block-diagonal in m_{12}', with each block describing transitions from $j_{12} j_1 j_2$ to $j_{12}' j_1' j_2'$, within the same value of m_{12}'. For convenience, the index m_{12}' can be omitted from the list of indexes for this matrix, namely, we can write $M^{j_{12} j_1 j_2}_{j_{12}' j_1' j_2'}$, meaning that such blocks should be computed for all values of m_{12}'.

Finally, using the two simplifications discussed above, we can rewrite Eq. (9) in the following convenient form, where transitions between the levels $j_{12} j_1 j_2$ (within m_{12}') are driven by matrix M, while transitions between the states m_{12}' (within j_{12}) are driven by matrix V:

$$\frac{\partial a^{m_{12}'}_{j_{12} j_1 j_2}}{\partial t} = -i \sum_{j_{12}' j_1' j_2'} a^{m_{12}'}_{j_{12}' j_1' j_2'} M^{j_{12} j_1 j_2}_{j_{12}' j_1' j_2'}(R) \exp\{i(E_{j_1 j_2} - E_{j_1' j_2'})t\} - i \sum_{m_{12}''} a^{m_{12}''}_{j_{12} j_1 j_2} \; V^{m_{12}'}_{m_{12}''} \dot{\Phi} \,. \qquad (17)$$

This is a system of coupled differential equations, of a form quite typical to quantum mechanics (except, may be, the presence of time-dependent classical variables R and Φ) which can propagated in time using any suitable method, such as general 4$^{\text{th}}$-order Runge-Kutta, or more specialized numerical methods.

The equations of motion for classical degrees of freedom, coordinates $R(t)$ and $\Phi(t)$ of the vector $\mathbf{Q}$, are derived using the Ehrenfest theorem as explained in our earlier work [29]. Interestingly, for the molecule + molecule system studied here, the classical

equations come out identical to those we derived earlier for the molecule + atom system.[29,31] This makes sense, simply because the variables R and Φ are exactly the same. Thus, we will not repeat the derivations here, and will only summarize the final equations, for the sake of completeness:

$$\dot{R} = \frac{P_R}{\mu}, \tag{18}$$

$$\dot{\Phi} = \frac{P_\Phi}{\mu R^2}, \tag{19}$$

$$\dot{P}_R = -\sum_{j'_{12} m''_{12} j'_1 j'_2} \sum_{j_{12} m'_{12} j_1 j_2} (a^{m''_{12}}_{j'_{12} j'_1 j'_2})^* a^{m'_{12}}_{j_{12} j_1 j_2} \exp\{i(E_{j'_1 j'_2} - E_{j_1 j_2})t\} \frac{\partial M^{j'_{12} j'_1 j'_2}_{j_{12} j_1 j_2}(R)}{\partial R} + \frac{P_\Phi^2}{\mu R^3}, \tag{20}$$

$$\dot{P}_\Phi = -i \sum_{j'_{12} m''_{12} j'_1 j'_2} \sum_{j_{12} m'_{12} j_1 j_2} (a^{m''_{12}}_{j'_{12} j'_1 j'_2})^* a^{m'_{12}}_{j_{12} j_1 j_2} \exp\{i(E_{j'_1 j'_2} - E_{j_1 j_2})t\} \left[\mathbf{M},\mathbf{V}\right]^{j'_{12} m''_{12} j'_1 j'}_{j_{12} m'_{12} j_1 j_2} . \tag{21}$$

Here μ is a molecule-molecule reduced mass. Equation (21) includes a commutator of matrixes $M^{j'_{12} j'_1 j'_2}_{j_{12} j_1 j_2}$ and $V^{m''_{12}}_{m'_{12}}$. These equations can be propagated in time and space numerically, together with equations for quantum degrees of freedom, Eq. (17). In practice, we compute matrix elements on a predefined grid of points R_i along the coordinate R, just as in the full-quantum approach. During the propagation, when MQCT trajectory comes to vicinity of a grid point, we simply spline those pre-computed matrix elements using 1D-spline of several points closest to this point. Such procedure is very efficient and accurate using quadratic or qubic spline, carries little overhead, and is similar to splining the PES (defined on a grid) during propagation of purely-classical trajectories.

5.2.4 Sampling of the Initial Conditions

Our procedure for computing state-to-state cross sections includes sampling of the initial conditions for classical degrees of freedom, but also it incorporates a sum over the final and an average over the initial degenerate states, just as in the full-quantum calculations. Namely, for a state-to-state transition of interest $j_1^{\rm ini} j_2^{\rm ini} \to j_1^{\rm fin} j_2^{\rm fin}$ a set of $(2j_1^{\rm ini}+1)(2j_2^{\rm ini}+1)$ independent calculations has to be carried out, with all possible values of the initial $j_{12}^{\rm ini}$ and $m_{12}^{\rm ini}$ needed to construct the average:

$$\sigma_{j_1^{\rm ini} j_2^{\rm ini} \to j_1^{\rm fin} j_2^{\rm fin}} = \frac{1}{(2j_1^{\rm ini}+1)(2j_2^{\rm ini}+1)} \sum_{j_{12}^{\rm ini}=\left|j_1^{\rm ini}-j_2^{\rm ini}\right|}^{j_1^{\rm ini}+j_2^{\rm ini}} \left(\sum_{m_{12}^{\rm ini}=-j_{12}^{\rm ini}}^{j_{12}} \sigma_{j_{12}^{\rm ini} m_{12}^{\rm ini} j_1^{\rm ini} j_2^{\rm ini} \to j_1^{\rm fin} j_2^{\rm fin}} \right). \qquad (22)$$

For each of these calculations we sample randomly and uniformly the value of J, that corresponds to the total angular momentum in the problem, through the range of $0 \le J \le J^{\max}$. The value of $J^{\max}$ is a convergence parameter, just as in the full-quantum calculations. For a given pair of $j_{12}^{\rm ini}$ and J we sample the value of l randomly and uniformly through the range $\left|J - j_{12}^{\rm ini}\right| \le l \le J + j_{12}^{\rm ini}$. It corresponds to the orbital angular momentum in the molecule-molecule system, $\mathbf{J} = \mathbf{l} + \mathbf{j}_{12}$, and is used to define classical initial conditions as follows:

$$P_\Phi = \sqrt{\ell(\ell+1)}\,, \qquad (23)$$

$$P_R = \sqrt{2\mu E - P_\Phi^2 / R^2}\,, \qquad (24)$$

where *E* is the kinetic energy of collision (not the total energy), while *R* is the initial molecule-molecule separation (about 25 Bohr). The initial value of Φ is arbitrary, and we use $\Phi = 0$. Note that although l is closely related to the classical collision impact

parameter, we do not sample or use the impact parameter directly. The goal is keep MQCT as close as possible to the quantum formalism.

With the initial conditions of Eqs. (23-24) the classical-like equations (18-21), and a system of quantum-like coupled equations (17) are propagated through the collision event, till the point when the molecule-molecule separation exceeds the initial limiting value. The final values of probability amplitudes are used to compute transition probability (summed over the degenerate final states):

$$\begin{aligned} P^{(i)}_{j_{12}^{\rm ini} m_{12}'^{\rm ini} j_1^{\rm ini} j_2^{\rm ini} \to j_1^{\rm fin} j_2^{\rm fin}} &= \sum_{j_{12}^{\rm fin}=\left|j_1^{\rm fin}-j_2^{\rm fin}\right|}^{j_1^{\rm fin}+j_2^{\rm fin}} \sum_{m_{12}'^{\rm fin}=-j_{12}^{\rm fin}}^{j_{12}^{\rm fin}} P^{(i)}_{j_{12}^{\rm ini} m_{12}'^{\rm ini} j_1^{\rm ini} j_2^{\rm ini} \to j_{12}^{\rm fin} m_{12}'^{\rm fin} j_1^{\rm fin} j_2^{\rm fin}} \\ &= \sum_{j_{12}^{\rm fin}=\left|j_1^{\rm fin}-j_2^{\rm fin}\right|}^{j_1^{\rm fin}+j_2^{\rm fin}} \sum_{m_{12}'^{\rm fin}=-j_{12}^{\rm fin}}^{j_{12}^{\rm fin}} \left| a^{m_{12}'^{\rm fin}}_{j_{12}^{\rm fin} j_1^{\rm fin} j_2^{\rm fin}} \right|^2 . \end{aligned} \tag{25}$$

Here index i labels independent trajectories in a batch of N trajectories. This number is also a convergence parameter (here, around 200 per one initial state, per energy point). Average of probability over the batch gives cross section:

$$\sigma_{j_{12}^{\rm ini} m_{12}'^{\rm ini} j_1^{\rm ini} j_2^{\rm ini} \to j_1^{\rm fin} j_2^{\rm fin}} = \frac{\pi J_{\max}}{N k^2} \sum_i (2J^{(i)}+1) P^{(i)}_{j_{12}^{\rm ini} m_{12}'^{\rm ini} j_1^{\rm ini} j_2^{\rm ini} \to j_1^{\rm fin} j_2^{\rm fin}} , \tag{26}$$

which has to be substituted into Eq. (22). Note that sampling over J and l is done in one step (two-dimensional sampling), since there is no requirement that every term in Eq. (26) is converged. We only require that the entire sum in Eq. (26) is converged (*i.e.*, only the average cross section, rather than each individual probability). Thus, the procedure is very efficient and only a moderate number of MQCT trajectories is needed.

5.3 Numerical Results for N_2+H_2

Theory developed in the previous section was applied to N_2 + H_2 system. We had no goal of describing this process as accurately as possible, or as completely as possible, but rather to test the equations we derived, the computational methodology we developed, and the codes we wrote so far. Thus, we only considered several exemplary state-to-state transition processes, and have taken into consideration only a few terms in the potential energy expansion, just enough for these transitions to occur in the N_2 + H_2 collisions. The following terms of the potential energy expansion in Eq. (14) were included: A_{000}, A_{202}, A_{022} and A_{224}. The potential energy surface of Ref. 40 was used.

In addition to MQCT calculations we also carried out the full-quantum CC-calculations using MOLSCAT,[41] and used those as a benchmark. MOLSCAT calculations were much more demanding computationally, compared to MQCT calculations. In fact, for the results presented below, the range of collision energies and the size of rotational basis set were dictated by numerical cost of the full-quantum CC-calculations, not by MQCT. In some cases, we intentionally have taken small basis set, in order to make the MOLSCAT calculations less costly. But, in all cases the MQCT and the MOLSCAT calculations were carried out with exactly the same rotational basis set and the same values of $J^{\max}$, in order to make comparison straightforward and meaningful.

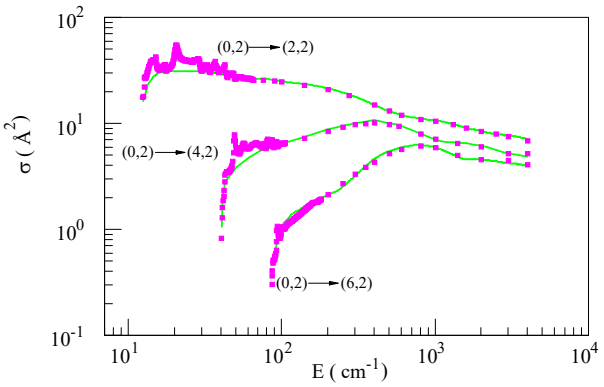

Figure 3: State-to-state cross sections for excitation of $N_2(j=0)$ by collisions with $H_2(j=2)$. Initial and final rotational states of collision partners are labelled as (j_1, j_2), where the first index belongs to N_2 while the second index belongs to H_2. Full-quantum benchmark data are shown by pink symbols, while results of MQCT are shown by green lines. See text for detailed description of this computational experiment.

The first test case was rotational excitation of $N_2(j_1 = 0)$ by $H_2(j_2 = 2)$, with no rotational transitions allowed in H_2. Excitations of N_2 into $j_1 = 2$, 4 and 6 were analyzed. Thus, molecular basis set for H_2 included only one rotational state, $j_2 = 2$, while the basis set for N_2 included 9 rotational states, up to $j_1 = 16$. Only even values of j_1 were included, since homo-nuclear N_2 is symmetric, so that only transitions with even values of Δj are allowed (notice that these quantum properties can be rigorously described by MQCT.) As it was explained in Sec. 5.2.4, our approach requires running $(2j_1^{\text{ini}} + 1)(2j_2^{\text{ini}} + 1)$ independent calculations. Accordingly, we carried out 5 calculations with initial states $-2 \le m'_{12} \le 2$ of $j_{12} = 2$. At low collision energies, we used $J^{\max} = 15$, while at high collision energies we used $J^{\max} = 120$, in both full-quantum and MQCT calculations. Results are presented in Fig. 3 for the range of collisional energies from the excitation threshold, which is 11.92 cm^{-1} for transition into $j_1 = 2$, up to the energy 4000 cm^{-1}.

The full-quantum benchmark data illustrate that energy dependencies of state-to-state cross sections are quite involved (see Fig. 3). For all three transitions the value of cross section rises quickly at the corresponding threshold. Scattering resonances are observed in a short energy range just above the threshold, after which the dependence is smooth, but not necessarily monotonic. Thus, the dependencies for excitation of $j_1 = 4$ and 6 exhibit pronounced maxima near collision energies of 400 cm^{-1} and 800 cm^{-1}, respectively. For excitation of $j_1 = 2$ the maximum is less important, and is hidden by resonances at low energies, near 20 cm^{-1}. At higher energies, cross sections for all three transitions tend to decrease. On top of these major trends, we also see some small-amplitude oscillations of cross section dependencies, most noticeable in the case of excitation into $j_1 = 2$ (see Fig. 3). Besides resonances, MQCT captures all these features. Even the excitation thresholds, and even the small oscillations of cross sections, are accurately reproduced.

At higher collision energies the results of MQCT become nearly identical to the full-quantum results (see Fig. 3). This, perhaps, is the most practically important aspect of MQCT, since the full-quantum calculations become prohibitively difficult at higher energies, while MQCT calculations remain affordable. At lower energies the treatment of resonances is probably possible within MQCT [36], but this topic is beyond the scope of the present thesis, and is less important in practice, since the full-quantum calculations are quite affordable in the low-energy regime. Accurate description of the excitation thresholds within MQCT is possible due to the symmetrized approach [22], also known as the average velocity approach, which we described in detail in our earlier paper [28].

The second test case we chosen was a process of quenching of rotationally excited $H_2(j_2 = 2)$ into its ground state $j_2 = 0$ by collision with ground state N_2 ($j_1 = 0$). In these calculations the basis set included $j_1 = 0$ and 2 for N_2, and, $j_2 = 0$ and 2 for H_2, which is just two states for each collision partner. Again, $(2j_1^{\text{ini}} + 1)(2j_2^{\text{ini}} + 1)$ of independent calculations were carried out, which is 5 for $j_{12} = 2$, with $-2 \le m'_{12} \le 2$. Note that this process does not have a threshold, since the internal rotational energy is released. The amount of energy released by H_2 is quite significant, close to 360 cm^{-1}, consistent with $\Delta j_2 = -2$. The range of collision energies considered here was also broad, from 1 cm^{-1} up to 4000 cm^{-1}. MQCT results are presented in Fig. 4, together with the full-quantum benchmark data obtained with MOLSCAT using the same basis set.

Figure 4 illustrates that, despite the fact that energy dependence of inelastic cross section is not simple for this state-to-state transition, the agreement between MQCT and the benchmark data is very good. Note that although there is no threshold for the process the value of cross section changes by more than an order of magnitude through the range of considered energies, and exhibits a pronounced minimum near collision energy of 60 cm^{-1}. In the low-energy regime the value of cross section growth, resembling the asymptotic Wigner law [42,43]. Here MQCT is less accurate, which is expected from a method like MQCT (that incorporates a classical component) in the quantum scattering regime (where the asymptotic Wigner law behavior is typical). Several broad resonances in the energy range below 20 cm^{-1} (see Fig. 4) are reproduced by MQCT only on average. At higher energies, the value of cross section also grows. Importantly, at collision energies above 50 cm^{-1} the results of MQCT are nearly identical to the full-quantum results.

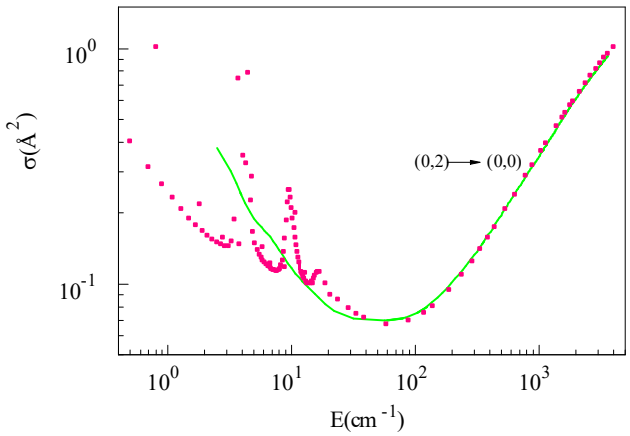

Figure 4. State-to-state cross sections for quenching of $H_2(j=2)$ by collisions with $N_2(j=0)$. Initial and final rotational states of collision partners are labelled as (j_1, j_2), where the first index belongs to N_2 while the second index belongs to H_2. Full-quantum benchmark data are shown by red symbols, while results of MQCT are shown by green line. See text for detailed description of this computational experiment.

In order to derive the scaling law of MQCT for the molecule + molecule case, we plotted in Fig. 5 the computational cost of our calculations presented in Fig. 3. The first frame, Fig. 5(a) shows CPU time as function of the number of channels. Here the notion of a "channel" should be discussed, since it is different from the channel in the molecule + atom case. Thus, in the molecule + atom case the channels are non-degenerate energy *levels*. Those are labelled by j in the case of the diatomic molecule (or by $j_{k_a k_c}$ in the case of a general asymmetric top) and include $2j+1$ degenerate *states* labelled by m', within each channel. In contrast, in the molecule + molecule case

considered here the non-degenerate channels are labelled by the pairs of indexes (j_1, j_2). Such "channels" include $(2j_1+1)(2j_2+1)$ degenerate states labeled by j_{12}, and for each value of j_{12} they include the $2j_{12}+1$ of degenerate projection states labelled by m'_{12}. So, the channels in the molecule + molecule case include more degenerate states than the channels in the molecule + atom case. Still, we prefer to analyze numerical performance as a function of channels, rather than a function of states, because this can be compared directly to the scaling law of the full-quantum calculations that also have channels, but involve no projection states labelled by m'.

For example, in the previous work we found that the cost of fully converged MQCT for the molecule + atom case scales as $n^{2.5}$, where n is the number of channels. In this work, we see from Fig. 4(a) that the cost scales as $n^{3.5}$, which makes sense. The additional factor of n comes from presence of additional degenerate states labelled by j_{12}. Note that this scaling law represents the overall cost of MQCT calculations, converged with respect to $J^{\max}$ at each collision energy. In contrast, when the scaling law of the full quantum calculations is discussed, it is usually reported for an idealized test, when the number of channels is changed, but the value of $J^{\max}$ and the number of partial scattering waves needed for convergence are kept constant. But in practice, when the collision energy is raised, the value of $J^{\max}$ needed for convergence also grows, and the cost of calculations increases dramatically, particularly for heavy collision partners. While the scaling law of the full-quantum calculations with respect to the number of channels is only on the order of n^4 in an idealized situation, in reality, when the calculations are carried out for a broad energy range, the overall cost reaches n^6 to

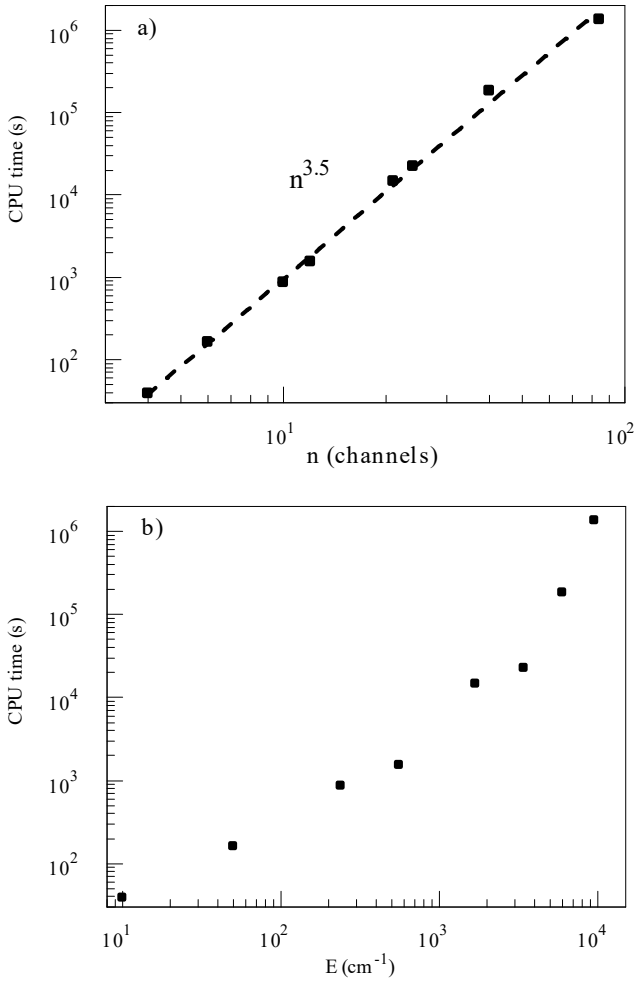

Figure 5. Computational cost of MQCT calculations presented in Fig. 3 for N_2 + H_2. Two frames correspond to two different variables: a) as a function of the number of channels included in calculations; b) as a function of collision energy.

n^7 . Importantly, in MQCT such "overhead" does not occur (since the scattering process is treated classically) and the cost remains low, $n^{3.5}$, as shown in Fig. 5(a).

In this respect, we want to mention that the data presented in Fig. 3 were reported only for collision energies below 4000 cm^{-1} due to significant computational cost of the MOLSCAT calculations at higher energies. Practical full-quantum calculations at higher collision energies would require the parallel version of MOLSCAT, which we did not use. However, MQCT calculations were quite efficient at even higher energies. For example, in Fig. 5(b) we presented the cost of MQCT calculations as a function of collision energy up to 10000 cm^{-1}.

We worked out the mixed quantum classical theory, MQCT, for inelastic collision of two molecules, where the internal (rotational) motion of the molecules is treated with quantum mechanics, while the molecule-molecule scattering is described by classical trajectories. The resultant MQCT formalism includes a system of coupled equations for quantum probability amplitudes, and the mean-field classical equations of motion. The procedure for sampling the initial conditions and computing cross sections has also been devised. Derivations presented here were carried out for two diatomic molecules treated as rigid rotors, but extension onto two polyatomic molecules, or inclusion of the vibrational states into the basis set, are both relatively straightforward. To our best knowledge such theory has never been formulated in the past.

5.4 Identical Particles

In the feature article published in JPCA [44] we outlined history and recent advances in development and applications of the mixed quantum-classical theory (MQCT) for inelastic scattering. In this method for description of molecular collisions the internal (rotational, vibrational) states of collision partners are treated using time-dependent Schrodinger equation, while their relative (translational) motion is treated using classical trajectories [30-36,45]. Energy is exchanged between vibrational, rotational and translational degrees of freedom, but the total energy is conserved [25-29].

The corresponding theory for all relevant cases, starting with the simplest *diatomic + atom*, and going to the most general *molecule + molecule* case, including collision of two *asymmetric-top* rotors, has been recently developed. Careful benchmark studies have also been carried out for several diatomic molecules, such as CO + He [29], N_2 + Na [33], and H_2 + He [34], triatomic H_2O + He [35], tetra-atomic CH_3 + He [44], and polyatomic molecule [36] $HCOOCH_3$ + He (all collided with an atom), but also for one molecule + molecule system, N_2 + H_2 [45]. These calculations included collisions of light and heavy collision partners, at low and high collision energies (in a broad range from 1 to 10^4 cm^{-1}), near threshold for excitation and for the quenching processes that have no threshold, for both rotational and vibrational transitions, of total and differential scattering cross sections (including forward scattering), at low levels of rotational excitation and for highly excited cases (*e.g.*, j = 22), running the fully-coupled MQCT calculations and a simplified (coupled-states) version of MQCT.

It was found that at high collision energies this method is accurate, often giving results *identical* to those of accurate full-quantum close-coupling calculations. At moderate collision energies (typical to room temperature and below) the differences on order of 10% have been observed for some of the systems listed above. At low collision energies predictions of MQCT are often less accurate, particularly near threshold energy, but even there they remain reasonable (within 30%, see Figs. 10 and 11 in Ref. 44). It is still not clear whether MQCT approach is suitable for description of individual scattering resonances but we saw that when resonances are multiple and narrow [33,45] MQCT describes well the non-resonant “background” value of scattering cross section, while

when the resonances are broad and overlapping [35,45] MQCT gives an averaged over resonances behavior.

Importantly, the computational cost of MQCT is much lower compared to the cost of full-quantum coupled-channel scattering calculations, and it scales more favorably with increasing complexity of the problem (collision energy, number of internal states, maximum value of total angular momentum J_{max}) [35,36,44,45]. This allows treating collisions of more complicated molecular systems than it was possible previously, including small organic molecules, such as $HCOOCH_3$, and triatomic + triatomic systems. Demands for such inelastic scattering calculations are significant nowadays due to the needs of astrochemical community [5,11,46-49], but also in other fields such as atmospheric chemistry [25-27,1,12] and combustion [3,50].

In order to enable broad and general applications of MQCT to the important problems in various fields we still have to demonstrate that this method is able to reproduce (with sufficient accuracy) several quantum phenomena important in scattering. As we outlined in the recent feature article [44], one of these remaining challenges was description of identical particle scattering. Indistinguishability of collision partners imposes symmetry constraints onto wave function of the system, which is important in all scattering regimes (low and high collision energy), for all systems (light and heavy), for all state-to-state transitions, and manifests in all kinds of observables. Thus, incorporation of the exchange symmetry into MQCT is very much needed. Examples of the systems where this feature is essential include $H_2 + H_2$ [7], CO + CO [51], NH + NH [52], and many other diatomic molecules, but also triatomic molecules, such as $H_2O + H_2O$ [53] or HCN + HCN [54] to name just a few. Theoretical prediction of cross sections for

rotational excitation and quenching of these (and many other) molecules is needed, for example, for interpretation of spectra emitted by various kinds of astrochemical objects, such as cold molecular clouds, pre-stellar cores, and cometary comas [5,11,46-49].

In the following subsection, we propose how this symmetry can be built into MQCT calculations, and we demonstrate that it works really well for the case of $H_2 + H_2$, which is the lightest, the most quantum (rather than classical) system. To our best knowledge this has never been done in the past.

5.5 Theory for Identical Particle Scattering within MQCT Framework

Probability distribution is an observable moiety, and it should not change under swap of two identical particles. This means that wave function of the system should either remain the same, or change its sign under this operation. In MQCT this wave function depends on quantum degrees of freedom that include, in the case of rotationally inelastic scattering, the angles needed to describe individual orientations of colliding molecules. For a diatomic + diatomic system those are $\mathbf{r}_1 = (r_1, \theta_1, \phi_1)$ and $\mathbf{r}_2 = (r_2, \theta_2, \phi_2)$, or using a composite notation $\mathbf{r} = (\mathbf{r}_1, \mathbf{r}_2)$. These quantum degrees of freedom are defined in the so-called body-fixed (BF) reference frame, *tied to the molecule-molecule vector* $\mathbf{Q}$, evolution of which is treated classically in the space-fixed (SF) reference frame. Note that, although here we focus on rotational transitions only, we still include, for generality, the bond length of each molecule, since this allows describing vibrational states and, in the future, will permit to study ro-vibrational transitions. The total time-dependent wave function of the system is expressed in MQCT as follows (in atomic units):

$$\psi(\mathbf{r},t) = \sum_{nm} a_{nm}(t)\, \Psi_{nm}(\mathbf{r})\, e^{-iE_n t}\,,$$

(1)

where a_{nm} are time-dependent expansion coefficients, Ψ_{nm} is basis set of rotational eigenstates of the system, while E_n are their corresponding energy eigenvalues. Index *n* is a composite index that labels states and its meaning depends on the system. For a diatomic + diatomic case $n \equiv \{j_1 j_2 j\}$, where j_1 and j_2 are angular momenta of individual molecules, while j represents the total angular momentum of two molecules, $\mathbf{j} = \mathbf{j}_1 + \mathbf{j}_2$, which is also quantized in MQCT: $|j_1 - j_2| \le j \le j_1 + j_2$. The meaning of *m* is projection of $\mathbf{j}$ onto the molecule-molecule vector **Q**, which plays role of *z*-axis in the BF reference frame. Energy E_n of an eigenstate depends on *n* only, and does not depend on *m*.

The rotational eigenstates $\Psi_{nm}(\mathbf{r}) \equiv \Psi_{j_1 j_2 j m}(\mathbf{r}_1, \mathbf{r}_2)$ are analytic for diatomic + diatomic systems, and are expressed though spherical harmonics of two molecules using Glebsch-Gordan coefficients[38]. In the case of non-identical molecules, say AB + CD, we use [45]

$$\Psi_{j_1 j_2 j m}(\mathbf{r}_1, \mathbf{r}_2) = \sum_{m_1 m_2} (j_1 m_1 j_2 m_2 \,|\, j\, m) Y_{j_1 m_1}(\mathbf{r}_1) Y_{j_2 m_2}(\mathbf{r}_2)\,. \qquad (2)$$

In the case of identical molecules, say AB + AB, under swap of the molecules 1 and 2, this expression transforms as follows

$$\begin{aligned}\widetilde{\Psi}_{j_1 j_2 j m}(\mathbf{r}_2,\mathbf{r}_1) &= \sum_{m_1 m_2}(j_2 m_2 j_1 m_1 \mid j\ m)\,Y_{j_1 m_1}(-\mathbf{r}_2)\,Y_{j_2 m_2}(-\mathbf{r}_1)\\ &= \sum_{m_1 m_2}(-1)^{j_1+j_2+j}(j_1 m_1 j_2 m_2 \mid j\ m)\,(-1)^{j_1}Y_{j_2 m_2}(\mathbf{r}_1)\,(-1)^{j_2}Y_{j_1 m_1}(\mathbf{r}_2)\\ &= (-1)^{j}\sum_{m_1 m_2}(j_1 m_1 j_2 m_2 \mid j\ m)\,Y_{j_2 m_2}(\mathbf{r}_1)\,Y_{j_1 m_1}(\mathbf{r}_2)\\ &= (-1)^{j}\Psi_{j_2 j_1 j\ m}(\mathbf{r}_1,\mathbf{r}_2).\end{aligned} \tag{3}$$

Note that here we replaced $\mathbf{r}_1$ by $-\mathbf{r}_1$, and $\mathbf{r}_2$ by $-\mathbf{r}_2$, because under this swap the direction of the molecule-molecule vector **Q** in the SF reference frame also changes, $(X,Y,Z)\rightarrow(-X,-Y,-Z)$, and thus orientation of the entire BF reference frame changes with respect to the SF reference frame. Using this transformed version, the symmetrized wave function of given parity can be written as

$$\begin{aligned}\Psi^{(\pm)}{}_{j_1 j_2 j\ m} &= \frac{1}{\sqrt{2(1+\delta_{j_1 j_2})}}\left[\Psi_{j_1 j_2 j m}(\mathbf{r}_1,\mathbf{r}_2) \pm \widetilde{\Psi}_{j_1 j_2 j m}(\mathbf{r}_2,\mathbf{r}_1)\right]\\ &= \frac{1}{\sqrt{2(1+\delta_{j_1 j_2})}}\left[\Psi_{j_1 j_2 j m}(\mathbf{r}_1,\mathbf{r}_2) \pm (-1)^{j}\Psi_{j_2 j_1 j m}(\mathbf{r}_1,\mathbf{r}_2)\right]\end{aligned} \tag{4}$$

Symmetrized states of positive and negative parity are degenerate if the set of quantum numbers $n=\{j_1 j_2 j\}$ is the same. Using these states in the expansion of Eq. (1), substituting this expansion into the time-dependent Schrodinger equation, and using the Ehrenfest theorem leads to a set of coupled differential equations for time-evolution of probability amplitudes a_{nm}, that are exactly equivalent to the MQCT equations reported earlier [44,45,30,34], except that now the state-to-state transition matrix is different, as explained next.

Consider transition from the initial state $n=\{j_1 j_2 j\}$ to the final state $n'=\{j_1' j_2' j'\}$. For the case of non-identical collision partners the corresponding state-to-sate transition matrix elements $M_{n'}^{n}$ for diatomic + diatomic system were derived in our recent paper (see Eq. (16) in Ref. 45). Using those, the matrix elements of given parity $M_{n'}^{n(\pm)}$ for collision of identical molecules can be conveniently expressed as follows

$$\begin{aligned} M_{n'}^{n(\pm)} &= \frac{1}{2\sqrt{(1+\delta_{j_1 j_2})(1+\delta_{j_1' j_2'})}}\left[M_{n'}^{n} \pm (-1)^{j'} M_{\tilde{n}'}^{n} \pm (-1)^{j} M_{n'}^{\tilde{n}} + (-1)^{j+j'} M_{\tilde{n}'}^{\tilde{n}}\right] \\ &= \frac{1}{\sqrt{(1+\delta_{j_1 j_2})(1+\delta_{j_1' j_2'})}}\left[M_{n'}^{n} \pm (-1)^{j'} M_{\tilde{n}'}^{n}\right], \end{aligned} \tag{5}$$

where $\tilde{n}=\{j_2 j_1 j\}$ is obtained from n by permutation of j_1 with j_2. From Eq. (4) it follows that $\Psi^{\pm}{}_{\tilde{n}m}$ is different from $\Psi^{\pm}{}_{nm}$ just by an overall sign change, *i.e.*, they are practically equivalent. Thus, the basis set size in Eq. (1) can be effectively reduced by a factor of roughly two (compared to the case of non-identical molecules) to include only the states with $j_1 > j_2$. However, two independent sets of MQCT calculations are needed, with basis sets of each parity. Still, the reduction of matrix size has a dominant effect, which makes MQCT calculations for identical molecules less expensive, compared to the case of non-identical molecules. The states with $j_1 = j_2$ are all special, since they require only one set of calculations, with either even or odd parity basis functions, depending on the value of total j . This is because the second of those wave functions vanishes, according to Eq. (4).

Classical-like equations for evolution of the molecule-molecule vector in the SF reference frame also remain identical to those that we recently published[44,45,30,34],

except the form of state-to-state transition matrix (as explained above) and its gradients. Note that the relative (orbital) angular momentum ℓ of two collision partners, and the total angular momentum of the system J, are classical moieties within MQCT framework. They are sampled continuously, uniformly and randomly trough the ranges $0 \le J \le J_{max}$ and $|J - j| \le \ell \le J + j$, and are not quantized [44,45,30,34]. In contrast, in the full-quantum calculations ℓ is quantized and, in the case of identical-particle scattering, its value affects symmetry of the total wave function. Namely, instead of the factor of $(-1)^j$ in Eq. (4) of MQCT, the full-quantum version of this formula contains a factor of $(-1)^{j_1+j_2+j+\ell}$ where ℓ is included (see, for example, Eq. (14) in Ref. 31). Due to this, the full-quantum calculations for identical-particle scattering are done with basis functions of different parities for even and odd values of ℓ (depending on the value of $j_1 + j_2 + j$ in a given state). In order to mimic this effect within MQCT framework we see to options. One option, similar to "binning" used in the classical trajectory simulations, would be to include 50% of MQCT trajectories (say, with ℓ closer to even integers) in the calculations for one parity, and the remaining 50% of MQCT trajectories (say, with ℓ closer to odd integers) in the calculations for the other parity. Alternatively, one could sample ℓ continuously in exactly the same way for two independent MQCT calculations of both parities (without pretending that ℓ is quantized) but, at the end, to divide the resultant transition probabilities by two. In the classical scattering limit $\ell >> 1$ the two options should give similar results, if properly converged. The first option may be closer to quantum interpretation in the case of small ℓ. We employed the second option, since the idea of binning seemed to be less general.

Initial conditions for MQCT calculations are set up by specifying $a_{nm}=1$ for the initial state, where $n=\{j_1 j_2 j\}$. The values of probability amplitudes $a_{n'm'}$, where $n'=\{j_1' j_2' j'\}$, at the final moment of time (after the collision) are used to compute the corresponding state-to-state transition cross sections as follows

$$\sigma_{j_1 j_2}^{j_1' j_2' (\pm)} = \frac{\pi(1+\delta_{j_1 j_2})(1+\delta_{j_1' j_2'})}{k^2 (2j_1+1)(2j_2+1)} \times \sum_{j=|j_1-j_2|}^{j_1+j_2} \sum_{m=-j}^{j} \left(\frac{1}{2N} \sum_i \left(\sum_{j'=|j_1'-j_2'|}^{j_1'+j_2'} \sum_{m'=-j'}^{j'} (2J^{(i)}+1) \left| a_{j_1' j_2' j' m'}^{(\pm,i)} \right|^2 \right) \right) \quad (6)$$

In short, the inner parenthesis in this equation contain a sum of transition probabilities over the final degenerate states m' of each final state j' varied in the range $|j_1'-j_2'| \le j' \le j_1'+j_2'$ for a given pair of the final j_1' and j_2'. Those are averaged, by two outermost sums in Eq. (6), over the degenerate initial states. There are $2j+1$ of such initial m states for each initial j, with j taking values in the range $|j_1-j_2| \le j \le j_1+j_2$, which results in $(2j_1+1)(2j_2+1)$ degenerate initial states total for a given pair of the initial j_1 and j_2, which shows up in denominator of Eq. (6) for the overall average.

Sampling of the initial classical conditions for MQCT trajectories has already been discussed in our earlier publications [44,45,30,34]. Index i in Eq. (6) labels N collision trajectories in a batch, and MQCT cross section is averaged over those as well. This is done by the sum in the middle of Eq. (6), which replaces summation over ℓ in the corresponding full-quantum expression for cross section. The factor of ½ in front of the sum symbol appears only in the case of identical-molecule scattering, as we discussed

above. Equation (6) is used to compute $\sigma_{j_1 j_2}^{j_1' j_2'(+)}$ and $\sigma_{j_1 j_2}^{j_1' j_2'(-)}$ in two sets of independent calculations, then $\sigma_{j_1 j_2}^{j_1' j_2'} = \sigma_{j_1 j_2}^{j_1' j_2'(+)} + \sigma_{j_1 j_2}^{j_1' j_2'(-)}$.

It should also be mentioned that the internal symmetry of each collision partner is fully incorporated into MQCT in a straightforward way, through the elements of state-to-state transition matrix $M_{n'}^{n}$. Some elements of this matrix vanish (due to integration of the product of symmetric and antisymmetric functions), naturally leading to forbidden transitions. This is entirely equivalent to the full-quantum theory. For example, in homonuclear diatomic molecules only the transitions with $\Delta j = \pm 2$ are allowed [33,34,45]. Here, we consider para-H_2 in the initial state $j = 0$. So, the allowed final states will have even values of the angular momentum quantum number, such as $j = 2, 4, 6$, etc. Allowed vs. forbidden transitions have also been discussed for triatomic [35] and tetra-atomic [44] molecules with identical atoms, all within MQCT framework.

5.6 Numerical Results for H_2+H_2

As one can see, incorporation of permutation symmetry into MQCT is possible, and it does not require any additional numerical effort. In this study, we considered the case of H_2 + H_2 and employed the potential energy surface (PES) of Boothroyd et al [55]. In the past, full-quantum calculations of H_2 + H_2 rotationally inelastic scattering have been done on this surface by three different groups [56-59], and those references are used here as a benchmark. Figure 6 reports cross sections for excitation of the ground rotational state $(j_1 j_2) = (0\ 0)$ into several excited rotational states: $(j_1' j_2') = (2\ 0)$, $(2\ 2)$, $(4\ 0)$ and $(4\ 2)$, in a broad range of collision energies (note that in the case when the initial state is the ground rotational state only one set of calculations, that of positive parity, is needed: $\sigma_{j_1 j_2}^{j_1' j_2'} = \sigma_{j_1 j_2}^{j_1' j_2' (+)}$). Dependencies of cross sections on collision energy presented exhibit threshold at low energies, and tend to plateau at higher energies (see Fig. 6). Full-quantum results of Lee *et al* [56-57] are shown by dashed line, our MQCT results are

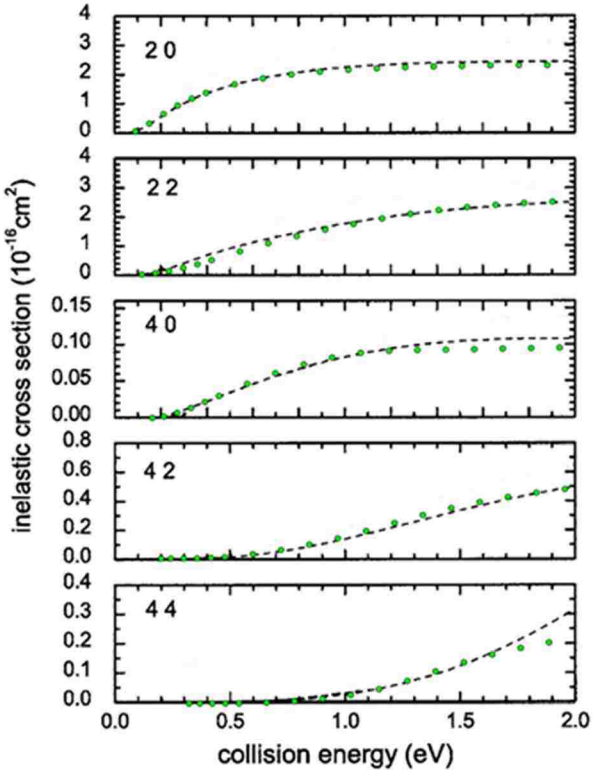

Figure 6. Inelastic cross section, as a function of energy in a broad range, for transitions into five lowest excited rotational states in H_2 + H_2 system, starting from the ground rotational state (0 0). Final state is indicated in the upper left corner of each frame. Full-quantum results of Lee *et al* [56] are shown by dashed line, our MQCT results are shown by green symbols. Reproduced with permission from Lee, T.-G.; Balakrishnan, N.; Forrey, R. C.; Stancil, P. C.; Schultz, D. R.; Ferland, G. J. *J. Chem. Phys*. **2006**, *125*, 114302-114302 (8)., Copyright AIP Publishing LLC.

shown by green symbols. We see that comparison is very good through the entire range of collision energies, and for all transitions. At higher collision energies the differences on order of ~10% are observed for excitation of state (4 0), and some larger deviations for state (4 4). Usually, MQCT is more accurate at higher energies, so, some non-vanishing deviations in that regime signal about possible differences in representation of the potential energy surface.

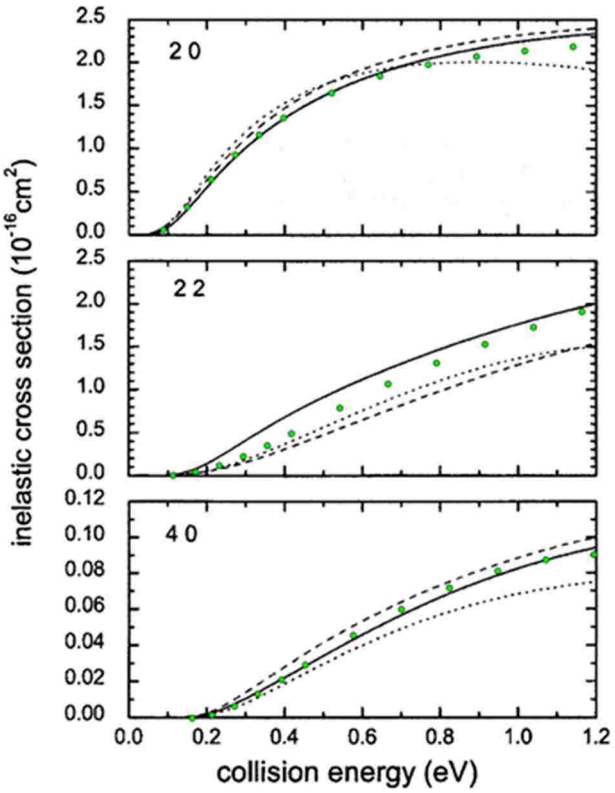

Figure 7. Inelastic cross section as a function of energy, with low-energy range emphasized, for excitation of three rotational states of H_2 + H_2 system, starting from the ground rotational state (0 0). Final state is indicated in the upper left corner of each frame. Full-quantum results of Lee *et al* [56] are shown by solid line, our MQCT results are shown by green symbols (same data as in Fig. 6). Results of Gatti *et al* [58] (dashed line) and of Lin and Guo [59] (dotted line) are also included. Reproduced with permission from Lee, T.-G.; Balakrishnan, N.; Forrey, R. C.; Stancil, P. C.; Schultz, D. R.; Ferland, G. J. *J. Chem. Phys.* **2007**, *126*, 179901, Copyright AIP Publishing LLC.

For these calculations, we expanded the PES of Ref. [55] over a symmetrized basis set of spherical harmonics, just as Lee *et al* [56] did. But we noticed that for convergence of numerical quadrature we needed more points that were used by Lee *et al* [56] (25 in our calculations vs 10 points in their). So, our *R*-dependent coefficients were slightly different from those presented in Fig. 2 of Ref. [56]. Also, we noticed that Eq. (12) of Lee *et al* [56] (or the same PES expansion of Diep *et al* [60]) was different from the original formula of Green (see Eq.

(4) in Ref. [38]) which is how the PES should be fed into the MOLSCAT [42] code. So, it looks like the differences observed in Fig. 6 at high energies for transitions into $(4\ 0)$ and $(4\ 4)$ are, most probably, due to some differences in PES representation.

Figure 7 focuses on the low energy regime for excitation of states $(j_1' j_2') = (2\ 0)$, $(2\ 2)$ and $(4\ 0)$, starting from the ground state $(j_1 j_2) = (0\ 0)$. Three sets of the full-quantum calculations are presented. Solid line represents results of time-independent coupled-channel calculations of Lee *et al* [56] (same data as in Fig. 6) and these data may be regarded as "exact". Dashed line represents results of Gatti *et al* [58], obtained using the time-dependent wave packet technique that, in principle, is also expected to be very accurate. Dotted line represents older results of Lin and Guo [59] obtained using an approximate method, with Coriolis coupling term neglected. One can see that out of three approximate methods our results (green dots) are closest to the "exact" results of Lee *et al* [56]. This underlines the importance of inclusion of the Coriolis coupling terms, which is done in MQCT in the mixed quantum/classical fashion, but appears to work really well even for the lightest, most non-classical molecule + molecule system, $H_2 + H_2$. For heavier molecules MQCT is expected to work even better.

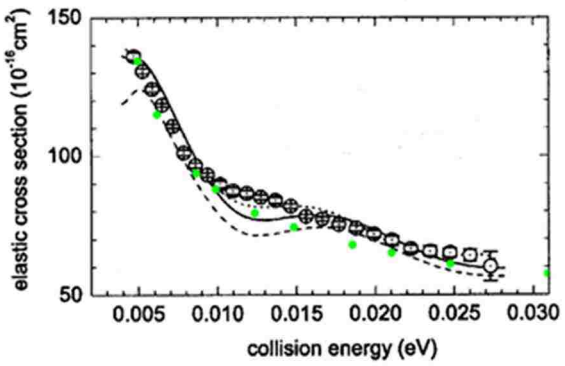

Figure 8. Elastic scattering cross section as a function of energy for the ground rotational state (00) of H_2 + H_2 system. Our MQCT results are shown by green symbols, experimental data of Bauer *et al* [61] are shown by large symbols with error bars. Solid, dashed and dotted lines represent results of calculations using different quantum methods and potential energy surfaces, as discussed by Lee *et al*[33] Reproduced with permission from Lee, T.-G.; Balakrishnan, N.; Forrey, R. C.; Stancil, P. C.; Schultz, D. R.; Ferland, G. J. *J. Chem. Phys*. **2006**, *125*, 114302-114302 (8)., Copyright AIP Publishing LLC.

Figure 8 compares results of several theoretical methods against experimental data of Bauer *et al* [61] (large symbols with error bars) for the elastic scattering channel, $(j_1 j_2) = (j_1' j_2') = (0\ 0)$. All theoretical data show good agreement with experiment, but some show more oscillations than it is observed in the experiment, where the dependence is rather smooth. MQCT results are certainly closer to experimental data than some of the earlier results, and are comparable to more recent theoretical data presented in Fig. 8.

It should be noted that some experimental data, at lower collision energies, are also available for the inelastic transition (00) → (20) in $H_2 + H_2$, from the work of Mate *et al* [62]. It was shown, however, that the BMKP PES of Boothroyd et al. [55] (employed here for benchmark purposes) disagrees with these experimental data. Another PES for $H_2 + H_2$ called DJ [60], is known to agree well with experimental data of Mate at all [62], but the range of validity of that PES is limited to collision energies below 3000 cm^{-1}. For this reason, the BMKP surface was chosen for the broad-range benchmark studies of this work, up to 2 eV, or ~16 000 cm^{-1}.

5.7 Conclusions for Chapter 5

We worked out the mixed quantum classical theory, MQCT, for inelastic collision of two molecules, where the internal (rotational) motion of the molecules is treated with quantum mechanics, while the molecule-molecule scattering is described by classical trajectories. The resultant MQCT formalism includes a system of coupled equations for quantum probability amplitudes, and the mean-field classical equations of motion. The procedure for sampling the initial conditions and computing cross sections has also been devised. Derivations presented here were carried out for two diatomic molecules treated as rigid rotors, but extension onto two polyatomic molecules, or inclusion of the vibrational

states into the basis set, are both relatively straightforward. To our best knowledge such theory has never been formulated in the past.

We also carried out some numerical tests of this theory, using a real system N_2 + H_2 with accurate potential energy surface, for a broad range of collision energies and several most important state-to-state transitions. Besides scattering resonances at low collision energies (which we did not try to describe here) the full-quantum results were reproduced by MQCT in detail, including the excitation thresholds, the maxima of cross sections, some small oscillations of energy dependencies, and the asymptotic behavior. Most importantly, at higher energies the results of MQCT become nearly identical to the full quantum results. It looks like in this energy range MQCT is a good alternative to the full-quantum calculations, since the latter become computationally expensive. The scaling law (computational cost *vs.* system complexity) was also determined for MQCT, and was found to be much more favorable compared to that of the full-quantum calculations.

One way of using MQCT is by blending its results with results of the full-quantum CC calculations. Namely, in order to compute rate coefficients, the values of cross sections are typically needed in a broad range of collision energies. One could start by running CC calculations at lower energies, because they are quite affordable there, and because scattering resonances may occur in this regime. At higher energies, where CC calculations become too demanding, one may start MQCT and check if it is in good agreement with CC method. If yes, one could stop CC calculations and continue with MQCT only, since it is more affordable and is sufficiently accurate at higher energies. The standard practice nowadays is to switch, at higher energies, from the exact CC to an approximate CS method. However, we showed in our recent work on several systems and in different collision regimes [33,35] that the fully-coupled MQCT is more accurate than CS approximation, where centrifugal coupling is neglected and transitions between different *m*-states do not occur. So, switching to MQCT, instead of CS, may be more advantageous.

Without the proper treatment of exchange symmetry, developed and tested in this article, the level of agreement that we see in Figs. 6-8 between MQCT and the full-quantum calculations or experiments, would be impossible. This development permits to carry out in the near future the calculations of rotationally inelastic scattering in such complex systems as H_2O + H_2O, and calculations of ro-vibrationally inelastic scattering in many

diatomic + diatomic systems which carries both fundamental and applied importance. Moreover, comparisons presented in Fig. 7 indicate that results of the fully-coupled MQCT (with Coriolis coupling included) are superior to results of the approximate quantum coupled-states calculations, where the corresponding coupling terms are omitted to reduce numerical cost. It is a very important conclusion, that it is better to include this type of interaction classically within MQCT framework, rather than neglect it completely. This finding has rather broad applications as well, in various sub-fields of the chemical reaction dynamics, beyond the rotationally inelastic scattering.

Several topics related to MQCT still require further work. Although less important from practical perspective, the question of scattering resonances is important from theoretical point of view. Earlier work by others indicates that it might be possible to use phase information to describe resonances within MQCT framework. Also, it is an interesting question whether MQCT is capable of describing accurately the so-called quasi-resonant energy transfer between two molecules. We plan exploring some of these issues in the near future.

Finally, from the method development perspective, it would be interesting to formulate MQCT using grid representation (DVR) of the rotational wave function, instead of the basis set expansion (FBR) used here. Such treatment of rotational wave packets may be more efficient for molecules and processes where large number of rotational states is excited, leading to large state-to-state transition matrixes that are difficult to handle. One important applications of such methodology would be in inelastic scattering by polyatomic molecules, where the spectra of rotational states are very dense.

BIBLIOGRAPHY for Chapter 5

1. M. Kirste, X. Wang, H.C. Schewe, G. Meijer, K. Liu, A. van der Avoird, L.M. Janssen, K.B. Gubbels, G.C. Groenenboom, S.Y. van de Meerakker, *Science* **338**, 1060-1063, (2012).

2. P. Dagdigian, M.H. Alexander, *J. Chem. Phys.* **135**, 064306, (2011).

3. N. Balakrishnan, G.C. Groenenboom, R.V. Krems, A. Dalgarno, *J. Chem. Phys.* **118**, 07386-07393, (2003).

4. E. Roueff, F. Lique*, Chem. Rev*. **113**, 8906-8938, (2013).

5. F. Daniel, M.-L. Dubernet, A. Grosjean, *Astron. Astrophys.* **A76**, 536-546 (2011).

6. F.S. dos Santos, N. Balakrishnan, R.C. Forrey, P.C. Stancil, *J. Chem. Phys.* **138**, 104302 (2013).

7. H. Song, Y. Lu, S.-Y. Lee, *J. Chem. Phys*. **136**, 114307 (2012).

8. A.M. Arthurs, A. Dalgarno, *Proc. Roy. Soc*. **A256**, 540-551 (1960).

9. J. Loreau, P. Zhang, A. Dalgarno. J. Chem. Phys **135**, 174301 (2011).

10. B. Yang, M. Nagao, W. Satomi, M. Kimura, P.C. Stancil, *Astrophys. J*. **765**, 77 (2013).

11. H.C. Schewe, Q. Ma, N. Vanhaecke, X. Wang, J. Kłos, M.H. Alexander, S.Y. van de Meerakker, G. Meijer, A. van der Avoird, P.J. Dagdigian, *J. Chem. Phys*. **142**, 204310 (2015).

12. A.Faure, L.Wiesenfeld, Y. Scribano, C. Ceccarelli, *Mon. Not. R. Astron. Soc.* **420**, 699- 704 (2012).

13. A. Mack, T.K. Clark, R.C. Forrey, N. Balakrishnan, T.-G. Lee, P.C. Stancil, *Phys. Rev. A* **74**, 052718 (2006).

14. R. Conte, P.L. Houston, J.M. Bowman*, J. Phys. Chem. A* **118**, 7742-7757 (2014).

15. G. Czakó, A.-L. Kaledin, J.M. Bowman, *J. Chem. Phys*. **132**, 164103 (2010).

16. D. Babikov, R.B. Walker, R.T. Pack, *J. Chem. Phys*. **117**, 8613-8622 (2002).

17. Y. Wang, J.M. Bowman, *J. Chem. Phys.* **139**, 154303 (2013).

18. R. Schinke, P. Fleurat-Lessard*, J. Chem. Phys.* **122**, 094317 (2005).

19. K.J. McCann, M.R. Flannery*, Chem. Phys. Lett*. **35**, 124-130 (1975).

20. K.J. McCann, M.R. Flannery, *J. Chem. Phys*. **63**, 4695-4707 (1975).

21. G.D. Billing, *Comp. Phys. Rep*. **1**, 237-296 (1984).

22. G.D. Billing, *The Quantum-Classical Theory*, Oxford University Press, (2002).

23. J. Avery, Z. Herman, *Review Article: Gert Due Billing (1946–2002), Chem. Soc. Rev.* **32**, iv-iv (1) (2003).

24. M.V. Ivanov, D. Babikov, *J. Chem. Phys*. **134**, 144107 (2011).

25. M.V. Ivanov, D. Babikov*, J. Chem. Phys*. **136**, 184304 (2012).

26. M.V. Ivanov, D. Babikov, *Proc. Natl. Acad. Sci*. **110**, 17708 (2013)

27. A. Semenov, D. Babikov, *J. Chem. Phys*. **138**, 164110 (2013).

28. A. Semenov, M.V. Ivanov, D. Babikov*, J. Chem. Phys*. **139**, 074306 (2013).

29. A. Semenov, D. Babikov, *J. Chem. Phys*. **139**, 174108 (2013).

30. G.D. Billing, *Chem. Phys. Lett.* **50**, 320-323, (1977).

31. M.V. Ivanov, M.-L. Dubernet, D. Babikov, *J. Chem. Phys*. **140**, 134301 (2014).

32. A. Semenov, D. Babikov, *J. Phys. Chem. Lett.* **5**, 275-278 (2014).

33. A. Semenov, D. Babikov, *J. Chem. Phys.* **140**, 044306 (2014).

34. A. Semenov, M.-L. Dubernet, D. Babikov, *J. Chem. Phys*. **141**, 114304 (2014).

35. A. Semenov, D. Babikov, *J. Phys. Chem. Lett*. **6**, 1854-1858 (2015).

36. K.J. McCann, M.R. Flannery, *J. Chem. Phys.* **69**, 5275-5287 (1978).

37. S. Green, *J. Chem. Phys*. **62**, 2271-2282 (1975).

38. D.A. Varshalovich, A.N. Moskalev, V.K. Khersonskii, *Quantum theory of angular momentum,* World Scientific, Singapore, (1988).

39. S. Green, *J. Chem. Phys.* **64**, 3463-3473 (1976).

40. L. Gomez, B. Bussery-Honvault, T. Cauchy, M. Bartolomei, D. Cappelletti, F. Pirani, *Chem. Phys. Lett*. **445**, 99–107 (2007).

41. J.M. Hutson, S.Green, MOLSCAT Computer Code, version 14;. Distributed by collaborative computational project No. 6 of the Engineering and Physical Sciences Research Council, Swindon, U.K.(1994).

42. N. Balakrishnan, A. Dalgarno R.C. Forrey, *J. Chem. Phys.* **113**, 621-632 (2000).

43. E.P. Wigner, *Phys. Rev*. **73**, 9, 1002 – 1009 (1948).

44. D. Babikov, A. Semenov, *J. Phys. Chem. A* **120**, 319-331 (2016).

45. A. Semenov, D. Babikov, *J. Phys. Chem. A* **119***,* 12329–12338 (2015).

46. M.Wernli, L.Wiesenfeld, A. Faure, P. Valiron, *Astron. Astrophys.* **464**, 1147-1154 (2007).

47. N. Troscompt, A. Faure, L. Wiesenfeld, C. Ceccarelli, P. Valiron, *Astron. Astrophys*. **493**, 687-696 (2009).

48. D. Rabli, D.R. Flower, *Mon. Not. R. Astron. Soc.* **406**, 95-110 (2010).

49. A. Faure, E. Josselin*, Astron. Astrophys.* **492**, 257-264, (2008).

50. O. Tkáč, Q. Ma, C.A. Rusher, S.J. Greaves, A.J. Orr-Ewing, P.J. Dagdigian, *J. Chem. Phys.* **140**, 204318 (2014).

51. S.A. Ndengue, R. Dawes, F. Gatti, *J. Phys. Chem. A* **119**, 7712-7723, (2015).

52. L.M.C. Janssen, A. van der Avoird, G.C. Groenenboom, *Phys. Rev. Lett.* **110**, 063201/1 (2013).

53. P.J. Agg, D.C. Clary, *J. Chem. Phys*. **95**, 1037-1048 (1991).

54. M. Hernández Vera, Y. Kalugina, O. Denis-Alpizar, T. Stoecklin, F. Lique, *J. Chem. Phys.* **140**, 224302 (2014).

55. A.I. Boothroyd, P.G. Martin, W.J. Keogh, M.J. Peterson, *J. Chem. Phys.* **116**, 666-689 (2002).

56. T.-G. Lee, N. Balakrishnan, R.C. Forrey, P.C. Stancil, D.R. Schultz, G.J. Ferland, *J. Chem. Phys*. **125**, 114302 (2006).

57. T.-G. Lee, N. Balakrishnan, R.C. Forrey, P.C. Stancil, D.R. Schultz, G.J. Ferland, *J. Chem. Phys.* **126**, 179901 (2007).

58. F. Gatti, F. Otto, S. Sukiasyan, H.-D. Meyer, *J. Chem. Phys.* **123**, 174311 (2005).

59. S. Lin, H. Guo, *J. Chem. Phys*. **117**, 5183-5191 (2002).

60. P. Diep, J.K. Johnson, *J. Chem. Phys*. **112**, 4465-4473 (2000).

61. W. Bauer, B. Lantzsch, J.P. Tonnies, K. Walaschewski, *Chem. Phys.* **17**, 19-26 (1976).

62. B. Maté1, F.Thibault, G.Tejeda, J.M. Fernández, S. Montero. *J. Chem. Phys.* **122**, 064313 (2005).

CHAPTER 6. INELASTIC SCATTERING OF TWO ASYMMETRIC-TOP ROTORS WITH APPLICATION TO H_2O + H_2O

6.1 The Limitations of the Full Quantum Approach and MQCT for Computationally Challengeable Systems

The standard full-quantum theory of molecular inelastic scattering, known as coupled channel (CC) formalism, leads to a large system of coupled differential equations [1,2]. The size of this system depends on the number of internal (rotational, vibrational) states of the molecules, but also on the number of molecule-molecule orbital angular momentum states (partial waves) taken into account for description of the scattering process. Numerically efficient methods and computer codes [3,4] have been developed to solve this problem, which enabled computational studies of many important scattering processes. Computationally affordable cases include atom + diatomic [5-7], diatomic + diatomic [8-11] and atom + triatomic [12] collisions.

As molecules become larger and heavier one has to deal with higher density of the internal states (*e.g.*, rotational levels in polyatomic molecules). The problem becomes severe at higher collision energies, when the number of accessible states becomes huge, simultaneously with a large number of partial waves required for description of heavy-particle scattering. For example, full-quantum calculations for rotationally inelastic scattering of diatomic + triatomic systems are very demanding [13-15]. Likewise, inelastic scattering calculations for polyatomic molecules appear to be affordable only at small scattering energies [16-19]. As the focus of community shifts towards more diverse and complex gas-phase chemistry [20], and as electronic structure calculations of potential energy surfaces become affordable for larger molecules, one starts begging for development of an alternative, more practical approach to molecular scattering.

In recent years, we developed a simplified mixed quantum/classical theory (MQCT) for inelastic scattering in which the relative motion of collision partners is treated approximately, classically, whereas their internal motion is still described rigorously using quantum mechanics. Since the scattering process is described by

independent classical trajectories there is no coupling between different values of orbital angular momentum, which reduces the sizes of matrixes and systems of equations (now determined only by the number of internal states of the molecules). Further speed up is achieved by intrinsic massive parallelism of MQCT, where different trajectories are independent and can be propagated simultaneously using different processors, without any message passing. The resultant computational gain is very substantial, allowing inelastic scattering calculations for larger molecules and at higher collision energies, compared to the standard full-quantum approach.

We thoroughly tested this approach, *vs.* rigorous full-quantum calculations for an atom collided with diatomic molecules (CO + He [21], H_2 + He [22], and N_2 + Na [23]), triatomic H_2O + He [24,25], tetratomic CH_3 + He [26], and polyatomic $HCOOCH_3$ + He [27], but also for diatomic + diatomic collisions (N_2 + H_2 [28] and H_2 + H_2 [29]). These systematic studies involved heavy and light collision partners, quenching and excitation at low and high collision energies, mostly rotational but also some vibrational transitions, including coherence effects for the elastic channel, scattering of identical partners, and computing both total and differential scattering cross sections. Typically, at intermediate and higher collision energies results of MQCT are very close, often identical to the full-quantum results. But even at low collision energies, where classical approximation is not expected to be particularly accurate, the results of MQCT are still reasonable (e.g., near excitation threshold). A proposal was made [26] to blend the full-quantum calculations at low collision energies, where they are indispensable and often affordable, with MQCT calculations at higher collision energies, where they are expected to be accurate, and where no other known method is practical.

This chapter is a capstone for our previous work, since here we expand MQCT theory onto the most general case – a collision of two asymmetric-top rotor molecules, and use it for calculations of H_2O + H_2O rotationally inelastic scattering.

The water molecule was a subject of several relevant studies using the full-quantum approach [12-15], but those included either H atom or H_2 molecule as its collision partner, which is much simpler. The H_2O + H_2O system is so complicated that accurate scattering calculations have never been attempted for it, to our best knowledge.

In fact, the two most popular scattering codes in use by community today, MOLSCAT [3] and HIBRIDON [4], do not even have capabilities of inelastic scattering calculations for the asymmetric-top + asymmetric-top systems. The only example of quantum H_2O + H_2O scattering calculations is found in the early work of Clary [30], but there a very approximate infinite order sudden (IOS) assumption for collision was employed.

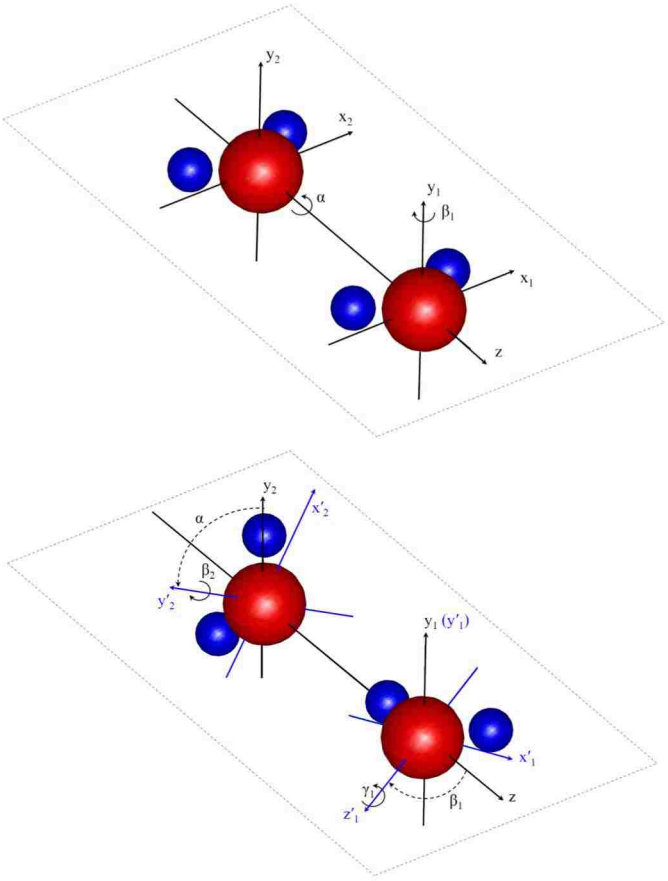

Figure 1. Euler angle rotations of two water molecules relative to the body-fixed frame tied to the instantaneous molecule-molecule vector **Q**, treated classically. *a*) Reference orientation with all angles set to zero. All axis labels are unprimed. The direction of first rotation is indicated for each molecule. *b*) New orientations, after first rotation of each molecule. New molecule-fixed axes, tied to the principal moments of inertia, are shown in blue and given primed labels. See text for further details.

Thus, this work also breaks the grounds in the inelastic scattering calculations for H_2O + H_2O system, which is important on its own, for example, as a probe of conditions in cometary comas [31-33], and other astrophysical environments [34].

6.2 Theory

6.2.1 Classical Degrees of Freedom

In MQCT the relative position of two scattering partners is given by vector **Q** that connects their centers of mass, as shown in Fig. 1. Time-evolution of this vector relative to the space-fixed reference frame (laboratory frame) describes the process of scattering.

Spherical coordinates are used for this: $\mathbf{Q} = (R, \Theta, \Phi)$. It is possible to demonstrate [22,23] that the average Ehrenfest potential, that governs this scattering process, possesses cylindrical symmetry for rotation around the vector **Q**, which keeps the collision trajectory planar and permits to restrict consideration to one plane, say the equatorial plane $\Theta = \pi/2$ (horizontal plane in Fig. 1), without loss of generality. The collision event can be thought of classically: At the initial moment of time two collision partners are in the asymptotic range, separated by large distance $R = |\mathbf{Q}|$, that shortens during the time of collision and increases again as collision partners leave the interaction region. The deflection process is determined by change of the azimuthal angle Φ, that simply describes the rotation of **Q** in the equatorial plane, as collision partners approach each other, collide and scatter. Thus, only two classical degrees of freedom are effectively used in this theory, R and Φ, together with their conjugate momenta P_R and P_Φ. Classical like equations of motion for time evolution of these *classical variables*, $R(t)$, $\Phi(t)$, $P_R(t)$ and $P_\Phi(t)$, were derived and discussed in the recent literature [22,23,27,28]. Here we also list them, for completeness, and in a slightly different form, found to be more suitable for efficient numerical implementation

$$\dot{R} = \frac{P_R}{\mu}; \tag{1}$$

$$\dot{\Phi} = \frac{P_\Phi}{\mu R^2}; \tag{2}$$

$$\dot{P}_R = -\sum_n \sum_{n'} e^{i\varepsilon_n^{n'} t} \sum_m \frac{\partial M_n^{n'}}{\partial R} a^*_{mn'} a_{mn} + \frac{P_\Phi^2}{\mu R^3}; \tag{3}$$

$$\dot{P}_\Phi = -i \sum_n \sum_{n'} e^{i\varepsilon_n^{n'} t} \sum_m M_n^{n'} [a^*_{m-1,n'} a_{mn} \sqrt{j'(j'+1) - m(m-1)} + a^*_{m+1,n'} a_{mn} \sqrt{j'(j'+1) - m(m+1)}$$
$$+ a^*_{mn'} a_{m-1,n} \sqrt{j(j+1) - m(m-1)} + a^*_{mn'} a_{m+1,n} \sqrt{j(j+1) - m(m+1)}] / 2. \tag{4}$$

In these equations $\varepsilon_n^{n'} = E_{n'} - E_n$ is used to label energy differences between the initial (lower index) and the final (upper index) internal *quantum states* of the system, whereas $a_{mn}(t)$ represent time-evolving probability amplitudes for these states

$$\dot{a}_{mn} = -i\sum_{n'} e^{i\varepsilon_{n'}^{n}t} M_{n'}^{n} a_{mn'} - i\dot{\Phi}[a_{m-1,n}\sqrt{j(j+1)-m(m-1)} + a_{m+1,n}\sqrt{j(j+1)-m(m+1)}]/2. \quad (5)$$

The last term of Eq. (5) describes Coriolis coupling between states with $\Delta m = \pm 1$, driven by classical angular speed $\dot{\Phi}(t)$. Neglecting this term leads to the coupled-states (CS) approximation within MQCT, while retaining this term corresponds to the fully-coupled version of MQCT (or coupled-channel MQCT). Matrix $M_{n'}^{n}(R)$ in Eqs. (3-5) is a potential coupling matrix, its *R*-dependent elements are real, time independent, and are different for different values of *m*. The range of *m* is between $-\min(j, j')$ and $+\min(j, j')$. The meaning of quantum numbers m, j and a composite label *n* are discussed next.

6.2.2 Quantum Degrees of Freedom and the Reference Frame

Here, for transparency, we will talk about two colliding water molecules -- molecule one and molecule two, but, since the water molecule is treated exactly, as a general asymmetric top rotor, this theory is applicable to collision of any two molecules. Adaptation of this theory to scattering of two identical molecules is made further below.

So, rotation of each scattering partner is treated quantum mechanically and is described by a set of usual Euler angles: $\Lambda_1 = (\alpha_1, \beta_1, \gamma_1)$ for molecule one and $\Lambda_2 = (\alpha_2, \beta_2, \gamma_2)$ for molecule two, as shown in Fig. 1. Rotational states of each molecule are quantized, described by the corresponding wave functions

$$\Psi_{m_1 j_1 k_1^A k_1^C}(\alpha_1, \beta_1, \gamma_1) = \sqrt{\frac{2j_1+1}{8\pi^2}} \sum_{k=-j_1}^{+j_1} b_k^{j_1 k_1^A k_1^C} D_{m_1 k}^{j_1}(\alpha_1, \beta_1, \gamma_1), \quad (6)$$

$$\Psi_{m_2 j_2 k_2^A k_2^C}(\alpha_2,\beta_2,\gamma_2)=\sqrt{\frac{2j_2+1}{8\pi^2}}\sum_{k=-j_2}^{+j_2} c_k^{j_2 k_2^A k_2^C} D^{j_2}_{m_2 k}(\alpha_2,\beta_2,\gamma_2)\,. \qquad (7)$$

A set of expansion coefficients for each molecule, $b_k^{j_1 k_1^A k_1^C}$ and $c_k^{j_2 k_2^A k_2^C}$, is obtained by diagonalization of asymmetric-top Hamiltonian matrix in a corresponding basis set of Wigner *D*-functions, $D^{j_1}_{m_1 k}(\alpha_1,\beta_1,\gamma_1)$ and $D^{j_2}_{m_2 k}(\alpha_2,\beta_2,\gamma_2)$, respectively [35]. According to standard notation, rotational states of an asymmetric top are labelled (in addition to j_1 and m_1 for molecule one) by quantum numbers k_1^A and k_1^C that represent projections of $\mathbf{j}_1$ onto the principal axis of inertia with smallest and largest values of rotational constants, respectively. And similar for k_2^A and k_2^C for the angular momentum $\mathbf{j}_2$ of molecule two (in addition to j_2 and m_2). Note that for water molecule this *A*-axis is also the axis of symmetry. It should be stressed that here we use the so-called *body-fixed* reference frame, where *z*-axis is defined to pass through the centers of mass of two molecules (*i.e.*, is tied to the classical molecule-molecule vector **Q**). As collision progresses, this axis turns together with collision partners relative to the space-fixed reference frame (same as vector **Q**), and this effect is incorporated into the equations of motion (1-5) as discussed in our earlier papers [21,27]. Projection m_1 of momentum $\mathbf{j}_1$ and projection m_2 of momentum $\mathbf{j}_2$ are made onto this body-fixed z-axis, or equivalently on **Q**. The Euler angles $\Lambda_1=(\alpha_1,\beta_1,\gamma_1)$ and $\Lambda_2=(\alpha_2,\beta_2,\gamma_2)$ are also defined relative to this body-fixed frame, using the so-called *intrinsic* rotations, or according to *z-y′-z″* convention (note that these are different from *extrinsic* rotations discussed in Appendix A). Since interaction between molecules is invariant under rotation around *z*-axes, one can set $\alpha_1=0$, and use only $\alpha_2=\alpha$. Figure 1a gives the "reference" orientation of the system, when $\Lambda_1=(0,0,0)$ and $\Lambda_2=(0,0,0)$, and the symmetry axis of each molecule is aligned with *z*-axis (or equivalently with **Q**). The direction for rotation of molecule two around *z*-axis by angle α, and the direction for rotation of molecule one around y_1 -axis by angle β_1 are also indicated in Fig. 1a. In Fig. 1b new positions of the molecule-fixed frames are shown are shown, (x_1',z_1') for

molecule one and (x_2', y_2') for molecule two, and the directions for the following rotations of each molecule are indicated: rotation around z_1'-axis by γ_1 (which is the last rotation for molecule one) and rotation around y_2'-axis by β_2 for molecule two. One remaining rotation, of molecule two by angle γ_2 is not shown in Fig. 1, since it occurs around new axis z_2''.

The total angular momentum of two molecules $\mathbf{j} = \mathbf{j}_1 + \mathbf{j}_2$ is also quantized in MQCT. The corresponding eigenfunctions can be formally expressed through states of two coupled rotors

$$\Phi_{m\, j\, j_1 k_1^A k_1^C\, j_2 k_2^A k_2^C}(\Lambda_1, \Lambda_2) = \sum_{m_1 m_2} (j_1 m_1 j_2 m_2 \mid jm) \Psi_{m_1 j_1 k_1^A k_1^C}(\Lambda_1) \Psi_{m_2 j_2 k_2^A k_2^C}(\Lambda_2) \tag{8}$$

Coefficients of this expansion, $(j_1 m_1 j_2 m_2 \mid jm)$, the so-called Clebsch-Gordan coefficients [36], are non-zero only if $m = m_1 + m_2$ and $|j_1 - j_2| \le j \le j_1 + j_2$, where *m* is projection of $\mathbf{j}$ on **Q**, so, the sum in Eq. (8) should include all possible cases. A composite index *n* is used to label the total set of quantum numbers for the system, $n = \{j\, j_1 k_1^A k_1^C\, j_2 k_2^A k_2^C\}$. This is exactly the same index *n* used in Eqs. (3-5), thus, Eq. (8) gives expression for Φ_{mn}. It is also convenient to use $n_1 = \{j_1 k_1^A k_1^C\}$ and $n_2 = \{j_2 k_2^A k_2^C\}$ for the states of molecules one and two, respectively, so that $n = \{j\, n_1 n_2\}$.

6.2.3 Potential Coupling Matrix Elements

We have already demonstrated (and will confirm it one more time further below) that the potential coupling matrix $M(R)$ is diagonal in *m*, *i.e.*, its elements for transition $nm \leftarrow n'm'$ are non-zero only if $m = m'$. However, the actual values of non-zero matrix elements depend on m. So, for given fixed m consider the matrix element for transition $n \leftarrow n'$

$$M^{\,n}_{\,n'}(R) = \left\langle \Phi_{m\,n}(\Lambda_1, \Lambda_2) \middle| V(R, \Lambda_1, \Lambda_2) \middle| \Phi_{m\,n'}(\Lambda_1, \Lambda_2) \right\rangle \tag{9}$$

Here $V(R,\alpha_1,\beta_1,\gamma_1,\alpha_2,\beta_2,\gamma_2)$ is the potential energy hypersurface for molecule-molecule interaction, expressed through the same variables: the molecule-molecule distance *R* and two sets of Euler angles. From Fig. 1 we can see that without loss of generality one of these angles can be eliminated, since the potential energy remains unchanged if the system, as a whole, rotates around **Q**. So, $V(R,\alpha_1,\beta_1,\gamma_1,\alpha_2,\beta_2,\gamma_2)=V(R,0,\beta_1,\gamma_1,\alpha,\beta_2,\gamma_2)$, where we defined the difference of angles as new variable $\alpha=\alpha_2-\alpha_1$. In recent literature, a new PES for water-water interaction was computed and presented using similar variables [37,38]. We adopted this surface for our calculations, as outlined in Appendix A.

One straightforward way of computing matrix elements is by numerical five-dimensional quadrature (e.g., Gauss-Legendre method along each angular coordinate)

$$
\begin{aligned}
&M^{n}_{n'}(R)\\
&=\int_0^{2\pi}d\alpha_1\int_0^{2\pi}d\alpha_2\int_0^{\pi}\sin\beta_1 d\beta_1\int_0^{2\pi}d\gamma_1\int_0^{\pi}\sin\beta_2 d\beta_2\int_0^{2\pi}d\gamma_2 V(R,\Lambda_1,\Lambda_2)\Phi^{*}_{mn}(\Lambda_1,\Lambda_2)\Phi_{mn'}(\Lambda_1,\Lambda_2)\\
&=2\pi\int_{-2\pi}^{0}d\alpha\int_0^{\pi}\sin\beta_1 d\beta_1\int_0^{2\pi}d\gamma_1\int_0^{\pi}\sin\beta_2 d\beta_2\int_0^{2\pi}d\gamma_2\\
&\qquad\times V(R,0,\beta_1,\gamma_1,\alpha,\beta_2,\gamma_2)\Phi^{*}_{mn}(0,\beta_1,\gamma_1,\alpha,\beta_2,\gamma_2)\Phi_{mn'}(0,\beta_1,\gamma_1,\alpha,\beta_2,\gamma_2)\\
&=2\pi\int_0^{2\pi}d\alpha\int_0^{\pi}\sin\beta_1 d\beta_1\int_0^{2\pi}d\gamma_1\int_0^{\pi}\sin\beta_2 d\beta_2\int_0^{2\pi}d\gamma_2\\
&\qquad\times V(R,0,\beta_1,\gamma_1,\alpha,\beta_2,\gamma_2)\Phi^{*}_{mn}(0,\beta_1,\gamma_1,\alpha,\beta_2,\gamma_2)\Phi_{mn'}(0,\beta_1,\gamma_1,\alpha,\beta_2,\gamma_2).
\end{aligned}
\tag{10}
$$

We implemented this method in our calculations, but also followed an alternative approach described below, since that second method could be more efficient computationally and, possibly, would allow more straightforward comparison with standard full-quantum calculations (if they would appear in the future).

Namely, in a method used normally in the typical full-quantum scattering calculations the multi-dimensional potential is expanded over a basis set of suitable functions. Following Szalewicz [37,38] we used

$$V(R,\Lambda_1,\Lambda_2)=\sum_{l_1\eta_1 l_2\eta_2 l} V_{l_1\eta_1 l_2\eta_2 l}(R)A_{l_1\eta_1 l_2\eta_2 l}(\Lambda_1,\Lambda_2),$$

(11)

where the real functions are employed, as follows

$$A_{l_1\eta_1 l_2\eta_2 l}(\Lambda_1,\Lambda_2) = \sum_{m_\ell}\frac{\sqrt{(2l_1+1)(2l_2+1)}}{8\pi^2}(l_1 m_\ell\, l_2 -m_\ell \mid l\,0)D^{l_1}_{m_\ell\eta_1}(\Lambda_1)D^{l_2}_{-m_\ell\eta_2}(\Lambda_2). \quad (12)$$

The range of m_ℓ is between $-\min(l_1,l_2)$ and $+\min(l_1,l_2)$. Note that in order to use this method, one should still compute the multi-dimensional integrals, to determine the values of expansion coefficients $V_{l_1\eta_1 l_2\eta_2 l}(R)$ by projecting the PES $V(R,\Lambda_1,\Lambda_2)$ onto the "basis functions" $A_{l_1\eta_1 l_2\eta_2 l}(\Lambda_1,\Lambda_2)$. But, if the expansion coefficients are determined on a grid of points along *R*, then those can be splined and the values of all matrix elements are computed quickly at any point along *R* (using the formula derived below). This is different from the first method, Eq. (10), where each matrix element should be precomputed on *R*-grid and then splined between those points. Depending on complexity of the PES, and the number of states of the system, the first or the second method can be better (faster). In order to test our theory and new code we implemented both methods and made sure they give identical results.

In order to use the expansion of Eq. (11) in Eq. (9) we have to be able to compute the following matrix element

$$\left\langle \Phi_{mn}(\Lambda_1,\Lambda_2)\middle| A_{l_1\eta_1 l_2\eta_2 l}(\Lambda_1,\Lambda_2)\middle|\Phi_{mn'}(\Lambda_1,\Lambda_2)\right\rangle, \quad (13)$$

by expressing them analytically through the coefficients $b_k^{j_1 k_1^A k_1^C}$ and $c_k^{j_2 k_2^A k_2^C}$ of Eqs. (6-7). The derivations are relatively straightforward but somewhat lengthy, and for the sake of transparency are presented separately, in Appendix B. The formula used to calculate matrix elements $M^n_{n'}(R)$ equation through the expansion coefficients $V_{l_1\eta_1 l_2\eta_2 l}(R)$ is also derived in Appendix C.

6.2.4 Identical Particle Exchange Symmetry

In addition to the wave function $\Phi_{mn}(\Lambda_1,\Lambda_2)$ defined by Eq. (8), consider another wave function $\widetilde{\Phi}_{mn}(\Lambda_1,\Lambda_2)$, obtained from it by swapping the molecules one and two. Several arguments should be taken into account. First of all, since the identity of molecules is retained, this swap, obviously, inverts direction of the classical vector **Q** in space, namely, $(X,Y,Z)\to(-X,-Y,-Z)$. Second, for an arbitrary orientation of molecule in space, defined by some $\Lambda=(\alpha,\beta,\gamma)$, inversion of **Q** changes the values of coordinates to new values [35]: $\widetilde{\Lambda}=(\pi+\alpha,\pi-\beta,\pi-\gamma)$, and this concerns each molecule. Third, if we swap two molecules, each takes the quantum state of the partner, and its corresponding wave function. The expansion coefficients used to give wave function of the entire system in Eq. (8), Clebsch-Gordan coefficients, should be modified accordingly. All these features are incorporated into new total wave function of the system, as follows

$$\begin{aligned}
&\tilde{\Phi}_{mn}(\Lambda_1,\Lambda_2)=\Phi_{mn}(\tilde{\Lambda}_2,\tilde{\Lambda}_1)\\
&=\sum_{m_1m_2}(j_1m_1j_2m_2\mid jm)\Psi_{m_1j_1k_1^Ak_1^C}(\tilde{\Lambda}_2)\Psi_{m_2j_2k_2^Ak_2^C}(\tilde{\Lambda}_1) \qquad (14)\\
&=(-1)^{j_1+j_2+j}\sum_{m_1m_2}(j_2m_2j_1m_1\mid jm)\Psi_{m_2j_2k_2^Ak_2^C}(\tilde{\Lambda}_1)\Psi_{m_1j_1k_1^Ak_1^C}(\tilde{\Lambda}_2).
\end{aligned}$$

The goal here is to make this expression look as the original formula of Eq. (8) multiplied by a phase factor (or, actually, to derive the expression for this phase factor). In the second part of Eq. (14) we have already inverted the order of states in the Clebsch-Gordan coefficient [36], which gave a part of this factor, $(-1)^{j_1+j_2+j}$. The remaining task is to transform individual asymmetric-top wave function of each molecule. Using their definitions, Eqs. (6-7), we can write (say, for the molecule two, now in the original rotational state of the molecule one)

$$
\begin{aligned}
&\Psi_{m_1 j_1 k_1^A k_1^C}(\pi+\alpha_2,\pi-\beta_2,\pi-\gamma_2) \\
&\quad=\sqrt{\frac{2j_1+1}{8\pi^2}}\sum_{k_1=-j_1}^{+j_1} b_{k_1}^{j_1 k_1^A k_1^C} D^{j_1}_{m_1 k_1}(\pi+\alpha_2,\pi-\beta_2,\pi-\gamma_2) \\
&\quad=\sqrt{\frac{2j_1+1}{8\pi^2}}\sum_{k_1=-j_1}^{+j_1} b_{k_1}^{j_1 k_1^A k_1^C} (-1)^{j_1+k_1} D^{j_1}_{m_1,-k_1}(\alpha_2,\beta_2,\gamma_2) \\
&\quad=(-1)^{j_1}\sqrt{\frac{2j_1+1}{8\pi^2}}\sum_{k_1=-j_1}^{+j_1}(-1)^{k_1} b_{k_1}^{j_1 k_1^A k_1^C} D^{j_1}_{m_1,-k_1}(\alpha_2,\beta_2,\gamma_2)
\end{aligned}
\tag{15}
$$

Here we used a property of Wigner *D*-function [36], which gave the factor of $(-1)^{j_1+k_1}$, but also swapped *D*-functions with positive and negative values of $\Lambda=(\alpha,\beta,\gamma)$. Same considerations, applied to wave function of the molecule one (in the original state of molecule two), which gives the factor $(-1)^{j_2+k_2}$.

Note that a product of $(-1)^{j_1}$ and $(-1)^{j_2}$ obtained in Eq. (15) multiplied by the factor $(-1)^{j_1+j_2+j}$ obtained in Eq. (14) gives simply $(-1)^{j}$, just as in our previous work on diatomic-diatomic scattering [29]. The factors $(-1)^{k_1}$ and $(-1)^{k_2}$ disappear if we split the total sum over k onto two, one of which includes only the terms with even values of k (both positive and negative) including zero, while the other includes only the terms with odd values of k, namely, from Eq. (15)

$$
\Psi_{m_1 j_1 k_1^A k_1^C}(\Lambda_2)=\sqrt{\frac{2j_1+1}{8\pi^2}}\left(\sum_{\text{evn } k_1} b_{k_1}^{j_1 k_1^A k_1^C} D^{j_1}_{m_1,-k_1}(\Lambda_2)-\sum_{\text{odd } k_1} b_{k_1}^{j_1 k_1^A k_1^C} D^{j_1}_{m_1,-k_1}(\Lambda_2)\right). \tag{16}
$$

The overall range of k_1-values is still $-j_1\le k_1\le+j_1$. And similar for the other molecule. Importantly, as it is shown in Appendix C, no rotational states of the asymmetric-top rotor include both even and odd k_1-values in the expansion (*i.e.*, even and odd k_1-values don't mix). Some states, called para-states, are described by the first sum in Eq. (15), while other states, called ortho-states, are described by the second sum in Eq. (16), which permits to simplify it as follows

$$
\Psi^{\text{p/o}}_{m_1 j_1 k_1^A k_1^C}(\Lambda_2)=(-1)^{\kappa_1}\sqrt{\frac{2j_1+1}{8\pi^2}}\sum_{\text{evn/odd } k_1} b_{k_1}^{j_1 k_1^A k_1^C} D^{j_1}_{m_1,-k_1}(\Lambda_2). \tag{17}
$$

The value of $\kappa_1 = 0$ (Greek kappa) is taken simultaneously with even k_1-values for para-states, while $\kappa_2 = 0$ is taken with odd k_1-values for ortho-states. And similar for the other molecule.

Moreover, as it is also shown in Appendix C, the coefficients of expansion obey the following property: $b_{k_1}^{j_1 k_1^A k_1^C} = p_1 b_{-k_1}^{j_1 k_1^A k_1^C}$ (for all values of k_1 in the range $-j_1 \le k_1 \le +j_1$), where $p_1 = \pm 1$ determines inversion parity of the rotational states of the molecule. This is equivalent to paring *D*-functions with different signs of k_1 into new basis functions of positive and negative parity

$$\begin{aligned}\Psi^{\mathrm{p/o}}_{m_1 j_1 k_1^A k_1^C}(\Lambda_2) &= (-1)^{\kappa_1}\sqrt{\frac{2j_1+1}{8\pi^2}}\sum_{\mathrm{evn/odd}\,k_1\ge 0} b_{k_1}^{j_1 k_1^A k_1^C}\left(D^{j_1}_{m_1,-k_1}(\Lambda_2) \pm D^{j_1}_{m_1 k_1}(\Lambda_2)\right) \\ &= (-1)^{\kappa_1} p_1\sqrt{\frac{2j_1+1}{8\pi^2}}\sum_{\mathrm{evn/odd}\,k_1\ge 0} b_{k_1}^{j_1 k_1^A k_1^C}\left(D^{j_1}_{m_1 k_1}(\Lambda_2) \pm D^{j_1}_{m_1,-k_1}(\Lambda_2)\right) \qquad (18)\\ &= (-1)^{\kappa_1} p_1 \Psi^{\pm\mathrm{p/o}}_{m_1 j_1 k_1^A k_1^C}(\Lambda_2)\end{aligned}$$

Note that here the range of k_1-values is reduced to non-negative values only, just $0 \le k_1 \le j_1$. And similar for the other molecule.

Overall, we can write for the wave function of two swapped molecules

$$\widetilde{\Phi}_{mn}(\Lambda_1,\Lambda_2) = (-1)^j (-1)^{\kappa_1+\kappa_2} p_1 p_2 \sum_{m_1 m_2} (j_1 m_1 j_2 m_2 \mid jm)\Psi^{\pm\mathrm{p/o}}_{m_2 j_2 k_2^A k_2^C}(\Lambda_1)\Psi^{\pm\mathrm{p/o}}_{m_1 j_1 k_1^A k_1^C}(\Lambda_2). \qquad (19)$$

Note that in Eqs. (18-19) we introduced new notation to label molecular eigenstates of given parity, $\Psi^{\pm}(\Lambda)$. These can also be used for the original wave functions (before the swap), since the property $b_{k_1}^{j_1 k_1^A k_1^C} = p_1 b_{-k_1}^{j_1 k_1^A k_1^C}$ is valid in either case

$$\Psi^{\pm\mathrm{p/o}}_{m_1 j_1 k_1^A k_1^C}(\Lambda_1) = \sqrt{\frac{2j_1+1}{8\pi^2}}\sum_{\mathrm{evn/odd}\,k_1\ge 0} b_{k_1}^{j_1 k_1^A k_1^C}\left(D^{j_1}_{m_1 k_1}(\Lambda_1) \pm D^{j_1}_{m_1,-k_1}(\Lambda_1)\right) \qquad (20)$$

And similar expression for the molecule two. It should be stressed that the para/ortho-states (with respect to the values of k in the basis), and the states of two parities (with

respect to inversion) occur in any asymmetric-top molecule, not just in water, and irrespective to the process of collision with any given partner (*e.g.*, in the absence of any collision partner).

Finally, the symmetrized overall wave function of the system of two molecules can be written as positive or negative superposition of the original and swapped wave function

$$\begin{aligned}\Phi^{\pm}_{mn}(\Lambda_1,\Lambda_2) &= \frac{\Phi_{mn}(\Lambda_1,\Lambda_2) \pm \tilde{\Phi}_{mn}(\Lambda_1,\Lambda_2)}{\sqrt{2(1+\delta_{12})}} \\ &= \frac{\Phi_{mn}(\Lambda_1,\Lambda_2) \pm (-1)^{j}(-1)^{\kappa_1+\kappa_2} p_1 p_2 \Phi_{m\tilde{n}}(\Lambda_1,\Lambda_2)}{\sqrt{2(1+\delta_{12})}} \\ &= \frac{1}{\sqrt{2(1+\delta_{12})}}(\Phi_{mn}(\Lambda_1,\Lambda_2) \pm p\Phi_{m\tilde{n}}(\Lambda_1,\Lambda_2))\end{aligned} \tag{21}$$

Here $\tilde{n} = \{j\, n_2 n_1\}$, where particles one and two have been swapped. We also introduced the total inversion parity of the overall wave function of two molecules as $p = \pm(-1)^{j}(-1)^{\kappa_1+\kappa_2} p_1 p_2$. Normalization coefficient includes Kronecker symbol for the states of two molecules: $\delta_{12} = \delta_{j_1 k_1^A k_1^C, j_2 k_2^A k_2^C}$. One can see that many combinations of para and ortho states of both parties of two molecules are possible. Next section discusses which state-to-state transitions are allowed/forbidden, and what are the corresponding matrix elements.

6.2.5 Transitions in the Case of Identical Particles

Exchange parity of the overall wave function of two-molecule system is very handy, because it appears that state-to-state transitions $n \leftarrow n'$ are allowed only between states of the same parity, which restricts the values of final quantum numbers $n = \{j n_1 n_2\}$ for a chosen initial state $n' = \{j' n_1' n_2'\}$, for every value of *m*. Let's demonstrate this. Consider the matrix element where exchange parities are the same (both are + or both are –)

$$
\begin{aligned}
&M_{n'}^{n(\pm)}(R) = \left\langle \Phi_{mn}^{\pm}(\Lambda_1,\Lambda_2)\middle|V(R,\Lambda_1,\Lambda_2)\middle|\Phi_{mn'}^{\pm}(\Lambda_1,\Lambda_2)\right\rangle \\
&= \left\langle \frac{\Phi_{mn}(\Lambda_1,\Lambda_2)\pm\tilde{\Phi}_{mn}(\Lambda_1,\Lambda_2)}{\sqrt{2(1+\delta_{12})}}\middle|V(R,\Lambda_1,\Lambda_2)\middle|\frac{\Phi_{mn'}(\Lambda_1,\Lambda_2)\pm\tilde{\Phi}_{mn'}(\Lambda_1,\Lambda_2)}{\sqrt{2(1+\delta'_{12})}}\right\rangle \qquad (22)\\
&= \frac{1}{2\sqrt{(1+\delta'_{12})(1+\delta_{12})}}\Big(\left\langle \Phi_{mn}(\Lambda_1,\Lambda_2)\middle|V(R,\Lambda_1,\Lambda_2)\middle|\Phi_{mn'}(\Lambda_1,\Lambda_2)\right\rangle \\
&+\left\langle \tilde{\Phi}_{mn}(\Lambda_1,\Lambda_2)\middle|V(R,\Lambda_1,\Lambda_2)\middle|\tilde{\Phi}_{mn'}(\Lambda_1,\Lambda_2)\right\rangle \\
&\pm\left\langle \Phi_{mn}(\Lambda_1,\Lambda_2)\middle|V(R,\Lambda_1,\Lambda_2)\middle|\tilde{\Phi}_{mn'}(\Lambda_1,\Lambda_2)\right\rangle \\
&\pm\left\langle \tilde{\Phi}_{mn}(\Lambda_1,\Lambda_2)\middle|V(R,\Lambda_1,\Lambda_2)\middle|\Phi_{mn'}(\Lambda_1,\Lambda_2)\right\rangle\Big);
\end{aligned}
$$

Next step is to take into account that with our choice of coordinates the value of potential does not change under the swap of two molecules. (Note that this is not necessarily the case with other choices of coordinates, see Appendix A.) So, using $V(R,\Lambda_1,\Lambda_2) = V(R,\tilde{\Lambda}_2,\tilde{\Lambda}_1)$ and $\tilde{\Phi}_{mn}(\Lambda_1,\Lambda_2) = \Phi_{mn}(\tilde{\Lambda}_2,\tilde{\Lambda}_1) = p\Phi_{m\tilde{n}}(\Lambda_1,\Lambda_2)$, see Eq. (19), we can group terms in the previous expression as follows

$$
\begin{aligned}
&M_{n'}^{n(\pm)}(R) = \frac{1}{2\sqrt{(1+\delta'_{12})(1+\delta_{12})}}\Big(\left\langle \Phi_{mn}(\Lambda_1,\Lambda_2)\right\rangle\middle|V(R,\Lambda_1,\Lambda_2)\middle|\Phi_{mn'}(\Lambda_1,\Lambda_2)\right\rangle \\
&+\left\langle \Phi_{mn}(\tilde{\Lambda}_2,\tilde{\Lambda}_1)\middle|V(R,\tilde{\Lambda}_2,\tilde{\Lambda}_1)\middle|\Phi_{mn'}(\tilde{\Lambda}_2,\tilde{\Lambda}_1)\right\rangle \\
&\pm p'\left\langle \Phi_{mn}(\Lambda_1,\Lambda_2)\middle|V(R,\Lambda_1,\Lambda_2)\middle|\Phi_{m\tilde{n}'}(\Lambda_1,\Lambda_2)\right\rangle \\
&\pm p'\left\langle \Phi_{mn}(\tilde{\Lambda}_2,\tilde{\Lambda}_1)\middle|V(R,\tilde{\Lambda}_2,\tilde{\Lambda}_1)\middle|\Phi_{m\tilde{n}'}(\tilde{\Lambda}_2,\tilde{\Lambda}_1)\right\rangle\Big) \qquad (23)\\
&= \frac{1}{\sqrt{(1+\delta'_{12})(1+\delta_{12})}}\Big(\left\langle \Phi_{mn}(\Lambda_1,\Lambda_2)\right\rangle\middle|V(R,\Lambda_1,\Lambda_2)\middle|\Phi_{mn'}(\Lambda_1,\Lambda_2)\right\rangle \\
&\pm p'\left\langle \Phi_{mn}(\Lambda_1,\Lambda_2)\middle|V(R,\Lambda_1,\Lambda_2)\middle|\Phi_{m\tilde{n}'}(\Lambda_1,\Lambda_2)\right\rangle\Big)
\end{aligned}
$$

where state $\tilde{n}' = \{j'n'_2n'_1\}$ is obtained from $n' = \{j'n'_1n'_2\}$ by swapping particles one and two.

Note that in Eq. (23) we employed the following properties

$$
\begin{aligned}
&\left\langle \Phi_{mn}(\Lambda_1,\Lambda_2)\middle|V(R,\Lambda_1,\Lambda_2)\middle|\Phi_{mn'}(\Lambda_1,\Lambda_2)\right\rangle = \left\langle \Phi_{mn}(\tilde{\Lambda}_2,\tilde{\Lambda}_1)\middle|V(R,\tilde{\Lambda}_2,\tilde{\Lambda}_1)\middle|\Phi_{mn'}(\tilde{\Lambda}_2,\tilde{\Lambda}_1)\right\rangle; \\
&\left\langle \Phi_{mn}(\Lambda_1,\Lambda_2)\middle|V(R,\Lambda_1,\Lambda_2)\middle|\Phi_{m\tilde{n}'}(\Lambda_1,\Lambda_2)\right\rangle = \left\langle \Phi_{mn}(\tilde{\Lambda}_2,\tilde{\Lambda}_1)\middle|V(R,\tilde{\Lambda}_2,\tilde{\Lambda}_1)\middle|\Phi_{m\tilde{n}'}(\tilde{\Lambda}_2,\tilde{\Lambda}_1)\right\rangle.
\end{aligned}
\qquad (24)
$$

One can compute non-zero matrix elements using Eq. (23) directly building, the basis of symmetrized functions. Alternatively, if the total state-to-state transition matrix (without taking into account the exchange symmetry) is computed as outlined in Sec. II-C and Appendix B, then the symmetrized matrix element for states of given parity can be easily constructed by superposition

$$M_{n'}^{n(\pm)} = \left(M_{n'}^{n} \pm p' M_{\tilde{n}'}^{n} \right) \Big/ \sqrt{(1+\delta_{12})(1+\delta'_{12})} \,. \tag{25}$$

And, it is possible to show that when the parities are different for the initial and the final states of the system, the matrix element is zero

$$\begin{aligned} M_{n'}^{n}(R) &= \left\langle \Phi_{mn}^{\pm}(\Lambda_1,\Lambda_2) \middle| V(R,\Lambda_1,\Lambda_2) \middle| \Phi_{mn'}^{\mp}(\Lambda_1,\Lambda_2) \right\rangle \\ &= \frac{1}{2\sqrt{(1+\delta'_{12})(1+\delta_{12})}} \Big(\left\langle \Phi_{mn}(\Lambda_1,\Lambda_2) \middle| V(R,\Lambda_1,\Lambda_2) \middle| \Phi_{mn'}(\Lambda_1,\Lambda_2) \right\rangle \\ &- \left\langle \Phi_{mn}(\tilde{\Lambda}_2,\tilde{\Lambda}_1) \middle| V(R,\tilde{\Lambda}_2,\tilde{\Lambda}_1) \middle| \Phi_{mn'}(\tilde{\Lambda}_2,\tilde{\Lambda}_1) \right\rangle \\ &\pm p' \left\langle \Phi_{mn}(\Lambda_1,\Lambda_2) \middle| V(R,\Lambda_1,\Lambda_2) \middle| \Phi_{m\tilde{n}'}(\Lambda_1,\Lambda_2) \right\rangle \\ &\mp p' \left\langle \Phi_{mn}(\tilde{\Lambda}_2,\tilde{\Lambda}_1) \middle| V(R,\tilde{\Lambda}_2,\tilde{\Lambda}_1) \middle| \Phi_{m\tilde{n}'}(\tilde{\Lambda}_2,\tilde{\Lambda}_1) \right\rangle \Big) = 0 \end{aligned} \tag{26}$$

6.2.6 Effect of Potential Symmetry for H_2O Molecules

Several properties of the potential energy surface expansion coefficients in Eq. (11) are worth mentioning [37,38]

$$V_{l_1\eta_1 l_2\eta_2 l} = (-1)^{l_1+l_2} V_{l_2\eta_2 l_1\eta_1 l} \tag{27}$$

$$V_{l_1\eta_1 l_2\eta_2 l} = (-1)^{l_1+\eta_1+l_2+\eta_2+l} V_{l_1-\eta_1 l_2-\eta_2 l} \tag{28}$$

$$V_{l_1\eta_1 l_2\eta_2 l} = 0, \qquad \text{for odd } \eta_{1,2} \,. \tag{29}$$

First of these is related to the fact that two collision partners are identical, and swapping them does not change the potential energy. The meaning of second is that potential should remain the same under simultaneous inversion of both molecules. The third reflects C_{2v} symmetry of each water molecule.

In our calculations reported in the next section we included in the expansion of Eq. (11) all terms with $l \le 6$ [37,38]. This is, roughly, two thousand terms total in the PES expansion. Using the properties of Eqs. (25,26) this number is reduced to just 254 non-zero and unique terms, with $l_{1,2} \le 6$ and even values of $\eta_{1,2}$.

6.3 Results for H_2O+H_2O

6.3.1 Properties of Potential and Matrix Elements

It is expected that a system of two polar water molecules would exhibit rather strong long-range dipole-dipole interaction. This property of the potential energy surface becomes clear if we analyze behavior of the expansion coefficients $V_{l_1\eta_1 l_2\eta_2 l}(R)$ in Eq. (11), as a function of molecule-molecule distance R. Several most important coefficients are presented in Fig. 2, labeled by five numbers: $l_1\eta_1 l_2\eta_2 l$. Recall that η_1 and η_2 are even, while l_1 and l_2 are such that $|l_1 - l_2| \le l \le l_1 + l_2$. The dipole-dipole interaction term corresponds to $l_1 = l_2 = 1$ ($l = 2$ and $\eta_1 = \eta_2 = 0$), so, it is labelled by 10102. From Fig. 2 we see that this term is negative and large. At a distance of $R = 20\ a_0$ (about 10Å) its value is about –2.7 kcal/mol. At a distance of $R = 40\ a_0$ its value is still non-negligible, about –0.34 kcal/mol. We checked and found that in the asymptotic range the expected dipole-dipole behavior, $V_{10102} \sim -1/R^3$, is well satisfied. Interestingly, from Fig. 2 we see that the magnitude of V_{10102} is larger than that of the isotropic (elastic scattering) term V_{00000}, through the entire

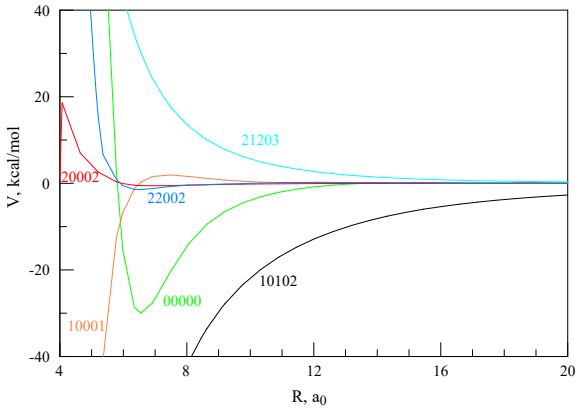

Figure 2. Expansion coefficients, as a function of molecule-molecule distance, for potential energy surface of the water-water system represented by Eq. (11). Six most important terms are shown. Labels include five indexes: $l_1\eta_1 l_2\eta_2 l$. The curves are color-coded, accordingly. Note that the dipole-dipole interaction term (black) exceeds the elastic scattering term (green), at all relevant distances.

relevant range of distances *R*. Well depth of V_{00000} is about 30 kcal/mol, with a minimum energy point located near $R \sim 6.5\ a_0$.

Several other most important dipole-like ($l_1 = 1$) and quadrupole-like ($l_1 = 2$) terms are also presented in Fig. 2. They all are smaller than the dipole-dipole term V_{10102} and vanish faster as molecule-molecule separation increases. Still, some of them are comparable in magnitude to the elastic term V_{00000}. This means that the PES is highly anisotropic, even at large distances.

As we are going to demonstrate below, one important consequence of the long-range anisotropy of the PES is that scattering calculations for water-water system must start from very large initial molecule-molecule distances, and must include very large values of the impact parameter. Of course, these numbers depend somewhat on collision energy, but in any case, are unusually large. For example, for collision energy of $E =$ 1500 cm^{-1} we had to take $R_{\max} \sim 100\ a_0$ and $b_{\max} \sim 30\ a_0$ in order to guarantee convergence of integral inelastic scattering cross sections (for excitation of several lower lying states, starting from the ground state of the system) within 0.5%. Situation is even worse for the elastic scattering channels (see below), where accurate treatment of scattering phase in the asymptotic range is essential for convergence.

Dominance of the dipole-dipole interaction is further reflected by state-to-state transition matrix elements $M_{n'}^{n(\pm)}$, computed as outlined in Sec. II and Appendix B. Here it becomes convenient to switch from state labelling employed above ($n_1 = \{j_1 k_1^A k_1^C\}$, $n_2 = \{j_2 k_2^A k_2^C\}$ and $n = \{j\, n_1 n_2\}$) to the standard labelling that uses subscripts: $j_{1_{k_1^A k_1^C}} j_{2_{k_2^A k_2^C}} (jm)$. For example, the ground states of two molecules are labelled as 0_{00} and 0_{00}, which gives total $j = 0$ and $m = 0$. Or, if we combine everything: $0_{00}0_{00}(00)$.

Now consider excitation of the state 1_{11} in *one* of two (identical) molecules. Since $|j_1 - j_2| \le j \le j_1 + j_2$ we have to include, into the basis set expansion of Eq. (8), the excited total $j = 1$ with its associated states $m = 0, \pm 1$. Since the initial state $0_{00}0_{00}(00)$ has $m = 0$, and since matrix $M_{n'}^{n(\pm)}$ is diagonal in *m*, we obtain non-zero transition element

only for the final state $1_{11}0_{00}(10)$. However, the final states with $m = \pm 1$ will receive population from the state with $m = 0$ due to the Coriolis coupling effect, $\Delta m = \pm 1$, see Eq. (4). Thus, we have to include the elastic (diagonal) matrix elements $M_{n'}^{n(\pm)}$ for these states as well, namely $1_{11}0_{00}(11)$. Note that the value of matrix element is the same for positive and negative values of projection m of the total j.

Similarly, for excitation of the state 1_{11} in *both* molecules, we include total $j = 0$, 1 and 2. If the initial state is ground state with $m = 0$, then non-zero transition matrix elements $M_{n'}^{n(\pm)}$, due to potential coupling, should be included just for the following states (all with final $m = 0$): $1_{11}1_{11}(00)$, $1_{11}1_{11}(10)$ and $1_{11}1_{11}(20)$. Coriolis coupling then would populate $1_{11}1_{11}(11)$ and $1_{11}1_{11}(21)$, and finally $1_{11}1_{11}(22)$.

Next, for excitation of state 2_{02} in one molecule only the state $2_{02}0_{00}(20)$ will have non-zero transition matrix elements $M_{n'}^{n(\pm)}$ due to potential coupling. State $2_{02}0_{00}(21)$ and eventually $2_{02}0_{00}(22)$ would be populated by Coriolis coupling. And so on. In Fig. 3 we present matrix elements, as a function of R, for state-to-state transitions from the ground state of the system $0_{00}0_{00}(00)$ to several most important exited states of positive exchange parity, but also the diagonal matrix elements for those excited states, important for the elastic scattering processes. The dipole-dipole interaction manifests here, first of all, through the largest matrix element for excitation of the state $1_{11}1_{11}(20)$, starting from the ground state

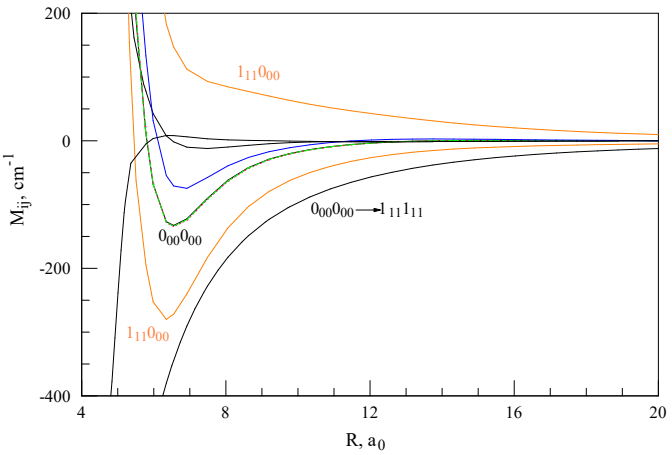

Figure 3. State-to-state transition matrix elements as a function of water-water distance R. Black curves correspond to transitions from the ground state $0_{00}0_{00}(00)$ to the following final states (including the elastic channel): $0_{00}0_{00}(00)$, $1_{11}0_{00}(10)$, $1_{11}1_{11}(20)$ and $2_{02}0_{00}(20)$. Orange curves, upper and lower, correspond to elastic scattering for $1_{11}0_{00}(10)$ and $1_{11}0_{00}(11)$ states, respectively. Blue curve is for the elastic scattering off the state $2_{02}0_{00}(20)$. Dashed green and magenta curves are for the elastic scattering off states $1_{11}1_{11}(20)$ and $1_{11}1_{11}(21)$, respectively (note that they nearly coincide with the elastic $0_{00}0_{00}$ term).

$0_{00}0_{00}(00)$. The value of this matrix element decays slowly at large distances (lower black curve in Fig. 3). For example, at $R = 20\ a_0$ its value is still significant, about –12 cm^{-1}. Even a distance of $R = 40\ a_0$ it is still non-negligible, about –1.5 cm^{-1}. Another consequence of large dipole-dipole interaction term is that the values of diagonal matrix elements for the elastic scattering of the states $1_{11}0_{00}(10)$ and $1_{11}0_{00}(11)$ are also large, and decay slowly (two red curves in Fig. 3). Indeed, the direct effect of the dipole-dipole potential term V_{10102} onto the states $1_{11}0_{00}$ can be explicitly demonstrated analytically using Eqs. (11) and (25).

Thus, in the following sections the focus is on inelastic transition to $1_{11}1_{11}$ state (from the ground state $0_{00}0_{00}$), and on elastic scattering off the $1_{11}0_{00}$, since both processes are driven by strong dipole-dipole components of the interaction potential.

6.3.2 Inelastic Scattering off the Ground State

Within MQCT framework, and using the potential expansion outlined above, we carried out inelastic scattering calculations for water-water system. Sampling of the initial conditions for collision, propagation of the mixed quantum/classical trajectories, calculations of the final transition probabilities, state-to-state cross sections and channel-to-channel cross sections (summed over the final and averaged over the initial degenerate states) follow the procedures outlined in our earlier papers [27-29], and will not be reviewed again for the purpose of brevity.

Here we only consider excitation of the ground state $0_{00}0_{00}$. Since initially the internal rotational angular momentum is null ($j = 0$ and $m = 0$), the value of orbital angular momentum ℓ (treated classically within MQCT) is equal to the grand angular momentum J of the system. Its maximum value J_{max} is a convergence parameter in MQCT calculations, just as in the full-quantum scattering calculations. The value of J_{max} (and ℓ_{max}) depends somewhat on collision energy. For example, at $E = 500$, 1500 and 5000 cm^{-1} we used J_{max}= 380, 660, and 1100 respectively. These numbers are rather large, by quantum mechanical standards. They reflect a rather heavy reduced mass of the system, and a long-range nature of the dipole-dipole interaction. In practice, instead of energy-dependent J_{max}, it is more convenient to specify the maximum value of impact

parameter b_{max}, since it is basically independent of collision energy (just weakly dependent in the considered energy range). As mentioned in the previous section, the value $b_{max} \sim 30\ a_0$ was used (together with $R_{max} \sim 100\ a_0$).

Another convergence parameter of MQCT calculations is the number of trajectories used to sample orbital angular momentum in the range from $\ell = 0$ (head-on collision, back scattering) to ℓ_{max} (forward scattering in the asymptotic range, with vanishing transition probability). Here the relevant range of ℓ was sampled continuously (non-integer values) and uniformly (using an equidistant grid of points in the range $0 \le \ell \le \ell_{max}$). These values of ℓ define initial conditions for a batch of independent MQCT trajectories. We found that 60 trajectories were typically sufficient to represent relatively smooth opacity functions in the considered energy range. Figure 4 gives example of opacity function (transition cross section *vs.* impact parameter) for the dipole-driven transition $0_{00}0_{00} \rightarrow 1_{11}1_{11}$ at collision energy of $E = 1500$ cm^{-1}. Note that our opacity functions include a factor of $(2J+1)$ for each trajectory, to properly reflect the importance of the process in the overall cross section. Results of two calculations are presented in Fig. 4, one obtained with $R_{max} = 50\ a_0$, and the other with $R_{max} = 100\ a_0$. This emphasizes that due to the long-range dipole-dipole interaction the initial value of molecule-molecule distance in scattering

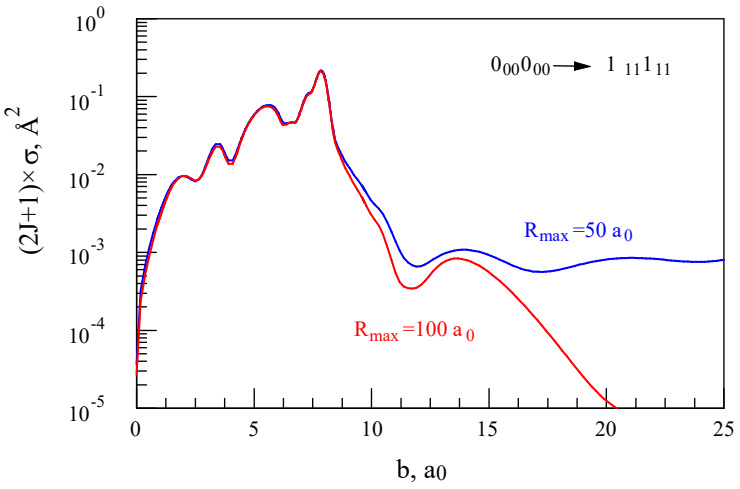

Figure 4. Demonstration of the effect of long-range dipole-dipole interaction onto the opacity function for excitation of $1_{11}1_{11}$ (starting from the ground state $0_{00}0_{00}$), through the choice of the initial value of molecule-molecule distance R_{max} for scattering calculations. A seemingly large value of $R_{max} = 50\ a_0$ appears to be insufficient, since it leads to non-zero transition probability at large impact parameters, but also to some deviations of the transition probability in the entire range of impact parameter. The value of $R_{max} = 100\ a_0$ is large enough.

calculations must be rather large in order to obtain well converged results. A seemingly large value of $R_{max} = 50\ a_0$ appears to be insufficient, since it leads to non-zero transition probability at large impact parameters, but also to some deviations of the transition probability in the entire range of impact parameter. The value of $R_{max} = 100\ a_0$ is large enough. The difference of integral inelastic cross sections in these two cases is close to 5%.

Figure 5 represents examples of opacity functions for three important transitions at various collision energies. Upper frame corresponds to the dipole-driven transition $0_{00}0_{00} \rightarrow 1_{11}1_{11}$. Second frame corresponds to excitation of $2_{02}0_{00}$, which (mostly) receives its population indirectly, through the state $1_{11}1_{11}$. Lower frame corresponds to excitation of $1_{11}0_{00}$, which can be characterized as a non-dipole driven, and thus is much weaker. Different curves in each

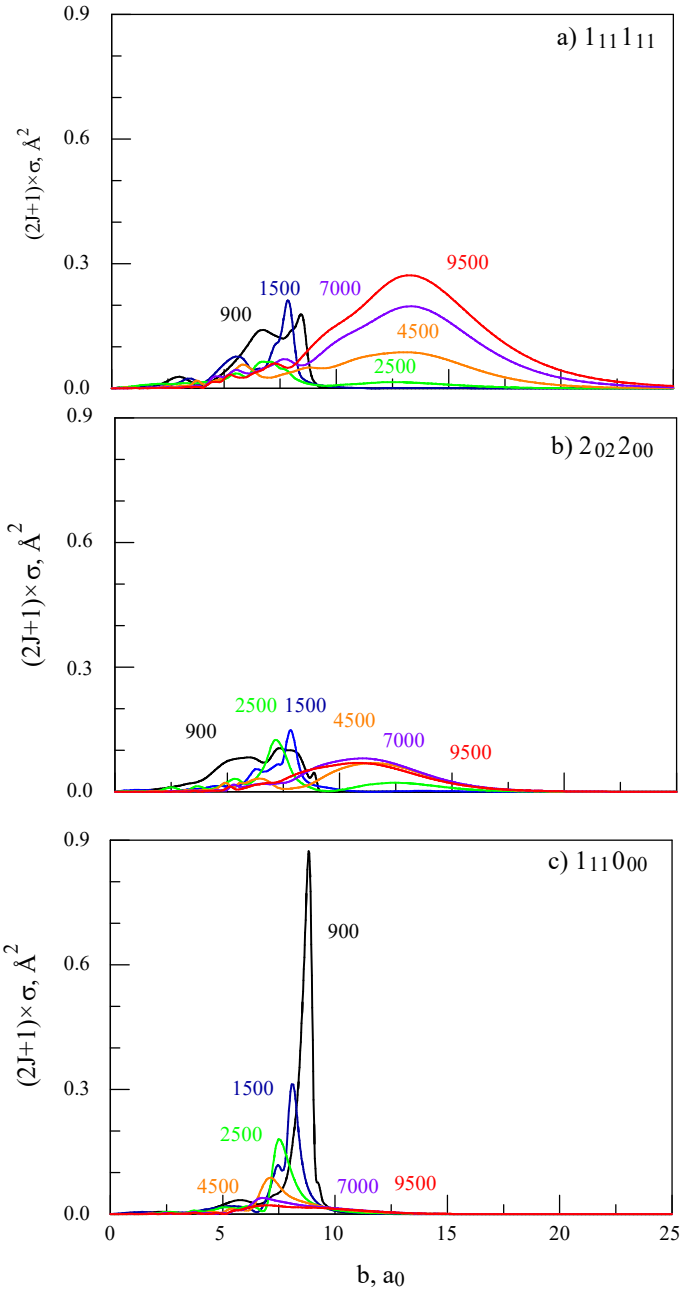

Figure 5. Opacity functions for three inelastic scattering processes, starting from the ground state $0_{00}0_{00}$. Collision energies are indicated in the figure. Three frames correspond to the following final states: *a*) $1_{11}1_{11}$; *b*) $2_{02}0_{00}$; and c) $1_{11}0_{00}$. See text for discussion.

frame show how the opacity function evolves as collision energy is changed. Here one can identify, very clearly, a presence of two scattering regimes. One, corresponds to lower collision energies and lover impact parameters (*e.g.*, $E \sim 1000$ cm^{-1} and $4 \le b \le 7$ a_0). This is a typical behavior seen in many inelastic scattering calculations in the past, on many molecules. But, in addition to this, the dipole-driven transition to $1_{11}1_{11}$ demonstrates very large probabilities at high collision energies and large impact parameters, simultaneously (*e.g.*, $E \sim$10000 cm^{-1} and $b \sim$ 13 a_0). Same effect translates into a consecutive excitation of $2_{02}0_{00}$ (from $1_{11}1_{11}$). This interesting feature is not typical, and is result of a long-range rather strong dipole-dipole interaction.

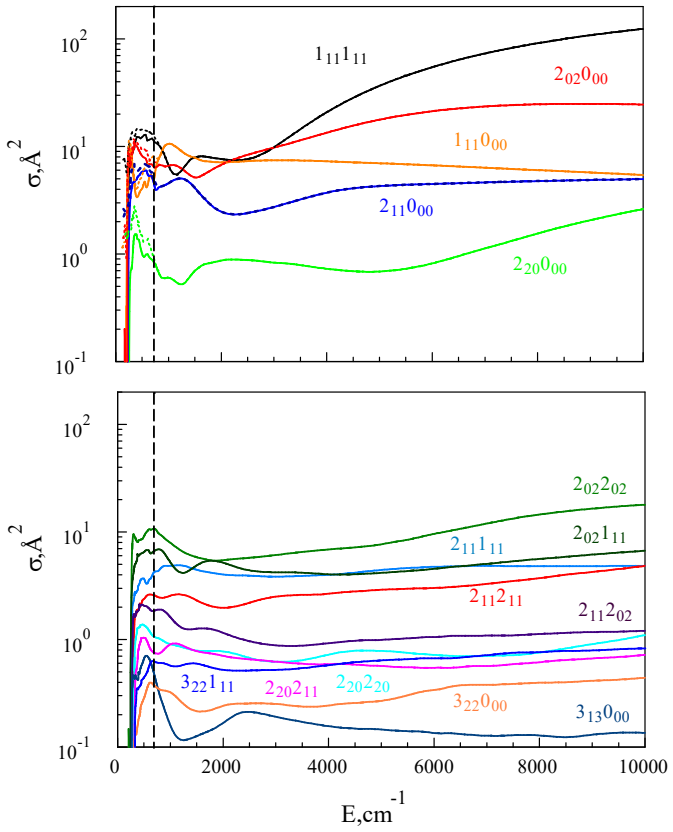

Figure 6. Inelastic scattering cross section as a function of collisional energy. All curves correspond to excitation from the ground state $0_{00}0_{00}$. The region to the left from dashed line is found to contain scattering resonances, not treated here. The effect of orbiting trajectories is shown by dashed lines (see text for details). Frame *a*) shows excitation of five lower-energy states. Frame *b*) shows excitation of the other 10 most important states. Convergence is within 5% for energies up to 1500 cm^{-1}, an is within 10-15% at higher energies.

The last convergence parameter in MQCT calculations is the number of internal rotational states in the basis set. Here we included all states with $j_1 \le 6$, $j_2 \le 6$ and $j \le 8$, such that $|j_1 - j_2| \le j \le j_1 + j_2$. All non-degenerate components $\{k_1^A k_1^C\}$ and $\{k_2^A k_2^C\}$ of these j_1 and j_2 states were included, which resulted in 132 non-degenerate levels, or scattering channels. Energies of these levels cover confidently the range up to 700 cm^{-1},

and some of them reach 990 cm^{-1}. With this basis set, cross sections for excitations of 15 lower-energy channels are converged within 5%, for collision energy E = 1500 cm^{-1}. For lower scattering energies, this basis set is certainly sufficient, but even for higher scattering energies (here we considered up to 10,000 cm^{-1}) the upper states of the basis receive very little populations, which means that results remain reasonably accurate (conservative estimate is within 10-15%). Note that we carried out the fully-coupled version of MQCT calculations, without the CS approximation (see Eq. (5) and the discussion just below it), including explicitly all degenerate components m of considered $j \le 8$ states, which resulted in 5932 states total in our calculations.

In Fig. 6 we plotted inelastic scattering cross sections as a function of collisional energy in the range from 100 to 10,000 cm^{-1}, for 15 most important excited states. Figure 6a shows data for excitation of five lower-lying rotational states: $1_{11}0_{00}$, $1_{11}1_{11}$, $2_{02}0_{00}$, $2_{11}0_{00}$, and $2_{20}0_{00}$, whereas Fig. 6b shows the data for the remaining 10 states. The range of confident prediction is to the right from the dashed line. For collision energies up to $500 \le E \le 1500$ cm^{-1} cross sections are converged within 5%, and within 10-15% in the range $1500 \le E \le 10000$ cm^{-1}. At collision energies E < 500 cm^{-1}, to the left from the dashed line, we observed many orbiting trajectories, which is a vestige of quantum scattering resonances.

It is not yet clear how to treat these cases. We tried removing orbiting trajectories completely, to obtain non-resonant contribution to inelastic cross section. In the energy range where resonances are present such data give non-resonant background of the overall energy dependence of cross section. In Fig. 6 these data are plotted by solid curves. They drop fast as collision energy is decreased below 500 cm^{-1}, because the number of orbiting trajectories in the batch also increases, as collision energy is reduced. For example, at energies $E \sim 200$ cm^{-1} close to 30% of trajectories in the batch describe orbiting. As an experiment, we tried, to stop orbiting trajectories, roughly, after one period of rotation, and include them into analysis. The resultant cross sections were significantly larger (compared to non-resonant background), as shown in Fig. 6 by dashed lines. A good recipe for analysis or resonant/orbiting trajectories is yet to be found. At present time, the range of confident MQCT predictions should be limited to higher

collision energies, $E > 500$ cm^{-1}. Hopefully, the full-quantum scattering calculations are affordable at lower energies, and could be done one day for $E < 500$ cm^{-1}. It would be interesting to compare those with our MQCT predictions at the matching point, somewhere near $E \sim 500$ cm^{-1}.

High energy behavior of the dipole-dipole driven excitation of the state $1_{11}1_{11}$, seen in Fig. 6a, is quite surprising. One could expect that at higher collision energies the process of scattering is dominated by the repulsive short-range interaction, and is limited to relatively small impact parameters. Normally, the long-range (usually weak and attractive) interaction dominates at low collision energies and large impact parameters. What we see here is neither case: the dipole-driven transition to $1_{11}1_{11}$ is more intense at higher collision energies (see Fig. 6a) and occurs mostly at large impact parameters (see Fig. 5a). Explanation is found in Figs. 2 and 3, where we see that although the dipole-dipole term is indeed a long-range, it is not weak at all and, of course, is not purely attractive (it is anisotropic). This term contributes to the repulsive part of potential too, and dominates scattering for all collision energies, and all impact parameters, in a somewhat unexpected way. As collision energy is increased from $E = 1000$ to 10,000 cm^{-1}, cross section for excitation of $1_{11}1_{11}$ increases by an order of magnitude, and still keeps growing. Excitation of state $2_{02}0_{00}$ follows similar trend, since it is populated through $1_{11}1_{11}$. This is one interesting finding of this work, which may have important implications for analysis of non-equilibrium population of the rotational states of water (end emission of those) in astrophysical environments, such as star-forming regions [39-41], proto-stellar discs [42-43] or cometary comas [44-45]. This

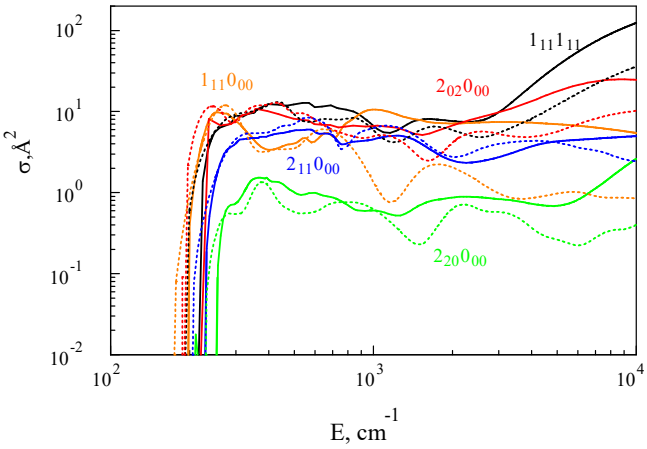

Figure 7. Inelastic scattering cross section as a function of collisional energy in CS approximation (dashed lines) in comparison with full CC (solid lines). All curves correspond to excitation from the ground state $0_{00}0_{00}$.

aspect is also interesting mechanistically, since very few quantum scattering calculations of the dipole-dipole driven transitions are available at this point, and, typically, at lower collision energies [46,47].

It is probably true to say that the full quantum scattering calculations for H_2O + H_2O system will be very expensive. One way to make those more affordable is to use the coupled-states (CS) approximation, which neglects the Coriolis coupling effect, but the accuracy of this approach is often hard to guarantee. Thus, we decided to test the accuracy of CS-approach for H_2O + H_2O, relative to the fully-coupled CC-approach, all within MQCT framework. Figure 7 gives comparison of results obtained using CC and CS methods. Typically, results of the approximate CS method deviate from the accurate CC method at low collision energies, but converge to them at higher collision energy. The reason for this is that al low scattering energies the long-range interaction dominates (large impact parameter) and the Coriolis coupling is important, while at higher energies the short-range interaction dominates (small impact parameters), and the Coriolis coupling is minor. What we see in Fig. 7 is different. Results of two methods are in reasonable qualitative agreement within an order of magnitude, but there is no monotonic convergence of CS (dashed lines) towards CC (solid lines of the same color). Agreement is the best for excitation of states $1_{11}1_{11}$, $2_{02}0_{00}$ and $2_{11}0_{00}$, particularly at collision energies below 1,000 cm^{-1}, where the differences are on the order of 30-50%. However, at higher collision energies the difference increases, reaching 200% (a factor of two). This can be explained by the fact that for the H_2O + H_2O system large impact parameters remain important even at higher collision energies (due to dipole-dipole interaction, see Fig. 5), thus, the Coriolis coupling is never minor. Larger differences seen for excitation of the state $2_{11}0_{00}$ have a different nature (specific to MQCT method itself rather than to the CS-approximation). Overall, our conclusion here is that CS approximation can be used only for semi-quantitative estimate of scattering cross sections, if the accuracy in the range of the factor of two is sufficient.

6.3.3 Most Important Elastic Scattering Channels

As it was emphasized in the past publications [22, 23, 28], and is further explored in a recent paper [48], it is possible to restore the scattering phase within MQCT approach, which enables rigorous calculations of differential cross sections, including that for the elastic scattering channel (impossible within the classical trajectory method). In Figure 8 we report differential cross section for the elastic scattering off the ground state $0_{00}0_{00}$ of the H_2O + H_2O system, for three values of scattering energies: 800, 2500 and 9500 cm^{-1}. We found that in all cases the forward scattering dominates. For scattering at 800 cm^{-1} the amplitude in significant only within the range of +0.6 degree or so. It shrinks to only +0.3 degree when the energy is raised to 9500 cm^{-1}.

In Figure 9 we plotted the value of integral cross section for the elastic scattering off the ground state $0_{00}0_{00}$, as a function of collision energy, and the same moiety for the exited level $1_{11}0_{00}$ which, as explained above, is easily populated by the intense dipole-dipole driven transitions. Recall that this level contains three degenerate states of the total $j = 1$, those with $m = 0, \pm 1$ (see Sec. III-A). Thus, we had to run two calculations, one with the initial state $1_{11}0_{00}(10)$, and the other with the initial state $1_{11}0_{00}(11)$. Separate calculation with $m = -1$ is not needed, since the results would be identical to that of $m = +1$, due to symmetry property of the

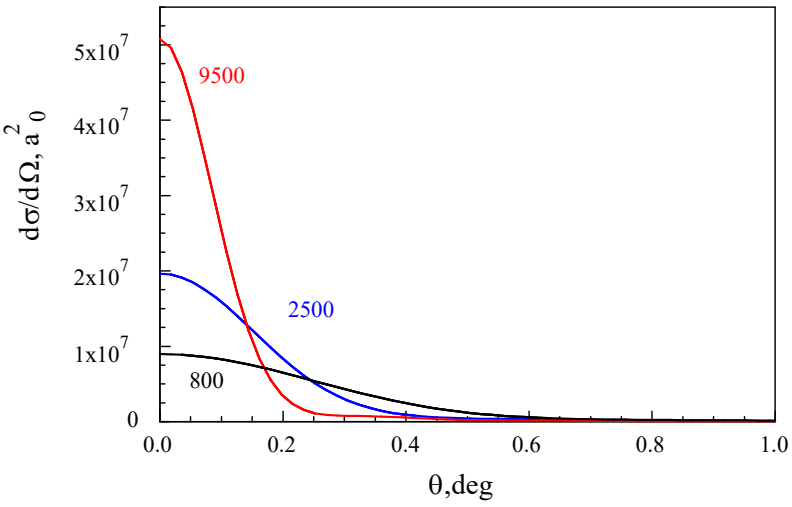

Figure 8. Differential (over scattering angle) cross section for the elastic channel of H_2O + H_2O system in the ground state $0_{00}0_{00}$. Three values of collision energy are considered, as indicated in the picture: 800, 2500 and 9500 cm^{-1}.

transition matrix elements. The total cross section is computed as a sum over final and average over the initial degenerate states, as usual.

Both dependencies in Fig. 9 are smooth and exhibit similar behavior: cross section progressively decreases as collision energy is raised. At higher energies the absolute value of elastic cross section for the excited state $1_{11}0_{00}$ is about two times smaller, compared to that of the ground state $0_{00}0_{00}$. This can be viewed as a symmetry effect. Namely, in contrast to the ground state of the system, $0_{00}0_{00}$, that has only one component of positive exchange parity, the total wave function for the excited state $1_{11}0_{00}$ contains two components according to Eq. (21). Since transitions between states of opposite exchange parities are forbidden (see Eq. (26), Section II-E), only the states of one parity need to be included in the basis set, and treated separately from states of opposite parity. The results presented here were carried out for the positive parity component only (as the initial state). Since for the elastic channel the final state is the same positive parity component of $1_{11}0_{00}$, such calculations account only for one-half of (all hypothetically possible) transitions, and predict the elastic cross section close to one-half of the total value. Calculations for the negative parity component of the excited state as the initial slate would recover another half of the cross section value.

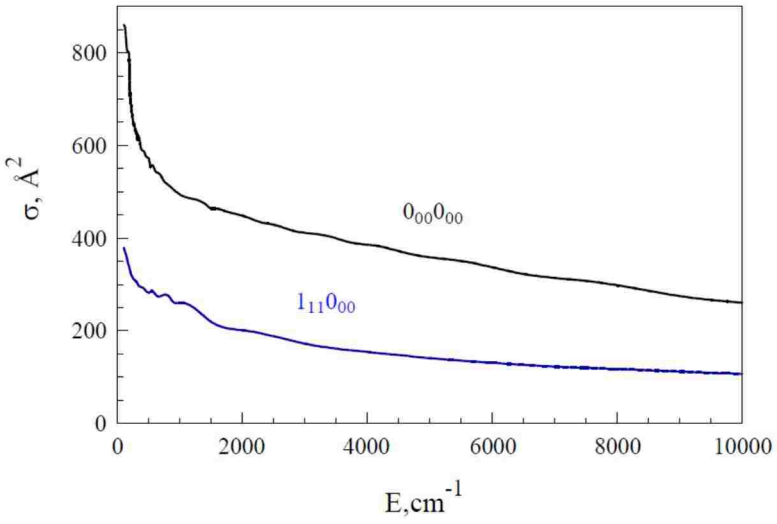

Figure 9. Integral cross section as a function of collision energy for the elastic scattering of the H_2O + H_2O system in the ground state $0_{00}0_{00}$ (black) and in the excited state $1_{11}0_{00}$ (blue).

6.4 Conclusions for Chapter 6

In this chapter, we worked out the mixed quantum/classical theory for inelastic collision of two asymmetric-top rotors, which is the most general case of two-body scattering. In this method the state-to-state transitions between the internal rotational (or ro-vibrational) states of molecules are treated quantum mechanically using time-dependent Schrodinger equation, whereas their relative translational motion (responsible for scattering) is treated classically, using the average trajectory (Ehrenfest) approach. Two versions of the formula for transition matrix elements were presented: a straightforward approach that uses numerical multi-dimensional quadrature over all internal degrees of freedom, and a (more standard) analytic approach that uses expansion of the PES over the basis set of spherical harmonics. Adaptation to the case of identical-molecules scattering was also presented.

This theory was then applied to rotational excitation of two water molecules, H_2O + H_2O, using the PES from recent literature. Properties of the expansion coefficients of the PES, and of the state-to-state transition matrix elements, were analyzed to reveal the major features of this system, such as a long range dipole-dipole interaction. Calculations of collisional excitation from the ground state of the system, $0_{00}0_{00}$, into a number of low-lying excited rotational states were carried out in a broad range of energies, up to 10,000 cm^{-1}. Analysis of computed opacity functions showed a rather unusual scattering regime, dominated by a strong anisotropic long-range interaction (dipole-dipole). Several most important dipole-driven transitions were identified and discussed in detail. The coupled-states approximation was tested, and found to agree semi-quantitatively (within a factor of two) with the fully-coupled version of the method. Differential cross sections for the elastic scattering were computed for several collision energies, and found to have a very narrow forward scattering peak.

The computer program written for this work is now being packaged into a user friendly suite and will be made available for community, as a part of a forthcoming publication: *Semenov A., Babikov D., "MQCT. II. User-Ready Program for Calculations of Inelastic Scattering of Two Molecules"*, which we would like to announce here. It is

being designed to have an interface similar to that of MOLSCAT, such as simple input files and the same way of feeding in the PES.

APPENDIX A: Conversion Between Two Definitions of Euler Angles

In Section 6.2.2 and Fig. 1 of the main text of the Chapter the *intrinsic* convention is employed for Euler angles that are used to describe rotational degrees of freedom for the molecules. That convention suits better for treatment of the collision dynamics, when the molecule-molecule axis (and the body-fixed reference frame tied to it) rotates in space as collision progresses, and each molecule rotates with respect to its instantaneous principal axis of inertia. However, for expansion of the PES of the system $V(R,\Lambda_1,\Lambda_2)$ a different approach is typically employed [37-38]. In this case the centers of mass of two molecules are placed on *z*-axis in the space-fixed reference frame (with a fixed distance *R* between them) as shown in Fig. A1, and do not move. Euler angles Λ_1 and Λ_2 are used to rotate each molecule in space to sample all possible orientations of the molecule-molecule system. Then the procedure is repeated for the next value of *R* (on a predefined grid), and the next. In this case the so called *extrinsic*, or *z*-*y*-*z* convention is preferred, when rotations by α, β and γ are performed relative to axes of the space-fixed reference. During this sequence of individual rotations the axes (of space-fixed reference frame) do not move.

Interestingly, the final orientation of the molecule after performing extrinsic rotations will be the same as in the intrinsic case *if* the order of rotations is reversed, namely, if molecule is first rotated around axis *z* by angle γ, then around *y* by angle β, and finally (again) around *z* axis by angle α. The reader is advised to compare Fig. A1 *vs.* Fig. 1. This property was used to generate the PES for the intrinsic case using the routine written for the extrinsic case [37-38].

Second, it is important to note that using extrinsic rotations one should be aware that the swap of two molecules reverses the molecule-molecule vector, but not the space-fixed axes

$$V(\mathbf{R},\Lambda_1,\Lambda_2)=V(-\mathbf{R},\Lambda_2,\Lambda_1); \qquad \text{(A1)}$$

Users of the PES routine supplied in Refs. [37-38] should be aware of this property too. Note that this is different from the intrinsic rotations in the body-fixed reference frame (used for description of scattering) when the swap of molecules gives

$$V(R,\Lambda_1,\Lambda_2)=V(R,\tilde{\Lambda}_2,\tilde{\Lambda}_1),$$

where $\Lambda=(\alpha,\beta,\gamma)$ and $\tilde{\Lambda}=(\pi+\alpha,\pi-\beta,\pi-\gamma)$, as discussed in the main text. This is because when we swap the molecules in that case, the directions of the body fixed axes x, y and z are reversed, so, orientations of the molecules relative to new axes are also changed, accordingly.

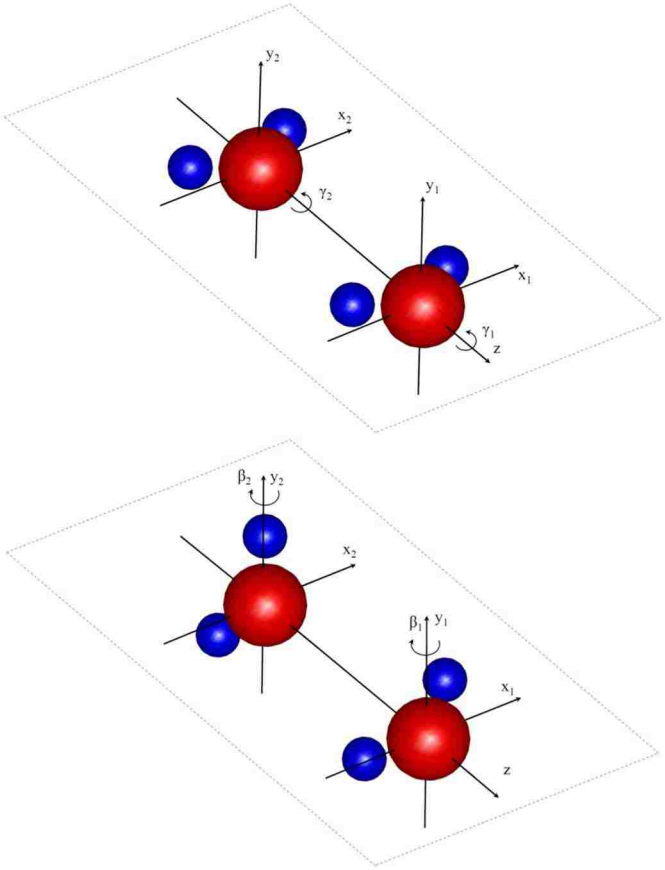

Figure A1. Demonstration of extrinsic *z*-*y*-*z* convention for Euler angles. In the upper frame both molecules are in the reference configuration, with values of all angle equal to zero. First rotation is performed around axis *z* by angles γ_1 and γ_2 (for molecules one and two), as shown in the upper frame. Lower frame shows positions of the molecules after that first rotation, and indicates direction of the second rotation for each molecule, around axes y_1 and y_2 by angles β_1 and β_2, respectively. Finally, the molecule two is rotated by angle α around axis *z*.

APPENDIX B: Calculation of Transition Matrix Elements

In order to compute matrix elements of Eq. (13) we have to substitute, first, Eqs. (6-7) into Eq. (8), for the initial and final states, which gives

$$\Phi_{mn}(\Lambda_1,\Lambda_2)=\Phi_{m\,j\,j_1k_1^{A}k_1^{C}\,j_2k_2^{A}k_2^{C}}(\Lambda_1,\Lambda_2)$$
$$=\sum_{m_1m_2}(j_1m_1j_2m_2\mid jm)\Psi_{m_1j_1k_1^{A}k_1^{C}}(\Lambda_1)\Psi_{m_2j_2k_2^{A}k_2^{C}}(\Lambda_2)$$
$$=\frac{\sqrt{(2j_1+1)(2j_2+1)}}{8\pi^2}\sum_{m_1m_2}(j_1m_1j_2m_2\mid jm)\left(\sum_{k_1=-j_1}^{+j_1}b_{k_1}^{j_1k_1^{A}k_1^{C}}D^{j_1}_{m_1k_1}(\alpha_1,\beta_1,\gamma_1)\right)\left(\sum_{k_2=-j_2}^{+j_2}c_{k_2}^{j_2k_2^{A}k_2^{C}}D^{j_2}_{m_2k_2}(\alpha_2,\beta_2,\gamma_2)\right);$$

$$\Phi_{m'n'}(\Lambda_1,\Lambda_2)=\Phi_{m'\,j'\,j_1'k_1'^{A}k_1'^{C}\,j_2'k_2'^{A}k_2'^{C}}(\Lambda_1,\Lambda_2)$$
$$=\sum_{m_1'm_2'}(j_1'm_1'j_2'm_2'\mid j'm')\Psi_{m_1'j_1'k_1'^{A}k_1'^{C}}(\Lambda_1)\Psi_{m_2'j_2'k_2'^{A}k_2'^{C}}(\Lambda_2)$$
$$=\frac{\sqrt{(2j_1'+1)(2j_2'+1)}}{8\pi^2}\sum_{m_1'm_2'}(j_1'm_1'j_2'm_2'\mid j'm')\left(\sum_{k_1'=-j_1'}^{+j_1'}b_{k_1'}^{j_1'k_1'^{A}k_1'^{C}}D^{j_1'}_{m_1'k_1'}(\alpha_1,\beta_1,\gamma_1)\right)\left(\sum_{k_2'=-j_2'}^{+j_2'}c_{k_2'}^{j_2'k_2'^{A}k_2'^{C}}D^{j_2'}_{m_2'k_2'}(\alpha_2,\beta_2,\gamma_2)\right).$$

These expressions are now substituted into the following integral, which represents contribution of one term of Eq. (11) to the matrix element of Eq. (9)

$$\left\langle\Phi_{mn}(\Lambda_1,\Lambda_2)\middle|A_{l_1\eta_1l_2\eta_2l}(\Lambda_1,\Lambda_2)\middle|\Phi_{m'n'}(\Lambda_1,\Lambda_2)\right\rangle=$$

$$=\frac{\sqrt{(2j_1+1)(2j_2+1)}}{8\pi^2}\cdot\frac{\sqrt{(2j_1'+1)(2j_2'+1)}}{8\pi^2}\cdot\frac{\sqrt{(2l_1+1)(2l_2+1)}}{8\pi^2}$$
$$\times\int_{\Lambda_1}\int_{\Lambda_2}\sum_{m_1m_2}(j_1m_1j_2m_2\mid jm)\sum_{k_1=-j_1}^{+j_1}b_{k_1}^{j_1k_1^{A}k_1^{C}}D^{j_1*}_{m_1k_1}(\Lambda_1)\sum_{k_2=-j_2}^{+j_2}c_{k_2}^{j_2k_2^{A}k_2^{C}}D^{j_2*}_{m_2k_2}(\Lambda_2)$$
$$\times\sum_{m_1'm_2'}(j_1'm_1'j_2'm_2'\mid j'm')\sum_{k_1'=-j_1'}^{+j_1'}b_{k_1'}^{j_1'k_1'^{A}k_1'^{C}}D^{j_1'}_{m_1'k_1'}(\Lambda_1)\sum_{k_2'=-j_2'}^{+j_2'}c_{k_2'}^{j_2'k_2'^{A}k_2'^{C}}D^{j_2'}_{m_2'k_2'}(\Lambda_2)$$
$$\times\sum_{m_\ell}(l_1m_\ell\,l_2-m_\ell\mid l0)\,D^{l_1}_{m_\ell\eta_1}(\Lambda_1)\,D^{l_2}_{-m_\ell\eta_2}(\Lambda_2).$$

$$=\frac{\sqrt{(2j_1+1)(2j_2+1)}}{8\pi^2}\frac{\sqrt{(2j_1'+1)(2j_2'+1)}}{8\pi^2}\frac{\sqrt{(2l_1+1)(2l_2+1)}}{8\pi^2}$$
$$\times\sum_{m_1m_2}(j_1m_1j_2m_2\mid jm)\sum_{k_1=-j_1}^{+j_1}b_{k_1}^{j_1k_1^{A}k_1^{C}}\sum_{k_2=-j_2}^{+j_2}c_{k_2}^{j_2k_2^{A}k_2^{C}}$$
$$\times\sum_{m_1'm_2'}(j_1'm_1'j_2'm_2'\mid j'm')\sum_{k_1'=-j_1'}^{+j_1'}b_{k_1'}^{j_1'k_1'^{A}k_1'^{C}}\sum_{k_2'=-j_2'}^{+j_2'}c_{k_2'}^{j_2'k_2'^{A}k_2'^{C}}$$
$$\times\sum_{m_\ell}(l_1m_\ell\,l_2-m_\ell\mid l0)$$
$$\times\int_{\Lambda_1}D^{j_1*}_{m_1k_1}(\Lambda_1)D^{l_1}_{m_\ell\eta_1}(\Lambda_1)D^{j_1'}_{m_1'k_1'}(\Lambda_1)\int_{\Lambda_2}D^{j_2*}_{m_2k_2}(\Lambda_2)D^{l_2}_{-m_\ell\eta_2}(\Lambda_2)D^{j_2'}_{m_2'k_2'}(\Lambda_2).$$

For the first of these integrals the following equality can be employed [36]

$$\int_{\Lambda_1}D^{j_1*}_{m_1k_1}(\Lambda_1)D^{l_1}_{m_\ell\eta_1}(\Lambda_1)D^{j_1'}_{m_1'k_1'}(\Lambda_1)=\frac{8\pi^2}{2j_1+1}(j_1'm_1'l_1m_\ell\mid j_1m_1)(j_1'k_1'l_1\eta_1\mid j_1k_1)\cdot$$

And, similarly for the second integral

$$\int_{\Lambda_2} D^{j_2 *}_{m_2 k_2}(\Lambda_2) D^{l_2}_{-m_\ell \eta_2}(\Lambda_2) D^{j_2'}_{m_2' k_2'}(\Lambda_2) = \frac{8\pi^2}{2j_2+1}(j_2' m_2' l_2 - m_\ell \mid j_2 m_2)(j_2' k_2' l_2 \eta_2 \mid j_2 k_2)\,.$$

With these, we have

$$\left\langle \Phi_{mn}(\Lambda_1,\Lambda_2) \middle| A_{l_1\eta_1 l_2\eta_2 l}(\Lambda_1,\Lambda_2) \middle| \Phi_{m'n'}(\Lambda_1,\Lambda_2) \right\rangle =$$

$$\begin{aligned}
&= \sqrt{\frac{2j_1'+1}{2j_1+1}} \cdot \sqrt{\frac{2j_2'+1}{2j_2+1}} \cdot \frac{\sqrt{(2l_1+1)(2l_2+1)}}{8\pi^2} \\
&\times \sum_{m_1 m_2} (j_1 m_1 j_2 m_2 \mid jm) \sum_{k_1=-j_1}^{+j_1} b^{j_1 k_1^A k_1^C}_{k_1} \sum_{k_2=-j_2}^{+j_2} c^{j_2 k_2^A k_2^C}_{k_2} \\
&\times \sum_{m_1' m_2'} (j_1' m_1' j_2' m_2' \mid j' m') \sum_{k_1'=-j_1'}^{+j_1'} b^{j_1' k_1'^A k_1'^C}_{k_1'} \sum_{k_2'=-j_2'}^{+j_2'} c^{j_2' k_2'^A k_2'^C}_{k_2'} \\
&\times (j_1' k_1' l_1 \eta_1 \mid j_1 k_1) \cdot (j_2' k_2' l_2 \eta_2 \mid j_2 k_2) \\
&\times \sum_{m_\ell} (l_1 m_\ell\, l_2 - m_\ell \mid l\,0) \cdot (j_1' m_1' l_1 m_\ell \mid j_1 m_1) \cdot (j_2' m_2' l_2 - m_\ell \mid j_2 m_2).
\end{aligned}$$

The last two Clebsch-Gordan coefficients are non-zero only if $m_1' + m_\ell = m_1$ simultaneously with $m_2' - m_\ell = m_2$. Adding these two conditions leads to $m_1' + m_2' = m_1 + m_2$, or simply $m' = m$. This means that these integrals are non-zero only if the value *m* of projection of total **j** (onto **Q**) remains unchanged. Consequently, the state-to-state transition matrix is diagonal in *m*. This property is incorporated into the equations of motion, Eq. (3-5).

Finally, the state-to-state transition matrix element is obtained by summing the contributions of all terms in Eq. (11), with *R*-dependent expansion coefficients, as follows (for given *m*)

$$
\begin{aligned}
M_{n'}^{n}(R) &= M^{\,j\; j_1 k_1^A k_1^C\; j_2 k_2^A k_2^C}_{\,j' j_1' k_1'^A k_1'^C\; j_2' k_2'^A k_2'^C} \\
&= \sqrt{\frac{2j_1'+1}{2j_1+1}} \cdot \sqrt{\frac{2j_2'+1}{2j_2+1}} \sum_{l_1\eta_1 l_2\eta_2 l} \frac{\sqrt{(2l_1+1)(2l_2+1)}}{8\pi^2} V_{l_1\eta_1 l_2\eta_2 l}(R) \\
&\times \sum_{m_1} (j_1 m_1 j_2 m_2 \mid jm) \sum_{k_1=-j_1}^{+j_1} b_{k_1}^{j_1 k_1^A k_1^C} \sum_{k_2=-j_2}^{+j_2} c_{k_2}^{j_2 k_2^A k_2^C} \\
&\times \sum_{m_1'} (j_1' m_1' j_2' m_2' \mid j'm) \sum_{k_1'=-j_1'}^{+j_1'} b_{k_1'}^{j_1' k_1'^A k_1'^C} \sum_{k_2'=-j_2'}^{+j_2'} c_{k_2'}^{j_2' k_2'^A k_2'^C} \\
&\times (j_1' k_1' l_1 \eta_1 \mid j_1 k_1) \cdot (j_2' k_2' l_2 \eta_2 \mid j_2 k_2) \\
&\times \sum_{m_\ell} (l_1 m_\ell\, l_2 - m_\ell \mid l\,0) \cdot (j_1' m_1' l_1 m_\ell \mid j_1 m_1) \cdot (j_2' m_2' l_2 - m_\ell \mid j_2 m_2).
\end{aligned}
$$

Note that in this final expression we have explicitly set $m' = m$, and should only use $m_2 = m - m_1$ and $m_2' = m - m_1'$, so that summation over m_1 and m_1' has one index. Overall, this expression has eight inner summations, but we chose not to use seven sets of parenthesis in order to make this formula easier to read. In practice, to avoid computing the terms that are anyways zero, the outermost summation over l_1 and l_2 is optimized, for a chosen initial $j_1 j_2$ and final $j_1' j_2'$ states, by taking only those terms that satisfy the "triangle rule" in the four Clebsch-Gordan coefficients in the final expression $\left|j_1' - l_1\right| \le j_1 \le j_1' + l_1$ and $\left|j_2' - l_2\right| \le j_2 \le j_2' + l_2$.

APPENDIX C: Properties of Asymmetric-Top Wave Functions

In this Appendix, we will talk about one asymmetric top rotor molecule only, and use notations different from the rest of the chapter (where two molecules are considered at the same time). Thus, here we will omit the molecule number, to avoid using subscripts 1 and 2. Results are applicable to any molecule.

Hamiltonian operator of the general asymmetric-top rotor can be conveniently written relative to the principal axis of inertia of the molecule (the *molecule-fixed* reference frame) as follows [35]

$$
\hat{H} = \frac{B+C}{2}\hat{\mathbf{j}}^2 + \left(A - \frac{B+C}{2}\right)\hat{j}_z^2 + \frac{B-C}{4}(\hat{j}_+^2 + \hat{j}_-^2) \qquad \text{(C1)}
$$

Here atomic units are used ($\hbar=1$), $\hat{j}_{\pm}=\hat{j}_x \pm \mathrm{i}\,\hat{j}_y$ are two ladder operators, while $\hat{j}_x$, $\hat{j}_y$ and $\hat{j}_z=-i\hbar\,\partial/\partial\gamma$ are operators for projections of $\hat{\mathbf{j}}$ onto the principal axis of inertia. If the last term of this expression is neglected, the problem is reduced to the case of a symmetric-top rotor with analytic eigenfunctions, given by Wigner *D*-functions D^j_{mk}, and eigenvalues E_{jk} given by

$$\begin{aligned}\hat{H}_{\mathrm{sym}}D^j_{mk} &= \frac{B+C}{2}\hat{\mathbf{j}}^2 D^j_{mk}+\left(A-\frac{B+C}{2}\right)\hat{j}_z^2 D^j_{mk}\\ &= \frac{B+C}{2}j(j+1)D^j_{mk}+\left(A-\frac{B+C}{2}\right)k^2 D^j_{mk}\\ &= E_{jk}D^j_{mk};\end{aligned} \tag{C2}$$

$$E_{jk}=\frac{B+C}{2}j(j+1)+\left(A-\frac{B+C}{2}\right)k^2. \tag{C3}$$

If the last term is included, the Wigner *D*-functions D^j_{mk} can be used as suitable basis functions to set up the Hamiltonian matrix of the asymmetric-top, and diagonolize it to determine the corresponding eigenvalues [35]. In that general case, for positive values of *k*:

$$\begin{aligned}\hat{H}D^j_{mk} = E_{jk}D^j_{mk}+\frac{B-C}{4}\Big(&\sqrt{[j(j+1)-(k+1)(k+2)][j(j+1)-k(k+1)]}\,D^j_{m,k+2}\\ &+\sqrt{[j(j+1)-(k-1)(k-2)][j(j+1)-k(k-1)]}\,D^j_{m,k-2}\Big).\end{aligned} \tag{C4}$$

Similarly, for negative values of *k*:

$$\begin{aligned}\hat{H}D^j_{m,-k} &= E_{jk}D^j_{m,-k}+\frac{B-C}{4}\Big(\sqrt{[j(j+1)-(-k+1)(-k+2)][j(j+1)+k(-k+1)]}\,D^j_{m,-k+2}\\ &\qquad+\sqrt{[j(j+1)-(-k-1)(-k-2)][j(j+1)+k(-k-1)]}\,D^j_{m,-k-2}\Big)\\ &= E_{jk}D^j_{m,-k}+\frac{B-C}{4}\Big(\sqrt{[j(j+1)-(k-1)(k-2)][j(j+1)-k(k-1)]}\,D^j_{m,-(k-2)}\\ &\qquad+\sqrt{[j(j+1)-(k+1)(k+2)][j(j+1)-k(k+1)]}\,D^j_{m,-(k+2)}\Big);\end{aligned} \tag{C5}$$

From analysis of Eqs. (C4) and (C5) it follows that, instead of the general basis functions D^j_{mk} it is advantageous to introduce the basis functions of given parity

$$F^{j(\pm)}_{mk} = \frac{D^j_{mk} \pm D^j_{m,-k}}{\sqrt{2(1+\delta_{k0})}}. \tag{C6}$$

Here $0 \le k \le j$ (positive only). The case of $k=0$ has different normalization constant and belongs to states of even parity. This gives $j+1$ positive parity states and j negative parity states, or $2j+1$ states total, as before. In this new basis

$$\hat{H}F^{j(+)}_{mk} = E_{jk}F^{j(+)}_{mk} + \frac{B-C}{4}(\sqrt{[j(j+1)-(k+1)(k+2)][j(j+1)-k(k+1)]}F^{j(+)}_{m,k+2} + \sqrt{[j(j+1)-(k-1)(k-2)][j(j+1)-k(k-1)]}F^{j(+)}_{m,k-2}). \tag{C6}$$

$$\hat{H}F^{j(-)}_{mk} = E_{jk}F^{j(-)}_{mk} + \frac{B-C}{4}(\sqrt{[j(j+1)-(k-1)(k-2)][j(j+1)-k(k-1)]}F^{j(-)}_{m,k-2} + \sqrt{[j(j+1)-(k+1)(k+2)][j(j+1)-k(k+1)]}F^{j(-)}_{m,k+2}). \tag{C7}$$

From Eqs. (C6) and (C7) the following properties of the Hamiltonian matrix are obtained (for any given j and m)

$$\left\langle F^{j(\pm)}_{mk} \middle| \hat{H} \middle| F^{j(\pm)}_{mk'} \right\rangle = \left\langle F^{j(\pm)}_{mk'} \middle| \hat{H} \middle| F^{j(\pm)}_{mk} \right\rangle, \text{ for any } k \text{ and } k'; \tag{C8}$$

$$\left\langle F^{j(\mp)}_{mk} \middle| \hat{H} \middle| F^{j(\pm)}_{mk'} \right\rangle = 0, \qquad \text{for any } k \text{ and } k'; \tag{C9}$$

$$\left\langle F^{j(\pm)}_{mk} \middle| \hat{H} \middle| F^{j(\pm)}_{mk'} \right\rangle = 0, \qquad \text{if } |k-k'| \neq 0,2. \tag{C10}$$

This means that such matrix is symmetric, with non-zero elements for $\Delta k = 0, \pm 2$ only, and no coupling between the states of positive and negative parity. Thus, the overall matrix can be split onto two independent blocks, $(j+1)\times(j+1)$ for positive and $j \times j$ for negative inversion parity states, for each j and m .

As a side note, these properties is a consequence of the fact that the inversion operator $\hat{I}$ commutes with the Hamiltonian operator. Indeed, $\hat{I}\hat{J}_{x,y,z} = \hat{J}_{x,y,z}$ and $\hat{H}\hat{I} = \hat{I}\hat{H}$. Thus, the eigenfunctions of the asymmetric-top Hamiltonian can be chosen as eigenfunctions of the inversion operator, defined as

$\hat{I}\,\Psi_{m\ j\ k^4k^C}(\Lambda) = \pm\Psi_{m\ j\ k^4k^C}(\Lambda)$. It is easy to check that for the basis functions of given parity: $\hat{I}\,F_{mk}^{j(+)}(\Lambda) = F_{mk}^{j(+)}(\Lambda)$, but $\hat{I}\,F_{mk}^{j(-)}(\Lambda) = -F_{mk}^{j(-)}(\Lambda)$.

In summary, two properties are relevant to the discussion of the main text (Sec. 6.2.4):

1) Eigenstates of the asymmetric-top rotor are split onto two independent groups: $j+1$ states of positive parity, and j states of negative parity. Those are expressed through the basis-functions of proper parity, as in Eqs. (16,19) of the main text.
2) Basis functions with even and odd values of *k* do not mix, and give independent states called para-states (with even *k*-values in the expansion, including zero) and orto-states (with odd *k*-values in the expansion), as in Eqs. (16,19) of the main text.

Assignments of several lower energy states of para- and ortho-water in terms of inversion parity is given in Table A.

Table A: Lower energy 36 levels of water as asymmetric rigid top.

State $j_{k^A k^C}$	**Para- or ortho-**	**Inversion parity**	**Energy, cm^{-1}**	**State** $j_{k^A k^C}$	**Para- or ortho-**	**Inversion parity**	**Energy, cm^{-1}**
0_{00}	p	(+)	0.00	2_{11}	p	(−)	95.21
1_{01}	o	(−)	23.80	2_{12}	o	(−)	79.53
1_{10}	o	(+)	42.39	3_{03}	o	(−)	136.90
1_{11}	p	(+)	37.16	3_{13}	p	(+)	142.37
2_{02}	p	(+)	70.13	3_{23}	o	(+)	173.53
2_{20}	p	(+)	136.56	3_{22}	p	(−)	206.70
2_{21}	o	(+)	135.31	3_{32}	o	(−)	212.57
4_{04}	p	(+)	222.37	3_{31}	p	(+)	287.30
4_{14}	o	(−)	225.07	3_{30}	o	(+)	287.50
4_{13}	p	(−)	276.01	4_{23}	o	(+)	300.89
4_{22}	p	(+)	316.47	4_{32}	o	(−)	384.52
4_{31}	p	(−)	385.84	4_{41}	o	(+)	494.62
4_{40}	p	(+)	494.64	5_{05}	o	(−)	325.90
5_{15}	p	(+)	327.10	5_{14}	o	(+)	400.58
5_{24}	p	(−)	417.09	5_{23}	o	(−)	447.92
5_{33}	p	(+)	506.19	5_{32}	o	(+)	511.10
5_{42}	p	(−)	616.38	5_{41}	o	(−)	616.60
5_{51}	p	(+)	757.62	5_{50}	o	(+)	757.63

BIBLIOGRAPHY for Chapter 6

1. A. M. Arthurs and A. Dalgarno, *Roy. Soc. of Lon. Proc. Ser. A* **256**, 540 (1960).

2. Green, S, J. *Chem. Phys.* **62**, 2271-2282, (1975); S. Green, *J. Chem. Phys* **64**, 3463-3473 (1976).

3. J. M. Hutson and S. Green; MOLSCAT computer code, version 14 (1994), distributed by Collaborative Computational Project No. 6 of the Engineering and Physical Sciences Research Council (UK). http://www.theochem.ru.nl/molscat/TOC.html

4. M.H. Alexander, D.E. Manolopoulos, H.-J. Werner, B. Follmeg, HIBRIDON; available at http://www2.chem.umd.edu/groups/alexander/hibridon/hib43/hibhelp.html

5. J. Loreau, P. Zhang, A. Dalgarno, *J. Chem. Phys*. **135**, 174301(2011).

6. N. Balakrishnan, A. Dalgarno, and R. C. Forrey, *J. Chem. Phys*. **113**, 621-627 (2000).

7. F. Lique, J. Cernicharo and P. Cox, *The Astrophysical Journal* **653**, 1342 (2006).

8. F.S. dos Santos, N. Balakrishnan, R.C. Forrey, P.C. Stancil, *J. Chem. Phys.* **138**, 104302 (2013).

9. S.A. Ndengue, R. Dawes, F. Gatti, *J. Phys. Chem. A* **119**, 7712-7723 (2015)

10. L.M.C. Janssen, A. van der Avoird, G.C. Groenenboom, *Phys. Rev. Lett.* **110**, 063201/1 (2013).

11. B. Yang, P. Zhang, X. Wang, P.C. Stancil, J.M. Bowman, N. Balakrishnan, R.C. Forrey, *Nature Communications* **6**, 6629 (2015).

12. B. Yang, M. Nagao, W. Satomi, M. Kimura, and P. C. Stancil, *Astrophys. J*. **765**, 77 (2013).

13. F. Daniel, M.-L. Dubernet, A. Grosjean, *Astron. Astrophys.* **A76**, 536-546 (2011).

14. C. H. Yang, G. Sarma, D. H. Parker, J. J. ter Meulen, and L. Wiesenfeld, *J. Chem. Phys*. **134**, 204308 (2011).

15. A.Faure, L.Wiesenfeld, Y. Scribano, C. Ceccarelli, *Mon. Not. R. Astron. Soc*. **420**, 699- 704 (2012).

16. M. Wernli, L. Wiesenfeld; A. Faure; P. Valiron, *Astron. Astrophys*. **464**, 1147-1154, (2007).

17. N. Troscompt, A. Faure, L.Wiesenfeld, C.Ceccarelli, P.Valiron, *Astron. Astrophys*. **493**, 687-696, (2009).

18. D. Rabli, D.R. Flower, *Mon. Not. R. Astron*. Soc. **406**, 95-110 (2010).

19. A.Faure , K. Szalewicz and L. Wiesenfeld, *J. Chem. Phys* **135**, 024301 (2011).

20. E. Roueff, F. Lique*, Chem. Rev*. **113**, 8906-8938, (2013).

21. A. Semenov, M. Ivanov and D. Babikov, *J. Chem. Phys*. **139**, 74306 (2013).

22. A. Semenov and D. Babikov, *J. Chem. Phys*. **140**, 044306 (2014).

23. A. Semenov and D. Babikov, *J. Phys. Chem. Lett*. **5**, 275 (2014).

24. M. Ivanov, M.-L. Dubernet and D. Babikov, *J. Chem. Phys*. **140**, 134301 (2014).

25. A. Semenov, M.-L. Dubernet and D. Babikov*, J. Chem. Phys*. **141**, 114304 (2014).

26. A. Semenov; D. Babikov*, J. Phys. Chem. Lett*. **6**, 1854-1858 (2015).

27. A. Semenov; D. Babikov, *J. Phys. Chem. A*. **119**, 12329-12338 (2015).

28. D. Babikov and A. Semenov, *J. Phys. Chem. A* **120**, 319-331 (2016).

29. A. Semenov and D. Babikov, *J. Phys. Chem. A* **120**, 3861 - 3866 (2016).

30. P.J. Agg, D.C. Clary, *J. Chem. Phys*. **95**, 1037-1048 (1991).

31. E. Jehin, D. Bockelée-Morvan, N. Dello Russo, J. Manfroid, D. Hutsem_ekers, H. Kawakita, H. Kobayashi, R. Schulz, A. Smette, J. Stöuwe, M. Weiler, C. Arpigny, N. Biver, A. Cochran, J. Crovisier, P. Magain, H. Rauer, H. Sana, R. J. Vervack, H. Weaver, and J.-M. Zucconi, *Earth Moon and Planets* **105**, 343 (2009).

32. P. Hartogh, D. C. Lis, D. Bockelée-Morvan, M. de Val-Borro, N. Biver, M. Küppers, M. Emprechtinger, E. A. Bergin, J. Crovisier, M. Rengel, R. Moreno, S. Szutowicz & G. A. Blake, *Nature* **478**, 218 (2011).

33. D. Bockelée-Morvan, N. Biver, B. Swinyard, M. de Val-Borro, J. Crovisier, P. Hartogh, D. C. Lis, R. Moreno, S. Szutowicz, E. Lellouch, M. Emprechtinger, G. A. Blake, R. Courtin, C. Jarchow, M. Kidger, M. Küppers, M. Rengel, G. R. Davis, T. Fulton, D. Naylor, S. Sidher, H. Walker, *Astron. & Astroph*. **544**, L15 (2012).

34. E. F. van Dishoeck, L. E. Kristensen, A. O. Benz, E. A. Bergin, P. Caselli, J. Cernicharo, F. Herpin, M. R. Hogerheijde, D. Johnstone, R. Liseau, B. Nisini, R. Shipman, M. Tafalla, F. van der Tak, F. Wyrowski, Y. Aikawa, R. Bachiller, A. Baudry, M. Benedettini, P. Bjerkeli, G. A. Blake, S. Bontemps, J. Braine, C. Brinch, S. Bruderer, L. Chavarria, C. Codella, F. Daniel, T. de Graauw, E. Deul, A. M. di Giorgio, C. Dominik, S. D. Doty, M. L. Dubernet, P. Encrenaz, H. Feuchtgruber, M.

Fich, W. Frieswijk, A. Fuente, T. Giannini, J. R. Goicoechea, F. P. Helmich, G. J. Herczeg, T. Jacq, J. K. J_rgensen, A. Karska, M. J. Kaufman, E. Keto, B. Larsson, B. Leoch, D. Lis, M. Marseille, C. McCoey, G. Melnick, D. Neufeld, M. Olberg, L. Pagani, O. Pani_c, B. Parise, J. C. Pearson, R. Plume, C. Risacher, D. Salter, J. Santiago-Garcffa, P. Saraceno, P. Stöauber, T. A. van Kempen, R. Visser, S. Viti, M.Walmsley, S. F.Wamper, and U. A. Yildiz, *Pub. Astron. Soc. Pacific*. **123**, 138 (2011).

35. W. Demtröder, Molecular Physics, John Wiley and Sons Ltd., (2008).

36. Varshalovich, D. A.; Moskalev, A. N.; Khersonskii, V. K.; Quantum theory of angular momentum, World Scientific, Singapore, (1988).

37. E. M. Mas, K. Szalewicz, R. Bukowski and B. Jeziorski, *J. Chem. Phys*. **107**, 4207-4218 (1997).

38. P. Jankowski, G. Murdachaew, R. Bukowski, O. Akin-Ojo, C. Leforestier, and K. Szalewicz, *J. Phys. Chem. A* **119**, 2940−2964 (2015).

39. E.F.van Dishoeck, L.E. Kristensen, E.A. Bergin, *et al. Astronomy and Astrophysics* **542**, A8 (2012).

40. C. Ceccarelli, D. J. Hollenbach, and A. G. G. M. Tielens, *Astrophys. J.* **471**, 400 (1996).

41. M. J. Kaufmann and D. A. Neufeld, *Astrophys. J*. **456**, 611 (1996).

42. A. Coutens, C. Vastel, E. Caux, C. Ceccarelli, S. Bottinelli, L. Wiesenfeld, A. Faure, Y. Scribano, and C. Kahane, *Astron. & Astrophys*. **539**, A132 (2012).

43. V. Taquet, P. S. Peters, C. Kahane, C. Ceccarelli, A. López-Sepulcre, C. Toubin, D. Duflot, and L. Wiesenfeld, *Astron. & Astrophys*. **550**, A127 (2013).

44. E. Jehin, D. Bockelée-Morvan, N. Dello Russo, J. Manfroid, D. Hutsem_ekers, H. Kawakita, H. Kobayashi, R. Schulz, A. Smette, J. Stöuwe, M. Weiler, C. Arpigny, N. Biver, A. Cochran, J. Crovisier, P. Magain, H. Rauer, H. Sana, R. J. Vervack, H. Weaver, and J.-M. Zucconi, *Earth Moon and Planets* **105**, 343 (2009).

45. P. Hartogh, D. C. Lis, D. Bockelée-Morvan, M. de Val-Borro, N. Biver, M. Küppers, M. Emprechtinger, E. A. Bergin, J. Crovisier, M. Rengel, R. Moreno, S. Szutowicz & G. A. Blake, *Nature* **478**, 218 (2011).

46. M. Kirste, X. Wang, H.C. Schewe, G. Meijer, K. Liu, A. van der Avoird, L.M. Janssen, K.B. Gubbels, G.C. Groenenboom, S.Y. van de Meerakker, *Science* **338**, 1060-1063, (2012).

47. S.A. Ndengue, R. Dawes, F. Gatti, *J. Phys. Chem. A* **119**, 7712-7723 (2015).

48. B. Mandal, A. Semenov, D.Babikov, *„On Calculations of Differential Cross Sections Using Mixed Quantum/Classical Theory of Inelastic Scattering”*, *Chem. Phys. Lett.* (submitted) (2017).

SUMMARY AND FUTURE WORK

At his point the mixed quantum/classical theory presents new and powerful instrument in the field of scattering dynamics. We saw that for a broad range of scattering systems (H_2O + He, H_2 + He, Na + N_2, CO + He, CH_3OOCH + He, H_2 +H_2, N_2 +H_2) the method demonstrates excellent accuracy for practical implementations and drastically decreases computational time in comparison with the full quantum treatment. This makes MQCT the viable candidate for scattering dynamics calculations relevant to astrochemical use where, among other tasks, it is especially important to study ro-vibrational transitions due to collisions at small organics molecules with background gas (H_2,He) and the full quantum treatment is practically impossible in the temperature range of interest, while the classical trajectory simulations have unresolved issues with final state analysis and cannot reproduce even the right order of magnitude of scattering cross sections. We want to emphasize that our implementation of MQCT is fully coupled which has never been developed and tested before. We carried out benchamark calucltions on several scattering systems covering various ranges of reduced mass, scattering potential features and molecular structure. The level of agreement between full quantum results and MQCT calculations is excellent and typically very detailed.

The significant impact on the field of study has been made by obtaining the scattering cross sections in collisions with helium for astrochemically very important molecule methyl formate (CH_3OOCH). We calculated scattering cross sections at collision energies where the full quantum treatment is practically impossible. This means that our results are the first results in a relatively broad range of scattering energies for a

complex organic molecule in space. For low scattering energies where quantum data is available the agreement with MQCT results is encouraging. This is a first successful attempt to use MQCT for astrochemical applications where other methods are not practical. Our results obtained within MQCT framework for CH_3OOCH + He can be used as reference data for practical astrochemical applications. Therefore, MQCT presents a substantial impact in the field of scattering dynamics as a fundamental theory and in the field of astrochemistry as a new computational tool which can complement and sometimes replace the existing full quantum approach. Currently we are working on packaging of the MQCT scattering code. It is going to be published as a friendly user suit and available for public use [1].

Another significant achievement to emphasize is inelastic scattering of two molecules. For such systems, even for realitevly small molecules, calculations of inelastic scattering of relatively can be challenging, and often computationally unaffordable. The most complicated case which has been treated within full quantum framework is H_2O + H_2 system. Interestingly, rotational state-to-state coefficients for such important systems as H_2O + H_2O or H_2O+ HCN remain formidable and have never been attempted within the full quantum framework. In the dissertation, we extended the range of MQCT applications to molecule + molecule scattering and applied it to H_2+H_2, N_2+H_2 and H_2O+H_2O systems. The level of agreement between MQCT and full quantum approach for H_2+H_2 and N_2+H_2 rotational scattering has been found excellent in a broad range of collisional energies and for various state-to-state transitions. Importantly MQCT treats correctly exchange symmetry and it is applicable for treatment of identical molecule scattering which was checked for the H_2 + H_2 system. For astrochemically important H_2O

+ H_2O system it allowed us to carry out inelastic scattering calculations in a broad range of scattering energies and with reasonably large rotational basis set. These data are the first and only data for this system. They are very useful for astrochemical calculations, but also set up the groundwork for possible full quantum calculations of H_2O + H_2O in the future.

Several methodological issues, within MQCT, remain to be unaddressed. First, there is a problem with description of differential cross sections for inelastic transitions and in the backscattering regime, which are not yet treated properly within MQCT framework. First steps to resolve this issue have already been made [2] and the results are encouraging.

The second issue is to define certain clear criteria of MQCT applicability. It was already shown [3] how MQCT errors (relative to full quantum data) correlate with state-to-state transition energy (size of the quanta), reduced mass of the system, and the De Broglie wavelength. Also, preliminary studies [4] revealed that the matrix elements of the interaction potential themselves can also play a significant role in determining whether MQCT results are expected to be accurate or not.

The third problem is that it is still unclear how to treat quantum scattering resonances within MQCT. Indeed, we see that trajectory orbiting occurs in the low scattering energy regime, which usually correspond to quantum resonant behavior. We could reproduce non-resonant background by excluding orbiting trajectories but future investigation is required to find out how to treat these orbiting trajectories, to describe scattering resonances. The idea is that in principle orbiting trajectories can indicate the Feshbach resonances, since they correspond to bound states due to coupling between

internal degree(s) of freedom and the scattering coordinate. On the other hand, “shape resonances” which correspond to quasi bound level where the internal state of the molecule remains unchanged (i.e. quantum tunneling through the barrier) may not be treated by MQCT, since this coordinate is described classically.

Importantly, there are also several potential areas where the MQCT method can be applied and may happen to be the only option. One of them is the description of rotatinal-vibrational transitions. For example, the bending vibrational mode in water (1594.7 cm^{-1}) can be involved in ro-vibrational energy transfer in collisions with He and H_2 in cosmic space, but inclusion of even single vibrational mode into the basis set (with a reasonably large number of rotational states) is already challenging to treat with full quantum dynamics. Moreover, calculations of energy transfer near dissociation threshold which is important for description of recombination and collision-induced dissociation is impossible within the full quantum framework where a large basis set with respect to both vibrational and rotational degrees of freedom is needed. On the contrary MQCT method is affordable for such problems and we have already applied it [5] for quenching of scattering resonances in S_2^* by Ar collision, a process that is important to understand for modelling of sulfur chemistry in the anoxic Archean atmosphere of ancient Earth. These developments are very encouraging and broaden applications of MQCT dramatically.

These areas define the future direction of MQCT development and may open up new opportunities for MQCT users and new applications for scattering dynamics.

BIBLIOGRAPHY for Summary

1. "MQCT. II. A User-Ready Program for Calculations of Inelastic Scattering, Including Collisions of Two Asymmetric-Top Rotor Molecules", A. Semenov and D. Babikov, *J. Comp. Chem.* (in preparation) (2017).

2. "On Calculations of Differential Cross Sections Using Mixed Quantum/Classical Theory of Inelastic Scattering", B. Mandal, A. Semenov, and D. Babikov, *Chem. Phys. Lett*. (to be submitted) (2017).

3. D. Babikov and A. Semenov, *J. Phys. Chem. A.* **120** (3), 319 (2016).

4. "On Issues with Ehrenfest Treatment of Collision Dynamics and Possible Ways of Resolving Those Within Framework of the Mixed Quantum/Classical Theory", A. Semenov and D. Babikov, *J. Chem. Phys.* (to be submitted) (2017).

5. "One Possible Source of Mass-Independent Fractionation of Sulfur Isotopes in the Archean Atmosphere of Earth" D. Babikov, A. Semenov and, A. Teplukhin, *Geochem. Cosmochem. Acta* (in press), (2017).